/VOLUME 81 JULY 28, 1977 NUMBER 15

JPCHAx

THE JOURNAL OF PHYSICAL CHEMISTRY

PUBLISHED BIWEEKLY BY THE AMERICAN CHEMICAL SOCIETY

THE JOURNAL OF

PHYSICAL CHEMISTRY

Published by the
AMERICAN CHEMICAL SOCIETY
BOOKS AND JOURNALS DIVISION

D. H. Michael Bowen, Director

Marjorie Laflin, Assistant to the Director

Editorial Department: Charles R. Bertsch, Head; Marianne C. Brogan, Associate Head; Celia B. McFarland, Joseph E. Yurvati, Assistant Editors

Magazine and Production Department: Bacil Guiley, Head

Research and Development Department: Seldon W. Terrant, Head

Advertising Office: Centcom, Ltd., 25 Sylvan Road South, Westport, Conn. 06880.

Published biweekly by the American Chemical Society at 20th and Northampton Sts., Easton, Pennsylvania 18042. Second class postage paid at Washington, D.C. and at additional mailing offices.

Editorial Information

Instructions for authors are printed in the first issue of each volume. Please conform to these instructions when submitting manuscripts.

Manuscripts for publication should be submitted to *The Journal of Physical Chemistry*, Department of Chemistry, University of Minnesota, Minneapolis, Minn. 55455. Correspondence regarding **accepted papers and proofs** should be directed to the Editorial Department at the ACS Easton address.

Page charges of $60.00 per page may be paid for papers published in this journal. Payment does not affect acceptance or scheduling of papers.

Bulk reprints or photocopies of individual articles are available. For information write to Business Operations, Books and Journals Division at the ACS Washington address.

Requests for **permission to reprint** should be directed to Permissions, Books and Journals Division at the ACS Washington address. The American Chemical Society and its Editors assume no responsibility for the statements and opinions advanced by contributors.

Subscription and Business Information

1977 Subscription rates—including surface postage

	U.S.	PUAS	Canada, Foreign
Member	$24.00	$33.00	$34.00
Nonmember	96.00	105.00	106.00
Supplementary material	15.00	19.00	20.00

Air mail and air freight rates are available from Membership & Subscription Services, at the ACS Columbus address.

New and renewal subscriptions should be sent with payment to the Office of the Controller at the ACS Washington address. **Changes of address** must include both old and new addresses with ZIP code and a recent mailing label. Send all address changes to the ACS Columbus address. Please allow six weeks for change to become effective. **Claims for missing numbers** will not be allowed if loss was due to failure of notice of change of address to be received in the time specified: if claim is dated (a) North America—more than 90 days beyond issue date, (b) all other foreign—more than 1 year beyond issue date; or if the reason given is "missing from files". Hard copy claims are handled at the ACS Columbus address.

Microfiche subscriptions are available at the same rates but are mailed first class to U.S. subscribers, air mail to the rest of the world. Direct all inquiries to Special Issues Sales, at the ACS Washington address or call (202) 872-4554. **Single issues** in hard copy and/or microfiche are available from Special Issues Sales at the ACS Washington address. Current year $4.75. Back issue rates available from Special Issues Sales. **Back volumes** are available in hard copy and/or microform. Write to Special Issues Sales at the ACS Washington address for further information. **Microfilm** editions of ACS periodical publications are available from volume 1 to the present. For further information, contact Special Issues Sales at the ACS Washington address. **Supplementary material** mentioned in the journal appears in the microfilm edition. Single copies may be ordered directly from Business Operations, Books and Journals Division, at the ACS Washington address.

	U.S.	PUAS, Canada	Other Foreign
Microfiche	$2.50	$3.00	$3.50
Photocopy			
1–7 pages	4.00	5.50	7.00
8–20 pages	5.00	6.50	8.00

Orders over 20 pages are available only on microfiche, 4 × 6 in., 24X, negative, silver halide. Orders must state photocopy or microfiche if both are available. Full bibliographic citation including names of all authors and prepayment are required. Prices are subject to change.

American Chemical Society
1155 16th Street, N.W.
Washington, D.C. 20036
(202) 872-4600

Member & Subscription Services
American Chemical Society
P.O. Box 3337
Columbus, Ohio 43210
(614) 421-7230

Editorial Department
American Chemical Society
20th and Northampton Sts.
Easton, Pennsylvania 18042
(215) 258-9111

Notice to Authors last printed in the issue of January 13, 1977

THE JOURNAL OF

PHYSICAL CHEMISTRY

Volume 81, Number 15 July 28, 1977

JPCHAx 81(15) 1437–1530 (1977)

ISSN 0022-3654

Free-Radical Chain Formation of Siloxanes in the Radiolysis of Monosilane–Nitric Oxide Mixtures . . . **J. P. Bare and F. W. Lampe*** 1437

Gas-Phase Photolysis of 1,2-Butadiene at 147.0 nm . . . . **Zaida Diaz and Richard D. Doepker*** 1442

On the Oxidation of Aqueous Br by OH Radicals, Studied by Pulse Radiolysis . . . **Avner Mamou, Joseph Rabani,* and David Behar** 1447

Transients in the Flash Photolysis of Aqueous Solutions of Tris(2,2′-bipyridine)ruthenium(II) Ion . . . **Dan Meisel,* Max S. Matheson, W. A. Mulac, and Joseph Rabani** 1449

Radiation Sensitized Chain Reactions. Aqueous Nitrous Oxide and 2-Propanol . . . **T. G. Ryan and G. R. Freeman*** 1455

Oscillatory Kinetics in Electrochemical Oxidation of Hydrogen in an Almost Anhydrous Solvent . . . **B. E. Conway* and D. M. Novak** 1459

Electron Trapping by Methanol Aggregates in Dilute Solution in Nonpolar Solvents . . . **Thomas E. Gangwer, Augustine O. Allen, and Richard A. Holroyd*** 1469

On the Calculation of the Electrostatic Lattice Energies of α-, β-, and γ-Glycine . . . **J. L. Derissen,* P. H. Smit, and J. Voogd** 1474

The Influence of Ion Pairing on the Electroreduction of Nitromesitylene in Aprotic Solvents. 1. Thermodynamic Aspects . . . . . **B. G. Chauhan, W. R. Fawcett,* and A. Lasia** 1476

A Mass Spectral Study of the Kinetics of Carbon Monoxide Displacement from a Nickel Surface . . . **L. A. Burchfield, L. D. Neff, and L. I. Bone*** 1481

Heterogeneous Photocatalytic Oxidation of Cyanide and Sulfite in Aqueous Solutions at Semiconductor Powders . . . . . **Steven N. Frank and Allen J. Bard*** 1484

Determination of Equilibrium Constants for Electron Donor–Acceptor Complexes by Resonance Raman Spectroscopy . . . **Kirk H. Michaelian, Klaus E. Rieckhoff, and Eva-Maria Voigt*** 1489

Raman Measurements of Temperature Effects on Self-Association in Glycerol . . . **Jerry E. Solomon** 1492

Microwave Study of Perchlorylbenzene . . . **Walther Caminati, Rinaldo Cervellati, and Bruno Lunelli*** 1494

Donor Energy Effects on the Triplet-Sensitized Isomerization of 11-*cis*-Retinal . . . **T. Rosenfeld, O. Kalisky, and M. Ottolenghi*** 1496

Second Moment Studies of the Electron Spin Resonance Line Shape of Trapped Electrons in Sodium–Ice Condensates. Relation to the Molecular Structure Around Trapped Electrons . . . **D. P. Lin and Larry Kevan*** 1498

Electron Spin Resonance Studies of Superoxide Ions Produced by Radiolysis in Alcoholic Media . . . **George W. Eastland and Martyn C. R. Symons*** 1502

Factors Affecting the Conformation of Aromatic Nitro Groups . . . **James R. Holden* and Charles Dickinson** 1505 ■

Ionic and Electrical Conductances in Polyelectrolyte Solutions . . . **A. Schmitt,* R. Varoqui, and J. P. Meullenet** 1514

Isotope Effect in Diffusion of Perdeuteriobenzene and Benzene in a Series of Normal Hydrocarbons at 25 °C . . . **Ian R. Shankland, Pawittar S. Arora, and Peter J. Dunlop*** 1518 ■

Solvent Dielectric Attenuation of Substituent Effects. Field Transmission in Partially Occluded Cavities . . . . . **S. Ehrenson** 1520

COMMUNICATIONS TO THE EDITOR

Hydrogen Bonding to the Charged π Clouds of the Cyclooctatetraene Dianion and Anion Radical . . . **Gerald R. Stevenson* and Aurora Vassos** 1526

Thermochemical Decomposition of Water Catalyzed by Zeolites . . . **Paul H. Kasai* and Roland J. Bishop, Jr.** 1527

Boundary Conditions for Integration of the Equation of Continuity . . . . . **Raymond M. Fuoss** 1529

■ Supplementary and/or miniprint material for this paper is available separately (consult the masthead page for ordering information); it will also appear following the paper in the microfilm edition of this journal.

* In papers with more than one author, the asterisk indicates the name of the author to whom inquiries about the paper should be addressed.

AUTHOR INDEX

Allen, A. O., 1469
Arora, P. S., 1518

Bard, A. J., 1484
Bare, J. P., 1437
Behar, D., 1447
Bishop, R. J., Jr., 1527
Bone, L. I. 1481
Burchfield, L. A., 1481

Caminati, W., 1494
Cervellati, R., 1494
Chauhan, B. G., 1476
Conway, B. E., 1459

Derissen, J. L., 1474
Diaz, Z., 1442
Dickinson, C., 1505
Doepker, R. D., 1442
Dunlop, P. J., 1518

Eastland, G. W., 1502
Ehrenson, S., 1520

Fawcett, W. R., 1476
Frank, S. N., 1484
Freeman, G. R., 1455
Fuoss, R. M., 1529

Gangwer, T. E., 1469

Holden, J. R., 1505
Holroyd, R. A., 1469

Kalisky, O., 1496
Kasai, P. H., 1527
Kevan, L., 1498

Lampe, F. W., 1437
Lasia, A., 1476
Lin, D. P., 1498
Lunelli, B., 1494

Mamou, A., 1447
Matheson, M. S., 1449
Meisel, D., 1449
Meullenet, J. P., 1514
Michaelian, K. H., 1489
Mulac, W. A., 1449

Neff, L. D., 1481
Novak, D. M., 1459

Ottolenghi, M., 1496

Rabani, J., 1447, 1449
Rieckhoff, K. E., 1489
Rosenfeld, T., 1496
Ryan, T. G., 1455

Schmitt, A., 1514
Shankland, I. R., 1518
Smit, P. H., 1474
Solomon, J. E., 1492
Stevenson, G. R., 1526
Symons, M. C. R., 1502

Varoqui, R., 1514
Vassos, A., 1526
Voigt, E. M., 1489
Voogd, J., 1474

THE JOURNAL OF
PHYSICAL CHEMISTRY

VOLUME 81, NUMBER 15 JULY 28, 1977

Free-Radical Chain Formation of Siloxanes in the Radiolysis of Monosilane–Nitric Oxide Mixtures[1]

J. P. Bare and F. W. Lampe*

Davey Laboratory, Department of Chemistry, The Pennsylvania State University, University Park, Pennsylvania 16802 (Received March 7, 1977)

Publication costs assisted by the U.S. Energy Research and Development Administration

The gas-phase radiation chemistry of SiH_4 and SiH_4–NO mixtures at 300 K has been investigated. γ-ray irradiation of pure SiH_4 at 100 Torr pressure yields H_2 and Si_2H_6 as principal products with 100-eV yields of $G(H_2) = 15.2$ and $G(Si_2H_6) = 7.0$. A brown polymeric deposit is also observed. The addition of NO at pressures of 2, 5, 10, 20, and 30 Torr reduces the yield of Si_2H_6 to $G(Si_2H_6) = 2.9$. This represents complete suppression of the formation of Si_2H_6 by reaction of SiH_3 radicals. The residual yield of Si_2H_6 must be due to reactions of SiH_3^+ and $Si_2H_7^+$ ions as well as SiH_2 radicals that are formed directly from SiH_4 following the primary act of energy absorption. NO is consumed by a free-radical chain reaction that involves SiH_4 and produces N_2O, $(SiH_3)_2O$, $(SiH_3O)_2SiH_2$, and $SiH_3(OSiH_2)_2OSiH_3$ as products.

Introduction

The radiolysis of gaseous SiH_4 produces H_2 and Si_2H_6 as the major products with trace amounts of Si_3H_8 and Si_4H_{10} and a polymeric film of silicon hydride polymer also being formed.[2-4] The addition of C_2H_4 suppresses the formation of both H_2 and Si_2H_6 but does not do so completely.[4] It has been suggested, therefore, that at least a part of the H_2 and Si_2H_6 formation must be due to processes not involving H atoms and SiH_3 radicals.[4] The choice of C_2H_4 as a radical-reaction suppressor is not a particularly good one because at the concentration required for complete scavenging[4,5] it absorbs an appreciable fraction of the radiation energy. In addition, it can compete effectively with SiH_4 for reaction with ionic species present[6] and both effects can greatly complicate the system. The use of NO as a radical scavenger in the radiolysis of SiH_4 has not been investigated in any detail, although preliminary experiments[4] indicated that it is much more efficient than C_2H_4 in suppressing Si_2H_6 formation.

The $Hg(^3P_1)$ photosensitized decompositon of SiH_4 has been well studied[7-10] and the free-radical scavenging effect of NO on the system[9,10] appears to be understood. The products of the photosensitized reaction are identical with those of the radiolysis but the reaction follows a purely free-radical path that is initiated by the formation of H and SiH_3 in the primary interaction of $Hg(^3P_1)$ with SiH_4. In the absence of NO these species react further by[8-13]

$$H + SiH_4 \rightarrow H_2 + SiH_3 \quad (1)$$

$$SiH_3 + SiH_3 \rightarrow SiH_4 + SiH_2 \quad (2)$$

$$SiH_3 + SiH_3 \rightarrow Si_2H_6^* \quad (3)$$

$$Si_2H_6^* + M \rightarrow Si_2H_6 + M \quad (4)$$

$$Si_2H_6^* \rightarrow SiH_4 + SiH_2 \quad (5)$$

$$SiH_2 + SiH_4 \rightarrow Si_2H_6 \quad (6)$$

The addition of very small amounts of NO completely suppresses the formation of Si_2H_6 by efficient interception of SiH_3, which prevents the occurrence of (2)–(6). The yield of H_2 is enhanced,[9] however, by the presence of NO; and N_2, N_2O, and $SiH_3(OSiH_2)_nOSiH_3$ (n = 0, 1, 2) are observed as additional products.[9-11] Moreover, the siloxanes and N_2O appear to be formed by a chain reaction.[9,11] It has been shown that the most likely mechanistic explanation of these facts involves the occurrence of[11]

$$SiH_3 + NO \rightarrow H_3SiON \quad (7)$$

$$H_3SiON + NO \rightarrow H_3SiO\cdot + N_2O \quad (8)$$

$$H_3SiO\cdot + SiH_4 \rightarrow H_3SiOSiH_2\cdot + H_2 \quad (9)$$

$$H_3SiOSiH_2\cdot + SiH_4 \rightarrow H_3SiOSiH_3 + SiH_3 \quad (10)$$

$$H_3SiOSiH_2\cdot + NO \rightarrow H_3SiOSiH_2ON \quad (11)$$

$$H_3SiOSiH_2ON + NO \rightarrow H_3SiOSiH_2O\cdot + N_2O \quad (12)$$

$$H_3SiOSiH_2O\cdot + SiH_4 \rightarrow H_3SiOSiH_2OSiH_2\cdot + H_2 \quad (13)$$

$$H_3SiOSiH_2OSiH_2\cdot + SiH_4 \rightarrow H_3SiOSiH_2OSiH_3 + SiH_3 \quad (14)$$

$$H_3SiOSiH_2OSiH_2 + NO \rightarrow H_3SiOSiH_2OSiH_2ON \quad (15)$$

etc.

It is to be expected that processes 1–6 and 7–15 will play a role in the radiolysis of SiH_4 and SiH_4–NO mixtures, respectively, and thereby suppress the free-radical component of the radiolysis. With this expectation, we have studied the effect of NO on the γ-ray radiolysis of gaseous SiH_4 and this paper is a report of our findings.

Experimental Section

All irradiations were conducted in the gas phase in cylindrical Pyrex vessels of 25-cm length and of 150–200-cm^3 volume. γ rays from the ^{60}Co irradiation facility of the Breazeale Nuclear Reactor of The Pennsylvania State University were used in all experiments as the initiating ionizing irradiation. Dose rates (to 100 Torr of SiH_4) ranged from 0.88×10^{16} to 1.17×10^{16} eV cm^{-3} h^{-1} as determined by propylene dosimetry ($G(H_2) = 1.1$)[15] and standard electron energy loss data.[16]

Analysis of the irradiated gases was accomplished by a combination of gas chromatography and mass spectrometry. A custom made gas chromatograph with a volumetric gas inlet system was employed, using a Gow-Mac thermal conductivity detector and Gow-Mac Model 40-001 power supply unit. Quantitative analysis of hydrogen was carried out by gas chromatography using a 7-mm o.d. by 3-m coiled glass column packed with 35 g of 5A molecular sieve from the Burrell Corp., nitrogen as carrier gas, and a flow rate of 40 mL min^{-1}. Quantitative analysis of silane and nitric oxide was carried out by mass spectrometry and/or by gas chromatography using a $^1/_8$-in. by 3.7-m coiled stainless steel column packed with Porapak Q-S from Supelco, Inc., with helium as a carrier gas at a flow rate of 60 mL min^{-1}. Mass-spectrometric analysis of all gases except hydrogen was carried out on an Associated Electrical Industries Model MS-902 mass spectrometer, using neon as an internal standard.

All gases used were obtained from the Matheson Co. and all except the gas chromatography carrier gases were further purified before use. Monosilane was purified by three repetitive cycles of degassing at −195 °C and thawing to room temperature followed by distillation from −131 °C to a trap at −195 °C to remove suspected major impurities, hydrogen and disilane. Nitric oxide was purified by freezing on to a degassed silica gel trap at −195 °C followed by degassing at 195 °C. The frozen nitric oxide was permitted to warm slowly and the middle 70% fraction was collected for use. Propylene was purified by three repetitive cycles of degassing at −195 °C and thawing to room temperature. Neon was purified by passing through a trap at −195 °C to remove any condensible impurities. Purity of all gases was checked via gas chromatography and mass spectrometry. No impurities greater than background level were observed.

Results and Discussion

1. *Monosilane.* The products of the γ-ray irradiation of SiH_4 at 100 Torr pressure and room temperature are

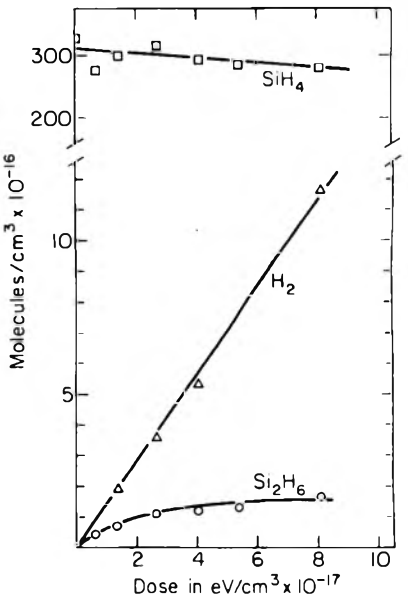

Figure 1. Dependence of reactant and product concentrations on dose in the γ irradiation of SiH_4.

H_2, Si_2H_6, and a light brown solid deposit on the surface of the vessel. In the highest dose experiments (8.06×10^{17} eV cm^{-3}), which correspond to about 8% conversion of SiH_4, mass-spectrometric peaks corresponding to Si_3H_8 were detected; however, quantitative analysis of this compound was not feasible.

The concentrations of H_2, Si_2H_6, and SiH_4 as functions of radiation dose are shown in Figure 1. From the initial slopes of the curves, we derive the following 100-eV yields: $G(H_2) = 15.2 \pm 0.4$, $G(Si_2H_6) = 7.0 \pm 2.0$, and $G(-SiH_4) = 36 \pm 27$ molecules/100 eV. These G values are in agreement, within experimental error, with previous studies[1-4] of the radiolysis of SiH_4 when the reported pressure and dose-rate dependencies are taken into account. As observed in previous work[2-4] $G(Si_2H_6)$ decreases quite sharply with increasing dose, an effect which is most probably due to the much more rapid reactions of H atoms,[17,18] SiH_3 radicals,[17] SiH_2^+ ions,[19] and SiH_3^+ ions[19] with Si_2H_6 than with SiH_4.

The magnitude of the 100-eV yields, which are considerably greater than the corresponding values in the radiolysis of CH_4,[20] have led to the suggestion[2,4,21] that the reaction proceeds, at least in part, by a short chain mechanism. There is no reason to doubt that radical reactions 1–6, established from photosensitization studies, are playing an important role in producing the major products of the radiolysis, but these processes do not constitute a chain. However, in addition to the free-radical reactions, ion/molecule reactions characteristic of ionized SiH_4 must also take part and it is this additional mode of reaction that distinguishes the radiolysis from the photosensitized decomposition.

The ion/molecule reactions characteristic of ionized SiH_4 have been identified and the specific reaction rates have been measured.[22,23] Considering only the major primary ions from SiH_4, namely, SiH_2^+ and SiH_3^+, the principal ionic reactions at the pressures obtaining in the radiolysis are

$$SiH_2^+ + SiH_4 \rightarrow SiH_3^+ + SiH_3 \quad (16)$$

$$SiH_2^+ + SiH_4 \rightarrow Si_2H_4^+ + H_2 \quad (17)$$

$$Si_2H_4^+ + SiH_4 \rightarrow Si_3H_6^+ + H_2 \quad (18)$$

$$SiH_3^+ + 2SiH_4 \rightarrow Si_2H_7^+ + SiH_4 \quad (19)$$

$$Si_2H_7^+ + SiH_4 \rightarrow Si_2H_6 + H_2 + SiH_3^+ \quad (20)$$

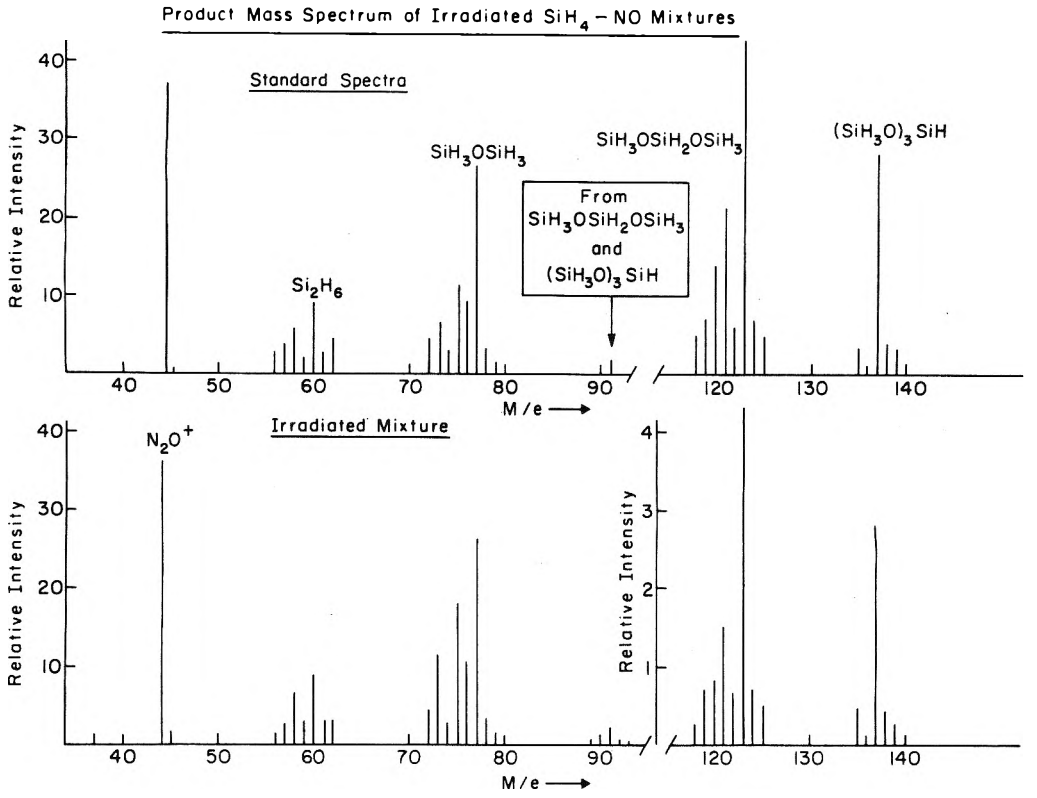

Figure 2. Comparison of the mass spectrum of a γ-irradiated SiH_4–NO mixture (100 Torr of SiH_4; 10 Torr of NO) with mass spectra of individual compounds.

Reactions 17, 18, and higher analogues provide the primary polymerization pathway leading to H_2 and the brown polymeric deposit. Reactions 19 and 20 constitute a chain reaction for formation of H_2 and Si_2H_6, which must necessarily be short, since the cycle of (19) and (20) is slightly endothermic.

It has recently been established in our laboratory[24] that SiH_3^+ ions do not react with NO and, since $Si_2H_7^+$ also contains an even number of electrons, it most probably does not react with NO either. On the other hand, as already mentioned, NO reacts very efficiently with SiH_3 radicals[9,10] and therefore should be an ideal reagent to suppress free-radical reactions 2–6 without affecting (19) and (20). Reactions 16 and 18 are so fast[22,23] that NO could affect their occurrence only at concentrations approaching that of SiH_4.

2. *Monosilane–Nitric Oxide Mixtures.* The addition of NO has a striking effect on the radiation chemistry of SiH_4. The yield of Si_2H_6 is reduced to about 41% of the value found in the absence of NO, while the yield of H_2 is very little affected. In addition, considerable amounts of N_2O and SiH_3OSiH_3 and smaller amounts of higher siloxanes are formed. As an example of the reaction product formation, Figure 2 shows a comparison of the mass spectrum of an irradiated mixture, containing initially 100 Torr of SiH_4 and 10 Torr of NO, with mass spectra of pure samples of N_2O,[5] Si_2H_6,[25] SiH_3OSiH_3,[26] SiH_3O-SiH_2OSiH_3,[26] and $(SiH_3O)_3SiH$[26] in the m/e range of 36–139. There is little doubt that the above five compounds plus H_2 account essentially quantitatively for the observed reaction products. N_2 may also be a product but analysis for it was not feasible. Although the spectrum of tetrasiloxane in the m/e 135–139 region matches that of $(SiH_3O)_3SiH$, we think it more likely that the compound produced in the irradiation is the isomer $SiH_3(OSiH_2)_2$-$OSiH_3$. It is often difficult to differentiate the mass spectra of structural isomers, especially in a limited mass range.

The selectivity of the radiation-induced reaction between

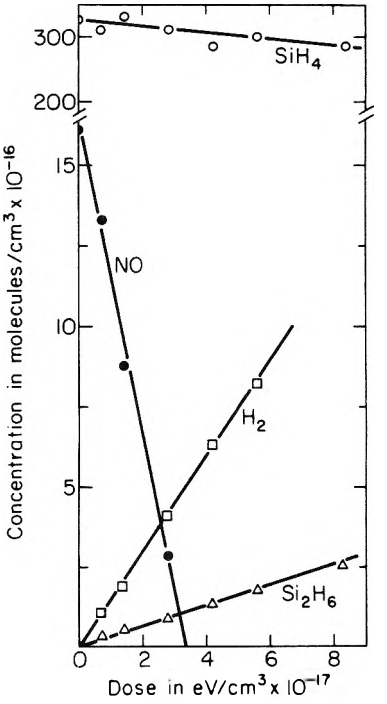

Figure 3. Dependence of reactant and product concentrations on dose in the γ irradiation of a SiH_4–NO mixture (100 Torr of SiH_4; 5 Torr of NO).

NO and SiH_4 deserves comment. Using the mass spectrum of the irradiated mixture in Figure 2 and standard mass spectra[25,26] of the pertinent compounds, one may conclude that N_2O accounts nearly quantitatively for the NO reacted with 70% of the NO reaction being accounted for by the following stoichimetry:

$$2SiH_4 + 2NO \rightarrow SiH_3OSiH_3 + N_2O + H_2 \quad (21)$$

The remainder of the NO reacted is accounted for by

TABLE I: 100-eV Yields in Radiolysis of SiH_4-NO Mixtures[a]

Compd	G(molecules/100 eV) at P(NO) in Torr					
	0	2	5	10[b]	20	30
SiH_4	−36 ± 27		−53 ± 18		−90 ± 22	
NO			−49 ± 3	−39 ± 3	−49 ± 8	−64 ± 10
H_2	−15.2 ± 0.4	13 ± 2	15.8 ± 0.3	13 ± 2	14 ± 2	12.7 ± 0.4
Si_2H_6	7.0 ± 2.0	3.0 ± 0.9	3.0 ± 0.1	(2.9 ± 0.9)[b]	2.8 ± 0.1	2.9 ± 0.3
N_2O			18.5 ± 0.8	16 ± 1	16.3 ± 0.8	15.4 ± 0.5
$(SiH_3)_2O$			12.0 ± 0.2	7 ± 1	7.6 ± 0.4	4.6 ± 0.2
$(SiH_3O)_2SiH_2$			3.5 ± 2.0	2.2 ± 0.5	2.3 ± 0.1	0.71 ± 0.1
$SiH_3(OSiH_2)_2OSiH_3$			1.0 ± 0.1	0.43 ± 0.10	0.55 ± 0.10	0.35 ± 0.10

[a] Pressure of SiH_4 was 100 Torr in all experiments. [b] For reasons unknown, but probably related to incorrect dose rate in these experiments, the G values of this series all appeared to be low. The values shown in this column have been corrected by the assumption that $G(Si_2H_6)$ would have the apparent plateau value of 2.9. The multiplicative factor was 1.25.

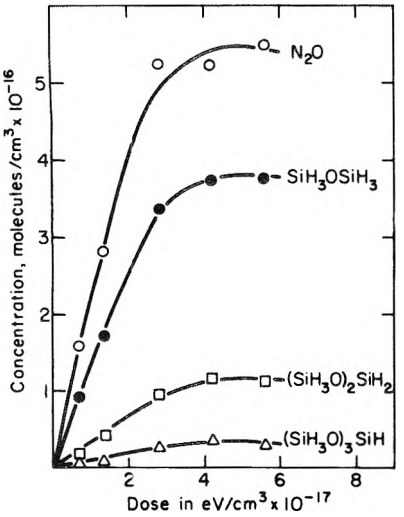

Figure 4. Dependence of product concentration of dose in the γ irradiation of a SiH_4-NO mixture (100 Torr of SiH_4; 5 Torr of NO).

stoichiometry analogous to (21) that produces the higher siloxanes.

In Figures 3 and 4 are shown typical data relative to the dependence of the concentrations of reactants and products on radiation dose for a mixture of 100 Torr of SiH_4 and 5 Torr of NO. Since pure siloxanes were not available to us for calibration, the concentrations of siloxanes were determined from the mass spectrometric data using the spectra of synthetic samples reported by Yoshioka[26] and the assumption that the ratio of total ionization cross sections of SiH_3OSiH_3 and Si_2H_6 is the same as that of CH_3OCH_3 and C_2H_6.[27] The estimated uncertainty in the concentrations of the siloxanes is ±25%.

As may be seen in Figure 3, NO is consumed very efficiently, the 100-eV yield being $G(-NO) = 49$ molecules/100 eV. The magnitude of this yield indicates that NO is being depleted by a chain reaction. The same conclusion was reached in studies of the effect of NO on the $Hg(^3P_1)$-photosensitized decomposition of SiH_4.[9,11] The 100-eV yields for the decomposition of SiH_4 are subject to considerable error because of the necessity of measuring small differences between relatively large numbers. However, the value from Figure 3 of $G(-SiH_4) = 53$ is probably a real increase over that obtained in the absence of NO (cf. Figure 1). It indicates that most of the SiH_4 is being consumed in the reaction with NO and that NO and SiH_4 are reacting with a nearly 1:1 stoichiometry as in (21). The yield of H_2, i.e., $G(H_2) = 15.8$, may represent a slight increase but one cannot be sure because within experimental error there could be no change. As will be seen later, the addition of more NO seems to lead ultimately to a slight decrease in $G(H_2)$.

In striking contrast to the photosensitized reaction[9,11] is the fact that in the radiolysis Si_2H_6 remains a primary product, with a 100-eV yield from Figure 3 of $G(Si_2H_6) = 3.0$. Comparing this with the results in Figure 1, it is seen that 5% of NO reduces $G(Si_2H_6)$ to 41% of the value found in the absence of NO. By comparison, in the photosensitized decomposition, the presence of less than 1% completely suppresses Si_2H_6 formation.[9,11] As will be shown, within experimental error, higher concentrations of NO do not change $G(Si_2H_6)$ from the value found with 5 Torr of NO. Therefore, one must conclude that in the radiolysis of SiH_4, 41% of the Si_2H_6 is formed by processes not involving SiH_3 radicals. This is to be compared with a value of 38% found in radical scavenging experiments using C_2H_4.[4]

It is worth pointing out that, as shown in Figure 3, the yield of Si_2H_6 does not decrease with increasing dose. Thus NO and the products derived from it appear to eliminate the autoscavenging effect that Si_2H_6 has on the radiolysis of pure SiH_4. A similar suppression of the autoscavenging by Si_2H_6 was observed when C_2H_4 was used as a radical suppressor.[4]

Most probably the nonsuppressible path of Si_2H_6 formation in the radiation chemistry of SiH_4 is that depicted by the chain process 19 and 20. Such chains are short because $G(Si_2H_6)$ is not very large. In addition, insertion reactions of SiH_2 radicals, originating, not by (2), but in a primary process following energy absorption, probably also contribute to the nonscavengable Si_2H_6. Recent experiments in this laboratory[28] have shown that in the 147-nm photolysis of SiH_4 about 50% of the Si_2H_6 formed cannot be suppressed by NO.

The concentrations of N_2O and the siloxanes as functions of the total dose are shown in Figure 4. From the initial slopes of these curves, it may be seen that these three siloxanes are stoichiometrically equivalent to the N_2O formed and that the concentrations of any other oxygen-containing products must be negligible. Moreover, comparison of the initial G values of Figure 4 with that for depletion of NO from Figure 3 shows that 92% of the NO reacted is accounted for by the four products shown. It is also worth pointing out that all siloxanes are primary products in that they are formed simultaneously and all appear to reach plateaus or maxima at about the same dose as the NO concentration approaches zero.

Initial 100-eV yields were obtained from data similar to that shown in Figures 3 and 4 for several concentrations of NO and the results are summarized in Table I. The large uncertainties in the yields of SiH_4 are due to the measurement of small differences in relatively large numbers but the magnitudes of $G(-SiH_4)$ and $G(-NO)$ indicate that they are being consumed by a chain process. Within experimental error, the values of $G(H_2)$ remain essentially constant although at the highest concentration of NO, there appears to be a slight decrease in yield. The

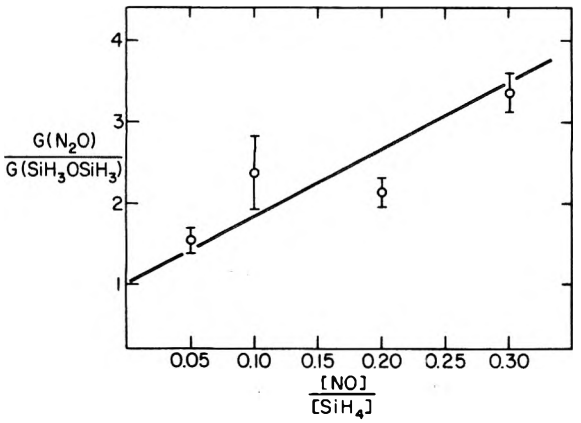

Figure 5. Relative yields of N_2O and SiH_3OSiH_3 as a function of $[NO]/[SiH_4]$ (cf. eq 23).

100-eV yield of Si_2H_6 is reduced to the average plateau value (i.e., complete radical scavenging) of 2.9 at all concentrations of NO employed.

The yields of N_2O and of the accompanying siloxanes leave little doubt that these compounds are the major products of the free-radical chain reaction that consumes NO and SiH_4. The fact that appreciable yields of $(SiH_3)_2O$ and $(SiH_3O)_2SiH_2$ are obtained suggests that the γ-ray irradiation of SiH_4–NO mixtures could be a useful method for their synthesis.

A steady-state treatment of (7)–(15) leads in a straightforward manner to the expression

$$\frac{G(N_2O)}{G(SiH_3OSiH_3)} = 1 + \frac{k_{11}}{k_{10}}\frac{[NO]}{[SiH_4]} \times \left\{2 + \frac{1}{1 + (k_{14}/k_{15})([SiH_4]/[NO])}\right\} \quad (22)$$

If one makes the reasonable assumption that $k_{15}/k_{14} = k_{11}/k_{10}$, then it may be shown that over the range of conditions in Table I, the term in brackets ranges from 2 to 2.6. Within the precision of our data we may take the bracketed term as constant at the average value of 2.3 and write

$$\frac{G(N_2O)}{G(SiH_3OSiH_3)} \simeq 1 + \frac{2.3k_{11}}{k_{10}}\frac{[NO]}{[SiH_4]} \quad (23)$$

The ratio k_{11}/k_{10} may be determined from a plot of the left-hand side of (22) vs. $[NO]/[SiH_4]$. Such a plot is shown in Figure 5, with the line drawn being the best line of intercept unity. The fact that a reasonable fit to the data with an intercept of unity can be made is consistent with the free-radical chain mechanism of (7)–(15). The slope in Figure 5 yields the rate constant ratio $k_{11}/k_{10} = 3.6$. In accord with our assumption in reducing (22) to (23), a similar value is expected for the ratio k_{15}/k_{14}. It is somewhat surprising to find the H abstraction from SiH_4 (10) to be only about 4 times slower than the addition reaction to NO, (11), but this is, in our opinion, the most reasonable interpretation of the results. This conclusion implies that the bond-dissociation energy $D(SiH_3OSiH_2–H)$ is probably significantly greater than the 89 ± 4 kcal/mol reported for $D(SiH_3–H)$.[29]

Acknowledgment. This work was supported by Contract No. EY 76-5-02-3416 with the U.S. Energy Research and Development Administration.

References and Notes

(1) U.S. Energy Research and Development Administration Document No. EY-76-S-02-3416-4.
(2) W. Ando and S. Oae, *Bull. Chem. Soc. Jpn.*, **35**, 1540 (1962).
(3) T. Tiernan, Ph.D. Dissertation, Carnegie Institute of Technology, Pittsburgh, Pa., 1966.
(4) J. F. Schmidt and F. W. Lampe, *J. Phys. Chem.*, **73**, 2706 (1969).
(5) E. Kamaratos, Ph.D. Dissertation, The Pennsylvania State University, University Park, Pa., 1969.
(6) T. M. Mayer and F. W. Lampe, *J. Phys. Chem.*, **78**, 2433 (1974).
(7) H. J. Emeleus and K. Stewart, *Trans. Faraday Soc.*, **34**, 1577 (1936).
(8) H. Niki and G. J. Mains, *J. Phys. Chem.*, **68**, 304 (1964).
(9) M. A. Nay, G. N. C. Woodall, O. P. Strausz, and H. E. Gunning, *J. Am. Chem. Soc.*, **87**, 179 (1965).
(10) R. Varma, A. K. Ray, and B. K. Sahay, *Inorg. Nucl. Chem. Lett.*, **5**, 497 (1969).
(11) E. Kamaratos and F. W. Lampe, *J. Phys. Chem.*, **74**, 2267 (1970).
(12) E. R. Austin and F. W. Lampe, *J. Phys. Chem.*, **80**, 2811 (1976).
(13) B. Reimann, A. Matten, R. Lampert, and P. Potzinger, *Ber. Bunsenges. Phys. Chem.*, **81**, in press.
(14) P. John and J. H. Purnell, *J. Chem. Soc., Faraday Trans. 1*, **69**, 1455 (1973).
(15) K. Yang and P. Grant, *J. Phys. Chem.*, **65**, 1861 (1961).
(16) National Bureau of Standards Circular No. 577, U.S. Government Printing Office, Washington, D.C., 1958.
(17) T. L. Pollock, H. S. Sandhu, A. Jodhan, and O. P. Strausz, *J. Am. Chem. Soc.*, **95**, 1017 (1973).
(18) E. R. Austin and F. W. Lampe, *J. Phys. Chem.*, **81**, 1134 (1977).
(19) T. M. H. Cheng, T-Y. Yu, and F. W. Lampe, *J. Phys. Chem.*, **78**, 1184 (1974).
(20) K. Yang and P. J. Manno, *J. Am. Chem Soc.*, **81**, 3507 (1959).
(21) G. W. Stewart, J. M. S. Henis, and P. P. Gaspapr, *J. Chem. Phys.*, **58**, 890 (1973).
(22) J. M. S. Henis, G. W. Stewart, M. K. Tripodi, and P. P. Gaspar, *J. Chem. Phys.*, **57**, 389 (1972).
(23) T-Y. Yu, T. M. H. Cheng, V. Kempter, and F. W. Lampe, *J. Phys. Chem.*, **76**, 3321 (1972).
(24) T. M. H. Cheng and F. W. Lampe, unpublished results.
(25) P. Potzinger and F. W. Lampe, *J. Phys. Chem.*, **73**, 3912 (1969).
(26) T. Yoshioka, Ph.D. Dissertation, University of Pennsylvania, Philadelphia, Pa., 1967.
(27) A. G. Harrison, E. G. Jones, S. K. Gupta, and G. P. Nagy, *Can. J. Chem.*, **44**, 1967 (1966).
(28) G. G. A. Perkins, E. R. Austin, and F. W. Lampe, unpublished results.
(29) P. Potzinger, A. Ritter, and J. R. Krause, *Z. Naturforsch. A*, **30**, 347 (1975).

Gas-Phase Photolysis of 1,2-Butadiene at 147.0 nm

Zaida Diaz and Richard D. Doepker*

Department of Chemistry, University of Miami, Coral Gables, Florida 33124 *(Received March 10, 1977)*

Publication costs assisted by the University of Miami

The vacuum-ultraviolet photolysis of 1,2-butadiene was investigated using xenon (147.0 nm) resonance radiation. The major products observed were vinylacetylene, methylacetylene, acetylene, 1,3-butadiene, allene, butatriene, and ethylene. Identification of radical species was made through the use of additives such as NO, HI, and CH_3I, and D_2 was used in a series of experiments to thermalize "hot" hydrogen atoms. Evidence is presented for the occurrence of nine primary processes to which quantum yields have been assigned. A hydrogen atom mechanism was postulated to account for the observed pressure dependence of the yields of methylacetylene, 1,3-butadiene, and allene. Relative rate constants for the addition of H atoms to the various carbon atoms of 1,2-C_4H_6 were determined, and the pattern of addition was found to be C_1 (56%) > C_2 (28%) > C_3 (15%).

Introduction

The vacuum ultraviolet photolysis of 1,2-butadiene was investigated in this laboratory several years ago.[1] At that time a reaction sequence was proposed which involved the participation of two neutral excited states of 1,2-C_4H_6 of different lifetimes. However, the results of later studies on similar systems[2,3] suggested that our early 1,2-butadiene investigation had overlooked an important reaction channel involving the addition of a hydrogen atom to the diene to produce an excited C_4H_7 species capable of undergoing decomposition:

$$H + 1,2\text{-}C_4H_6 \rightarrow (C_4H_7)^* \rightarrow \text{products}$$

In an attempt to verify this point we undertook a reinvestigation of the photolysis of 1,2-butadiene at 147 nm.

Experimental Section

Materials. 1,2-Butadiene was purified by gas chromatography using a 60-ft. column of dimethyl sulfolane on Chromosorb maintained at 30 °C. The purified material contained 0.042% 2-butyne. Purification of other materials has been described elsewhere.[1]

Irradiation and Analysis. The vacuum ultraviolet photolysis of 1,2-C_4H_6 was carried out at room temperature in a standard static system using a "gettered" xenon (147 nm) resonance lamp. Analysis was performed by vapor chromatography using a 25-ft. squalane column as reported previously.[4] Quantum yields were determined using 1-butyne ($\Phi_{C_4H_4} = 0.33$[3]) or cyclobutene ($\Phi_{C_4H_4} = 0.23$[2]).

Results

Using either 1-butyne or cyclobutene as an actinometer, the quantum yields of the products of the 147-nm photolysis of 1,2-butadiene was determined. The results of unscavenged and NO scavenged experiments are collected in Tables I and II. For the purpose of comparison Tables I and II also include some of the results of our earlier investigation, in which a different type of xenon lamp was used.[1] Also presented in Table II are the results of several experiments in which a large excess of nitrogen was added to the photolysis mixtures in order to further examine the effect of pressure on the product yields. The product quantum yields in these experiments have been corrected for the fact that nitrogen has several absorption band systems in this wavelength region[5] and thus absorbs a fraction of the incident light.

In addition to the results presented in Tables I and II, the following observations are summarized.

1. In several experiments HI replaced H_2S as in the previous study[1] as a test for the presence of free radicals. From the results of experiments, varying HI pressures from 3 to 50% of the 1,2-C_4H_6 pressure it was found that a 10% addition of HI appeared to be sufficient to intercept the radical species present. A representative set of this data is presented in Table III for a 1,2-butadiene pressure of 1 Torr.

2. Methyl iodide was added to the photolysis mixture in several instances both to try to detect the presence of radicals and to establish the participation of hydrogen atoms in the processes leading to the formation of certain products. CH_3I pressures were varied from 10 to 50% of the 1,2-butadiene pressure. A noteworthy result of these experiments was an increase in the quantum yield of nearly 0.1 for the formation of 1-butyne as compared to the NO scavenged experiments.

3. The possibility exists that hydrogen atoms formed when 1,2-C_4H_6 absorbs a quantum of light may be "hot". Since experiments involving CH_3I addition require consideration of the relative rates of competing reactions, D_2 was added to the mixture in order to thermalize the hydrogen atoms present. D_2 addition of nearly 5 times the 1,2-butadiene pressure produced desirable effects. The pertinent results of these experiments are summarized for a 1 Torr 1,2-butadiene pressure in Table III. It should be noted though that 1,3-butadiene, allene, and methylacetylene all decreased with increasing methyl iodide pressure when D_2 was present in the photolysis mixture.

Discussion

The absorption of a 147-nm photon (8.4 eV) by 1,2-butadiene, which has an ionization energy equal to 9.57 ± 0.02 eV,[6] results in the formation of an electronically excited neutral molecule. If the lifetime of this excited molecule is shorter than the collisional interval at the pressures used, fragmentation will occur which is independent of total pressure. On the other hand, a long-lived excited state would result in decreasing fragmentation and/or increasing isomerization with increasing total pressure.

The pressure dependence of the yields of allene, methylacetylene, and 1,3-butadiene (Tables I and II) has been explained[1] in terms of the presence of such a long-lived excited state of 1,2-C_4H_6. However, this pressure effect is best explained by means of a hydrogen atom mechanism, as will be discussed later.

Vinylacetylene Formation. The quantum yield of vinylacetylene is independent of pressure and the presence of additives which do not absorb significantly at 147 nm,

as shown in Tables I–VI. This suggests that it is formed in a primary process, probably by elimination of two hydrogen atoms from carbons 1 and 4 of 1,2-C_4H_6:

$$1,2\text{-}C_4H_6 + h\nu \rightarrow C_4H_4 + 2H \quad \Delta H = -57.6 \text{ kcal/mol} \quad (I)$$

An isomer of vinylacetylene, butatriene, which has the structure $H_2C{=}C{=}C{=}CH_2$ and was labeled C_4H_4', is also formed in the photolysis of 1,2-butadiene. As in the case of vinylacetylene the most likely pathway for the formation of this product is elimination of hydrogen atoms (from carbons 3 and 4) of the excited state of the diene:

$$1,2\text{-}C_4H_6 + h\nu \rightarrow C_4H_4' + 2H \quad \Delta H = -13.6 \text{ kcal/mol} \quad (II)$$

Formation of Methylacetylene and Allene. Examination of Table II reveals that the quantum yield of methylacetylene and, to a lesser extent, allene decreases with pressure. This suggests the existence of a reaction sequence analogous to that leading to the formation of allene from 1-butyne:[3]

$$H + C_4H_6 \rightarrow (C_4H_7)^* \quad (1)$$

$$(C_4H_7)^* \rightarrow CH_3 + C_3H_4 \quad (2)$$

$$(C_4H_7)^* + M \rightarrow C_4H_7 + M \quad (5)$$

Although the rate constant for reaction 1 has not been determined, it may be estimated to be similar to that for the reaction of a hydrogen atom with 1,3-C_4H_6, i.e., 5×10^{12} cm^3 mol^{-1} s^{-1} at 25 °C.[7] In the presence of D_2 and methyl iodide the yield of C_3H_4 decreases as the pressure of CH_3I is increased. This can be explained in terms of reaction 6, which has a second-order rate constant of

$$CH_3I + H \rightarrow HI + CH_3 \quad (6)$$

approximately 10^{13} cm^3 mol^{-1} s^{-1} at room temperature[8] and competes with reaction 1 for the available hydrogen atoms. An additional channel for the formation of C_3H_4 would be a primary process in which methylene is also formed:

$$1,2\text{-}C_4H_6 + h\nu \rightarrow CH_2 + C_3H_4 \quad \Delta H = -97.5 \text{ kcal/mol} \quad (III)$$
$$-95.6$$

At very high pressures this reaction is probably the only source of C_3H_4.

1,3-C_4H_6 Formation. It may be seen in Table II that the yield of 1,3-butadiene decreases with increasing pressure. This pressure dependency suggests the following reaction sequence for 1,3-C_4H_6 formation:

$$H + 1,2\text{-}C_4H_6 \rightarrow (C_4H_7)^* \quad (1)$$

$$(C_4H_7)^* \rightarrow H + 1,3\text{-}C_4H_6 \quad (3)$$

$$(C_4H_7)^* + M \rightarrow C_4H_7 + M \quad (5)$$

This hydrogen atom sensitized isomerization process is similar to the one proposed for the formation of 1,3-C_4H_6 in the vacuum-ultraviolet photolysis of cyclobutene.[2] The observed decrease in the yield of 1,3-C_4H_6 as the pressure of CH_3I is increased in the presence of D_2 is just what would be expected from the competition of reactions 1 and 6, and serves as additional evidence of the existence of a hydrogen atom mechanism leading to the formation of 1,3-C_4H_6. The increase in the quantum yield of C_4H_6 in unscavenged experiments, as well as in experiments carried out in the presence of HI (Table III) is not due to 1,3-butadiene but to 1-butyne, which is formed by a free radical mechanism and has a retention time in the squalane column almost identical with that of the 1,3-butadiene, so that their separation is not possible under our standard experimental conditions.

Formation of Ethylene and Acetylene. The formation of ethylene in the 147-nm (195 kcal/einstein) photolysis of 1,2-butadiene may be primarily attributed to the direct split of the excited parent molecule into ethylene and acetylene.

$$1,2\text{-}C_4H_6 + h\nu \rightarrow C_2H_2 + C_2H_4 \quad (IV)$$
$$\Delta H = -167.1 \text{ kcal/mol}$$

Such a process in the case of cyclobutane[9] and methylcyclopropane[10] results in the highly pressure-dependent secondary decomposition of C_2H_4 into C_2H_2 and H_2 fragments. Although the ethylene formed from 1,2-butadiene by process IV probably takes off most of the 167 kcal/mol that must be partitioned between the acetylene

TABLE I: Pressure Effect on the Photolysis (147.0 nm) of 1,2-C_4H_6 in the Absence of Additives

1,2-C_4H_6 (Torr)	0.45[a]	1.0[b]	5.0[a]	25.0	5.0[c]
CH_4	0.05	0.04	0.04	0.04	0.02
C_2H_2	0.17	0.14	0.13	0.10	0.06
C_2H_4	0.05	0.03	0.03	0.03	0.03
C_2H_6	0.19	0.18	0.11	0.07	0.09
C_3H_6	0.02	0.01	0.01	t[g]	0.01
C_3H_4[d]	0.29	0.22	0.10	0.05	0.09
C_3H_4[e]	0.07	0.05	0.03	0.01	0.03
C_4H_4	0.25	0.24	0.22	0.22	(0.22)
C_4H_6[f]	0.22	0.19	0.14	0.09	0.12[h]
trans-2-C_4H_8	0.02	0.03	0.05	0.04	0.03
cis-2-C_4H_8	0.02	0.02	0.03	0.03	0.02
2-C_4H_6	0.02	0.02	0.01	nd[i]	nd
C_4H_4'	0.05	0.04	0.05	0.04	nd
Ref	*j*	*j*	*j*	*j*	*k*

[a] Consists of two runs. [b] Consists of three runs. [c] Because no quantum yields were determined in the earlier study, the relative yields reported have been normalized taking C_4H_4 as a base. [d] Methylacetylene. [e] Allene. [f] 1,3-C_4H_6 and 1-C_4H_6. [g] Trace. [h] Consists of 0.04 1,3-C_4H_6 and 0.08 1-C_4H_6. [i] Not determined. [j] This work. [k] Reference 1 of text.

TABLE II: Effect of Pressure on the Photolysis (147.0 nm) of 1,2-C_4H_6 and Scavenger NO

1,2-C_4H_6 (Torr)	0.45[a]	1.0[b]	5.0[a]	9.9	24.5	1.0[c]	10.0[c,d]
NO (Torr)	0.045	0.1	0.5	1.0	2.5	0.1	1.0
CH_4	0.04	0.04	0.03	0.02	0.02	0.02	nd[h]
C_2H_2	0.17	0.14	0.17	0.15	0.15	0.12	0.13
C_2H_4	0.05	0.04	0.04	0.05	0.04	0.05	0.07
C_3H_6	0.02	t[i]	0.01	t	t	t	0.01
C_3H_4[e]	0.23	0.25	0.13	0.09	0.04	0.22	0.11
C_3H_4[f]	0.06	0.06	0.04	0.03	0.01	0.06	0.04
C_3H_8	0.01		0.01	0.03			
C_4H_4	0.28	0.28	0.31	0.32	(0.30)	(0.28)	(0.32)
C_4H_6[g]	0.12	0.11	0.06	0.05	0.02	0.11	0.05
2-C_4H_6	0.01	0.01				nd	nd
C_4H_4'	0.08	0.08	0.10	0.06	0.10	nd	nd
Ref	*j*	*j*	*j*	*j*	*j*	*k*	*k*

1,2-C_4H_6 (Torr)	1.1	1.0	1.0
NO (Torr)	0.1	0.1	0.1
N_2 (Torr)	49	95	132
CH_4	0.02	0.03	0.03
C_2H_2	0.18	0.15	0.13
C_2H_4	0.04	0.03	0.03
C_3H_6	0.01	0.04	0.03
C_3H_4[e]	0.03	0.02	0.02
C_3H_4[f]	0.01	0.01	0.01
C_3H_8	0.01	0.01	0.01
C_4H_4	(0.30)	(0.30)	(0.30)
C_4H_6[g]	0.01	0.01	t[i]
2-C_4H_6	0.01		
C_4H_4'	0.06	0.06	0.07
Ref	*j*	*j*	*j*

[a] Consists of two runs. [b] Consists of three runs. [c] Relative yields have been normalized taking C_4H_4 as a base. [d] $\phi_{H_2} = 0.15$. [e] Methylacetylene. [f] Allene. [g] 1,3-C_4H_6 and 1-C_4H_6. [h] Not determined. [i] Trace. [j] This work. [k] Reference 1 of text.

and ethylene fragments, the lack of a pressure effect on the C_2H_2/C_2H_4 ratio indicates that the lifetime of the excited C_2H_4 species must be shorter than the collision interval at the pressures used in this study.

$$1,2\text{-}C_4H_6 + h\nu \rightarrow C_2H_2 + C_2H_2 + H_2 \quad (V)$$
$$\Delta H = -125.4 \text{ kcal/mol}$$

This was also found to be the case in the vacuum-ultraviolet photolyses of 1,3-butadiene,[11] cyclobutene,[2] 1-butyne,[3] and methylenecyclopropane.[12] An additional source of ethylene may be a process such as VI, in which ethynyl radicals are also formed. There is yet another channel for

$$1,2\text{-}C_4H_6 + h\nu \rightarrow H + C_2H_4 + C_2H \quad (VI)$$
$$\Delta H = -47.2 \text{ kcal/mol}$$

the formation of acetylene which is a primary process and, as such, pressure independent.

$$1,2\text{-}C_4H_6 + h\nu \rightarrow C_2H_2 + C_2H_3 + H \quad (VII)$$
$$\Delta H = 67.9 \text{ kcal/mol}$$

Radical Formation. In previous studies in this laboratory[1-4,10,12,13] H_2S has been successfully used to intercept CH_2, CH_3, C_2H, C_2H_3, and C_4H_5 radicals, but it has failed to intercept the C_3H_3 radical. Ausloos, Rebbert, and Lias[14] investigated the photolysis of propane in the presence of HI as a radical scavenger, and from a comparison of their results with the results of analogous experiments using H_2S as a scavenger they concluded that HI is a more efficient radical interceptor than H_2S. In this work we have used HI in an attempt to obtain a more quantitative measure of the radicals present in our system, and to intercept those radicals (mostly unsaturated) which do not react with H_2S. It must be kept in mind, however, that the "quantitative" titration of radicals with HI in this case is somewhat open to question due to the competition of the diene for the radicals in the system. From a comparison of the results in Tables II and III it is evident that the yield of methane increases considerably in the presence of HI. It further appears from the results cited that HI concentration of about 10% of 1,2-butadiene pressure is sufficient to intercept most of the methyl radicals produced in the system. Reaction 2 in which methyl radicals and C_3H_4 are produced from the decomposition of an excited C_4H_7 species has already been discussed. A second channel for the formation of methyl radicals may be a primary process in which C_3H_3 radicals are also formed.

$$1,2\text{-}C_4H_6 + h\nu \rightarrow CH_3 + C_3H_3 \quad (VIII)$$
$$\Delta H = -124.5 \text{ kcal/mol}$$

The increase in the quantum yields of methylacetylene and allene observed in Table III certainly indicates both the presence of the C_3H_3 radical, and the (qualitative) ability of HI to intercept it. An additional indication of the presence of the propargyl radical in our system is the observed increase in the yield of C_4H_6 (1-butyne) when methyl iodide is added to the reaction mixture (Results 2). Under these conditions there are a considerable number of methyl radicals in the system due to reaction 6, and possibly to decomposition of CH_3I by absorption of some of the incident light.[15]

$$CH_3I + h\nu \rightarrow CH_3 + I$$

The reaction of a methyl radical with a propargyl radical would result in the formation of 1-butyne.[16]

$$CH_3 + C_3H_3 \rightarrow 1\text{-}C_4H_6$$

The increased yields of *cis*- and *trans*-2-butene seen in Table III are probably due to the interception by HI of the C_4H_7 radicals formed in reaction 5. The increase in the C_4H_6 yield, as well as the small increase in ethylene (Table III), suggest the presence of C_4H_5 and C_2H_3 radicals. The former is probably formed in the process:

$$1,2\text{-}C_4H_6 + h\nu \rightarrow H + C_4H_5 \quad \Delta H = -114.7 \text{ kcal/mol} = -96.7 \text{ kcal/mol} \quad (IX)$$

while the latter appears as a consequence of reaction VII.

Quantum Yields and Rate Constants

Considering the above material, the mechanism shown in Scheme I for the photolysis of 1,2-butadiene at 147 nm is proposed. It can be seen from the mechanism that reaction I is the only source of vinylacetylene. Therefore the quantum yield of this reaction channel should be equal to the quantum yield of vinylacetylene, which has an average value of 0.30. Thus, $\phi_I = 0.30$. Likewise, the quantum yield of reaction II may be assigned a value of 0.08 equal to the quantum yield of C_4H_4', which is formed exclusively by this process. The quantum yields of reactions VI, VII, and IX are equal to the quantum yields of C_2H, C_2H_3, and C_4H_5 radicals, respectively, and may be determined by comparing the data presented in Tables II and III. From the increase in the quantum yields of C_2H_2, C_2H_4, and C_4H_6 when HI is present we obtain $\phi_{VI} = \Phi_{C_2H} = 0.02$, $\phi_{VII} = \Phi_{C_2H_3} = 0.03$, and $\phi_{IX} = \Phi_{C_4H_5} = 0.09$. Ethylene requires two reaction channels for its formation, reactions IV and VI, thus, $\phi_{IV} + \phi_{VI} = \Phi_{C_2H_4} = 0.04$ (Table II). Since the quantum yield of process VI as determined in the HI experiments is 0.02, $\phi_{IV} = 0.02$. In a similar manner, the quantum yield of reaction V may be obtained from the known yield of acetylene (Table II), and the previously determined yields of processes IV and VII, by means of the relationship:

$$\phi_{IV} + 2(\phi_V) + \phi_{VII} = \Phi_{C_2H_2} = 0.15$$
$$0.02 + 2(\phi_V) + 0.03 = 0.15$$

Hence, $\phi_V = 0.05$. There are two sources of C_3H_4 (methylacetylene and allene): primary process III and secondary process 2. The rate of formation of C_3H_4 is thus given by

$$R_{C_3H_4} = k_2(C_4H_7)^* + \phi_{III}I_a$$

Assuming steady state conditions for $(C_4H_7)^*$ and H, and neglecting the contribution of the reaction of hydrogen atoms with NO and of reactions 3 and 4 to the steady state

Scheme I

$$1,2\text{-}C_4H_6 + h\nu \rightarrow (1,2\text{-}C_4H_6)^*$$
$$(1,2\text{-}C_4H_6)^* \rightarrow C_4H_4 + 2H \quad (I)$$
$$\rightarrow C_4H_4' + 2H \quad (II)$$
$$\rightarrow CH_2 + C_3H_4 \quad (III)$$
$$\rightarrow C_2H_2 + C_2H_4 \quad (IV)$$
$$\rightarrow 2C_2H_2 + H_2 \quad (V)$$
$$\rightarrow H + C_2H_4 + C_2H \quad (VI)$$
$$\rightarrow C_2H_2 + C_2H_3 + H \quad (VII)$$
$$\rightarrow CH_3 + C_3H_3 \quad (VIII)$$
$$\rightarrow H + C_4H_5 \quad (IX)$$
$$H + 1,2\text{-}C_4H_6 \rightarrow (C_4H_7)^* \quad (1)$$
$$(C_4H_7)^* \rightarrow CH_3 + C_3H_4 \text{ (methylacetylene)} \quad (2A)$$
$$\text{(allene)} \quad (2B)$$
$$\rightarrow H + 1,3\text{-}C_4H_6 \quad (3)$$
$$\rightarrow H + 2\text{-}C_4H_6 \quad (4)$$
$$(C_4H_7)^* + M \rightarrow C_4H_7 + M \quad (5)$$

TABLE III: Photolysis (147.0 nm) of 1,2-C_4H_6 in the Presence and Absence of Additives

1,2-C_4H_6 (Torr) Additive (Torr)	1.0[a] None	1.0[a] NO(0.1)	1.0[b] HI(0.3)	1.0 CH_3I(0.5) D_2(4.7)
CH_4	0.04	0.04	0.68	0.13
C_2H_2	0.14	0.14	0.16	0.16
C_2H_4	0.03	0.04	0.06	0.06
C_2H_6	0.18		0.03	0.25
C_3H_6	0.01	t[f]	0.01	0.02
C_3H_4[c]	0.22	0.25	0.28	0.08
C_3H_4[d]	0.05	0.06	0.08	0.02
C_4H_4	0.24	0.28	0.27	(0.30)
C_4H_6[e]	0.19	0.11	0.19	0.11
trans-2-C_4H_8	0.03		0.14	nd[g]
cis-2-C_4H_8	0.02		0.08	nd
2-C_4H_6	0.02	0.01	0.03	
C_4H_4'	0.04	0.08	0.07	0.08

[a] Consists of three runs. [b] Consists of two runs. [c] Methylacetylene. [d] Allene. [e] 1,3-C_4H_6 and 1-C_4H_6. [f] Trace. [g] Not determined.

concentration of hydrogen atoms, our rate equation becomes

$$R_{C_3H_4} = \frac{k_2\phi' I_a}{k' + k_5(M)} + \phi_{III} I_a$$

where $\phi' = 2\phi_I + 2\phi_{II} + \phi_{VI} + \phi_{VII} + \phi_{IX} = 0.90$ and $k' = k_2 + k_3 + k_4$. Rearranging

$$\frac{1}{\Phi_{C_3H_4(total)} - \phi_{III}} = \frac{k'}{k_2\phi'} + \frac{k_5(M)}{k_2\phi'}$$

The value of ϕ_{III} then may be obtained by trial and error as the value that makes a plot of $1/(\Phi_{tot} - \phi_{III})$ against pressure a straight line. These plots for methylacetylene and allene are shown in Figure 1. The values of ϕ_{III} that give the best straight lines are 0.014 for methylacetylene and 0.003 for allene. The sum of these corresponds to the total quantum yield of primary process III, i.e., $\phi_{III} = 0.014 + 0.003 \simeq 0.02$. The quantum yield of secondary process 2 may be obtained from the yields of C_3H_4 in the presence of NO (Table II) and the known yield of primary process III. Thus, $\Phi_2 = 0.31 - \phi_{III} = 0.29$.

The only source of 1,3-butadiene formation is the hydrogen mechanism. It is thus possible to construct a Stern–Volmer type plot of the inverse of the quantum yield vs. total pressure, in the following manner:

$$R_{C_4H_6} = k_3(C_4H_7)^* = \frac{k_3\phi' I_a}{k' + k_5(M)}$$

$$\frac{1}{\Phi_{C_4H_6}} = \frac{k'}{k_3\phi'} + \frac{k_5(M)}{k_3\phi'}$$

Such a plot is shown in Figure 1. In agreement with the proposed mechanism, a linear relationship is found.

The least-squares slopes and intercepts of the lines in Figure 1 may be used to estimate the relative values of the experimental rate constants to which they are related. From the slopes of the lines

$k_5/k_{2A} = 1.23(0.90) = 1.11$

$k_5/k_{2B} = 3.30(0.90) = 2.97$

$k_5/k_3 = 1.78(0.90) = 1.60$

and from the intercepts

$k'/k_{2A} = 2.46$

$k'/k_{2B} = 11.60$

$k'/k_3 = 6.24$

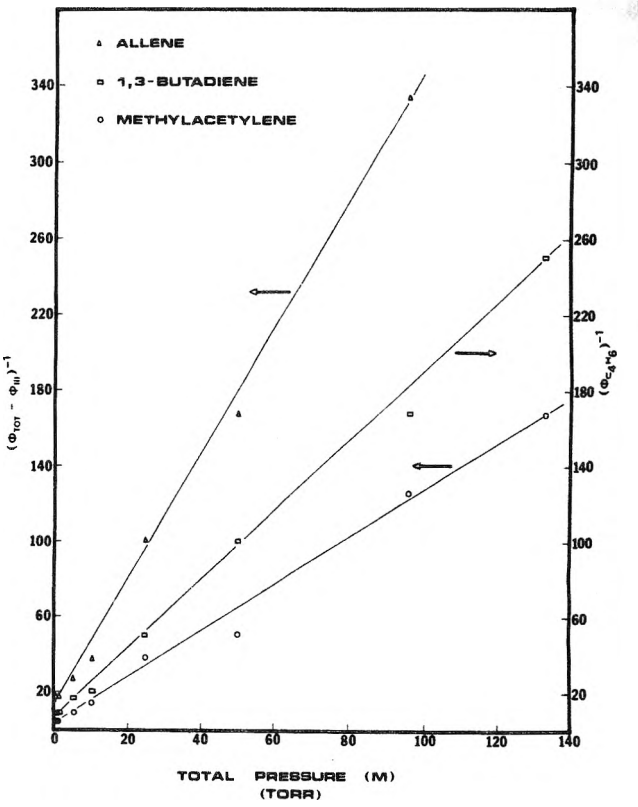

Figure 1. Stern–Volmer plot of $(\Phi_{tot} - \Phi_{III})^{-1}$ vs. total pressure (M) for the formation of methylacetylene and allene and a similar plot $(\Phi_{C_4H_6})^{-1}$ for the formation of 1,3-butadiene from the photolysis of 1,2-butadiene.

Expressing all rate constants in terms of k_{2B}:

$k_{2A}/k_{2B} = 3.70 \pm 1.02$

$k_3/k_{2B} = 1.86 \pm 0.01$

$k_5/k_{2B} = 2.97$

$k_4/k_{2B} = 5.04$

The error limits quoted represent the deviation of the individual values from the average. Because of the nature of the assumptions made, the relative values of k_4 and k_5 are highly uncertain. The relative values of k_{2A}, k_3, and k_{2B}, 3.70:1.86:1.00, indicate the pattern of addition of hydrogen atoms to 1,2-C_4H_6 with respect to orientation. Attack on carbon 1 to form methylacetylene is the preferred reaction (56%), followed by attack on carbon 2 to produce 1,3-C_4H_6 (28%). Attack on carbon 3 to form allene occurs only to the extent of 15%. Klein and Scheer[17] in an investigation of the hydrogen atom addition to condensed 1,2-C_4H_6 in the 77 K region also found that terminal hydrogen atom addition is the preferred reaction. However, the orientation of addition of other radicals such as $O(^3P)$,[18] C_2H_5S,[19] and $(CH_3)_3Sn$[20] to 1,2-C_4H_6 in the gas phase has usually been found to be $C_2 > C_1 > C_3$.

Since secondary process 3 is the only source of C_4H_6, its quantum yield is equal to the quantum yield of C_4H_6 in the scavenged experiments, i.e., $\Phi_3 = 0.12$.

Likewise, the quantum yield of secondary process 4 is equal to the quantum yield of 2-butyne, $\Phi_4 = 0.01$. The quantum yield of reaction VIII is equal to the yield of C_3H_3 radicals and may be estimated from a comparison of the data in Tables II and III. From the increase in the yield of C_3H_4 (methylacetylene and allene) when HI is present, $\Phi_{C_3H_3} = \phi_{VIII} \geq 0.06$. This value is identical with the one obtained if one considers the increase in the yield of C_4H_6 when methyl iodide is added to the system, and must therefore be considered only a minimum value, since the

titration of C_3H_3 with CH_3I is known not to be quantitative.[4,13] A better estimate can be made based on the yield of CH_3 radicals. From an examination of the data in Table III the total average quantum yield of CH_2 and CH_3 radicals is 0.67. These radicals lead to the formation of methane in the presence of HI. Hence, it is found

$$\phi_{III} + \phi_{VIII} + \Phi_2 = 0.67$$

$$0.02 + \phi_{VIII} + 0.29 = 0.67$$

$$\phi_{VIII} = 0.36$$

The presence of methane, ethane, propylene, 1-butyne, and *cis*- and *trans*-2-butene in unscavenged experiments can be explained in terms of radical reactions, as follows:

$$CH_3 + M \rightarrow CH_4 + M'$$

$$CH_3 + CH_3 \rightarrow C_2H_6$$

$$C_2H_3 + CH_3 \rightarrow C_3H_6$$

$$C_4H_5 + M \rightarrow 1\text{-}C_4H_6 + M'$$

$$C_4H_7 + M \rightarrow C_4H_8 + M'$$

Based on the previous discussion, the quantum yields of the major modes of decomposition of 1,2-butadiene at 147 nm may be assigned.

Primary Process

$1,2\text{-}C_4H_6 + h\nu \rightarrow (1,2\text{-}C_4H_6)^*$	
$(1,2\text{-}C_4H_6)^* \rightarrow C_4H_4 + 2H$	0.30
$\rightarrow C_4H_4' + 2H$	0.08
$\rightarrow CH_2 + C_3H_4$	0.02
$\rightarrow C_2H_2 + C_2H_4$	0.02
$\rightarrow 2C_2H_2 + H_2$	0.05
$\rightarrow H + C_2H_4 + C_2H$	0.02
$\rightarrow C_2H_2 + C_2H_3 + H$	0.03
$\rightarrow CH_3 + C_3H_3$	0.36
$\rightarrow H + C_4H_5$	0.09
Total =	0.97

Secondary Process

$$H + 1,2\text{-}C_4H_6 \rightarrow (C_4H_7)^*$$

$$(C_4H_7)^* \rightarrow CH_3 + C_3H_4$$

$$\rightarrow H + 1,3\text{-}C_4H_6$$

$$\rightarrow H + 2\text{-}C_4H_6$$

$$(C_4H_7)^* + M \rightarrow C_4H_7 + M$$

Acknowledgment. The authors wish to thank the Graduate School of the University of Miami for the Maytag Research Fellowship enjoyed by one of the investigators.

References and Notes

(1) R. D. Doepker and K. L. Hill, *J. Phys. Chem.*, **73**, 1313 (1969).
(2) A. DeLeon and R. D. Doepker, *J. Phys. Chem.*, **75**, 3656 (1971).
(3) K. L. Hill and R. D. Doepker, *J. Phys. Chem.*, **76**, 1112 (1972).
(4) C.-K. Tu and R. D. Doepker, *J. Photochem.*, **3**, 13 (1974–1975).
(5) Y. Tanaka, M. Ogawa, and A. S. Jursa, *J. Chem. Phys.*, **40**, 3690 (1964).
(6) J. G. Calvert and J. N. Pitts, Jr., "Photochemistry", Wiley, New York, N.Y., 1966, p 815–827.
(7) E. E. Daby, H. Niki, and B. Weinstock, *J. Phys. Chem.*, **75**, 1601 (1971).
(8) R. A. Holroyd, *J. Am. Chem. Soc.*, **91**, 2208 (1969).
(9) (a) R. D. Doepker and P. Ausloos, *J. Chem. Phys.*, **43**, 3814 (1965); (b) K. Obi, H. Akimoto, Y. Ogata, and I. Tanaka, *ibid.*, **55**, 3822 (1971).
(10) R. D. Doepker, *J. Phys. Chem.*, **73**, 3219 (1969).
(11) R. D. Doepker, *J. Phys. Chem.*, **72**, 4037 (1968).
(12) K. L. Hill and R. D. Doepker, *J. Phys. Chem.*, **76**, 3153 (1972).
(13) C.-K. Tu and R. D. Doepker, *J. Photochem.*, **1**, 271 (1972–1973).
(14) P. Ausloos, R. E. Rebbert, and S. G. Lias, *J. Photochem.*, **2**, 267 (1973–1974).
(15) R. D. Doepker and P. Ausloos, *J. Chem. Phys.*, **41**, 1865 (1964).
(16) J. Collin and F. P. Lossing, *Can. J. Chem.*, **35**, 778 (1957).
(17) R. Klein and M. D. Scheer, *J. Phys. Chem.*, **67**, 1874 (1963).
(18) J. J. Havel, *J. Am. Chem. Soc.*, **96**, 530 (1974).
(19) T. L. Jacobs and G. E. Illingworth, Jr., *J. Org. Chem.*, **28**, 2692 (1963).
(20) H. G. Kuivila, W. Rahman, and R. H. Fish, *J. Am. Chem. Soc.*, **87**, 2835 (1965).

On the Oxidation of Aqueous Br^- by OH Radicals, Studied by Pulse Radiolysis

Avner Mamou, Joseph Rabani,*

Department of Physical Chemistry, The Hebrew University of Jerusalem, Jerusalem 91 000, Israel

and David Behar

Israel Atomic Energy Commission, Soreq Nuclear Research Center, Yavne 70600, Israel *(Received September 27, 1976)*

The equilibria $Br^- + OH \rightleftarrows BrOH^-$ and $2Br^- + OH \rightleftarrows Br^- + BrOH^- \rightleftarrows Br_2^- + OH^-$ were studied in the pH range 9.5–10.7, in view of an apparent disagreement in the literature over the equilibrium constants. The apparently conflicting results are shown to be in agreement when the absorbance of the transient $BrOH^-$ is considered. The following equilibrium constants have been estimated: $BrOH^- + Br^- \rightleftarrows Br_2^- + OH^-$, $K = 70 \pm 30$; $Br + Br^- \rightleftarrows Br_2^-$, $K = (1.1 \pm 0.3) \times 10^5\ M^{-1}$.

Introduction

The oxidation of Br^- by OH radicals has been a subject of several publications.[1-3] OH radicals react with Br^- and produce the intermediate $BrOH^-$ which may react with Br^-, H^+, or dissociate spontaneously to form Br in equilibrium with Br_2^-. Reactions 1–5 are reversible.

$$OH + Br^- \rightleftarrows BrOH^- \quad (1)$$

$$BrOH^- + Br^- \rightleftarrows Br_2^- + OH^- \quad (2)$$

$$BrOH^- + H^+ \rightleftarrows Br + H_2O \quad (3)$$

$$BrOH^- \rightleftarrows Br + OH^- \quad (4)$$

$$Br + Br^- \rightleftarrows Br_2^- \quad (5)$$

Of the rate and equilibrium constants, $k_1^{(2)} = (1.06 \pm 0.08) \times 10^{10}\ M^{-1}\ s^{-1}$, $k_{-1}^{(2)} = (3.3 \pm 0.4) \times 10^7\ s^{-1}$, $k_2^{(2)} = (1.9 \pm 0.3) \times 10^8\ M^{-1}\ s^{-1}$, $k_3^{(2)} = (4.4 \pm 0.8) \times 10^{10}\ M^{-1}\ s^{-1}$, $k_4^{(2)} = (4.2 \pm 0.6) \times 10^6\ s^{-1}$, $K_1^{(3)} = (2.9 \pm 1.4) \times 10^3\ M^{-1}$, $K_2^{(3)} = 3.7 \pm 1.5$, and $K_5^{(4)} = (2.2 \pm 1) \times 10^5\ M^{-1}$ were reported. Note that $K_4 = K_2/K_5 \simeq 2 \times 10^{-5}$ M. The value reported for $K_1^{(3)}$ from equilibrium optical absorbances data is about tenfold the ratio[2] k_1/k_{-1}, as calculated from kinetic measurements. This difference called for additional experiments. The purpose of this work is the redetermination of K_1 from optical density measurements in the pH range 7–11. We will also show that the experimental data are not in disagreement with $k_1/k_{-1} = K_1 = 320$[2] when the absorbance of $BrOH^-$ is taken into account.

Experimental Section

The experimental procedure was precisely as reported before.[2] The pH values which are reported were measured with the aid of a pH meter, $[OH^-]$ calculated as equal to $10^{(pH-14)}$. The temperature was (24 ± 2) °C.

Materials. NaOH and NaBr were Baker's (Analyzed grade). $HClO_4$ was Merck (pro analysi). N_2O was Matheson's, and was bubbled through an acidic solution of ammonium metavanadate in contact with zinc amalgam to eliminate traces of O_2. The water was triply distilled. Other materials were used as received.

Results and Discussion

Solutions saturated with N_2O were used in order to convert e_{aq}^- to OH radicals.[4] The optical density was measured at 366 nm. During and after the electron pulse, OH radicals which were produced reacted with Br^- leading to the reaction scheme 1–5. This resulted in a buildup of optical density, due to the absorptions of Br_2^- and $BrOH^-$.[2] Finally, the absorption decayed away as Br_2^- yielded Br^- and Br_3^-. The buildup of absorbance obeyed first-order kinetics while its decay was second order. At sufficiently low pulse intensities, the formation and decay processes became well separated in time, and it was possible to determine D_{max}, defined as the optical density when the buildup of absorption was just completed, before any of the transient absorbing species decayed away. With very low concentrations of Br^-, corrections (up to about 10%) were carried out for the absorbance which disappeared during the building up processes. This was carried out by extrapolation of the decay traces to the middle time of the formation process. D_{max} is related to the optical absorption of Br_2^- and $BrOH^-$ according to

$$D_{max} = \epsilon_{Br_2^-}[Br_2^-]_{eq} + \epsilon_{BrOH^-}[BrOH^-]_{eq} \quad (6)$$

where ϵ_X is the extinction coefficient of species X, $[Br_2^-]_{eq}$ and $[BrOH^-]_{eq}$ represent the concentrations of Br_2^- and $BrOH^-$, respectively, when equilibria 1–5 exist. If the same pulse intensity which gave a certain D_{max} is applied to a neutral solution of Br^- (>3×10^{-4} M) all the OH radicals eventually yield Br_2^-, because under such conditions equilibria 1–5 are shifted toward total formation of Br_2^-. (Note that equilibrium 3 is not important under our conditions, where only neutral and slightly alkaline solutions were used.) Under these conditions, the value of D_{max}, which will be referred to as D_{max}^{total}, equals the right-hand side of eq 7, where the various $[Y]_{eq}$ represent

$$D_{max}^{total} = \epsilon_{Br_2^-}([Br_2^-]_{eq} + [OH]_{eq} + [Br]_{eq} + [BrOH^-]_{eq}) \quad (7)$$

the appropriate equilibrium concentrations of the type Y species, in *slightly alkaline* solutions. D_{max}^{total}, however, is measured in *neutral* solution at sufficiently high $[Br^-]$ (>3×10^{-4} M), so that equilibrium 5 is shifted strongly to the right, using as noted above equal pulse intensities (total radical concentrations) in both neutral and alkaline solutions. Let $D_{max}^{neutral}$ represent D_{max} in a neutral solution where the Br^- concentration precisely equals its concentration in a parallel experiment carried out under the same conditions at pH 9.5–10.7. $D_{max}^{neutral} = D_{max}^{total} \cdot [Br_2^-]_{eq}/([Br_2^-]_{eq} + [Br]_{eq})$. $D_{max}^{neutral}$ and D_{max} measured in parallel experiments, where the same dose per pulse was applied, were used for the calculation of K_2 with

$$K_2 = \frac{([OH^-]/[Br^-])(1 + K_1^{-1}[Br^-]^{-1} - U\epsilon_r)}{U - 1 - K_5^{-1}[Br^-]^{-1}} \quad (8)$$

Equation 8 is obtained after inserting in (7) the various $[Y]_{eq}$, expressed by $[Br_2^-]$, $[OH^-]$, $[Br^-]$, and equilibrium

TABLE I: Evaluation of K_2 in the pH Range 10-10.75[a]

pH	$[Br^-]$, μM	$D_{max}^{neutral}$	D_{max}	K_2[b]
10.1	100	0.065	0.045	81
10.1	200	0.067	0.060	82
10.15	50	0.058	0.023	97
10.45	100	0.068	0.039	108
10.75	100	0.064	0.023	87
10.75	200	0.067	0.044	80
10.75	300	0.071	0.060	105
				Av 90

[a] Solutions saturated N_2O. 12.3 cm light path. Measured at 366 nm. The differences in values of $D_{max}^{neutral}$ reflect, in addition to equilibria 2 and 5, changes in pulse intensities. [b] Calculated with eq 8, using $K_1 = 320\ M^{-1}$,[2] $\epsilon_r = 0.67$,[2] and $K_5 = 1.1 \times 10^5\ M^{-1}$ (see text).

constants. ϵ_r is the ratio $\epsilon_{BrOH^-}/\epsilon_{Br_2^-}$ at 366 nm, and was found to equal 0.67.[2] U is defined by

$$U = (D_{max}^{neutral}/D_{max})(1 + K_5^{-1}[Br^-]^{-1}) \quad (9)$$

A set of K_2 values, calculated with 8, at various pH values and $[Br^-]$, are presented in Table I. Note that under our conditions only $\sim 0.3\ \mu M$ radicals are formed, accompanied by roughly equivalent amounts of H^+ and OH^- so that the pH is not seriously affected.

Another set of results in the pH range 9.5–10.7 gave an average $K_2 = 53 \pm 20$ (maximum deviation). The larger scatter is probably due to several factors: the calculation of K_2 is very sensitive to the measured values of $D_{max}^{neutral}$, D_{max}, pH, and probably temperature. In addition, the calculations are affected to various degrees by the choice of K_1, K_5, and ϵ_r. The errors in these parameters may introduce an additional systematic error in K_2.

We have determined K_5 using various Br^- concentrations at pH 3.7 ($HClO_4$) in N_2O saturated or aerated solutions. When $[Br^-]$ was changed from 5 to 50 μM, considerable changes in D_{max} were observed. D_{max} values at this pH will be referred to as D_{max}^{acid}. D_{max}^{acid} changed only little, in the Br^- concentration range 1–10 mM, corresponding to the slight variation of the radical G values with the solutes' concentration. The optical density values obtained by extrapolating from 1–10 mM Br^- to the lower $[Br^-]$ solutions will be referred to as $D_{max}^{plateau}$ (extrapolation gives total initial yield of OH and therefore of $([Br_2^-] + [Br])$). $K_5 = (1.1 \pm 0.3) \times 10^5\ M^{-1}$ was calculated as an average of eight determinations using

$$K_5 = [Br^-]^{-1} D_{max}^{acid}/(D_{max}^{plateau} - D_{max}^{acid}) \quad (10)$$

pH 3.7 was chosen in order to enhance the formation of Br atoms[2] so that better time separation between the formation and decay of Br_2^- was obtained. This was important since at the very low $[Br^-]$ used, the formation of Br at neutral pH is too slow for a good time separation, even with the low pulse intensities used in these experiments (0.26 μM radicals produced per pulse). The value $K_5 = 1.1 \times 10^5\ M^{-1}$ is in reasonably good agreement with previous measurements.[5]

Conclusions

When $\epsilon_{BrOH^-}/\epsilon_{Br_2^-} = 0.67$ is taken for the calculations of K_2, it is shown that consistent values of K_2 are obtained in the pH range 9.5–10.7 using $K_1 = 320\ M^{-1}$.[2] Rough calculations, assuming optimal conditions for the measurements of θ in the previous work of Behar,[3] indicate that his results agree within experimental error with the present data, and yield the same K_2 values using the same parameters as here in eq 8. Exact calculations were not possible, since his data[3] are presented in a manner that is not directly applicable to eq 8.

At pH values lower than 10, the scatter of the results was greater (not shown in Table I). This is probably due to effects of impurities, as the $[Br^-]$ must be very low at the lower pH's to make it possible to observe the relevant equilibria. At pH >11, K_2 values as defined by eq 8 decreased systematically with increasing pH. This became particularly evident at pH >11.5. This effect is perhaps due to the ionic dissociation of OH[6] and/or $BrOH^-$. (Nothing is known at the moment about the possible acid properties of $BrOH^-$.) Despite the highly scattered data the constancy of K_2 as calculated by eq 8 in the pH range 9.5–10.7 may indicate that none of these dissociations are important in the above pH range.

References and Notes

(1) M. S. Matheson, W. A. Mulac, J. L. Weeks, and J. Rabani, *J. Phys. Chem.*, **70**, 2092 (1966).
(2) D. Zehavi and J. Rabani, *J. Phys. Chem.*, **76**, 312 (1972).
(3) D. Behar, *J. Phys. Chem.*, **76**, 1815 (1972).
(4) M. S. Matheson and L. M. Dorfman, "Pulse Radiolysis", The M.I.T. Press, Cambridge, Mass., 1969.
(5) B. Cercek, M. Ebert, C. W. Gilbert, and A. J. Swallow, "Pulse Radiolysis", M. Ebert, J. P. Keene, A. J. Swallow, and J. H. Baxendale, Ed., Academic Press, New York, N.Y., 1965, p 83.
(6) (a) J. Rabani and M. S. Matheson, *J. Am. Chem. Soc.*, **86**, 3175 (1964); (b) J. L. Weeks and J. Rabani, *J. Phys. Chem.*, **70**, 2100 (1966).

Transients in the Flash Photolysis of Aqueous Solutions of Tris(2,2′-bipyridine)ruthenium(II) Ion[1]

Dan Meisel,* Max S. Matheson, W. A. Mulac, and Joseph Rabani[2]

Chemistry Division, Argonne National Laboratory, Argonne, Illinois 60439 *(Received January 25, 1977)*

Publication costs assisted by Argonne National Laboratory

Aqueous solutions of $Ru(bpy)_3^{2+}$ (bpy = 2,2′-bipyridine) were flash photolyzed and pulse irradiated in the presence and in the absence of other additives. Hydrated electrons are produced in a process which is suggested to involve electron ejection from the first triplet of $Ru(bpy)_3^{2+}$, upon the absorption of a second photon. Most of the effective light (~70%) was in the range 300–340 nm, while ~30% of the effective light was at wavelength >340 nm. The efficiency of e_{aq}^- production relative to the efficiency of production of the lowest triplet charge transfer state was measured under our conditions as 0.0015, independent of $[Ru(bpy)_3^{2+}]$ and of flash intensity over a wide range. During our work on the biphotonic process for e_{aq}^- formation, a number of other reactions were investigated. Thus, hydrated electrons react with $Ru(bpy)_3^{2+}$ with a reaction rate constant of $(5.8 \pm 0.3) \times 10^{10}$ M^{-1} s^{-1}. The metal ions Zn^+, Co^+, and Cd^+ reduce $Ru(bpy)_3^{2+}$ with reaction rate constants $(1.5 \pm 0.2) \times 10^9$, $(1.7 \pm 0.2) \times 10^9$, and $(6.1 \pm 0.6) \times 10^8$ M^{-1} s^{-1}, respectively, producing $Ru(bpy)_3^+$. $Ru(bpy)_3^+$ reacts with O_2, Cu^{2+}, and duroquinone; the reaction rate constants are $(7.2 \pm 0.8) \times 10^9$, $(3.4 \pm 0.3) \times 10^8$, and $(4.0 \pm 0.5) \times 10^9$ M^{-1} s^{-1}, respectively. The possibility for a biphotonic effect leading to H_2 formation is discussed.

Introduction

In recent years, there has been a growing interest in the photodecomposition of water as a means to store solar energy. $Ru(bpy)_3^{2+}$ (bpy = 2,2′-bipyridine) has certain features which make it a potential mediator in photodecomposition of water by visible light. Particular features are: (a) the existence of a relatively long-lived charge transfer triplet state[3-7] accessible by visible light; (b) the fairly high negative reduction potential of $Ru(bpy)_3^{3+}$ to this state[8,9] ($E^\circ_{(Ru(bpy)_3^{3+}/^3Ru(bpy)_3^{2+})} = -0.84$ V) as compared to the highly positive redox potential of the ground state[10] ($E^\circ_{(Ru(bpy)_3^{3+}/Ru(bpy)_3^{2+})} = +1.27$ V); and (c) the high positive reduction potential of $^3Ru(bpy)_3^{2+}$ ($E^\circ_{(^3Ru(bpy)_3^{2+}/Ru(bpy)_3^+)} = +0.84$ V) as compared to the highly negative value of the reduction potential of ground state $Ru(bpy)_3^{2+}$.[11,12]

The use of Ru(II) in photogalvanic systems[9,13,14] has been suggested. Recently, the decomposition of water to H_2 and O_2 photoassisted by a derivative of $Ru(bpy)_3^{2+}$ has been reported.[15a] However, at present this report should be considered with reservations.[15b]

Reactions of the ^3CT state of $Ru(bpy)_3^{2+}$ are well known. These include a great number of electron transfer reactions to various emission quenchers,[8,9,11,16-19] electron transfer reactions to the $Ru(bpy)_3^{2+}$ triplet,[11] and energy transfer reactions.[20-22] The $Ru(bpy)_3^{3+}$ which is formed by electron transfer from the triplet $Ru(bpy)_3^{2+}$ to a quencher, usually back reacts with the reduced quencher.[17] However, in principle, $Ru(bpy)_3^{3+}$ is able to oxidize OH^- to molecular O_2, a reaction which has been demonstrated.[13]

Very little is known about the photochemistry of the $Ru(bpy)_3^{2+}$ complex itself. Steady photolysis has shown that the aqueous solutions of $Ru(bpy)_3^{2+}$ are practically inert to the effects of light at ambient temperatures.[7,16] Studies at 95 °C in acidic solutions indicate a ligand photodisplacement.[7]

Our study is expected to contribute toward a better understanding of the photochemistry of the $Ru(bpy)_3^{2+}$ complex itself.

Experimental Section

Flash photolysis experiments were done with a Xenon Corp. (Model 720) instrument. Cylindrical pyrex cells (cutoff at λ ~300 nm) 10 cm long (analyzing optical path) and 1 cm diameter (photoflash path length) were used in conjunction with the syringe technique for deaeration. The cell holder for this instrument was redesigned to incorporate desired filters in the photolyzing light path. When $Fe(ClO_4)_3$ or $Cu(ClO_4)_2$ were used, filters were employed to cut out photoflash light below 340 nm, minimizing absorption by Fe^{3+} or Cu^{2+}. A Spex spectrophotometer with a 1P28 photomultiplier was used for detection of the transients. Cutoff filters were used to minimize photolysis by the analyzing light. Unless otherwise stated, the energy delivered to the photoflash lamps was about 200 J with a flash duration of 15 μs (90%). Neutral density filters were usually used in order to investigate light intensity effects.

The pulse radiolysis setup using a Biomation 8100 transient recorder has been described earlier.[23] The pulse width was 4 ns. The optical path was 2 cm and 10^{-2} M KCNS saturated with N_2O was used as a dosimeter, taking $\epsilon_{CNS_2^-} = 7600$ M^{-1} cm^{-1} (at 480 nm).[24] The following materials were used as received: ferric perchlorate and calcium perchlorate (both Frederick Smith reagent grade), copper sulfate (Baker Analyzed), cadmium sulfate (99.999% Apache), perchloric acid (70%, Frederick Smith reagent grade), argon (Matheson 99.998% pure), N_2O (Liquid Carbonic, 99.9% purity), O_2 (Matheson 99.6%), KCNS (Baker and Adamson, reagent grade), *tert*-butyl alcohol (Fisher Scientific Certified). Water was triply distilled. $Cu(ClO_4)_2$ and 2,2′-bipyridineruthenous dichloride hexahydrate (both Frederick Smith reagent grade) and $ZnSO_4$ (Baker Analyzed) were recrystallized from triply distilled water. Concentrations of $Cu(ClO_4)_2$, $Fe(ClO_4)_3$ and $Ca(ClO_4)_2$ in stock solutions were determined by titration. The spectrum of each solution was taken with a Cary Model 14 spectrophotometer. The additives used were found to have no effect on the $Ru(bpy)_3^{2+}$ spectrum. Emission measurements were carried out with an Hitachi Perkin-Elmer spectrofluorimeter.

All the solutions were transferred to syringes and vigorously bubbled with argon for at least 10 min. Desired concentrations of O_2 were prepared by dilutions from an O_2 saturated solution. Unless otherwise stated, 2.0×10^{-5} and 4.0×10^{-5} M $Ru(bpy)_3^{2+}$ were used for the flash photolysis and pulse radiolysis, respectively. The pH of

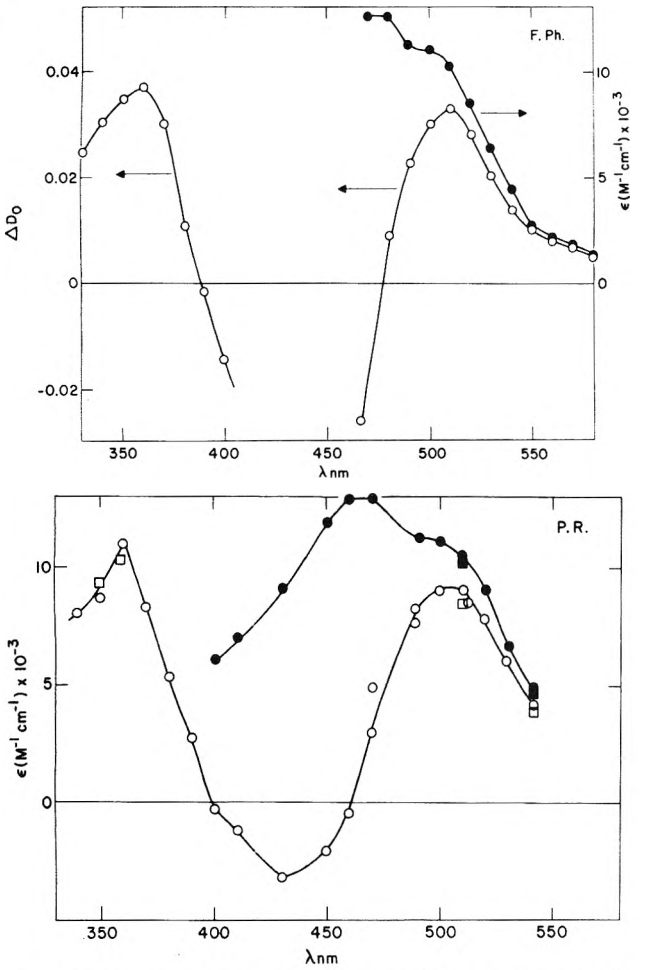

Figure 1. Transient spectra in flash photolyzed (upper curve) and pulse radiolyzed (lower curve) solutions of $Ru(bpy)_3^{2+}$ (2×10^{-5} and 4×10^{-5} M, respectively): (O) observed spectra; (●) corrected spectra (see text). All solutions were deaerated at pH 6.1. In the pulse radiolysis experiments 0.017 M *t*-BuOH was added. (□, ■) experiments in the presence of 50 mM $ZnSO_4$.

the unbuffered solutions, which were usually used, was between 6.1 and 7.0. Phosphate buffers, perchloric acid, or NaOH were used in some experiments to adjust the pH. The temperature was 24 ± 1 °C.

Results

Flash Photolysis. Flash photolysis of unbuffered 2×10^{-5} M $Ru(bpy)_3^{2+}$ solutions (pH 6–7) produced transient absorbance changes which are shown in Figure 1. At a given wavelength, λ, the absorbance change that was observed at the end of the flash, ΔD_0^{λ}, showed no dependency on repetitive flashing (up to 30 flashes were tested). The positive value of ΔD_0^{510} is attributed to formation of transient species which absorb more than $Ru(bpy)_3^{2+}$. The net absorption disappeared within several milliseconds, with a rate which sometimes slowed down after several flashes. It will be later shown that this effect was due to traces of impurities, presumably O_2 at $<10^{-7}$ M. At some wavelengths, a net bleaching of the absorbance was observed (negative ΔD_0^{λ}). This was followed by a slow recovery of the absorbance, which we found to take place in two steps: a relatively fast one, which paralleled the decay of absorbance at 510 nm, followed by a slower process, the rate of which was difficult to estimate due to low absorbance changes and high noise problems.

The half-life of the 510-nm absorption, under the most strict O_2 free conditions, was 2 ± 0.6 ms. It did not depend on the flash intensity over a portion of the experimental

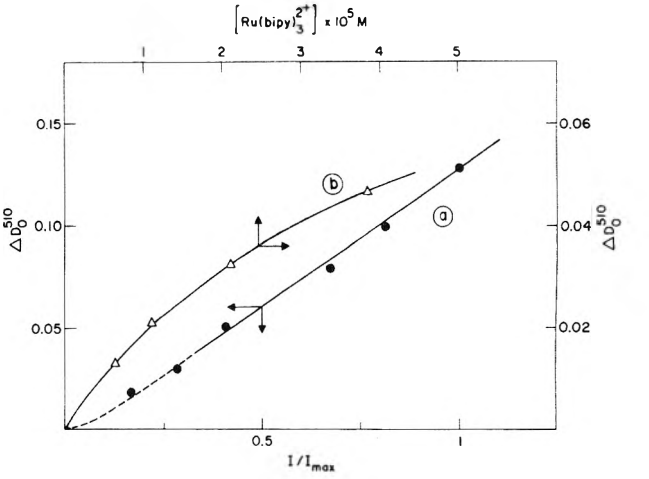

Figure 2. Dependence of ΔD_0^{510} (●) on light intensity (2×10^{-5} M Ru(II)) and (△) on $[Ru(bpy)_3^{2+}]$ using 200 J and no filters. Note the flash duration is greater for 1000 J than for 200 J.

range. The decay was found, however, to contain a significant second-order contribution at flash intensities tenfold higher than those usually used.

Figure 2 shows the linear dependence of ΔD_0^{510} on the flash intensity varied with the aid of neutral density filters using a constant amount of energy, ~1000 J, delivered to the photoflash lamps. (This method was preferred to changing the energy delivered to the flashlamps so that a constant time profile for the photoflashes was assured.)

ΔD_0^{510} increased steadily with $[Ru(bpy)_3^{2+}]$, at constant flash intensities (Figure 2). This can be rationalized if we assume that the role of increasing $[Ru(bpy)_3^{2+}]$ is to increase the amount of effective photoflash light which is being absorbed. We have found that about 70% of ΔD_0^{510} arises from light in the range ~300–340 nm, while 30% comes from light at wavelengths > ~340 nm. The fraction of light which is absorbed by $Ru(bpy)_3^{2+}$ at a given concentration can be calculated from its absorption spectrum. Rough calculations using a reasonable average effective ε show that ΔD_0^{510} is probably directly proportional to I_{abs}, in the entire $[Ru(bpy)_3^{2+}]$ range of Figure 2. This conclusion is certainly correct for the two lowest $[Ru(bpy)_3^{2+}]$, where the absorbance of the solution before the flash is low enough so that I_{abs} is approximately proportional to $[Ru(bpy)_3^{2+}]$.

The effect of several additives on the decay of the net absorbance at 510 nm was tested. We chose concentrations of O_2, $CuSO_4$, and duroquinone (DQ) so that the decay of the net absorbance at 510 nm was at least three times faster than the decay in the absence of these solutes. Yet, only a negligible effect on ΔD_0^{510} was observed except at the highest $[Cu^{2+}]$. The net absorbance change at time *t*, ΔD_t^{510}, decayed away with a pseudo-first-order rate law, the reaction being first order in both ΔD_t^{510} and [additive]. In Table I we present the second-order reaction rate constants, defined as $[\text{additive}]^{-1}\,(d/dt)\ln \Delta D_t^{510}$, corrected for the decay of ΔD_t^{510} in the absence of additives.

Addition of either $ZnSO_4$ or $CdSO_4$ to a solution containing 2×10^{-5} M $Ru(bpy)_3^{2+}$ had a negligible effect on the rate of decay of ΔD_t^{510}. However, in Figure 3 we can see that the buildup of absorbance became slower, as compared with solutions containing $Ru(bpy)_3^{2+}$ only. This slower buildup, as will be discussed later, is attributed to a reaction of the monovalent ions (Zn^+ and Cd^+) with $Ru(bpy)_3^{2+}$. The results are presented in Table II.

The effects of $Fe(ClO_4)_3$ and $Cu(ClO_4)_2$ on ΔD_0^{480} and on the decay of ΔD_t^{480} was investigated in 1 M $HClO_4$ at ionic strength 1.9 M. $Cu(ClO_4)_2$ was used also in neutral so-

TABLE I: Rate Constants for $Ru(bpy)_3^{+}$ + Oxidants[a]

$[O_2]$	k	$[Cu^{2+}]$	k	[Duroquinone]	k
0.5	7.0	2.6	0.36	0.61	5.0
0.95	6.5	3.2	0.35	1.5	3.5
1.1	8.1	5.9	0.37	2.3	3.2
1.2	6.5	15.0	0.33	3.0	4.5
2.0	8.5	39.0	0.27		
2.5	6.6				
	av (7.2 ± 0.8)[b]		av (0.34 ± 0.03)		av (4.0 ± 0.5)

[a] Oxidant concentrations in units 10^{-6} M. k in units 10^9 M^{-1} s^{-1}. [b] 1.8×10^9 reported in ref 25.

TABLE II: Rate Constants of $Ru(bpy)_3^{2+}$ with $M^{(n-1)+}$

$[Ru(bpy)_3^{2+}]$	$[M^{n+}]$	k, M^{-1} s^{-1}	ΔD_0^{510} [a]	Method
9.0×10^{-6}			0.0140	e
		$M^{n+} = Zn^{2+}$		
9.0×10^{-6}	1.3×10^{-3}	1.33×10^9	0.0143	e
9.0×10^{-6}	1.0×10^{-2}	1.55×10^9	0.0140	e
1.8×10^{-5}			0.0139	e
1.8×10^{-3}	3.7×10^{-4}		0.0155	e
1.8×10^{-5}	3.0×10^{-3}	1.60×10^9	0.0170	e
2.7×10^{-5}			0.0140	e
2.7×10^{-5}	3.5×10^{-3}		0.0165	e
5.0×10^{-5}	5.0×10^{-2}	1.55×10^9 (2.5×10^9)[d]		f
		$M^{n+} = Co^{2+}$		
4.0×10^{-5}	2.5×10^{-3}	1.80×10^9		f
1.6×10^{-5}	2.5×10^{-3}	1.7×10^9		f
		$M^{n+} = Cd^{2+}$		
4.0×10^{-5}	3.0×10^{-2}	6.1×10^8		f
4.0×10^{-5}		5.6×10^{10}[b,c]		f
4.0×10^{-5}		(8.0×10^{10})[b,d]		f

[a] Flash energies were varied so that ΔD_0^{510} did not vary with $[Ru(bpy)_3^{2+}]$, as tested in the absence of M^{n+}. [b] $k(e_{aq}^- + [Ru(bpy)_3^{2+}])$. [c] In the presence of 17 mM *t*-BuOH, followed at 600 nm. [d] Reference 25. [e] Flash photolysis. [f] pulse radiolysis.

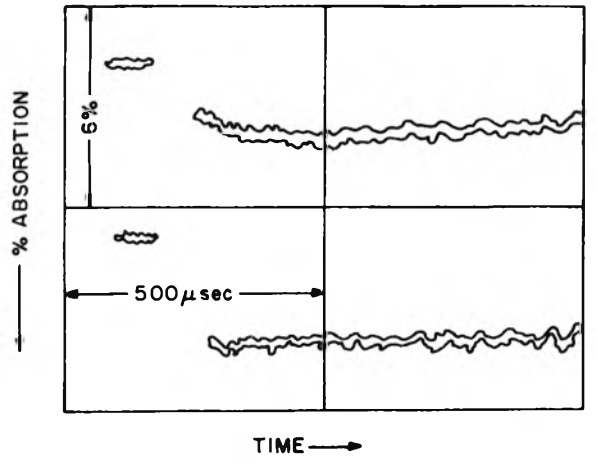

Figure 3. Oscillograms showing absorbance changes at λ 510 nm on flash photolyzing 9×10^{-6} M $Ru(bpy)_3^{2+}$ in the absence (lower curve) and presence of 1×10^{-2} M $Zn(ClO_4)_2$ (upper curve).

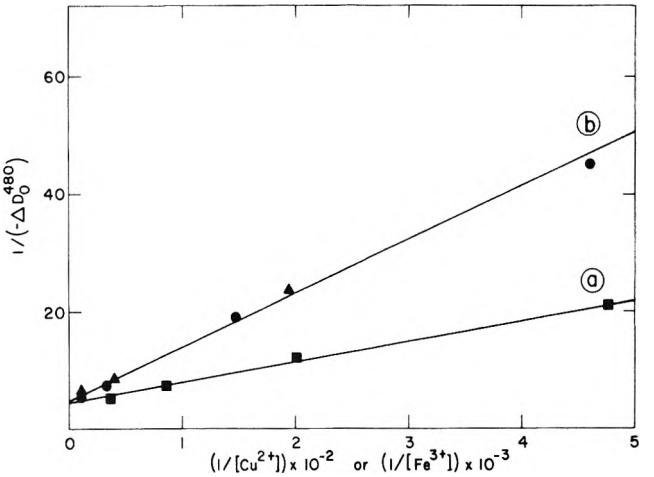

Figure 4. Competition plots for electron transfer from $^3Ru(bpy)_3^{2+}$ to $Fe(ClO_4)_3$ or $Cu(ClO_4)_2$: (a) ■, $Fe(ClO_4)_3$ at 1 M $HClO_4$; (b) ●, $Cu(ClO_4)_2$ at pH 6.1; ▲, $Cu(ClO_4)_2$ in 1 M $HClO_4$; all experiments were done at constant ionic strength of 1.9 M obtained by $Ca(ClO_4)_2$.

lutions. $Ca(ClO_4)_2$ was added to maintain the constant ionic strength, μ = 1.9 M. Note that ΔD_t^{480} was negative in all cases. The absorbance changes in the presence of either Cu^{2+} or Fe^{3+} are much larger than those observed in the absence of these solutes. $|\Delta D_0^{480}|$ increased with the [additive], until a limiting value was approached at the highest concentrations used. Plots of $1/|\Delta D_0^{480}|$ vs. 1/[additive] were linear, as demonstrated in Figure 4. The data of Figure 4 were taken under conditions where only a relatively small (but not always negligible) fraction of the $Ru(bpy)_3^{2+}$ was destroyed during the low intensity flash. Assuming that the bleaching of the absorbance at 480 nm involves no formation of absorbing products, we can calculate the average concentration of $Ru(bpy)_3^{2+}$ during the flash. All the ΔD_0^{480} values used in Figure 4 were normalized to an average $[Ru(bpy)_3^{2+}] = 2.0 \times 10^{-5}$ M. As discussed in relation to Figure 2, the only effect of changing $[Ru(bpy)_3^{2+}]$ is to vary the amount of photoflash light which is absorbed. Both $Cu(ClO_4)_2$ and $Fe(ClO_4)_3$ possess some optical absorption in the spectral range of the photoflash light above 300 nm. For this reason, we used cutoff filters so that only photoflash light above 340 nm was absorbed by the solutions. Under these conditions, even at the highest $[Cu(ClO_4)_2]$ and $[Fe(ClO_4)_3]$ used, light

TABLE III: Comparison between Rate Constant Ratios of e_{aq}^- and $k_{R,X}$

$[Ru(bpy)_3^{2+}]$, μM	[X], μM	$k_{(e_{aq}^- + X)}/k_{(e_{aq}^- + Ru(bpy)_3^{2+})}$	$k_{R,X}$
22	CCl_4, 72[a]	0.35[b]	0.32 ± 0.02[g]
21	$Eu(ClO_4)_3$, 17.4[c]	1.09[d]	0.78 ± 0.05[g]
21	N_2O, 250[e]	0.16[d]	0.14 ± 0.01[g]
20-60	H^+, 8-450[f]	0.39[d]	0.44 ± 0.1[g]

[a] A saturated aqueous solution of CCl_4 was prepared and deaerated by shaking water with excess CCl_4 four times with Ar for 12 min (5.0 mM CCl_4). This same solution was used as a stock solution for both flash and pulse experiments (see footnote *b*). [b] Based on our measurements of $k_{(e_{aq}^- + CCl_4)} = (1.95 \pm 0.15) \times 10^{10}$ and $k_{(e_{aq}^- + Ru(bpy)_3^{2+})} = (5.6 \pm 0.3) \times 10^{10}$ M^{-1} s^{-1} by pulse radiolysis. Lifetimes of e_{aq}^- (~1 μM) were of the order of 10^2 ns, time resolution 20 ns; control experiments showed that the decay of e_{aq}^- by either second order or reactions with impurities was negligible. Note that both $k_{(e_{aq}^- + CCl_4)}$ and $k_{(e_{aq}^- + Ru(bpy)_3^{2+})}$ are somewhat lower than those reported previously.[25,29] [c] Determined spectrophotometrically at the 394.3-nm peak, taking $\epsilon_{Eu^{3+}} = 2.55$ M^{-1} cm^{-1}. Although a more recent value for $\epsilon_{Eu^{3+}}$ is 3.06 M^{-1} cm^{-1}, we used the other value because it was used in the pulse radiolytic experiments where $k_{(e_{aq}^- + Eu^{3+})}$ was determined.[30] [d] $k_{(e_{aq}^- + X)}$ is from ref 31. $k_{(e_{aq}^- + Ru(bpy)_3^{2+})} = 5.6 \times 10^{10}$ M^{-1} s^{-1}. [e] Using a Henry coefficient of 0.02 atm^{-1} for N_2O. [f] Total of seven different combinations of $[Ru(bpy)_3^{2+}]$ and $[HClO_4]$. [g] Maximum deviations of the data.

absorption by the additives could be neglected.

ΔD_0^{510} decreased upon the addition of certain additives, which had a negligible effect, if any, on the decay of ΔD_t^{510}. Hence the decrease of ΔD_0^{510} must be due to competition by these additives for a precursor of the 510-nm absorbance. We identify any of these additives as X in our calculations. In Table III values of $k_{R,X}$, calculated from eq 1, are given. $\Delta D_{0,X}^{510}$ and $\Delta D_{\infty,X}^{510}$ are the initial absorbance

$$k_{R,X} = \frac{(\Delta D_0^{510} - \Delta D_{0,X}^{510})[Ru(bpy)_3^{2+}]}{(\Delta D_{0,X}^{510} - \Delta D_{\infty,X}^{510})[X]} \quad (1)$$

changes at 510 nm in the presence of [X] and in the presence of a relatively high [X], respectively. (At sufficiently high [X], $\Delta D_{0,X}^{510}$ did not change further upon changing [X], being usually negative (except for $X \equiv H^+$).)

No effect on the $Ru(bpy)_3^{2+}$ emission at 605 nm could be observed upon the addition of the solutes listed in Table III at the concentrations employed.

Pulse Radiolysis. Comparison between the flash photolysis data and pulse radiolysis results taken under similar conditions proved to be helpful in the identification of the transients.

Pulse irradiations of solutions containing 4×10^{-5} M $Ru(bpy)_3^{2+}$ in the presence of 0.017 M *tert*-butyl alcohol produced transient increases and decreases in absorption as shown by the spectrum in Figure 1. Replacement of *tert*-butyl alcohol by 0.01 M sodium formate had no effect on the absorbance change at 510 nm. Under the experimental conditions, the primary OH and e_{aq}^- quickly reacted with *tert*-butyl alcohol and with $Ru(bpy)_3^{2+}$, respectively. The spectra of the transient species produced by e_{aq}^- and H reaction with $Ru(bpy)_3^{2+}$ differ.[25] However, H atoms were assumed to react like e_{aq}^-, since the H atom yield is only one-fifth that of e_{aq}^-, and consequently the error introduced is small.

The absorption of e_{aq}^- at 600 nm was also measured, and its decay was found to be in agreement with previous results, as shown in Table II.

When 0.05 M $ZnSO_4$ was also present, e_{aq}^- reacted with Zn^{2+} to form Zn^+ rather than with $Ru(bpy)_3^{2+}$.[26] The spectrum observed after 50–200 μs was essentially the same as measured in the absence of $ZnSO_4$ (see Figure 1). The kinetics of absorbance formation in the presence of $ZnSO_4$ was measured at 510 nm, using various $[Ru(bpy)_3^{2+}]$. The formation was first order in both $[Ru(bpy)_3^{2+}]$ and $[Zn^+]$. A typical result is given in Table II. Other ions were used to substitute for Zn^{2+}. Of these, Co^{2+} and Cd^{2+} (as sulfates) gave results similar to those observed in the $ZnSO_4$ solutions (Table II). In the presence of 2.5×10^{-3} M $NiSO_4$, 1.5×10^{-3} M $In_2(SO_4)_3$, 0.2 M $MnSO_4$, 0.05 M $Al_2(SO_4)_3$, 0.03 M $FeSO_4$, or 0.016 M $Cr_2(SO_4)_3$, no absorption was produced at 510 nm.

Solutions containing 4×10^{-5} M $Ru(bpy)_3^{2+}$, 0.005 M $NaHCO_3$, and 0.005 M Na_2CO_3 saturated with N_2O were pulse irradiated with 4-ns pulses (2.8 μM radicals per pulse). In this system, e_{aq}^- was rapidly converted to OH radicals by N_2O, and OH reacted with the carbonate to produce CO_3^-. The absorption of CO_3^- at 600 nm decayed to zero, a reaction which we found was pseudo first order. At 510 nm a small absorption of CO_3^- could be observed initially. When all the CO_3^- radical ions decayed away, we found that there was bleaching of the initial $Ru(bpy)_3^{2+}$ absorption. The kinetics of this bleaching at several $[Ru(bpy)_3^{2+}]$ corresponded to $k(CO_3^- + Ru(bpy)_3^{2+}) = (4.0 \pm 0.4) \times 10^8$ M^{-1} s^{-1}. The spectrum of the reaction product corrected for the $Ru(bpy)_3^{2+}$ absorption very closely resembled the shape of the spectrum of $Ru(bpy)_3^{2+}$, however, with an extinction coefficient <2000 M^{-1} cm^{-1} at 455 nm. One might expect a decreased absorbance if the CO_3^- adds to or oxidizes a ligand, so as to destroy some aromaticity of a ligand or symmetry of the molecule. The OH–$Ru(bpy)_3^{2+}$ adduct also apparently has little absorption in the 400–600-nm region, although it has a broad absorption at 600–850 nm.[13]

Discussion

ΔD_0^{λ} is attributed to the formation of $Ru(bpy)_3^+$ and $Ru(bpy)_3^{3+}$ at the expense of the initially present $Ru(bpy)_3^{2+}$. The extinction coefficient of $Ru(bpy)_3^+$ (Figure 1) was calculated as follows: First, we measured $\epsilon_{Ru(bpy)_3^+}^{510}$ by pulse radiolysis in $Ru(bpy)_3^{2+}$–*tert*-butyl alcohol solutions, using the CNS^- dosimeter (see Experimental Section) and taking $G_{e_{aq}^-} = 2.8$ and $G_H = 0.6$ in the $Ru(bpy)_3^{2+}$ solutions, and $(G_{e_{aq}^-} + G_{OH}) = 5.8$ in the CNS^-–N_2O solutions. The absorbance change induced by a single pulse gives $(\epsilon_{Ru(bpy)_3^+}^{510} - \epsilon_{Ru(bpy)_3^{2+}}^{510})$ from which $\epsilon_{Ru(bpy)_3^+}^{510}$ was calculated. This value was used in combination with ΔD_0^{510} (flash photolysis) in order to determine $[Ru(bpy)_3^+]$ which was formed by each flash. From ΔD_0^{λ} and $[Ru(bpy)_3^+]$ we calculated $\epsilon_{Ru(bpy)_3^+}^{\lambda}$, neglecting the absorbance of $Ru(bpy)_3^{3+}$, the absorbance of the latter being small above 450 nm. Note that in the pulse radiolysis experiments, in the presence of *tert*-butyl alcohol, one $Ru(bpy)_3^{2+}$ ion is destroyed for every $Ru(bpy)_3^+$ ion formed, while in the flash photolysis experiments two $Ru(bpy)_3^{2+}$ ions disappeared for each $Ru(bpy)_3^+$ produced. The very good agreement between the pulse and flash spectra of $Ru(bpy)_3^+$ substantiates our analysis. The deviations between the observed pulse radiolytic data and the flash data (Figure 1) at the shorter wavelengths seem to be due to the $Ru(bpy)_3^{3+}$ absorbance. Thus, $Ru(bpy)_3^{3+}$,

which has a relatively weak absorption in that region, accounts for the small difference between pulse radiolysis and flash photolysis in that region. Our spectrum for $Ru(bpy)_3^+$ differs from that reported by Baxendale and Fiti,[25] who probably did not apply enough of a correction for the bleaching of $[Ru(bpy)_3^{2+}]$. The spectrum which was observed in the presence of $ZnSO_4$ (Figure 1) is consistent with the spectrum in the absence of $ZnSO_4$. Zn^+ can reduce $Ru(bpy)_3^{2+}$ to $Ru(bpy)_3^+$ (see Table II), according to eq 2. The agreement between k_2 values

$$Zn^+ + Ru(bpy)_3^{2+} \rightarrow Zn^{2+} + Ru(bpy)_3^+ \quad (2)$$

measured by flash photolysis and pulse radiolysis indicate that Zn^+ is formed in both cases. In pulse radiolysis, e_{aq}^- is known to react efficiently with Zn^{2+} according to

$$e_{aq}^- + Zn^{2+} \rightarrow Zn^+ \quad (3)$$

The enhanced decay of ΔD_t^{λ} upon the addition of oxidizing additives (Table I) is also consistent with the identification of $Ru(bpy)_3^+$ as a product of the photolysis:

$$Ru(bpy)_3^+ + OX \rightarrow Ru(bpy)_3^{2+} + OX^- \quad (4)$$

The observed decay of ΔD_t^{510} in the absence of additives other than $Ru(bpy)_3^{2+}$ is probably due to catalysis by traces of O_2 ($<10^{-7}$ M) which are left in the solution despite the bubbling with Ar. We tentatively suggest that the catalysis by O_2 takes place according to reactions 4 and 5 where OX

$$Ru(bpy)_3^{3+} + OX^- \rightarrow Ru(bpy)_3^{2+} + OX \quad (5)$$

$= O_2$. (The reduction of $Ru(bpy)_3^{3+}$ by O_2^- is thermodynamically favorable ($E^\circ_{(O_2/O_2^-)} = -0.32$ V)[32] and ($E^\circ_{(Ru(bpy)_3^{3+}/Ru(bpy)_3^{2+})} = 1.27$ V).) Such a mechanism can account for the pseudo-first-order nature of the decay of ΔD_t^{510}. In the absence of such catalysis, the decay is expected to be second order, due to oxidation of $Ru(bpy)_3^+$ by $Ru(bpy)_3^{3+}$. In fact, the greater part of the $Ru(bpy)_3^+$ absorption decayed away by a first-order rate law, with some small fraction ($\sim$0.25) which was stable for a much longer time. We were unable to investigate the residual absorbance due to low frequency noise problems. Apparently there are additional reactions which may affect the decay (e.g., some H_2O_2 may form as an intermediate). Baxendale and Fiti[25] reported a second-order decay of the absorption of $Ru(bpy)_3^+$, measured by pulse radiolysis. We also find second-order behavior in flash photolysis when considerably higher (5–10-fold higher than usual) $[Ru(bpy)_3^+]$ was generated. Under such conditions, the reaction was a mixed first and second order. The catalysis by traces of O_2 was demonstrated, however, using 5×10^{-7} M O_2 and 6.8×10^{-7} M $Ru(bpy)_3^+$ (produced by a single flash, see Table I). Under these conditions the reaction was still pseudo first order and the reaction rate constant k_4 was precisely the same as measured in the presence of excess O_2. Regeneration of O_2 by reaction 5 seems to be a reasonable explanation. In addition, had reaction 5 not been very efficient (in fact, diffusion controlled), one would expect ΔD_t^{510} to change at the end of reaction 4 to a small, but definitely negative value. This is expected because after $Ru(bpy)_3^+$ disappears, there is still an amount of $Ru(bpy)_3^{2+}$ (equivalent to surviving OX^-) which was converted to the nonabsorbing $Ru(bpy)_3^{3+}$. (If we obtain $Ru(bpy)_3^+$ from $Ru(bpy)_3^{2+}$ without the involvement of other materials, as we suggest to be the initial process, $Ru(bpy)_3^{3+}$ must also form at the same time.) The experimental results show that ΔD_t^{510} decayed to zero and not to a negative value, in the presence of either O_2 or duroquinone. This can be accounted for by reaction 5, if fast enough. In the case of duroquinone, absorption at 360 nm is expected to form by reaction 4, due to OX^-. Such an absorption was not observed, indicating, again, that reaction 5 is also fast in this case.

From the results presented in Figure 4 it is possible to calculate the "relative efficiency of formation" of $Ru(bpy)_3^+$. The intercept in Figure 4 did not depend on whether Fe^{3+} or Cu^{2+} were used. It represents the absorbance change at 480 nm under limiting conditions, namely, when all the $^3Ru(bpy)_3^{2+}$ reduces either Cu^{2+} or Fe^{3+} (see below). Neither Cu^+ nor Fe^{2+} absorb at 480 nm (and the same is true also for $Ru(bpy)_3^{3+}$ which is formed by electron transfer from $^3Ru(bpy)_3^{2+}$ to the acceptor). The coincidence of intercepts in Figure 4 means that the fraction of $^3Ru(bpy)_3^{2+}$ transferring electrons to Fe^{3+} or Cu^{2+} is the same for either acceptor. This result is unlikely unless the fraction is one, so that our results are consistent with earlier conclusions[9,17a] that Fe^{3+} quenching is essentially all by electron transfer. Therefore, the limiting value of ΔD_0^{480} gives the total amount of $^3Ru(bpy)_3^{2+}$ which was produced by a single flash. (An effective extinction coefficient for $Ru(bpy)_3^{2+}$ (6300 M^{-1} cm^{-1}) at 480 nm was measured in the flash photolysis setup.) Since the quantum yield for triplet formation is 1,[4-7] comparison of the limiting ΔD_0^{480} in the presence of Cu^{2+} or Fe^{3+} to ΔD_0^{510} in Cu^{2+}, Fe^{3+}-free solutions, makes it possible to calculate for our experimental conditions "the relative quantum efficiency of formation" of $Ru(bpy)_3^+$ as 0.0015 ± 0.0002 ($\lambda > 340$ nm). That is, only 0.0015 $Ru(bpy)_3^+$ are formed relative to the number of $^3Ru(bpy)_3^{2+}$ which the flash could form from ground state $Ru(bpy)_3^{2+}$ maintained at the initial concentration during the flash. Note that ΔD_0^{510} (Cu, Fe free) was measured with a light intensity 180 ± 10 times higher than that used for the measurements of ΔD_0^{480} in the presence of either Cu^{2+} or Fe^{3+} ions.

The disappearance of ΔD_t^{480} followed second-order kinetics in both Fe^{3+} and Cu^{2+} solutions at 1 M $HClO_4$ ($\mu = 1.9$). This agrees with the regeneration of $Ru(bpy)_3^{2+}$ according to reaction 5. We find $k_5 = 1 \times 10^8$ and 8.5×10^5 M^{-1} s^{-1} for $X^- = Cu^+$ and $X^- = Fe^{2+}$, respectively. The latter value agrees with a previously reported one.[17a]

After establishing the formation of $Ru(bpy)_3^+$ and that the efficiency of its formation is low, the question arises as to the mechanism of $Ru(bpy)_3^+$ and $Ru(bpy)_3^{3+}$ formation by the photolysis. $Ru(bpy)_3^+$ must have a precursor which can reduce Zn^{2+} and Cd^{2+} to Zn^+ and Cd^+, respectively (see Table II and related text). In addition it reacts with several additives (CCl_4, Eu^{3+}, N_2O, H^+) which were found to prevent the formation of $Ru(bpy)_3^+$ without reacting with it. We suggest that the precursor of $Ru(bpy)_3^+$ is e_{aq}^-, and the decrease in ΔD_0^{510} upon the addition of those additives is due to the competition between the following reactions:

$$e_{aq}^- + Ru(bpy)_3^{2+} \rightarrow Ru(bpy)_3^+ \quad (6)$$

$$e_{aq}^- + X \rightarrow X^- \quad (7)$$

(X represents an electron scavenger such as CCl_4, etc). It might be argued that the additives compete for the relatively long-lived ^3CT state of $Ru(bpy)_3^{2+}$, which is undoubtedly produced in our experiments. This is ruled out by the lack of any decrease in the emission of $^3Ru(bpy)_3^{2+}$ at 605 nm (excited at 450 nm) by any of the above additives at the highest concentrations used.

The formation of hydrated electrons by a thermal process from $^3Ru(bpy)_3^{2+}$ can be ruled out on a thermodynamic basis, as e_{aq}^- has a standard redox potential of -2.7 V while $^3Ru(bpy)_3^{2+}$ (first triplet) has only -0.85 V. In fact, even a triplet–ground state reaction (reaction 8)

$$^3Ru(bpy)_3^{2+} + Ru(bpy)_3^{2+} \rightarrow Ru(bpy)_3^{+} + Ru(bpy)_3^{3+} \quad (8)$$

can be ruled out on kinetic grounds. Bensasson et al.[27] find the lifetime for decay of $^3Ru(bpy)_3^{2+}$ independent of $[Ru(bpy)_3^{2+}]$ from 0.15×10^{-4} to 6×10^{-4} M, and we find the "efficiency of formation" of $Ru(bpy)_3^{+}$ does not increase upon increasing $[Ru(bpy)_3^{2+}]$ (see Figure 2 and related text). These results are also valid to rule out reactions such as (8) of higher excited states which might form under our conditions.

We propose a biphotonic effect as responsible for the formation of $Ru(bpy)_3^{+}$ and $Ru(bpy)_3^{3+}$ from two $Ru(bpy)_3^{2+}$ ions, e_{aq}^- being an intermediate, according to reactions 9 and 10.

$$Ru(bpy)_3^{2+}\ (\text{ground state}) \xrightarrow{h\nu} {}^3Ru(bpy)_3^{2+}\ (\text{lowest triplet}) \quad (9)$$

$$^3Ru(bpy)_3^{2+} \xrightarrow{h\nu} Ru(bpy)_3^{3+} + e_{aq}^- \quad (10)$$

The production of the $Ru(bpy)_3^{2+}$ lowest triplet from the allowed $Ru(bpy)_3^{2+}$ transitions has been previously discussed.[4-7] Reaction 10 is followed by reaction 6.

The $^3Ru(bpy)_3^{2+}$ (first triplet) has a lifetime in water of 0.65 μs and calculations of its steady state concentrations during the flash show that most of the $Ru(bpy)_3^{2+}$ ions were in the first triplet form, when the usual flash intensities were employed. With most of $Ru(bpy)_3^{2+}$ in the first triplet state during the flash, the concentration of $^3Ru(bpy)_3^{2+}$ is essentially independent of flash intensity, while the number of $^3Ru(bpy)_3^{2+}$ excited by a second photon (reaction 10) will be proportional to light intensity and to $[^3Ru(bpy)_3^{2+}]$, the latter being $\simeq [Ru(bpy)_3^{2+}]$ in the solution. Thus the biphotonic mechanism is in accord with the results in Figure 2. At very low light intensities, the yield of $Ru(bpy)_3^{+}$ deviates from linear dependence on intensity toward a square dependence, because low flash intensities are insufficient to maintain most of the $Ru(bpy)_3^{2+}$ in the triplet state. Owing to the low efficiency for $Ru(bpy)_3^{+}$ production and resultant difficulties of measurement, we could not use flash intensities sufficiently low to show a true intensity squared dependence. Figure 2 results are not in agreement with a monophotonic process at these high light intensities, since as the flash intensity is increased the small fraction of ground state $Ru(bpy)_3^{2+}$ maintained during the flash decreases even further and any monophotonic yield would level off. Figure 2 results are also not in agreement with a triplet–triplet mechanism (reaction between two triplet ions) for formation of e_{aq}^- (or $Ru(bpy)_3^{+}$). With most of the $Ru(bpy)_3^{2+}$ in the triplet state the yield from a triplet–triplet reaction would be independent of light intensity at high intensities and proportional to the square of $[Ru(bpy)_3^{2+}]$ at a fixed intensity. Reactions of the second triplet (from reaction 10) as such, without the formation of e_{aq}^-, are highly unlikely in view of the fact that relatively low concentrations of e_{aq}^- scavengers compete for the precursor of $Ru(bpy)_3^{+}$ without affecting the emission at 605 nm. Further, as previously mentioned, Table III strongly supports the participation of e_{aq}^-.[33]

Other facts are also consistent with the proposed biphotonic process. On the basis of redox potentials cited above, monophotonic production of e_{aq}^- can occur only at wavelengths $\leq$330 nm, while we find in our experiments about 30% as much $Ru(bpy)_3^{+}$ produced at $\lambda \geq$340 nm as in the range 300–340 nm. Although wavelengths $\leq$667 nm would provide sufficient energy for reaction 10, we find wavelengths $\geq$400 nm ineffective. In accord with this, Bensasson et al.[27] report that $^3Ru(bpy)_3^{2+}$ has an absorption band with a peak at 360 nm (ϵ^{360} = 27 300 M^{-1} cm^{-1}) and little absorption above 400 nm ($\epsilon^{453} = 0$, λ = 500 nm limit of measurement). These authors "assign the observed excited state absorption as a spin-allowed intraligand transition of the bpy-coordinated radical, which leads to an upper "triplet" charge transfer excited state of the $Ru(bpy)_3^{2+}$ complex". It is reasonable that such a charge-transfer upper state could be the origin of the hydrated electron, although, the apparently low efficiency of e_{aq}^- formation suggests that this is only a minor pathway for decay of this state.

Sprintschnik et al.[15a] reported the formation of H_2 by the illumination of $Ru(bpy)_3^{2+}$ derivatives in a monolayer in contact with water. Putting aside reservations concerning H_2 formation[15b] one is tempted to postulate a possible mechanism for H_2 production involving absorption of a second photon by $^3Ru(bpy)_3^{2+}$. However, for the indicated absorbed light intensity (0.5 cm^3 gas formed in 24 h with a quantum yield of 0.1),[15a] the estimated yield of gas from the biphotonic process is a factor of 10^6 low,[28] even if one H_2 is formed per photon absorbed by $^3Ru(bpy)_3^{2+}$.

Acknowledgment. We thank Don Ficht, Joseph Becker, and Lee Rawson for consistently excellent operation of the electron Linac. We are also grateful to Patricia Walsh and Robert Clarke for invaluable assistance.

References and Notes

(1) Work performed under the auspices of the U.S. Energy Research and Development Administration.
(2) Permanent address: Department of Physical Chemistry, The Hebrew University, Jerusalem 91000, Israel.
(3) J. P. Paris and W. W. Brandt, *J. Am. Chem. Soc.*, **81**, 5001 (1959).
(4) D. M. Klassen and G. A. Crosby, *J. Chem. Phys.*, **48**, 1853 (1968).
(5) J. N. Demas and G. A. Crosby, *J. Mol. Spectrosc.*, **26**, 72 (1968).
(6) J. N. Demas and G. A. Crosby, *J. Am. Chem. Soc.*, **93**, 2841 (1971).
(7) J. Van Houten and R. J. Watts, *J. Am. Chem. Soc.*, **98**, 4853 (1976).
(8) C. R. Bock, T. J. Meyer, and D. G. Whitten, *J. Am. Chem. Soc.*, **97**, 2909 (1975).
(9) C. T. Lin and N. Sutin, *J. Phys. Chem.*, **80**, 97 (1976).
(10) F. E. Lytle and D. M. Hercules, *Photochem. Photobiol.*, **13**, 123 (1971).
(11) A. Juris, M. T. Gandolfi, M. F. Manfrin, and V. Balzani, *J. Am. Chem. Soc.*, **98**, 1047 (1976).
(12) C. Creutz and N. Sutin, *J. Am. Chem. Soc.*, **98**, 6384 (1976).
(13) C. Creutz and N. Sutin, *Proc. Natl. Acad. Sci.*, **72**, 2858 (1975).
(14) S. O. Kobayashi, N. Furuta, and O. Simamura, *Chem. Lett.*, 503 (1976).
(15) (a) G. Sprintschnik, H. W. Sprintschnik, P. P. Kirsch, and D. G. Whitten, *J. Am. Chem. Soc.*, **98**, 2337 (1976); (b) S. J. Valenty and G. L. Gaines, *ibid.*, **99**, 1285 (1977).
(16) (a) H. D. Gafney and A. W. Adamson, *J. Am. Chem. Soc.*, **94**, 8238 (1972); (b) J. N. Demas and A. W. Adamson, *ibid.*, **95**, 5159 (1973); (c) P. Natarajan and J. F. Endicott, *ibid.*, **94**, 5909 (1972).
(17) (a) C. R. Bock, T. J. Meyer, and D. G. Whitten, *J. Am. Chem. Soc.*, **96**, 4710 (1974); (b) R. C. Young, T. J. Meyer, and D. G. Whitten, *ibid.*, **97**, 4781 (1975).
(18) G. S. Laurence and V. Balzani, *Inorg. Chem.*, **13**, 2976 (1974).
(19) G. Navon and N. Sutin, *Inorg. Chem.*, **13**, 2159 (1974).
(20) J. N. Demas and A. W. Adamson, *J. Am. Chem. Soc.*, **93**, 1800 (1971).
(21) F. Bolletta, M. Maestri, L. Moggi, and V. Balzani, *J. Am. Chem. Soc.*, **95**, 7864 (1973).
(22) M. Wrighton and J. Markham, *J. Phys. Chem.*, **77**, 3042 (1973).
(23) S. Gordon, K. H. Schmidt, and E. J. Hart, *J. Phys. Chem.*, **81**, 104 (1977).
(24) J. H. Baxendale, P. L. T. Bevan, and D. A. Stott, *Trans. Faraday Soc.*, **64**, 2389 (1968).
(25) J. H. Baxendale and M. Fiti, *J. Chem. Soc., Dalton Trans.*, 1995 (1972).
(26) J. Rabani, W. A. Mulac, and M. S. Matheson, *J. Phys. Chem.*, **81**, 99 (1977).
(27) R. Bensasson, C. Salet, and V. Balzani, *J. Am. Chem. Soc.*, **98**, 3722 (1976).
(28) Assumptions: $2.5 \times 10^{16} h\nu/(cm^2\ s)$ in 300–500-nm range (corresponds to intensity ~50 cm from 100-W Hg lamp); 187.5 cm^2 of monolayer on 10 slides; 40 $Å^2$ per Ru derivative in monolayer; 0.5% absorption (average ϵ for $Ru(bpy)_3^{2+}$ = 7000 M^{-1} cm^{-1} between 300 and 500 nm); $^3Ru(bpy)_3^{2+}$ lifetime = 0.65 μs; average ϵ for $^3Ru(bpy)_3^{2+}$ = 14 000 M^{-1} cm^{-1} between 300 and 400 nm; and quantum yield H_2 = 1.0 for second photon absorption. Since the H_2 formation would increase as intensity squared, one can calculate a yield of 0.5 cm^3

of gas with the above assumptions if the lamp is very close to the films.
(29) S. Gordon, E. J. Hart, M. S. Matheson, J. Rabani, and J. K. Thomas, *Discuss Faraday Soc.*, **36**, 193 (1963).
(30) (a) J. K. Thomas, S. Gordon, and E. J. Hart, *J. Phys. Chem.*, **68**, 1524 (1964); (b) S. Gordon, private communication.
(31) M. Anbar, M. Bambenek, and A. B. Ross, *Natl. Stand. Ref. Data Ser., Natl. Bur. Stand.*, **No. 43** (1973).
(32) D. Meisel and G. Czapski, *J. Phys. Chem.*, **79**, 1503 (1975).
(33) NOTE ADDED IN PROOF: In further studies currently underway using nitrogen laser flash photolysis e_{aq}^- was directly observed. J. Rabani, M. Ottolengi, and U. Lachish, private communication.

Radiation Sensitized Chain Reactions. Aqueous Nitrous Oxide and 2-Propanol[1]

T. G. Ryan and G. R. Freeman*

Chemistry Department, University of Alberta, Edmonton, Alberta, Canada, T6G 2G2 *(Received February 1, 1977)*

Publication costs assisted by the University of Alberta

The radiolysis of aqueous solutions containing 2-propanol and nitrous oxide were examined in the temperature range 513–583 K. The yields of nitrogen and acetone at 573 K were $G(N_2) = G(\text{acetone}) = 1100$. The high yields are explained by a radiation induced chain process. The proposed mechanism involves the transfer of an oxygen atom from N_2O to a $\cdot C(CH_3)_2OH$ radical producing $\cdot OC(CH_3)_2OH$. The supporting evidence for the mechanism is a linear dependence of $G(N_2)$ and $G((CH_3)_2CO)$ on the square root of both the N_2O and the 2-propanol concentrations, a linear dependence of the G values on $D^{-1/2}$ for large dose rates, and the same Arrhenius parameters for both $G(N_2)$ and $G((CH_3)_2CO)$.

Introduction

The radiolysis of aqueous solutions of methanol containing nitrate ion has been studied by Allan at room temperature.[2] A reaction between $\cdot CH_2OH$ and NO_3^{2-} producing formaldehyde, NO_2^- and OH^- in equal proportions was proposed. Mellows[3] has suggested a reaction between N_2O and $\cdot CH_2OH$ to explain high yields of nitrogen from radiolysis of methanol vapor containing N_2O at 20 °C. The reaction was believed to yield OH radicals and equal amounts of nitrogen and formaldehyde. Since OH radicals can react with methanol to produce $\cdot CH_2OH$, high yields of nitrogen are produced. Baxendale[4] has proposed that the reaction between N_2O and $\cdot CH_2OH$ could account for high yields of N_2 obtained from the radiolysis of gaseous mixtures of water, methanol, and N_2O at 120 °C.

The present work leads to the conclusion that reaction between N_2O and the $(CH_3)_2\dot{C}OH$ radical occurs above 470 K in aqueous solutions of 2-propanol and N_2O.

Experimental Section

Materials. The water used was triply distilled, the first distillation being from acid dichromate, the second from alkaline permanganate, and the third from a flask with no additive. Research Grade nitrous oxide (Matheson Co.) was freed of nitrogen dioxide by bubbling through three concentrated potassium hydroxide solutions. It was then passed through a 30-cm column of Drierite and thoroughly degassed by freeze–pump–thaw and distillation cycles under vacuum. The 2-propanol was obtained from Fisher Scientific Co. (Spectro Grade), acetone (Analytical Grade) from Mallinckrodt Canada Ltd., and salicylaldehyde (Reagent Grade) from Fisher Scientific Co.; Linde Molecular Sieves 5A and helium (99.995%) were from Union Carbide Corp. Drierite was from Hammond Drierite Co., and potassium hydroxide from Baker Chemical Co.

Sample Preparation. Five milliliters of water was introduced into the sample cell (8.5-mL capacity) and degassed using conventional vacuum techniques. Appropriate amounts of alcohol and nitrous oxide were then added, using extreme care to ensure removal of nitrogen and oxygen. Most irradiations were carried out at temperatures in excess of 470 K. At these high temperatures, the combined vapor pressure of the components (>20 atm) greatly exceeded the breaking limit of the seals on the glass cells. The cells were therefore enclosed in a steel pressure vessel containing water, then positioned in a portable heating apparatus[5] and heated to the required temperature using a two-mode controller obtained from APD Instruments. The exact temperature was determined using an Helwett-Packard 3420A differential voltmeter. After irradiation the pressure vessel was allowed to cool to room temperature, and the sample cells were removed.

Irradiation. The samples were normally irradiated in a ^{60}Co Gamma Cell 220 (Atomic Energy of Canada Ltd.), to a dose of 1.4×10^{17} eV/g. The dose rate determined by Fricke dosimetry was 1.4×10^{17} eV/g min. A ^{60}Co source in an irradiation cave was used for the dose rate dependence study over the range 0.5 to 4.8×10^{17} eV/g min and total dose from 0.25 to 1.4×10^{17} eV/g.

Product Analysis. Nitrogen was extracted by a vacuum distillation through two cold traps at 77 K, collected and measured in a Macleod-Toepler apparatus, and analyzed using gas chromatography. A 2.5-m Molecular Sieves 5A gas chromatography column was used at 298 K, with helium carrier gas and a Gow Mac thermal conductivity detector. Acetone was determined using salicylaldehyde.[6] The method was calibrated with standard samples.

Results

Nitrogen and acetone were the principal products found from the radiolysis of water containing nitrous oxide and 2-propanol at elevated temperatures. At 573 K, with $[(CH_3)_2CHOH] = 0.3$ M and $[N_2O] = 8.7$ mM the yields were $G(N_2) = G[(CH_3)_2CO] = 1100$.

1. *Effect of Nitrous Oxide Concentration.* The Ostwald solubility coefficient for N_2O in water at 573 K has not been measured. However measurements have been made to a temperature of 433 K,[7] and by analogy with the solubility of other gases at high temperatures, it is possible to estimate that the Ostwald solubility coefficient for N_2O in water at 573 K is between 0.3 and 1.4. With the

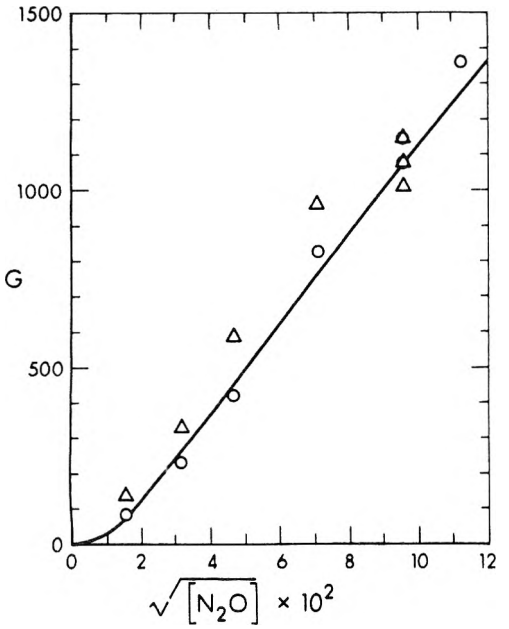

Figure 1. Product yields plotted against the square root of the nitrous oxide molarity at 573 K. $[(CH_3)_2CHOH] = 0.30 \pm 0.03$ M: (O) $G(N_2)$; (Δ) G(acetone). The full curve was calculated from eq 11 and 12 using the rate constant values given in Table II.

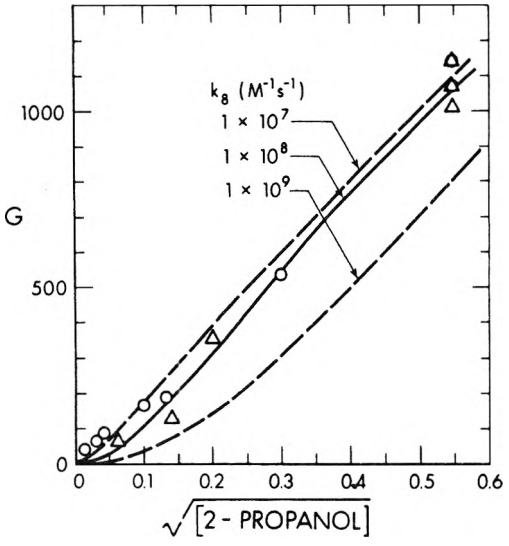

Figure 2. Product yields plotted against the square root of the 2-propanol molarity at 573 K. $[N_2O] = 8.7 \pm 0.4$ mM: (O) $G(N_2)$; (Δ) G(acetone). The full curve was calculated from eq 15 and 16 using the rate constant values given in Table II, with $k_8 = 1 \times 10^8$ L/mol s. The dashed curves show the effect of assuming $k_8 = 1 \times 10^7$ or 1×10^9 L/mol s.

technique used, a change in the coefficient from 0.3 to 1.4 would produce a twofold change in the N_2O concentration. A change from 0.3 to ∞ would produce a 2.6-fold change in the N_2O concentration. A value of 0.7 was assigned to the coefficient to calculate the N_2O concentrations.

Figure 1 displays the yields of nitrogen and acetone from irradiations at 573 K and 0.30 ± 0.03 M 2-propanol. The nitrous oxide concentration was varied from 0.24 to 12.7 mM and $G(N_2)$ values were in the range 83 to 1370. The acetone yields were equal to those of nitrogen within experimental error and varied from 138 to 1150. Blank sample yields of nitrogen and acetone were between 10 and 50 at 573 K and appropriate blank yields have been subtracted from all values reported in this work.

2. *Effect of 2-Propanol Concentration.* Figure 2 contains results from the irradiation of samples containing 8.7 ± 0.4 mM nitrous oxide and concentrations of 2-propanol between 0.18 and 300 ± 30 mM. The irradiation

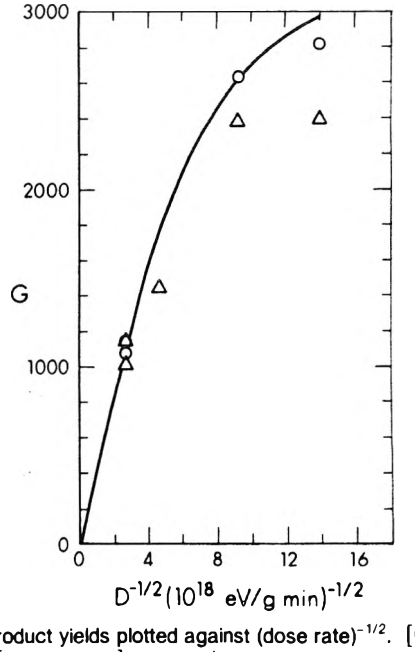

Figure 3. Product yields plotted against (dose rate)$^{-1/2}$. $[N_2O] = 8.7 \pm 0.4$ mM, $[(CH_3)_2CHOH] = 0.30 \pm 0.03$ M, $T = 573$ K: (O) $G(N_2)$; (Δ) $G((CH_3)_2CO)$.

TABLE I: Effect of Adding Acetone at 573 K

$[(CH_3)_2CHOH]$, M	$[(CH_3)_2CO]$, M	$[N_2O]$, mM	Dose, 10^{17} eV/g	$G(N_2)$
0.02	0.00	3.8	1.40	194
0.02	0.02	3.8	1.34	280
0.30	0.00	3.8	1.34	1050
0.30	0.01	3.8	1.34	1020
0.30	0.30	3.8	1.34	430
0.30	0.00	3.8	1.34	1050
0.00	0.02	3.8	1.34	2[a]
0.30	0.30	3.8	0.00	45[b]
0.02	0.02	3.8	0.00	8[b]
0.00	0.02	3.8	0.00	6[b]

[a] The blank (zero dose) sample yield was not substracted from this. [b] The amount of nitrogen obtained from the zero dose sample was equivalent to this G value at 1.34×10^{17} eV/g.

TABLE II: Rate Constant Values (L/mol s) at 573 K

k_3	2.9×10^6
k_4	8.7×10^3
k_6	1×10^{10}[a]
k_7	1×10^{10}[a]
k_8	$\leq 1 \times 10^8$

[a] Assumed.

temperature was 573 K. The nitrogen and acetone yields were equal within experimental error and ranged from about 50 to 1100.

3. *Effects of Dose Rate and Temperature.* The samples contained 8.7 ± 0.4 mM nitrous oxide and 0.30 ± 0.03 M 2-propanol. Yields of nitrogen and acetone as a function of (dose rate)$^{-1/2}$ at 573 K are given in Figure 3. The G values decreased as the dose rate was increased from 0.5 to 13.6 (10^{16} eV/g min).

As the temperature was increased from 513 to 583 K nitrogen and acetone yields increased from about 200 to 1300. An Arrhenius plot of the results is shown in Figure 4.

4. *Effect of Adding Acetone.* The product acetone is an electron scavenger and might interfere with the reaction mechanism. Addition of acetone to the samples showed that a large concentration, ~0.1 M, was necessary to appreciably reduce the nitrogen yields (Table I).

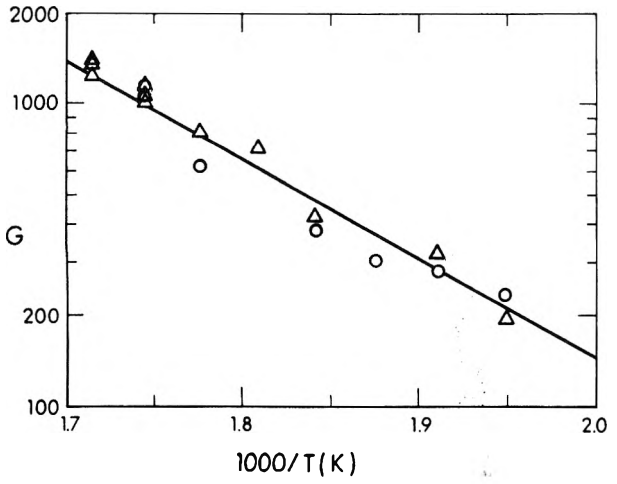

Figure 4. Arrhenius plot of chain product yields. $[N_2O] = 8.7 \pm 0.4$ mM, $[(CH_3)_2CHOH] = 0.30 \pm 0.03$ M: (O) $G(N_2)$; (Δ) $G((CH_3)_2CO)$.

Discussion

The following set of reactions is consistent with the results:

$$H_2O \rightsquigarrow H, OH \quad (1)$$

$$H,OH + HC(CH_3)_2OH \rightarrow H_2,H_2O + \cdot C(CH_3)_2OH \quad (2)$$

$$N_2O + \cdot C(CH_3)_2OH \rightarrow N_2 + \cdot OC(CH_3)_2OH \quad (3)$$

$$OC(CH_3)_2OH + HC(CH_3)_2OH \rightarrow HOC(CH_3)_2OH + \cdot C(CH_3)_2OH \quad (4)$$

$$HOC(CH_3)_2OH \rightleftarrows C(CH_3)_2O + H_2O \quad (5)$$

$$2\cdot C(CH_3)_2OH \rightarrow P_1 \quad (6)$$

$$\cdot OC(CH_3)_2OH + \cdot C(CH_3)_2OH \rightarrow P_2 \quad (7)$$

$$2\cdot OC(CH_3)_2OH \rightarrow P_3 \quad (8)$$

Solvated electrons are also produced in reaction 1, but they initiate chains by reacting with nitrous oxide, which forms an O^- ion that reacts with 2-propanol to form $\cdot C(CH_3)_2OH$. The net result for chain initiation is the same whether the initiators are (e_{solv}^-, H_3O^+, OH) or (H,OH). For simplicity only the latter are presented in the chain mechanism. Reaction 2 is well established[8] but reactions 3 and 4 are proposed for the first time. Processess similar to reaction 3 have been offered before. The reaction of nitrous oxide with a hydrogen atom has been used to explain radiation-induced chain reactions in H_2O–N_2O mixtures containing hydrogen.[9-11]

$$N_2O + H\cdot \rightarrow N_2 + \cdot OH \quad (9)$$

The gas phase rate constant for reaction 9 (k_9) has been found to have a value of 7×10^6 L/mol s at 540 °C, with an activation energy of 16 kcal/mol.[12] This indicates that at 300 °C the value of k_9 is 1×10^5 L/mol s. In water solution the $HOC(CH_3)_2OH$ dissociates readily (reaction 5). The value of the constant

$$K_{eq} = [C(CH_3)_2O]/[HOC(CH_3)_2OH] \quad (10)$$

is 5×10^2 at room temperature.[13]

It if is assumed that reactions 3 and 4 are the important propagation processes, and that termination is by reactions 6 and 7, then a steady state treatment leads to a third-order equation.

$$k_6k_7[\cdot C(CH_3)_2OH]^3 + \{k_3k_7[N_2O] + k_4k_6[HC(CH_3)_2OH]\}[\cdot C(CH_3)_2OH]^2 - k_7I[\cdot C(CH_3)_2OH] - k_4I[HC(CH_3)_2OH] = 0 \quad (11)$$

where $I = [10^{-2}DG(\text{int})]$ is the rate of initiation of the chain process, $G(\text{int}) = G(-H_2O) = 5$ is the G value for initiation,[14] and D is the dose rate. Equation 11 can be solved for the $[\cdot C(CH_3)_2OH]$ by an iterative method using a computer if values can be assigned to the rate constants. The value of k_6, the rate constant for the recombination and disproportionation of two $\cdot C(CH_3)_2OH$ radicals, is 0.7×10^9 L/mol s in water at room temperature.[15] The rate constant for a diffusion-controlled reaction in water has a value of $\sim 10^9$ L/mol s at room temperature,[16] so reaction 6 is approximately diffusion controlled at 25 °C. The coefficient of viscosity of water changes by a factor of 10 between 25 and 300 °C, so 1×10^{10} L/mol s is a reasonable estimate for k_6 at 300 °C. The rate constant for the combination and disproportionation of $\cdot C(CH_3)_2OH$ and $\cdot OC(CH_3)_2OH$ radicals is assumed to have a value $k_7 = 1 \times 10^{10}$ L/mol s.

The magnitudes of k_3 and k_4 are determined from the experimental data. The line drawn through the data in Figure 1 is calculated using $k_3 = 2.9 \times 10^6$ L/mol s and $k_4 = 8.7 \times 10^3$ L/mol s. First the $\cdot C(CH_3)_2OH$ concentration is calculated by solving eq 11 and then the $G(N_2)$ and $G((CH_3)_2CO)$ values are obtained from

$$G(N_2) = G((CH_3)_2CO) = \frac{k_3[N_2O][\cdot C(CH_3)_2OH]}{10^{-2}D} \quad (12)$$

There is considerable scatter in the experimental data in Figure 1 but the experimental points indicate that $G(N_2)$ and $G((CH_3)_2CO)$ vary approximately linearly with the square root of the N_2O concentration for $[N_2O]^{1/2} > 0.02$ $M^{1/2}$. This can be understood by realizing that for high concentrations of nitrous oxide the $[\cdot C(CH_3)_2OH]$ will be small, so it is reasonable to neglect the contribution of reaction 6 to termination under these conditions. A steady state treatment assuming that reaction 7 is the only mode of termination leads to

$$G(N_2) = G((CH_3)_2CO) = (G(\text{int}))^{1/2}\left(\frac{k_3k_4}{k_7}\right)^{1/2} \times \frac{[N_2O]^{1/2}[HC(CH_3)_2OH]^{1/2}}{(10^{-2}D)^{1/2}} \quad (13)$$

For constant 2-propanol concentration eq 13 predicts a linear dependence of $G(N_2)$ and $G((CH_3)_2CO)$ on the square root of the nitrous oxide concentration.

At low N_2O concentration the $\cdot C(CH_3)_2OH$ concentration will be increased and termination by reaction 6 will be more important. Considering the extreme case where reaction 6 is the only mode of termination one obtains

$$G(N_2) = G((CH_3)_2CO) = (G(\text{int}))^{1/2}\frac{k_3}{(k_6)^{1/2}}\frac{[N_2O]}{(10^{-2}D)^{1/2}} \quad (14)$$

The data in Figure 1 appear to show a first-order dependence on the N_2O concentration for $[N_2O]^{1/2} < 0.02$ $M^{1/2}$, in agreement with eq 14. The calculated curve obtained using the general eq 11 fits the data reasonably well at all nitrous oxide concentrations studied (Figure 1).

If one considers reactions 7 and 8 to be the important termination reactions and propagation by 3 and 4, then eq 15 can be derived. The line through the data in Figure

$$k_7k_8[\cdot OC(CH_3)_2OH]^3 + \{k_3k_8[N_2O] + k_4k_7[HC(CH_3)_2OH]\}[\cdot OC(CH_3)_2OH]^2 + k_7I[\cdot OC(CH_3)_2OH] - k_3I[N_2O] = 0 \quad (15)$$

2 was obtained by solving eq 15 for the $\cdot OC(CH_3)_2OH$

concentration and using eq 16 to calculate $G(N_2)$ and $G((CH_3)_2CO)$. To fit the data at low 2-propanol con-

$$G(N_2) = G((CH_3)_2CO) = \frac{k_4[\cdot OC(CH_3)_2OH][HC(CH_3)_2OH]}{10^{-2}D} \quad (16)$$

centrations it was necessary to assume that $k_8 \leq 1 \times 10^8$ L/mol s. At higher 2-propanol concentrations reaction 4 will proceed at a higher rate so that the $\cdot OC(CH_3)_2OH$ radical concentration will be reduced and termination by reaction 7 becomes more probable. As mentioned above, assuming that reaction 7 is the only mode of termination leads to eq 13, so a square root dependence of $G(N_2)$ and $G((CH_3)_2CO)$ on the 2-propanol concentration is predicted. The $G(N_2)$ and $G((CH_3)_2CO)$ values in Figure 2 show such square root dependence for $[2\text{-propanol}]^{1/2} \geq 0.1$ $M^{1/2}$.

At lower 2-propanol concentrations the $\cdot OC(CH_3)_2OH$ concentration will be increased and termination by reaction 8 becomes more probable. If one assumes that reaction 8 is the only mode of termination then eq 17 can be de-

$$G(N_2) = G((CH_3)_2CO) = \frac{k_4}{(k_8)^{1/2}} \frac{(G(\text{int}))^{1/2}[HC(CH_3)_2OH]}{(10^{-2}D)^{1/2}} \quad (17)$$

rived. The bending of the experimental data at $[2\text{-propanol}]^{1/2} \leq 0.1$ $M^{1/2}$ (Figure 2) is most likely due to a change to first-order dependence on 2-propanol concentration as predicted by eq 17. The calculated curve obtained from eq 15 and 16 fits the data reasonably well for all 2-propanol concentrations studied (Figure 2).

It should be pointed out that the 2-propanol concentration study involves a high enough N_2O concentration that eq 13 is applicable at higher 2-propanol concentrations (Figures 1 and 2). The N_2O concentration was varied while keeping the 2-propanol concentration large enough that eq 13 applies at higher N_2O concentrations (Figures 1 and 2).

Figure 3 shows the dependence of $G(N_2)$ and $G((CH_3)_2CO)$ on the dose rate. The study was carried out using 8.7 ± 0.4 mM nitrous oxide and 0.30 ± 0.03 M 2-propanol. These are conditions where eq 13 is applicable, as discussed above, so that a linear dependence of both $G(N_2)$ and $G((CH_3)_2CO)$ on the reciprocal of the square root of the dose rate is predicted. The data in Figure 3 indicate a curvature for lower dose rates but a reasonable linear dependence for higher dose rates.

The temperature study was performed using conditions where eq 13 is applicable, 8.7 ± 0.4 mM nitrous oxide and 0.30 ± 0.03 M 2-propanol. The mechanism predicts that $G(N_2)$ and $G((CH_3)_2CO)$ show the same temperature behavior. The data in Figure 4 indicate that this is the case. The slope of the line in Figure 4 yields $^1/_2(E_3 + E_4 - E_7) = 15$ kcal/mol. Reaction 7 is assumed to be diffusion controlled with an activation energy of about 3 kcal/mol, so $E_3 + E_4 = 33$ kcal/mol. From the present work it is not possible to determine individual values for the activation energies.

Effect of Adding Acetone. Acetone is an electron scavenger with a rate constant for reaction with hydrated electrons of $\sim 6 \times 10^9$ L/mol s at room temperature.[17] The reaction of N_2O with hydrated electrons at room temperature has a rate constant of 7.9×10^9 L/mol s.[18] If the mechanism were ionic one would expect that 0.02 M acetone would be sufficient to reduce the chain length substantially in a sample containing 3.8 mM N_2O and the first two samples listed in Table I indicate that this is not the case. Even the addition of 0.3 M acetone only reduced the yield of N_2 from about 1000 to 430 (Table I). These results support the hypothesis that the mechanism involves free-radical chain carriers.

References and Notes

(1) Financially assisted by the National Research Council of Canada.
(2) J. T. Allan, *J. Phys. Chem.*, **68**, 2697 (1964).
(3) M. Meaburn and F. W. Mellows, *Trans. Faraday Soc.*, **61**, 1701 (1965).
(4) J. H. Baxendale and G. P. Gilbert, *Science*, **147**, 1571 (1965).
(5) J. C. Russell and G. R. Freeman, *J. Phys. Chem.*, **72**, 808 (1968).
(6) S. Berntsson, *Anal. Chem.*, **28**, 1337 (1956).
(7) W. Schröder, *Chem. Ing. Tech.*, **45**, 603 (1973).
(8) A. Kato and R. J. Cvetanović, *Can. J. Chem.*, **46**, 235 (1968).
(9) C. H. Cheek and J. W. Swinnerton, *J. Phys. Chem.*, **68**, 1429 (1964).
(10) F. S. Dainton and D. C. Walker, *Proc. R. Soc. London, Ser. A*, **85**, 339 (1965).
(11) C. H. Cheek, *J. Phys. Chem.*, **71**, 2363 (1967).
(12) R. R. Baldwin, A. Gethin, J. Plaistowe, and R. W. Walker, *J. Chem. Soc., Faraday Trans. 1*, **71**, 1265 (1975).
(13) Y. Ogata and A. Kawasaki in "Chemistry of Carbonyl Compounds", Vol. 2, S. Patai, Ed., Interscience, New York, N.Y., 1970, p 1.
(14) K. N. Jha, T. G. Ryan, and G. R. Freeman, *J. Phys. Chem.*, **79**, 868 (1975).
(15) M. Simic, P. Neta, and E. Hayon, *J. Phys. Chem.*, **73**, 3794 (1969).
(16) E. F. Caldin, "Fast Reactions in Solution", Wiley, New York, N.Y., 1964, p 12.
(17) Z. D. Draganić and I. G. Draganić, *J. Phys. Chem.*, **75**, 3950 (1971).
(18) G. L. Bolton and G. R. Freeman, *J. Am. Chem. Soc.*, **98**, 6825 (1976).

Oscillatory Kinetics in Electrochemical Oxidation of Hydrogen in an Almost Anhydrous Solvent

B. E. Conway* and D. M. Novak†

Chemistry Department, University of Ottawa, Ottawa, Ontario, Canada *(Received March 9, 1977)*

Publication costs assisted by the University of Ottawa

In a number of electrochemical (and chemical) reactions, a situation can arise where no stable steady state of the reaction is established. The system then exhibits sustained oscillations around an unstable steady state. The conditions giving rise to this state of affairs often involve diffusion and inhibition of a reaction, leading to a current–potential relation for the process which shows an inversion corresponding to negative resistance or positive feedback. In the present work, the inhibition of oxidation of H_2 at a Pt anode has been studied in trifluoroacetic acid containing controlled traces of water. Under these conditions, only a small fraction of the surface is anodically oxidized and H_2 oxidation occurs in a kinetically periodic way when potentials are reached at which the oxide layer can begin to be reduced and readsorption of trifluoroacetate anion can occur. The oscillations are related to the diffusion-controlled mass transport of H_2. Sustained, rather than damped oscillations, are observed under potentiostatic conditions since electrical power is provided to the reaction from the external circuit. The participation of the surface oxide and anion adsorption/desorption in the oscillations was deduced indirectly by in situ observation of periodic changes of relative reflectance in-phase with the oscillations. The changing period, Δt, of oscillation which arises in a cathodic potential sweep can be related to the current pulse amplitudes, Δi. A linear relation to $(\Delta t)^{1/2}$ is demonstrated which provides a key indication that the oscillations arise because of coupling between the kinetics of the electrocatalytic oxidation reaction and diffusional mass transfer of H_2.

I. Introduction

While many chemical processes can take place under steady-state conditions, provided a uniform supply of reactants is maintained, it is very interesting that a number of chemical,[1-3] electrochemical,[4-6] and enzyme-catalyzed reactions[7,8] take place in a kinetically *periodic* manner.

Renewed interest in oscillatory phenomena in chemical reactions has arisen recently both in physical chemistry and biochemistry.[7-10] In these cases, no stable steady state can exist and the process oscillates around an unstable steady state. In homogeneous reactions, oscillatory kinetics are rare (cf. ref 2 and 3) but in heterogeneous, especially electrochemical, reactions they are well known but the conditions under which they can arise have not been well defined.

Oscillations in electrochemical systems can originate in two ways: (a) by coupling with appropriate impedance components of an external circuit to make an "electrochemical oscillator" device[11] and (b) intrinsically, as a property of the kinetics and mechanism of the process itself.[1,12] The latter type of oscillatory phenomenon is of more fundamental interest in the kinetics of coupled electrochemical reactions.

Oscillatory electrochemical reactions usually arise (a) when a current-density (i)–potential (V) curve having a negative resistance component, $dV/di < 0$, characterizes the process.[13,14,16,17] Usually this condition arises when passivation of the reaction occurs, e.g., by an oxide film,[5,12,13] but similar behavior can originate from double-layer effects;[14] (b) when the electrode process is coupled with a diffusion-limited, or partially diffusion-limited, step associated with transport of the reactant to the electrode surface.[12,15] Usually the electrode process itself must have the negative resistance characteristic referred to in (a).

The negative resistance characteristic provides the positive feedback function commonly required for self-sustaining oscillations, e.g., as in an oscillator with inductive coupling. The impedance characteristics of this type of situation at electrodes have been considered by Epelboin.[16]

Oscillatory processes can be of two types: (i) a damped oscillatory approach toward a steady state (in kinetics) or toward an equilibrium (in thermodynamics of a reversible process); (ii) a sustained oscillation associated with consumption of a continuously supplied reactant and/or provision of free energy from some exo-energetic process. In electrochemical sustained oscillations, this is provided from the external power source or from the electrochemical free energy of a cell reaction.

In two previous papers,[6,15] we have examined the theory of oscillatory phenomena in the oxidation of HCOOH and C_2H_4 at electrodes and demonstrated the role of reactive oxide films and diffusion effects. The electrochemical reactions which HCOOH and C_2H_4 undergo[6] at electrodes are known to be complex,[18-21] so the study of a simpler system which exhibits oscillations is desirable.

In the present paper we report the results of work in which oscillatory kinetics in the electrochemical oxidation of H_2 at Pt were found. In water, oscillatory oxidation of H_2 is not normally observed[23,24] although Butler and Armstrong[26] found oscillations in an undivided H_2-electrolysis cell due to cross diffusion. By conducting the oxidation of H_2 in an almost anhydrous solvent medium, trifluoroacetic acid, we have found that sustained current oscillations can be observed under controlled-potential conditions and limited oscillations under linear potential-sweep[6] conditions. The nature of this oscillatory behavior will be described and tentative explanations for it offered.

II. Experimental Section

1. *Choice of Solvent System.* Trifluoroacetic acid (TFA) was chosen as solvent because (a) it can be made initially almost anhydrous (cf. ref 27), pure by normal solvent purification and drying procedures, and very anhydrous by "gettering" remaining traces of water by addition of a trace of trifluoroacetic anhydride through the

† On leave of absence from the Laboratory for Physico-Chemical Separations, Center for Marine Research, "Ruder Boskovič" Institute, Zagreb, Yugoslavia.

reaction $CF_3CO{\cdot}O{\cdot}COCF_3 + H_2O$ traces $\rightarrow 2CF_3COOH$; (b) it is a good ionizing solvent for a number of salts including potassium trifluoroacetate (KTFA); (c) it is itself, with KTFA as electrolyte, not oxidizable until above +3.0 V E_H when it undergoes the Kolbe reaction.[27] Hence there exists a large anodic potential range over which the solvent is electrochemically inactive; for example, no H atoms dissociatively active at Pt exist in the molecule as they do with some other nonaqueous solvents such as CH_3OH, C_2H_5OH, or CH_3COOH. TFA is thus an ideal electrochemically inactive solvent, anodically,[47] and since it does not have actively available the "elements of oxygen" there is also no possibility of oxidation of the Pt electrode surface over a wide potential range until the carboxylate function is discharged.[27] Hence, effects of controlled trace additions of water which lead to limited surface oxidation of the Pt and to oscillatory behavior in H_2 oxidation, can conveniently be examined.

2. *Chemicals and Purification Procedures.* All chemicals used were analytical reagent grade. Further purification procedures were performed as described below:

(a) TFA (Eastman Kodak Co.) was first gently refluxed over $KMnO_4$ (Fisher Co., Ltd.) for at least 24 h. The mixture was then slowly distilled, three successive distillations being performed. Prior to the third distillation, 0.05% of trifluoroacetic anhydride was added to diminish the water content in the acid to be used immediately after the distillation in the experimental run.

(b) Trifluoroacetic anhydride (Eastman Kodak Co.) was used to diminish water content in the TFA, as mentioned above. It was purified by performing a slow distillation at 39.5 °C, prior to use in a run. Later, the anhydride was also distilled from $KMnO_4$.

(c) KTFA, used as electrolyte, was prepared by neutralization of previously purified TFA with 5 M potassium carbonate (Fisher ACS analytical grade). The mixture was heated gently until saturation was achieved. The solution was then left to crystallyze slowly. The crystals were washed with the mother liquor and dried under vacuum at 100 °C.

(d) Water used for water additions in the runs was obtained by the pyrocatalytic distillation procedure previously described.[29]

(e) H_2 and N_2 gases used for bubbling in the cell were purified and dried as described previously.[30,31]

3. *Solutions.* The solutions used consisted of 0.5 M KTFA dissolved in the pure 100% TFA liquid. The dryness or wetness of each solution was controlled with successive additions of trifluoroacetic anhydride or of the pyro-distilled water, respectively.

4. *Glassware and Cleaning Procedures.* A small cell having a volume of 40 cm^3 was employed. The cell was first cleaned with concentrated H_2SO_4, rinsed repetitively with pyro-distilled water, and then dried at 200 °C for 12 h prior to use in a run. After cooling it for a few minutes just before the run, the inside of the cell was rinsed with trifluoroacetic anhydride to ensure complete dryness.

5. *Apparatus.* Potentiodynamic sweep experiments (cf. ref 32) were carried out using a Wenking potentiostat driven by a Servomex LF 141 function generator. Regular and oscillatory current–potential curves were recorded on an Hewlett-Packard XY recorder though a high-impedance cathode follower. Oscillations generated at constant potential, in time, were recorded on a fast Y-time recorder.

6. *Electrodes and Their Purity.* Spectroscopically pure Pt wires and gauzes were used. The electrodes were stored in BDH Aristar H_2SO_4, then rinsed with the pyro-distilled water and stored in it for 1 day. They were rinsed with trifluoroacetic acid just prior to use in a run. A small bead Pd/H electrode was used as a reference electrode within a Luggin capillary.[30,31]

7. *Experimental Procedure.* After deoxygenation of the solution, the current–potential profiles generated by a repetitive linear sweep were recorded. The amount of water present in the solution could easily be characterized (cf. ref 33) by the quantity of charge associated with the oxide reduction peak[32,34] at Pt.

When only traces were present, holding the potential at the anodic end of the sweep for a few minutes increases the oxide reduction peak, corresponding to diffusion of H_2O and growth of the oxide film. The same procedure provides a test for ultra-dryness of the solution; thus, on anodic holding, no change in the flat current–potential profile occurs over the oxide reduction region if no water is present. This was found to be the case for 5 min holding in solutions "gettered" with trifluoroacetic anhydride.

In order to record oscillations in H_2-oxidation current, the solution was bubbled with H_2 initially for at least 20 min and after each run for a further 2 min. Bubbling was terminated, of course, during the observation of the oscillations.

In some experiments, simultaneous relative reflectance ($\Delta R/R$) experiments (cf. ref 35) were performed while the electrode was giving a periodic H_2-oxidation current.

III. Results and Preliminary Discussion

In the presence of H_2 in TFA solution, current oscillations at the Pt electrode were observed under both potentiostatic and potentiodynamic conditions. The oscillatory behavior was found to depend (a) on degree of dryness of the solution, i.e., on the extent to which the Pt electrode surface was oxidized at appropriate positive potentials, and (b) on stirring.

It was first necessary to define the state of the Pt electrode surface in anhydrous TFA solutions and those containing traces of water by establishing the H adsorption characteristics at Pt in this solution and the extent of surface oxidation that arises in the presence of various trace concentrations of water. In these initial experiments, no molecular H_2 which gives rise to the oscillatory behavior was present.

1. *The Current–Potential Profiles for Pt in Anhydrous TFA and with Added Traces of Water.* (i) *Effects of Added Water.* We show first the potentiodynamic i–V profiles at Pt for the most anhydrous TFA solutions (Figure 1a) and then comparatively (Figures 1b,c) those for the same solutions with controlled additions of water. Holding effects at the positive limit E_a of the anodic sweep are also shown. These results demonstrate (Figure 1a) the initial dryness of the solution where no detectable (<1% coverage) surface oxidation of Pt occurs (cf. ref 33) and how a small and controllable degree of surface oxidation arises (Figure 1b,c) when traces of water are present.[48] If the initial dried preparation of distilled TFA contains, as it usually does, a trace of water, this is indicated by small but significant oxide film formation currents at potentials more positive than ca. 0.95 V E_H and a small oxide reduction current peak in the cathodic sweep. An ultra-dry solution can then be obtained by controlled trace additions of trifluoroacetic anhydride until the i–V profile takes the form of Figure 1a with zero surface oxidation current and no oxide reduction peak in the cathodic sweep. Confirmation of ultra-dryness is given by holding the potential at the positive end of the sweep for 1–5 min (cf. section II.7) and demonstrating (Figure 1a, curves 2 and 3) no development of any Pt-surface oxide reduction peak in a following cathodic sweep.

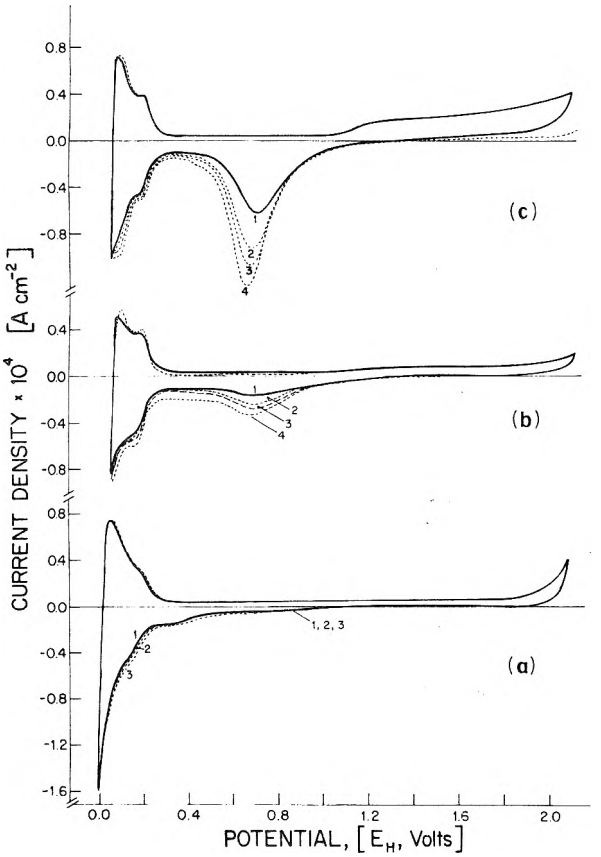

Figure 1. Potentiodynamic $i-V$ profiles for a Pt electrode in anhydrous TFA + KTFA as electrolyte with addition of traces of water. (a) Anhydrous TFA gettered by a trace of trifluoroacetic anhydride: (1) multisweep; (2, 3) holding at 2.164 V for 120 and 300 s. Sweep rate = 8.2×10^{-2} V s^{-1}. (b) TFA with water added: (1) multisweep; (2, 3, 4) holding at 2.164 V for 30, 60, and 120 s, respectively. Sweep rate = 8.2×10^{-2} V s^{-1}. Water concentration = 0.19 mol %. (c) TFA with water added: (1) multisweep; (2, 3, 4) holding at 2.09 V for 30, 60, and 120 s. Sweep rate = 8.2×10^{-2} V s^{-1}. Water concentration = 0.42 mol %.

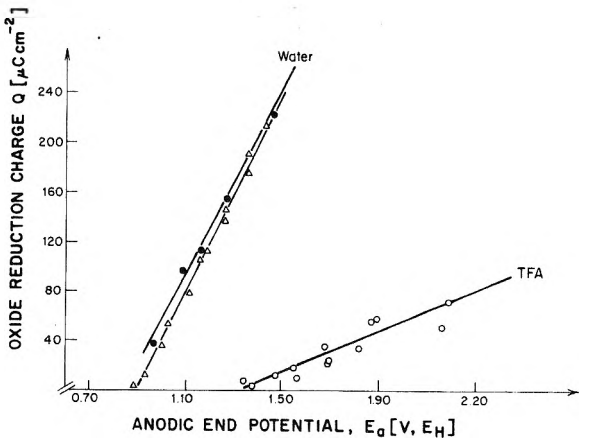

Figure 2. Effect of diminishing positive and potential E_a in the anodic sweep at Pt in TFA containing 0.42 mol % H_2O (and in 0.1 and 1.0 M aqueous $HClO_4$ for comparison) on the charge for surface oxide formation and reduction: (△) 1 M aqueous $HClO_4$; (●) 0.1 M aqueous $HClO_4$; (○) 0.5 M KTFA in TFA.

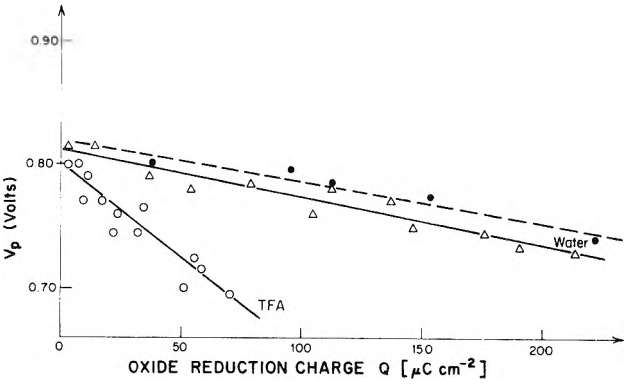

Figure 3. Plot of cathodic peak potential V_p for reduction of surface oxide at Pt as a function of the charge for reduction in TFA and aqueous 0.1 and 1.0 M $HClO_4$: (△) 1 M aqueous $HClO_4$; (●) 0.1 M aqueous $HClO_4$; (○) 0.5 M KTFA in TFA with 0.42 mol % H_2O. Scale for V_p: H_2/H potential in the same (aqueous or TFA) solution.

The extents of surface oxidation of Pt in Figure 1a–c are found, as expected, to be substantially below a monolayer (this is obvious in comparison with the H atom charge for the same electrode) when only traces of water are present.

(ii) *H Adsorption in Anhydrous and Almost Anhydrous TFA.* It is interesting that even in the driest solution, current peaks for adsorbed H atom deposition and ionization[32] are observed (Figure 1a), indicating that underpotential deposition[36] of chemisorbed H in at least two states (there are four or five observable in water[35,36]) on the Pt surface is possible in a solvent other than water. Comparative experiments in 0.1 M aqueous $HClO_4$ on the *same* electrodes showed that the H accommodation at Pt in anhydrous TFA up to the H_2-reversible potential is about 40% of that in water. The charge for H deposition and ionization on the same electrode studied in 0.1 M aqueous $HClO_4$ was therefore used as a standard of reference[36] for evaluation of extents of surface oxidation of Pt in the TFA solutions.

Absence of impurity effects in TFA was demonstrated by showing that the H charge attains a well-defined value (Figure 1c) of 109 ± 10 μC cm^{-2}, independent of the extents of surface oxide generated from traces of water (Figure 1b,c) by the "holding" experiments, at 2.090 V vs. PdH. In 0.1 M aqueous $HClO_4$, the same electrode gave 270 μC cm^{-2}.

(iii) *Surface Oxidation of Pt in Almost Anhydrous TFA in Relation to that in Water.* The effects of added water on the $i-V$ profiles for Pt in TFA were shown in Figure 1a–c. The behavior of the oxide film formed at Pt from traces of water in TFA, i.e., when the oxide film is present only at low coverages, is seen to be surprizingly similar to that of fuller films on Pt in water[34] (Figures 2 and 3). Despite the low coverage ($\theta_{OH} \leq 0.1$ can easily be achieved in a "fairly dry" solution), the surface oxide begins to be formed in TFA at ca. 0.95 V E_H (Figure 1b) but is reduced only at appreciably less positive potentials, commencing at 0.95 V E_H. This suggests that the small coverage by oxide may be present as islands on the Pt surface.

The oxide reduction charge decreases linearly with diminishing end potential E_a in the previous anodic sweep (Figure 2) and the reduction peak potential V_p is linear in the oxidation charge Q (Figure 3). These two figures also show comparatively the behavior in aqueous $HClO_4$ solutions. However, the slope $-dV_p/dQ$ in Figure 3 is much larger in TFA than it is in aqueous solution while dQ/dE_a (Figure 2) is much smaller. This suggests that there is a relatively greater stabilization due to place exchange of the oxide film grown in TFA from traces of water than that grown from fully aqueous solution.[34]

2. *Oscillations in H_2 Oxidation under Potentiostatic Conditions.* From potential-sweep experiments (see section III.3) it was found that oscillations in the molecular H_2-oxidation current arise at a critical potential, V_c, corresponding to the commencement of reduction of surface oxide at Pt. The potential V_c depends on the surface coverage of the oxygen film as can be seen from

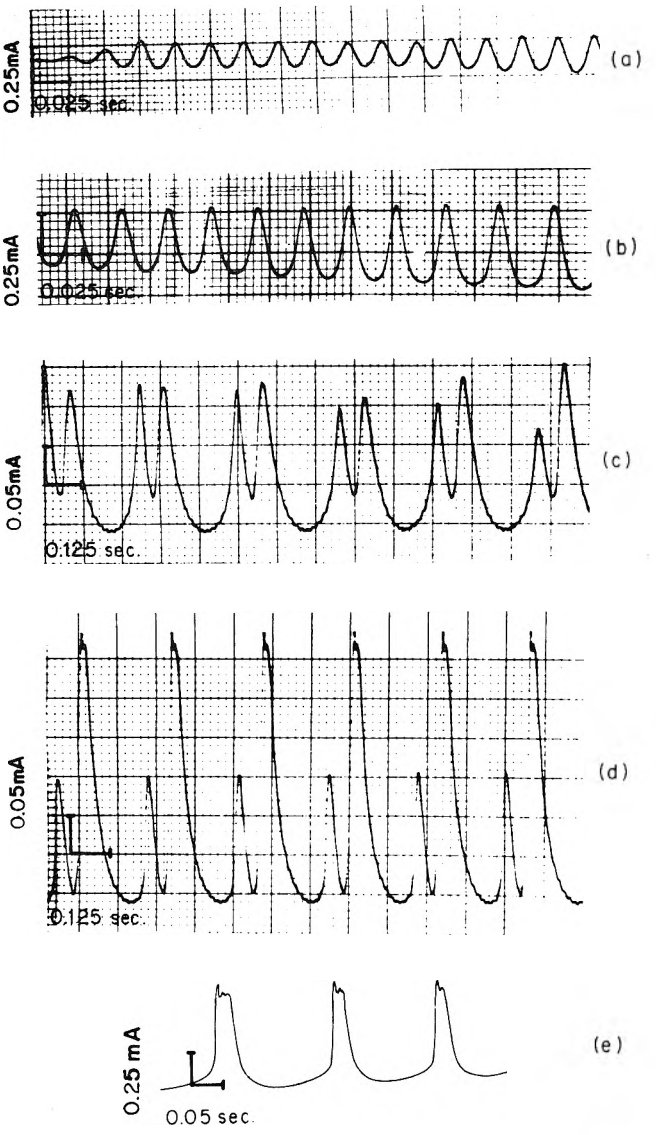

Figure 4. Four examples (a, b, c, d) of potentiostatic (+1.24 V) oscillations of H_2 oxidation current at the Pt electrode in TFA: (a) is the almost sinusoidal oscillation occurring initially; (b) is the nonsinusoidal, but still simple, oscillation which develops later; (c) and (d) are compound oscillations which develop subsequently (the relative amplitudes of the two components also vary slowly with time). The time base was 4 cm s^{-1}. (e) Record of an apparent simple type oscillation on a faster time base (20 cm s^{-1}) showing "nonsinusoidal" behavior (the very low amplitude oscillations superimposed on this record are due to writing noise in the recorder).

Figure 2 and is, of course, dependent on water concentration since the latter determines the extent of surface oxidation at a given potential. That the oscillations are not due to participation of the external circuit (cf. ref 11) was shown by varying the resistance from which the current measurement is made or by varying a series resistance in the reference-electrode circuit. They are thus intrinsic kinetic oscillations of the types that have been previously observed in other systems.[4-6]

Sustained oscillations could be demonstrated by adjusting the potential potentiostatically at the value V_c and following the oscillating current on a high input-impedance potential–time recorder system. Examples of the oscillating current behavior for H_2 oxidation are shown in Figure 4a–d.

In contrast to the oscillatory behavior of HCOOH or C_2H_4 oxidation,[6] the H_2-current periodicity is initially (Figure 4a and to some extent as in 4b) almost sinusoidal corresponding to "linear-oscillation"[37] behavior. This may

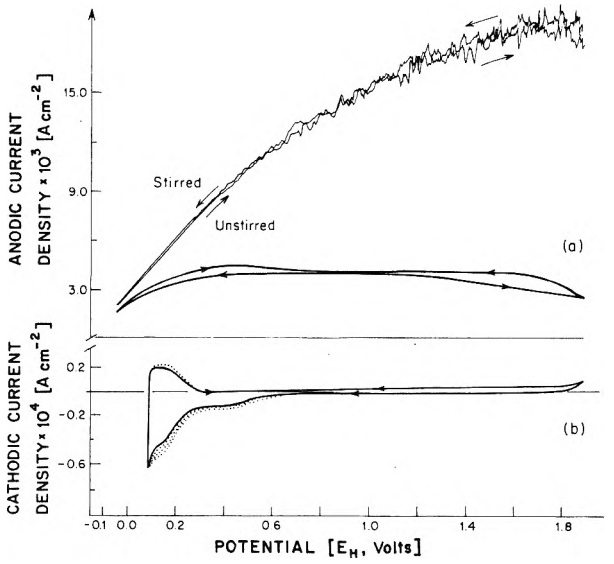

Figure 5. (a) Current–potential profiles for H_2 oxidation in a very dry TFA + 0.5 M KTFA solution (stirred and unstirred): $s = 7.7 \times 10^{-2}$ V s^{-1}, $T = 298$ K. (b) Background $i-V$ profile for Pt in the TFA solution in absence of H_2.

be connected with the simpler reaction involved with H_2 than with HCOOH or C_2H_4. However, it is evident from Figure 4c,d for example, that there is some compound oscillation (reminiscent of forced oscillations, ref 38) also involved as there are two components in the "sinusoidal" oscillations which develop in Figure 4c,d and show a superimposed longer-period change of amplitude. No oscillations arise if the solution is "absolutely anhydrous" nor if excess water is present (see section III.3).

An enlarged record of a single-peaked oscillation on a faster time base is shown in Figure 4e from which it is clear that once the oscillations have become established, they deviate substantially from the almost regular sinusoidal form of Figure 4a.

The charges q_τ in each oscillation can be evaluated from $\int_0^i i\,dt$ over a single oscillation. At the beginning of the potentiostatic oscillation q_τ is small (ca. 6 μC cm^{-2}, Figure 4a) while later, when the oscillations have developed in amplitude, q_τ attains values in double peaks (Figure 4c) up to 296 μC cm^{-2}. The latter values are much larger than would correspond to periodic reduction and re-formation of the oxide film in almost dry solutions (viz. 20–40 μC cm^{-2}) and must therefore correspond to oxidation of H_2 itself by periodic partial depletion of H_2 from the diffusion layer. Complete depletion of H_2 from a 0.02-cm thick diffusion layer would correspond to 8800 μC cm^{-2} for the H_2 solubility of 4.4×10^{-8} mol cm^{-2} in such a lamina, as determined in separate experiments.

3. *Oscillations in H_2-Oxidation Current under Potentiodynamic Conditions.* (i) *Behavior in Almost Dry Solutions.* In an extremely dry solution, gettered by the anhydride, the $i-V$ profile of Figure 5 is observed and no oscillations arise. Under these conditions, inhibition of H_2 oxidation which normally occurs at ca. 0.9–1.0 V (see Figure 8) does not arise; H_2 oxidation then continues with substantial currents up to high positive potentials (+1.86 V in Figure 5). Then both the anodic and cathodic $i-V$ profiles are almost identical and no oxide inhibition effect occurs. This is consistent with the background $i-V$ profile for the Pt electrode in anhydrous TFA in the absence of H_2 (curve b of Figure 5) which shows no sign of surface oxidation, even after holding the potential for up to 5 min at 1.86 V. Stirring increases the current substantially (Figure 5), depending on stirring rate, so that H_2 oxidation is diffusion controlled.

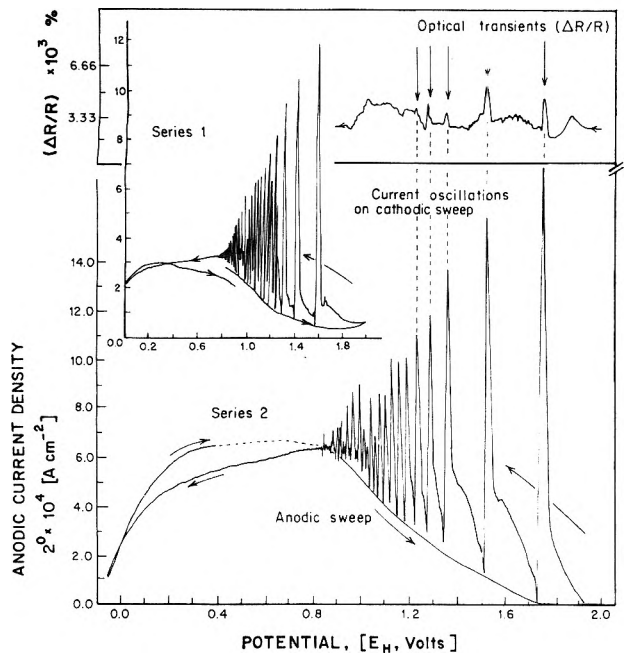

Figure 6. Current oscillations in H_2 oxidation on the cathodic sweep in two potentiodynamic experiments on H_2 oxidation at Pt in almost dry TFA + 0.5 M KTFA ($s = 8 \times 10^{-2}$ V s^{-1}, $T = 298$ K). Note: potential scale of series 1 is half the sensitivity of that for series 2 to accomodate the results on a single graph. Upper curve, relative reflectance changes $(\Delta R/R)_{\parallel}$ measured simultaneously with the oscillations.

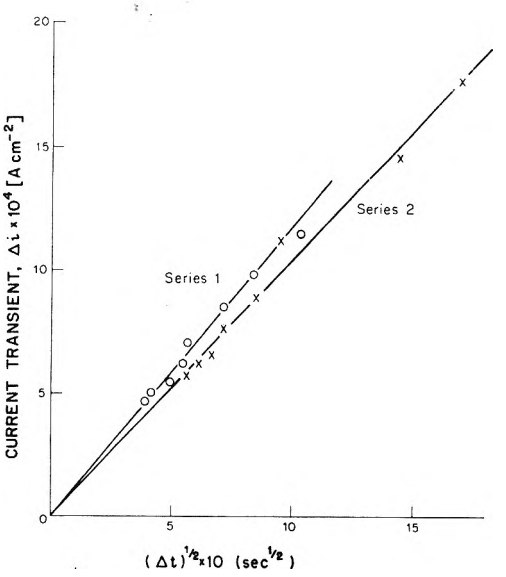

Figure 7. Test of relation between current oscillation amplitudes Δi in Figure 6 and the square root of the time interval, Δt, between successive oscillations for the two series of oscillations shown in Figure 6 for separate experiments.

If a very small trace of water is, however, still present, the system exhibits oscillations on the cathodic sweep right from the most positive end of the sweep as shown in Figure 6. The oscillations, it seems, are not dependent, in this case, on the reduction of a fractional oxide film on the Pt surface as they are when more water is present (see Figures 8, 11, and 12). They have an amplitude which almost reaches the current profile attained in a well-stirred solution (Figure 5) and their lower limits are seen (Figure 6) to coincide with the locus of currents generated on the previous anodic sweep. This situation is again quite different from that arising when sufficient water is present to produce a significant oxide film (see Figures 8, 11, 12, and 14).

Inspection of the series of oscillations in Figure 6 shows that their interval diminishes as their amplitude decreases during the progress of the cathodic sweep. This suggests that each current pulse occurs after an interval of time, Δt, from the previous pulse (Figure 6) determined by the period required for the H_2 concentration at the electrode to recover, by diffusion, almost to its bulk value in the diffusion layer. When this situation is established, the electrode is reactivated for H_2 oxidation and a new current pulse is generated. This mechanism leads to the expectation, based on well-known principles of diffusional transport and the concept of "transition time",[45] that the magnitude of successive current pulses in the sweep should decrease with the square root of the time interval, Δt, between the successive oscillations of Figure 6. This is elegantly proved by the plots in Figure 7 which show that the amplitude of successive oscillations is a good linear function of $(\Delta t)^{1/2}$ for two separate examples of oscillatory behavior. As required for this mechanism, the i vs. $(\Delta t)^{1/2}$ plots extrapolate through the origin. The key role of diffusion coupled with the electrode reaction at the Pt surface is thus established by the plots in Figure 7.

The "on–off" nature of the periodicity of current under potentiodynamic conditions (Figure 6), where the oscillations are virtually well separated pulses, suggests that the integrated equation for diffusion of H_2 at an electrode at which the H_2 is oxidized at a current density i, viz.

$$c_b - c_e = \frac{2i}{zF}\left(\frac{t}{\pi D}\right)^{1/2} \quad (1)$$

can be applied to each pulse as though it were a current transient with an associated transition time, Δt, for c_e to approach zero. In eq 1, c_b is the bulk concentration of H_2 in mol cm^{-3}, c_e that at the electrode, D is the diffusion constant of H_2, t the time, and z the number of Faradays per mol for the oxidation reaction. From the maximum (initial) current pulse in Figure 6 and the corresponding time interval Δt (see relation in Figure 7), an estimate of $c_b - c_e$ can be made. It is found to be almost equal to c_b, the saturation solubility of H_2. Thus the current oscillation consumes almost all the H_2 built up previously in the diffusion layer while H_2 oxidation was inhibited.

The upper curve of Figure 6 shows that the oscillations are accompanied by significant periodic relative reflectivity (cf. ref 35) changes of the surface, indicating that the current periodicity is not just due to periodic diffusion effects but also to changes of state of the surface of the electrode. In this experiment, the TFA was almost, but not completely, dry as indicated by the anodic current profile for H_2 oxidation and a separate background experiment in the absence of H_2. In these circumstances, it seems that the periodic transients in $\Delta R/R$ should be related to anion desorption/readsorption rather than to oxidation and reduction of the surface involving the traces of water (see section IV.3).

(ii) *Relation to Surface Oxidation of Pt in TFA with Controlled Additions of Water.* Under potentiodynamic conditions where a *range* of potentials is scanned, it was always easy to generate temporary oscillations as the potential in the sweep passed through a range near V_c (see section III, 2) provided that (a) the solution was not too dry or (b) a substantial concentration of water (>5%) was not present (see below). The behavior observed was reproduced on many occasions at various electrodes and from different solutions over a period of 2 years.

If the quantity of water present is small, so that only a fraction of the Pt surface is covered by an oxide film, then oscillations occur on the cathodic sweep (three or four, or more, are observed depending on extent of prior oxi-

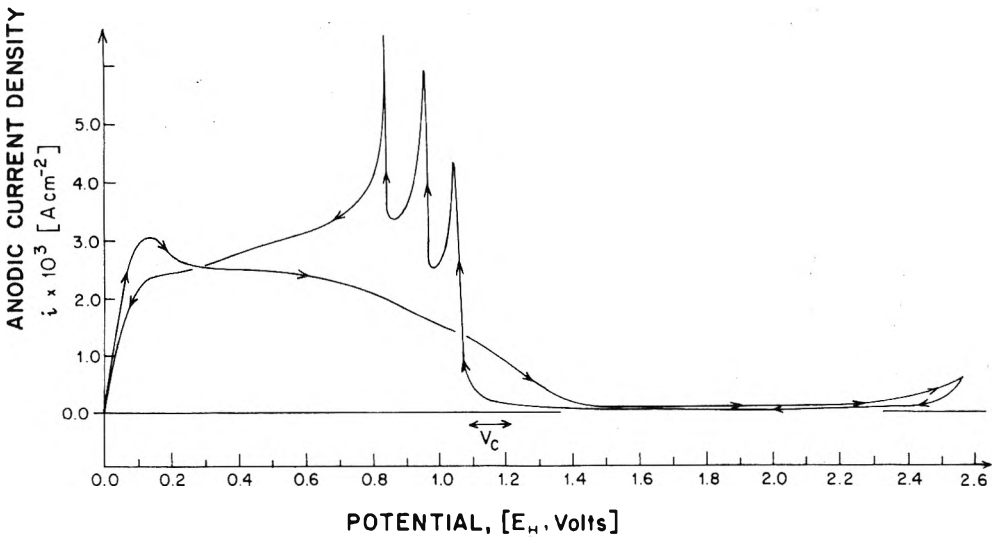

Figure 8. Current oscillations in H_2 oxidation on the cathodic sweep in a potentiodynamic experiment at Pt in TFA + 0.2 mol % added water.

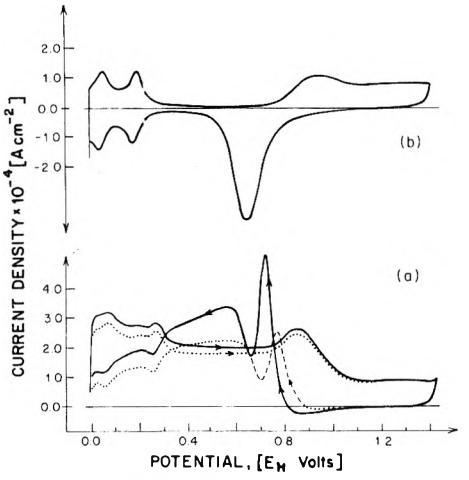

Figure 9. Potentiodynamic $i-V$ profiles for H_2 oxidation at Pt in 0.1 M aqueous $HClO_4$ without (broken line) and with (solid line) holding at 1.453 V E_H for 2 min; (a) Background curve (without H_2 present) for Pt surface oxidation and reduction over the same potential range at the same sweep rate is shown above for comparison in (b). Sweep rate = 1.15×10^{-1} V s^{-1}.

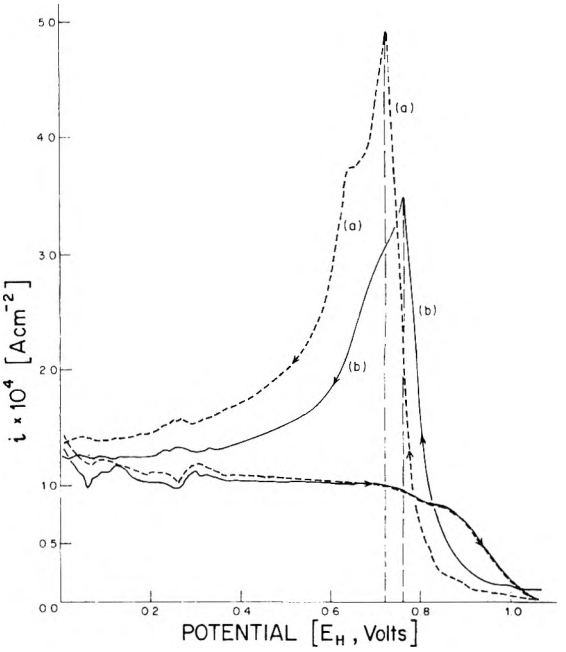

Figure 10. Current difference curves for H_2 oxidation at Pt in 0.1 M aqueous $HClO_4$ with holding for 2 min (a) and without holding (b) (as in Figure 9), i.e., after subtraction of background $i-V$ profile for Pt in absence of H_2.

dation of the electrode) once the potential for commencement of oxide reduction has been reached at V_c. The charges associated with the oscillations vary from ca. 0.6 to 4 mC cm^{-2}, i.e., comparable with the charge required for depletion of H_2 in the diffusion layer. Figure 8 shows an example of the potentiodynamic $i-V$ profile for H_2 oxidation at Pt in TFA + 0.2 mol % H_2O.

In order to understand this behavior, it is useful first to relate it to the $i-V$ profiles for H_2 oxidation which arise (without oscillations) in aqueous solutions at Pt. Under such conditions, H_2 is oxidized in a diffusion-controlled reaction over the potential range 0.0 to 0.75 V E_H (Figure 9). Around +0.75 V, however, inhibition of H_2 oxidation commences, until by 1.1 V where the Pt electrode is fully covered by OH species,[34] the H_2-oxidation current has become negligible. The behavior is illustrated in Figure 9 where the $i-V$ profile for H_2 oxidation at Pt is compared with that for formation and reduction of the surface oxide in the absence of H_2. The H_2-oxidation current is to a close approximation (cf. ref 24 and 25), the difference between these two curves as shown in Figure 10.

The main point of similarity to Figure 8 is that as soon as oxide-film reduction begins, a sharp increase in the anodic current component for H_2 oxidation arises but subsequently the cathodic current for oxide film reduction becomes temporarily appreciable and reverses the direction of change of the current giving a minimum in the net anodic current (since the oxide-film reduction current increases in proportion to sweep rate, this component appears more important at higher sweep rates).

In the "nonaqueous" solution case with TFA, it is significant that the derivative di/dV at the point where oxide film reduction just commences (Figure 8) is larger than for the case of aqueous solutions and approaches "infinity" where the oscillations commence, i.e., no stable steady state is realized. This behavior is similar to that associated with a bifurcation set in the cusp-catastrophe theory of discontinuous processes.[42]

An important part of the sudden increase of H_2-oxidation currents in Figures 9 and 10 at the commencement of oxide film reduction, especially after anodic holding (Figure 10, curve b), must be due to the accumulation of H_2 in the diffusion layer during the time in the sweep when H_2 oxidation was inhibited. When inhibition is relieved by surface oxide reduction or anion desorption in the

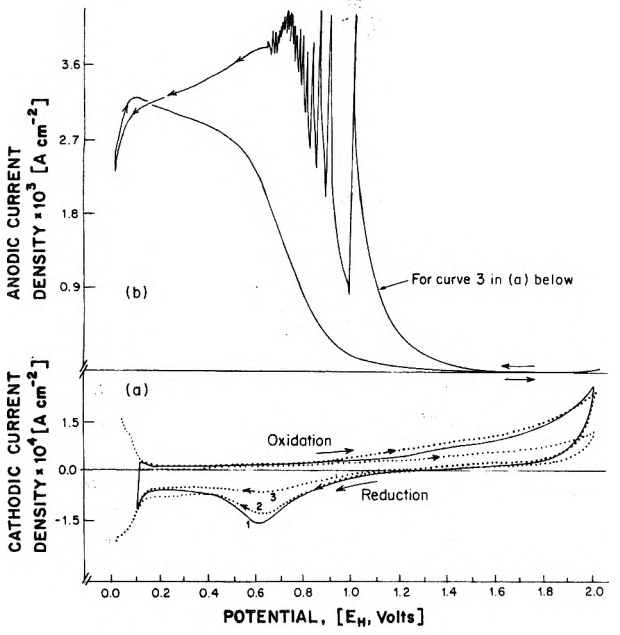

Figure 11. Transitional case between oscillatory behavior in Figure 6 and that in Figure 8. A small quantity of water is present and corresponding small surface oxide coverage is generated: (a) background $i-V$ profile for Pt for two additions of trifluoroacetic anhydride (curves 2,3) in relation to initial curve (1) for wetter solution; (b) oscillatory behavior of H_2 current.

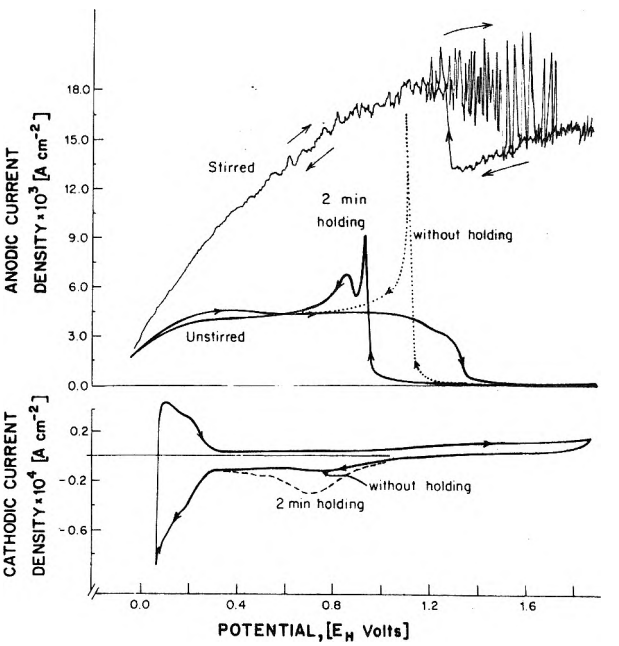

Figure 12. Current oscillations in H_2 oxidation at Pt in TFA as in Figure 8 but with an increased quantity of added water. Lower curve shows background $i-V$ profile for Pt in the TFA solution in absence of H_2.

cathodic sweep, a sudden increase of current to values larger than on the anodic sweep arises because (a) the free catalytic surface of Pt is generated having high activity (as also observed in oxidation of organic substances at Pt) and (b) the H_2 concentration at the interface in the diffusion layer has become increased up to the bulk value. The same will apply to the behavior in the almost anhydrous TFA solutions in the oxide inhibition region but the quantity of oxide generated as a film in Figures 9 and 10 (ca. 600 $\mu C\ cm^{-2}$) when water is in excess is, of course, much greater than that in Figure 8 for TFA solution.

The importance of diffusion and oxidation following periodic H_2 accumulation is substantiated by the observation that stirring eliminates the periodic current behavior (cf. the case of C_2H_4, ref 6) and increases all currents up to a new mass-transfer-controlled limit. Then, apart from some inhibition effects when the oxide film is formed and relief of inhibition when the oxide film reduction commences (Figures 8, 12, and 14), the anodic and cathodic $i-V$ profiles are almost the same (Figures 12 and 14). Although effects of stirring indicate the role of diffusion, it is clear from the existence of the oscillations that the reaction conditions must change in a periodic way between partial and virtually complete diffusion control. Thus, if the reaction were at all times completely diffusion controlled, no periodic increases in its rate would be observed in unstirred solutions.

Transitional behavior between that in Figure 6 for almost completely dry TFA and that in Figure 8 for a less dry solution is shown in Figure 11. Here oscillations again commence when the oxide film begins to be reduced but a sequence of many current pulses is generated on the cathodic sweep as in Figure 6. The lower series of curves (a) show the $i-V$ profiles for Pt in the absence of H_2 for two successive additions of trifluoroacetic anhydride to a TFA solution that was initially slightly wet. The quantity of oxide measured by the charge under the reduction peak becomes progressively smaller with the additions of anhydride. The oscillations in Figure 11b correspond to a condition of surface oxidation characterized by curve 3 in Figure 11a. The behavior in a wetter solution is shown in Figure 12.

Figures 8, 11, and 12 show that in TFA with traces of water, H_2 oxidation is almost completely inhibited beyond potentials of ca. 1.2 V despite the fact that only about 10% of the surface is covered by an oxide film under the conditions of experiments giving Figures 8 and 12. Only in the very driest solutions, "gettered" with the trifluoroacetic anhydride (Figure 5), are appreciable H_2-oxidation currents maintained up to ca. +1.86 V without inhibition.

These somewhat surprising results suggest that the H_2-oxidation reaction takes place normally on only a small fraction of the Pt surface where active centers, or suitable edges or steps, are available. The behavior is not inconsistent with Somorjai's recent findings[40] on the catalytic activity of Pt single-crystal surfaces cut at high index planes.

Further additions of water allow the electrode to become more extensively oxidized in the sweep, or with anodic holding. Then, in the cathodic sweep, only a single current spike is initiated at the commencement of surface oxide reduction but no oscillations occur (Figure 13). Its maximum value approaches the (steady) current which can be generated in a strongly stirred solution where diffusion effects are diminished. Of course, at the moment the spike current is established, there is no almost concentration gradient of H_2 at the electrode surface since the H_2-oxidation current has previously remained inhibited at more positive potentials in the cathodic sweep, as explained earlier.

If the sweep is taken anodically just into the region where surface oxidation of Pt just commences in TFA, multiple oscillations arise as shown in Figure 14. These occur as the very small quantity of surface oxide, generated in the restricted range anodic sweep, is reduced.

IV. General Discussion

1. *Origins of Oscillatory Behavior.* Oscillating kinetic behavior in a reaction arises under special conditions when no stable steady state exists,[6-8,13] stability in this case being defined as a zero or positive rate of entropy production for displacements from the steady state. Such systems are well

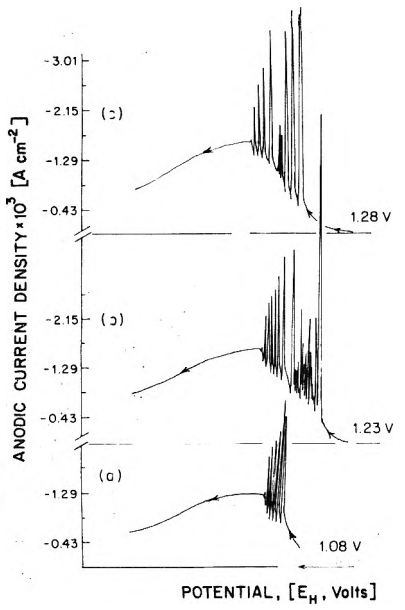

Figure 13. Oscillations in H_2 oxidation at Pt in TFA containing traces of water on a cathodic sweep initiated just at the potential where surface oxidation commences.

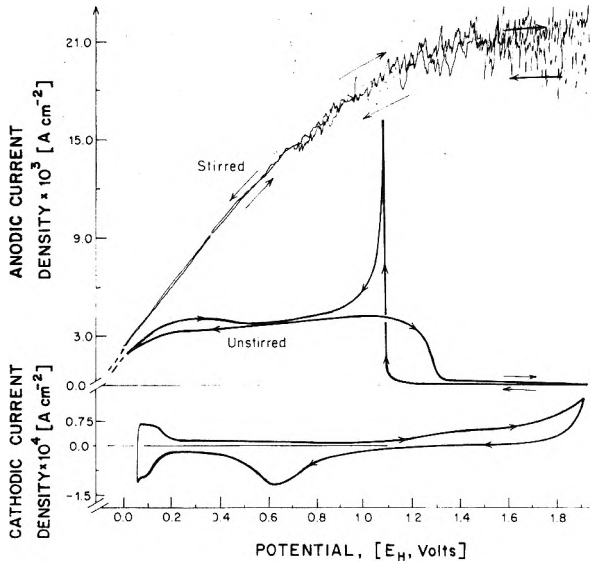

Figure 14. As in Figure 11 but with further addition of traces of water. Lower curve shows background $i-V$ profile for Pt in the TFA solution in absence of H_2. Note larger surface oxide reduction peak than in Figure 11, curve 3.

known in mechanics, resonant electrical circuits, and in biological systems, e.g., at membranes. Oscillatory behavior arises when the differential equation representing the kinetics of the reaction has a periodic solution in time rather than a unique steady-state solution. The simplest case of periodicity is that of a sine function which is generated when the restoring force in a system is linearly related to the displacement (Hooke's law; harmonic oscillator case). In a chemical reaction, this would correspond to some linear, and hence usually small, displacement from equilibrium through an affinity change or, in electrochemical reactions, to a linear displacement of the rate by a small overpotential ($\beta\eta F << RT$). Of course, in most cases, the spontaneous return to equilibrium is an asymptotic one with no overshoot or oscillation. However, in a number of reactions, especially electrochemical ones which are driven by the existence of nonequilibrium reactant concentrations (chemical potentials) or by a nonequilibrium electrode potential, oscillatory kinetics can arise.[2,5,6,9,10,13,16] In many cases, the periodicity is of a *nonlinear* kind, i.e., the restoring force in the system is a higher-order function of the displacement than the first power; then nonsinusoidal periodicity arises and the system can have more than one[42] characteristic period of oscillation as is often observed[13,29,42,43] in electrical, chemical, and electrochemical oscillations.

We have shown previously[6,13] that oscillatory behavior can often arise when an electrode surface reaction is coupled to a reactant diffusion process,[15] especially when the surface process is one of passivation which exhibits a negative-resistance characteristic giving positive feedback. This is the situation with the present case of H_2 oxidation. The diffusion process provides a kind of capacitance for the reaction (in a Warburg impedance element), so that coupling of these two conditions can, in principle, give rise to periodic kinetic behavior analogous to that in an inductively coupled oscillator. The positive feedback component is usually an *autocatalytic step* or one that behaves in a kinetically equivalent manner, e.g., the negative resistance characteristic of a passivation $i-V$ profile or a sigmoid shaped curve arising from double-layer effects.[12]

It is to be noted that the oscillations occur only on the cathodic sweep. This arises presumably because in the anodic-going sweep a situation of increasing kinetic stability obtains, with oxide film coverage tending to increase and anion adsorption becoming stronger. In the cathodic sweep, the contrary situation arises and tends to cause increasing rates of H_2 oxidation as the potential decreases, i.e., a positive feedback situation is established leading to oscillatory behavior in the kinetics.

2. *Kinetic Equations.* In order to illustrate the complexity of the problem of oscillations at an electrode, it will be useful to enumerate the factors which control the kinetics and write the appropriate rate equations. Six factors must be taken into account in formulating a system of kinetic equations that represent the behavior of the H_2-oxidation reaction: (a) the role of diffusion[15] of H_2 indicated by stirring effects; (b) the reactivity of an incomplete oxide film at Pt;[24,25] (c) the electrode potential; (d) the free surface area, "$1 - \theta$", available for direct electrocatalytic reaction of H_2; (e) inhibition of catalytic activity by anion adsorption; and (f) reversibility and irreversibility (hysteresis[34]) in the formation and reduction of the oxide film on Pt.

We shall denote the concentration of H_2 at the electrode as c_e and that the bulk as c_b, and the distance variable over which a concentration gradient can be set up as x. The diffusion process is

$$H_2\,(\text{bulk})(c_b) \rightarrow H_2\,(\text{electrode})(c_e) \qquad (I)$$

for which

$$dq_{H_2}/dt = -D(dc/dx) = i/2F \qquad (2a)$$

per unit area where i is the current density and D the diffusion coefficient of H_2. Also Fick's second law gives

$$D(\partial^2 c/\partial x^2)_t = (\partial c/\partial t)_x \qquad (2b)$$

and we are interested in the condition $x = 0$ where $c = c_e$.

The reactions of H_2 which can occur at the surface are

$$H_2 + 2Pt \rightarrow 2PtH \qquad (II)$$

$$PtH \rightarrow H^+ + e^- + Pt \qquad (III)$$

and (cf. ref 24 and 25)

$$H_2 + 2PtOH \rightarrow 2H_2O + 2Pt \qquad (IV)$$

Scheme I

H_2 concentration in diffusion layer approaches bulk value (inhibited state; H_2-flux minimized; current minimum)

↑ H_2 flux diminishes

Inactivated surface; H_2 concentration in diffusion layer recovers to larger values

Reactivation due → to increase of H_2 concentration at electrode surface—positive feedback step

$+ A^- + H_2O$ ←

Surface inactivated due to anion readsorption and/or surface oxidation (hysteresis with respect to desorption directions of these processes)

Reactivated surface due to oxide reduction by H_2 and/or desorption of adsorbed anions by reaction $H^+ + A^-_{ads} \rightarrow HA$ from H^+ produced by H_2 oxidation at surface

↓ H_2 consumption facilitated

Diffusion layer depleted in H_2; flux of H_2 maximized (active state, H_2-oxidation current maximized)

Anion adsorption at coverage θ_A is represented by

$$A^- + Pt \rightarrow Pt(A^-) \quad (V)$$

The surface oxidation reactions of Pt are

$$Pt + H_2O \text{ (traces)} \rightarrow PtOH + H^+ + e^- [\rightarrow PtO + H^+ + e^- \text{ at higher potentials}] \quad (VI)$$

$$PtOH \rightarrow \text{"OHPt"} \text{ (place-exchanged state of deposited OH)} \quad (VII)$$

Both H_2 and adsorbed H generated in step II could react with the surface oxide species[24,25] but ionization reaction III is very rapid at Pt at potentials >0.4 V E_H, so the coverage by H at potentials where the Pt surface is oxidized will be negligible. Then the following kinetic equations can be written, noting that the subscript numbers on rate constants, k, refer to the reaction steps enumerated above with corresponding Roman numerals:

$$d\theta_H/dt = k_2(1 - \theta_H - \theta_{PtOH} - \theta_{A^-})^2 c_e - k_3\theta_H \exp(V/b) \quad (3)$$

where b is a Tafel slope factor $RT/\beta F$;

$$d\theta_{OH}/dt = k_5(1 - \theta_{PtOH} - \theta_{OHPt} - \theta_{A^-}) \times \exp(V/b) - k_4\theta_{PtOH} c_e \quad (4)$$

The overall velocity of H_2 oxidation in terms of current density i can be written

$$i/2F = v_{II} + v_{IV} \quad (5)$$

where (II) is coupled with (I) through diffusion involving c_e (eq 2a and 2b), i.e.

$$i/2F = -dc_e/dt = k_2(1 - \theta_H - \theta_{PtOH} - \theta_{A^-})c_e - k_4\theta_{PtOH}{}^2 c_e \quad (6)$$

The concentration c_e would normally be obtained, as in other diffusion problems, through eq 2b by integration with suitable boundary conditions. However, in the case of oscillatory i, c_e will be periodic. If the periodicity is treated as a series of pulses (cf. the form of Figure 6), the boundary conditions are a little easier to define, at least for the maximum current pulses: when $i \rightarrow i_{max}$, eq 1 indicates $c_e \rightarrow 0$; when $i \rightarrow i_{min}$ or 0 (i.e., when inhibition prevails), $c_e \rightarrow c_b$.

Szpak and Rice[46] treated a related problem by *assuming* a periodic boundary condition of a sinusoidal form. This does not seem an acceptable procedure since the form of the oscillatory behavior has then virtually been assumed in advance. The periodic "boundary condition" is really generated by the kinetics of the oscillatory process itself which makes the solution of the coupled kinetic and diffusion equations singularly difficult.

Inhibition effects arise in eq 6 through the "$1 - \theta$" terms and probably additionally (see below) through the coverage θ_{A^-} by adsorbed TF anions, and reactivation (in a cathodic sweep) as this term becomes smaller. Autocatalytic effects can arise[6] in the oxide film stripping step IV. Potential dependence of i arises indirectly through the dependence of θ_H, θ_{OH}, θ_A, and the corresponding "$1 - \theta$" terms on (V). Neither steady-state nor quasi-equilibrium expressions can be assumed for these coverage terms, e.g., $1 - \theta_H - \theta_{OH}$ and θ_{PtOH} in eq 6 or eq 3 and 4.

3. *Role of Inhibition by Anion Adsorption and H_2 Accumulation and Transport in the Diffusion Layer.* The oscillatory behavior appears to arise from periodic inhibition and reactivation of the surface, coupled with diffusion (indicated by the results of Figure 7) and H_2 accumulation in the diffusion layer, as discussed in relation to the results of Figure 6. The behavior in this figure also indicates that the oscillations are unlikely to arise directly from periodic formation and reduction of the oxide film at low coverages since they commence already at 1.8 V and persist down to ca. 1.0 V under conditions where only a very small coverage by "oxide species" can exist. Thus the behavior of the oxide film itself in the absence of H_2 shows (Figure 11) that, even for the small coverages generated by traces of water, there is a large hysteresis between the formation and reduction processes with respect to the potential range involved so that oxide existing at 1.8 V could hardly be reduced and re-formed in a periodic manner over a short potential range. The oscillatory behavior is, however, also accompanied by "in-phase" periodic changes of state of the electrode surface as indicated by the $\Delta R/R$ results of Figure 6. The combination of these results indicates that the inhibition/reactivation involved in the oscillatory behavior is more likely to be associated with anion adsorption since the oxide coverage in many of the experiments is insufficient to provide inhibition of H_2 oxidation on more than ca. 10% of the apparent surface.

If oxidation of H_2 is initiated by a fluctuation, the pH will be locally decreased (note, the solvent is ca. 100% TFA) due to production of H^+ from H_2 in the diffusion layer which could decrease inhibiting anion adsorption by protonation of adsorbed trifluoroacetate anions giving increased H_2 oxidation in a positive feedback (autocatalytic) process and a consequent current pulse. As the H_2 in the diffusion layer is consumed, its rate of oxidation at the electrode becomes diminished ($c_e < c_b$) and anion readsorption with inhibition is restored as the pH recovers

its initial value at the electrode surface.

Figures 8, 12, and 13 show that in the presence of larger traces of water the oscillations are initiated at the potential where reduction of the oxide film commences. At first it was thought (cf. ref 6 and 15) that the oscillations were directly associated with periodic formation and reduction of the oxide film at ca. 1.0 V through its reversible component (cf. ref 34). The results of Figure 6 and the transitional case, Figure 11, suggest, however, that the oscillations which arise at the potential of commencement of reduction of the film are also associated with anion desorption/adsorption effects. The presence of traces of water causes complete inhibition of H_2 oxidation in the anodic sweep despite the fact that only 10–20% of the surface is covered by oxide film—this oxide presumably is preferentially formed on high energy (least noble) catalytically active sites which are thereby blocked. Inhibition remains effective on the cathodic sweep until the (island?) regions of surface oxide are just reduced; then new free surface sites are generated at which a large H_2-oxidation current density can be temporarily sustained. The behavior in Figure 6 for an almost dry solution gives a clue to the origin of the oscillatory behavior in the wetter solutions: the trifluoroacetate anion can cause inhibition at the newly regenerated free Pt sites but as the reduction of the limited oxide film continues, reactivation of H_2 oxidation can occur several times depending on the water content, i.e., oxide film coverage (Figures 11 and 14), and the potential range in the cathodic sweep over which it is reduced. No H_2 oxidation can occur until new active sites are regenerated in the wetter solutions by reduction of the small coverage by oxide which blocks the active regions of the surface in that case.

4. *Cycle of Processes in Periodic H_2 Oxidation.* It will be useful to summarize the effects associated with the reactions given above by means of the cycle of activity of the electrode as shown in Scheme I.

Acknowledgment. Grateful acknowledgment is made to the National Research Council of Canada for support of this work. We are indebted to Dr. F. C. Ho in our laboratory for carrying out the relative reflectance measurements.

References and Notes

(1) E. S. Hedges and J. E. Myers, "The Problem of Physicochemical Periodicity", Longmans, Green and Co., New York, N.Y., 1926.
(2) J. Bray, *J. Am. Chem. Soc.*, **43**, 1262 (1921).
(3) M. G. Peard and C. F. Cullis, *Trans. Faraday Soc.*, **47**, 616 (1951); R. J. Field, E. Kovos, and R. M. Noyes, *J. Am. Chem. Soc.*, **94**, 8649 (1972).
(4) K. F. Bonhoeffer and G. Langhammer, *Z. Elektrochem.*, **52**, 60, 67 (1948).
(5) K. F. Bonhoeffer and H. Gerischer, *Z. Elektrochem.*, **52**, 149 (1948); cf. K. F. Bonhoeffer, *ibid.*, **52**, 24 (1948). See also K. S. Indira, S. K. Rangarajan, and K. S. Doss, *J. Electroanal. Chem.*, **21**, 57 (1969), on periodic effects in passivation.
(6) J. Wojtowicz, N. Marincic, and B. E. Conway, *J. Chem. Phys.*, **48**, 4333 (1968).
(7) J. Higgins, *Proc. Natl. Acad. Sci. U.S.A.*, **51**, 989 (1964); R. A. Spangler and F. M. Snell, *J. Theor. Biol.*, 16, 381 (1967).
(8) J. Higgins, *J. Ind. Eng. Chem.*, 59, 18 (1967).
(9) U. F. Franck, *Symp. Faraday Soc.*, **9**, 137 (1974).
(10) G. Viniegra-Gonzalez, "Biological and Biochemical Oscillators", Academic Press, New York, N.Y., 1972, p 71.
(11) H. F. Hunger, *J. Electrochem. Soc.*, **115**, 492 (1968).
(12) J. Wojtowicz, "Modern Aspects of Electrochemistry", Vol. 8, B. E. Conway and J. O'M. Bockris, Ed., Plenum Press, New York, N.Y., 1972, Chapter 4.
(13) D. Gilroy and B. E. Conway, *J. Phys. Chem.*, **69**, 1269 (1965).
(14) A. N. Frumkin, O. A. Petril, and N. W. Nikolaeva-Fedorovich, *Dokl. Acad. Nauk.*, **133**, 1158 (1961).
(15) J. Wojtowicz and B. E. Conway, *J. Chem. Phys.*, **52**, 1407 (1970).
(16) I. Epelboin, M. Ksouri, and R. Wiart, *J. Electroanal. Chem.*, **65**, 373 (1975).
(17) I. Epelboin, C. Gabrielli, M. Keddam, and H. Takenout, *Z. Phys. Chem.*, in press; cf. I. Epelboin, *Corros. Sci.*, **15**, 441 (1975).
(18) B. E. Conway and M. Dzieciuch, *Nature (London)*, **189**, 914 (1961).
(19) M. Breiter, *J. Electroanal. Chem.*, **15**, 221 (1967).
(20) A. N. Frumkin, B. I. Podlovschenko, and H. Lal, *J. Electroanal. Chem.*, **11**, 12 (1966).
(21) R. Parsons and A. Capon, *J. Electroanal. Chem.*, **44**, 239 (1973).
(22) A. N. Frumkin and B. Slygin, *Acta Physicochim. URSS*, **3**, 791 (1935); **4**, 991 (1936); **5**, 819 (1936).
(23) S. Schuldiner, M. Rosen, and D. R. Flinn, *J. Electrochem. Soc.*, **117**, (10) 1251 (1970).
(24) S. Shibata and M. P. Sumino, *Electrochim. Acta*, **20**, 739 (1975).
(25) C. G. Rader and B. V. Tilak, *J. Electrochem. Soc.*, **123**, 1708 (1976).
(26) J. A. V. Butler and Armstrong, *J. Chem. Soc.*, 743 (1934); *Nature (London)*, **129**, 613 (1932).
(27) A. K. Vijh and B. E. Conway, *J. Phys. Chem.*, **71**, 3637 (1967).
(28) R. Woods, *Electrochim. Acta*, **15**, 815 (1970); see also A. Inesi and L. Rampazzo, *J. Electroanal. Chem.*, **49**, 85 (1974).
(29) B. E. Conway, W. B. A. Sharp, and H. Angerstein-Kozlowska, *Anal. Chem.*, **45**, 1331 (1973).
(30) D. Gilroy and B. E. Conway, *Can. J. Chem.*, **46**, 875 (1968).
(31) J. J. MacDonald and B. E. Conway, *Proc. R. Soc. London, Ser. A*, **169**, 419 (1962).
(32) F. G. Will and C. A. Knorr, *Z. Elektrochem.*, **64**, 270 (1960).
(33) B. E. Conway and A. K. Vijh, *J. Org. Chem.*, **31**, 4283 (1966).
(34) H. Angerstein-Kozlowska, B. E. Conway, and W. B. A. Sharp, *J. Electroanal. Chem.*, **43**, 9 (1973).
(35) B. E. Conway, H. Angerstein-Kozlowska, and F. C. Ho, *J. Vac. Sci. Technol.*, in press.
(36) B. E. Conway, H. Angerstein-Kozlowska, and W. B. A. Sharp, Symposium on Electrocatalysis, The Electrochemical Society, San Francisco, Calif., 1974, p 94.
(37) N. Minorsky, "Nonlinear Oscillations", Van Nostrand, Princeton, N. J., 1962.
(38) C. Hayashi, "Nonlinear Oscillations in Physical Systems", McGraw-Hill, New York, N.Y., 1964; see also A. A. Andronov and C. E. Chaikin, "Theory of Oscillations", Princeton University Press, Princeton, N.Y., 1949.
(39) P. Stonehart, H. A. Kozlowska, and B. E. Conway, *Proc. R. Soc. London, Ser. A*, **310**, 541 (1969).
(40) G. A. Somorjai and D. W. Blakeley, *Nature (London)*, **258**, 580 (1975).
(41) N. A. Balashova and V. E. Kazarinov, *Elektrokhimiya*, **1**, 512 (1965); *Collect. Czech. Chem. Commun.*, **30**, 4184 (1965).
(42) E. C. Zeeman, *Sci. Am.* **234**, 65 (1976).
(43) W. Schultze, *Ber. Bunsenges. Phys. Chem.*, **73**, 483 (1969).
(44) S. Trasatti, *J. Electroanal. Chem.*, **54**, 437 (1974); **64**, 128 (1975); **65**, 815 (1975); *J. Chim. Phys.*, 72, 561 (1975).
(45) H. J. S. Sand, *Phil. Mag.*, **1**, 45 (1900); see also M. Rosebrugh and J. Lash-Miller, *J. Phys. Chem.*, **14**, 816 (1910).
(46) S. Szpak and R. E. Rice, *J. Chem. Phys.*, 52, 6336 (1970).
(47) There is evidence[28] that, in aqueous media, cathodic reduction of TFA can occur. However, in the present work, the effects studied were mostly at potentials well positive to those where reduction of the molecule could occur.
(48) It is found that the extent of surface oxidation attained on holding or during a sweep is independent of solution stirring. This is presumably because the oxide growth process is sufficiently slow and the quantity of H_2O molecules required is sufficiently small, ca. 4×10^{-10} mol cm^{-2}, in a fairly dry solution, that the process of oxide film growth is not diffusion controlled with respect to H_2O.

Electron Trapping by Methanol Aggregates in Dilute Solution in Nonpolar Solvents

Thomas E. Gangwer, Augustine O. Allen, and Richard A. Holroyd*

Chemistry Department, Brookhaven National Laboratory, Upton, New York 11973 *(Received December 30, 1976)*

Publication costs assisted by Brookhaven National Laboratory

In order to further elucidate the mechanism of electron solvation in polar liquids we have determined the rate of electron attachment to solute methanol aggregates, as a function of methanol concentration, in two nonpolar solvents. An infrared technique was used to measure the extent of methanol aggregation in the solutions. The methanol is present as monomer at low concentration but at high concentration forms aggregates which are mostly pentamers. The electron is unreactive with monomer but reacts at high rate with aggregate species. The reaction with pentamers is reversible, but the electron reacts irreversibly with larger aggregates. The results indicate a dynamic nature for the electron which can autodetach from shallow traps.

Introduction

Of the processes following ionization in liquids, one of the most important but least thoroughly understood is the process of solvation of electrons in polar media. One approach to the problem is to note the effects of diluting the polar solvents such as alcohol with a nonpolar liquid such as a hydrocarbon. Previous studies along this line,[1-3] mainly using spectroscopic techniques for studying the electron, have concluded the electron probably reacts with aggregates of the alcohol molecules. These aggregates are known to exist in the hydrocarbon from thermodynamic and infrared studies. To study the situation in more detail we undertook a determination of the rates of reaction of electrons in dilute solutions of methanol in three nonpolar solvents which show widely different electron mobilities: normal hexane, 2,2,4-trimethylpentane, and tetramethylsilane. To determine the state of aggregation of methanol in these solvents, an infrared study of the solutions was also undertaken.

Experimental Section

Materials. CP methanol was further purified by refluxing over metallic magnesium and then distilling through a 50-plate column. The process was repeated until no change was noted in the reactivity of the methanol with electrons when dissolved in hexane. The liquid was stored in a silica vessel on a vacuum line. Tetramethylsilane and hydrocarbons were purified as previously described.[4]

Infrared Studies. The solutions were examined in the region of the first overtone of the OH stretching vibration, 1.3–1.65 μm. Measurements were made in a Cary-14 recording spectrophotometer, using a pair of matched 2-cm silica cells with the methanol solution in one cell and pure solvent in the other. For temperatures other than that of the room, the temperature of the solution cell was controlled, but with the setup used the reference cell with pure solvent was kept at room temperature and a correction was made for the difference in absorptivity of the pure solvent at the two temperatures.

Electron reaction rate measurements were made by an adaptation of the Hudson mobility method described in detail in our previous papers.[4,5] A liquid is placed in a uniform electric field between parallel plates, an x-ray beam is suddenly turned on, and the resulting current in the liquid is determined as a function of time over a period of many microseconds, depending upon the characteristics of the system. The observed current is given by the integral of the electron concentration, n_e

$$i = (v_e e/d)\int_0^d n_e \, dx \qquad (1)$$

where d is the distance between the plates, e is the electronic charge, and v_e is the drift velocity of the electrons in the field. In a material which does not react with electrons the current rises parabolically with time and at $t = d/v_e$ reaches a maximum which is equal to just half the steady-state current observed at very long times. If electron trapping substances are present the electron current is cut off short of this plateau value and the new plateau value provides a method of measuring the rate of reaction of the electrons with the trapping material. In this case the electron concentration is determined by application of the continuity equation

$$\partial n_e/\partial t = a - v_e \partial n_e/\partial x - k_s[S]n_e \qquad (2)$$

where a is the rate of formation of electrons per unit volume by the x rays and $k_s[S]$ is the pseudo-first-order rate constant for destruction of the electrons by the trapping material S. This method was used to determine the reaction rates of a considerable number of substances.[5]

When solutions of CO_2 were examined a new phenomenon appeared[6] which was later also found in solutions of a number of aromatic substances:[7] the current started to rise rapidly as usual but this was followed by a slower rise which continued far beyond the normal drift time d/v_e. The interpretation must be that the ions initially formed are unstable and return electrons to the medium; this cycle is repeated manyfold during migration to the anode.

A similar phenomenon occurred in many of the runs with methanol solutions, but here it was found that instead of leveling off at a point nearly half of the steady state current, as occurred in solutions of CO_2, the electron current leveled off at much lower values. At sufficiently high concentrations the current was too small to be measured and was lost in electronic noise. The interpretation here is that some of the methanol exists in molecular aggregations (A_m) which hold the electron very firmly so that it does not return to the solution during the total time of experiment, but some aggregations (A_n) exist in which the electron is held less firmly and is returned to the solution in a time short enough to be seen. The electron is then assumed to react reversibly with A_n and irreversibly with A_m:

$$e^- + A_n \underset{k_2}{\overset{k_1}{\rightleftharpoons}} A_n^- \qquad (3)$$

$$e^- + A_m \xrightarrow{k_3} A_m^- \qquad (4)$$

Thus the continuity equation for electrons is

$$\partial n_e/\partial t = a - v_e \partial n_e/\partial x - (k_1' + k_3')n_e + k_2[A_n^-] \qquad (5)$$

where pseudo-first-order rate constants $k_1' = k_1[A_n]$ and $k_3' = k_3[A_m]$ are assumed. The continuity equation for A_n^- is

$$\partial[A_n^-]/\partial t = k_1' n_e - k_2[A_n^-] \quad (6)$$

Equations 5 and 6 must be solved for the concentration of electrons $n_e(x, t)$. The boundary conditions are $n_e = [A_n^-] = 0$ at $t = 0$.

For the condition $t < x/v_e$ the solution to the coupled partial differential eq 5 and 6 is

$$n_e = \frac{a(w_1 + k_2)}{w_1(w_1 - w_2)} \exp(w_1 t) + \frac{a(w_2 + k_2)}{w_2(w_2 - w_1)} \exp(w_2 t) + a/k_3' \quad (7)$$

where

$$w_1 = -{}^1/_2(k_1' + k_2 + k_3') + {}^1/_2[(k_1' + k_2 + k_3')^2 - 4k_2k_3']^{1/2}$$

and

$$w_2 = -{}^1/_2(k_1' + k_2 + k_3') - {}^1/_2[(k_1' + k_2 + k_3')^2 - 4k_2k_3']^{1/2}$$

As shown below, the complete solution is a modification of the above equation.

The solution of eq 5 and 6 with the drift term included has been obtained by the method of Laplace transforms by Tachiya.[8] The solution for $t > x/v_e$ is

$$n_e(x, t) = \frac{a(w_1 + k_2)}{w_1(w_1 - w_2)}(F_1) \exp(w_1 t) + \frac{a(w_2 + k_2)}{w_2(w_2 - w_1)}(F_2) \exp(w_2 t) + \frac{a}{k_3'}(F_3) \quad (8)$$

where

$$F_i(x, t) = 1 - [(w_i + k_2) \exp(-bx/v_e)] \int_{x/v_e}^{t} I_0\{2[k_1' k_2(t' - x/v_e)x/v_e]^{1/2}\} \exp(-(w_i + k_2)t')\, dt'$$

and $b = k_1' - k_2 + k_3'$, I_0 is the modified Bessel function, and $w_3 = 0$.

The current dependence involves the set of parameters k_1', k_2, k_3', v_e, and d. The last two are fixed in each experiment. The value of k_3' is obtained from the maximum electron current which is reached in the long x-ray pulses used. Under these conditions $\partial[A_n^-]/\partial t = 0$ and eq 5 reduces to eq 2 with $k_3' = k_s[S]$. The solution to this is shown,[4] and k_3' is obtained from the ratio of the electron current at the maximum to the steady state current.

To fit the experimental trace, the current is calculated for a trial set of rate constants: k_1' and k_2. This involves calculating n_e at each point from eq 8 and integrating to obtain the current. The process is repeated until a satisfactory fit to the data is obtained.

Results

Spectroscopic Studies. Typical spectra are shown in Figure 1. The narrow peak at 1.405 μm is found in all alcohol solutions and is due to the first overtone of the OH stretching in the isolated alcohol molecule. In hydrogen-bonded aggregations of these molecules the absorption appears at longer wavelengths. In solutions of ethanol and higher alcohols it is generally assumed that some terminal molecules on linear polymers contribute to the absorption at or near 1.405 μm, in addition to the monomers; but Fletcher and Heller[9] found good reasons to believe that

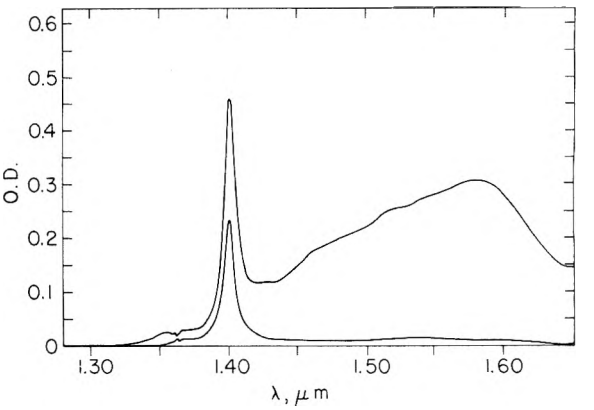

Figure 1. Infrared absorption spectra of solutions of methanol in 2,2,4-trimethylpentane at 22 °C: upper curve, 0.988 M; lower curve, 0.0988 M.

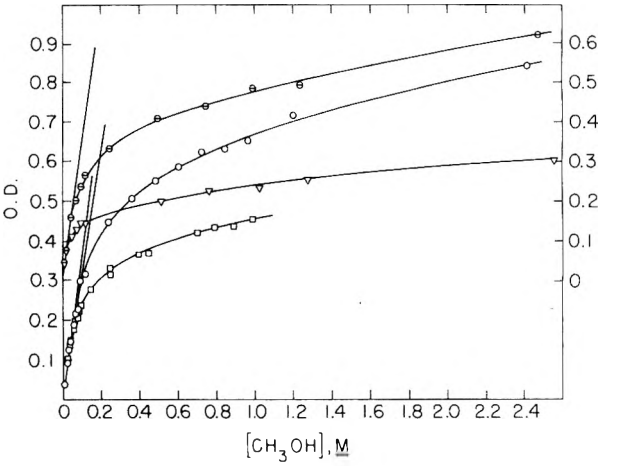

Figure 2. Optical density at 1.405 μm in 2-cm cells, of solutions of methanol in 2,2,4-trimethylpentane at 22 °C (□) and 45 °C (○) (left-hand scale), and in tetramethylsilane at 0 °C (▽) and 22 °C (⊖) (right-hand scale).

in solutions of methanol in hydrocarbons this peak is due entirely to the unassociated molecules. We assume here that the optical density at this peak, minus the optical density at 1.30 μm, is proportional to the concentration of unassociated methanol molecules in the solution. Figure 2 shows the optical densities found with a 2-cm light path at 1.405 μm for solutions of methanol in 2,2,4-trimethylpentane and tetramethylsilane. At low concentrations the optical density increases linearly with concentration and it is assumed that here the alcohol exists essentially all as unassociated molecules. Then the initial slope of the curves in Figure 2 is 2ϵ, where ϵ is the extinction coefficient of the monomer at 1.405 μm in cm^{-1} M^{-1}. At higher concentrations the increase of optical density with concentration becomes smaller, which is assumed to result from polymerization of the molecules leading to the appearance of the absorptions at longer wavelength. Let (M) = total concentration of methanol in the solution in moles per liter and A_1 = the concentration of unassociated or monomeric methanol. Then

$$A_1 = \mathrm{OD}/2\epsilon \quad (9)$$

The concentration A_n of aggregates containing n methanol molecules is related to A_1 by the equilibrium expression

$$[A_n] = K_n A_1^n \quad (10)$$

If the polymer consists mainly of aggregates of size n then

$$(M) - A_1 = nK_n A_1^n \quad (11)$$

TABLE I: Equilibrium Constants for Methanol Association

Solvent	Temp, °C	2ϵ	$2K_2$	$3K_3$	$4K_4$	$5K_5$	$6K_6$	n	nK_n
2,2,4-Trimethylpentane	22	3.65	0	0	6×10^2	1.9×10^4	4×10^4	4.82	1.93×10^4
2,2,4-Trimethylpentane	45	3.12	0	0	3×10^1	1.4×10^3	5×10^2	4.95	1.53×10^3
Tetramethylsilane	0	3.29	0	0	0	3.6×10^5	1.3×10^6	5.11	5.97×10^5
Tetramethylsilane	22	3.39	0	0	5×10^2	1.1×10^4	Small	4.69	7.95×10^3

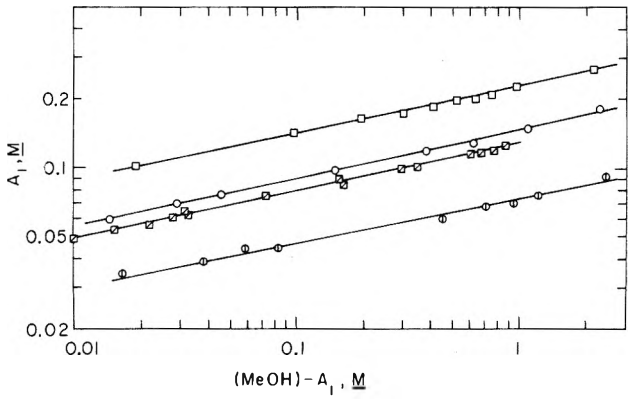

Figure 3. Monomer concentration A_1 vs. total associated methanol concentration [MeOH] − A_1: tetramethylsilane at 22 °C (O); at 0 °C (Φ); 2,2,4-trimethylpentane at 22 °C (⊠); at 45 °C (□).

A plot of log A_1 against log[$(M) - A_1$] would give a straight line of slope n^{-1}. Such a plot is shown in Figure 3. It is seen that all the data we have, for solutions in two solvents at two different temperatures, fall remarkably well on straight lines over a factor of more than 100 in concentration. The values of n obtained are given in the next to the last column of Table I and all lie in the neighborhood of 5. This shows that the methanol aggregates in these solutions consist mostly of pentamers with small quantities of lesser and greater degrees of aggregation. In order to get an approximate idea of the distribution of these aggregates a graphical method was employed. The concentration of methanol is actually given by

$$(M) = A_1 + 2K_2A_1^2 + 3K_3A_1^3 + 4K_4A_1^4 + 5K_5A_1^5 + \ldots \quad (12)$$

Thus if we plot $(M)/A_1^2 - 1/A_1$ against A_1, we should find a curve with intercept $2K_2$ and initial slope $3K_3$. Typical results of this procedure are shown in Figure 4. The curve delineated by the circles in this figure clearly appears to have a very small or essentially zero intercept, showing that the concentration of dimers in this solution is negligible. We therefore proceed to plot $(M)/A_1^3 - 1/A_1^2$, indicated by the squares in the figure, and again we find that the intercept is near zero indicating that the trimer also is negligible. Proceeding to the next step, the plot of $(M)/A_1^4 - 1/A_1^3$ clearly shows a positive intercept in the neighborhood of 500 M^{-3}, although the scatter of the points has now become so great that the exact value is rather uncertain. However we continue the process by taking a value for $4K_4$ and plotting $(M)/A_1^5 - 1/A_1^4 - 4K_4$, thus obtaining a curve with intercept of $5K_5$ and presumably an initial slope of $6K_6$. The intercept of this curve should in theory match the slope of the preceding. Sets of values obtained by this procedure which give a good fit to the data are shown in Table I. Their values are mostly illustrative; the values of $4K_4$ are probably good to a factor of about 1.5, of $5K_5$ to about the same accuracy, while $6K_6$ is probably good to a factor of 2 or 3. This analysis indicates tetramers, pentamers, and hexamers are present, but pentamers dominate, comprising two-thirds or more of the total polymer, in the concentration range studied.

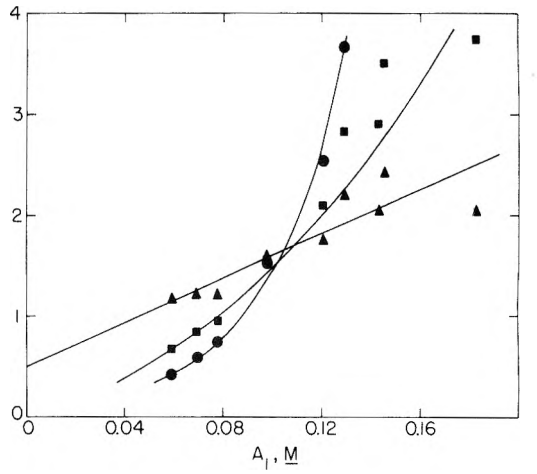

Figure 4. Typical plots for estimation of association equilibria (methanol in tetramethylsilane at 22 °C). With [M] = total methanol concentration and A_1 monomer concentration, the ordinates are: for the circles, $([M]A^{-2} - A^{-1})10^{-1}$ M^{-1}; for the squares, $([M]A^{-3} - A^{-2})10^{-2}$ M^{-2}; for the triangles, $([M]A^{-4} - A^{-3})10^{-3}$ M^{-3}.

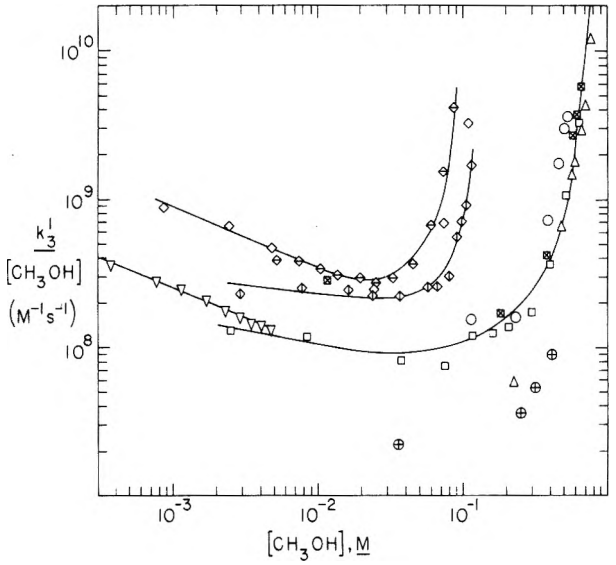

Figure 5. Pseudo-first-order electron decay rates divided by the methanol concentration in solutions of methanol in nonpolar solvents: (▽) n-hexane at room temperature (about 22 °C); ◇ and ◈, two runs in 2,2,4-trimethylpentane at room temperature; Φ, same solvent at 44 °C; other symbols show the results of different runs in tetramethylsilane at room temperature.

Figure 3 and the last two columns of Table I actually offer a more accurate overview of the results. The degree of polymerization at room temperature is distinctly greater in 2,2,4-trimethylpentane than in tetramethylsilane. The amount of aggregate decreases with increasing temperature, but in all cases the aggregate consists largely of pentamer.

Electron Reaction Rates. At room temperature and above, values of k_3' were obtained over wide ranges of concentration. The results, summarized in Figure 5, are plotted as the pseudo-first-order electron decay rate k_3', divided by the methanol concentration, against the methanol concentration, on a log–log scale, in order to

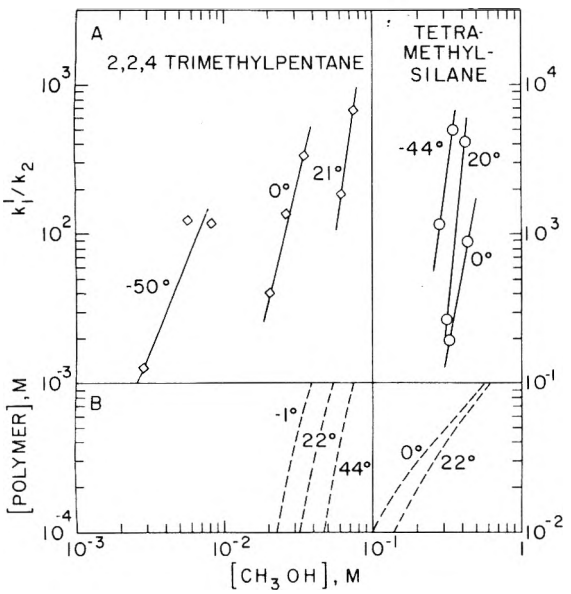

Figure 6. A. Upper: Ratio of attachment to detachment rate constants for reaction 3 vs. methanol concentration; ◇, left side is data for 2,2,4-trimethylpentane; O, right side is data for tetramethylsilane. B. Lower: Concentration of polymer, defined as $([MeOH] - A_1)/n$ vs. methanol concentration in the two solvents. Temperatures as indicated.

bring out more clearly the relations between rate and methanol concentration.

The behavior at methanol concentrations above 0.02 M in 2,2,4-trimethylpentane and above 0.3 M in tetramethylsilane is quite clear, in spite of the irreproducibility.[10] The rate of electron capture rapidly accelerates with concentration, and at the highest concentrations that could be studied in the two solvents, it is seen to be increasing with approximately the tenth power of the methanol concentration. Thus at the higher concentrations the electrons must be reacting with aggregates of ten or more methanol molecules. Although the infrared study showed that the methanol is present mainly in aggregations of five molecules, a small percentage of larger aggregates might be present at the highest concentrations studied. Since in tetramethylsilane specific reaction rates of 10^{14} M^{-1} s^{-1} or more are possible for the reaction of the electron with aggregate, the observed rate of 10^{10} s^{-1} in 0.8 M methanol (where the concentration of polymer is 0.13 M) is not unreasonable.

In the same concentration range where k_3' increases rapidly the reversible reaction 3 is also observed and, as is shown in the upper part of Figure 6, k_1'/k_2 increases rapidly with concentration. The data on polymer grow-in are shown in the lower half of Figure 6; and at 22 °C polymer is seen to grow-in rapidly in this same concentration range. The increase in the ratio k_1'/k_2 with methanol concentration is due mainly to an increase in k_1', equal to $k_1(A_n)$, which increases with the concentration of the aggregate species, A_n. There is a similar correlation at 0 °C in 2,2,4-trimethylpentane. Here the polymer grows in at lower concentrations starting at 0.02 M and the reversible reaction of the electron is observed in this same concentration range. The value of k_3' also increases rapidly above 0.02 M at −1 °C. For 2,2,4-trimethylpentane, k_2 is about 10^5 s^{-1} at −50 °C and increases to over 10^6 s^{-1} at 21 °C. The attachment rates, k_1', are between 10^8 and 10^9 s^{-1} at 21 °C and less at the lower temperatures. If A_n is identified with pentamer then k_1 would have a value of about 10^{12} M^{-1} s^{-1} which is not an unreasonable value for this solvent.[4,5]

The results for tetramethylsilane are qualitatively similar to those for 2,2,4-trimethylpentane. The reversible reaction is observed at methanol concentrations between 0.2 and 0.4 M where the polymer is growing in. The ratio k_1'/k_2 increases with concentration; however, the increase is faster than the growth of total polymer. In this solvent the electrons appear to be retained preferentially by aggregates which are larger than average (see Discussion). For tetramethylsilane, k_2 also increases with temperature from values near 10^5 s^{-1} at −44 °C to greater than 10^7 at 20 °C. The value of k_1' is about 10^{10} s^{-1} at 20 °C and less at lower temperatures.

The reversible reaction 3 is observed only over a restricted concentration range. At low concentrations of methanol the concentration of the species A_n is too low and thus aggregate anions are not formed. At high concentrations k_3' and k_1' became so large that the electron current is too small to properly analyze the time dependence for values of k_1' and k_2.

At lower methanol concentrations, the rate k_3' increases with methanol concentration to a power less than unity. The results in *n*-hexane were the first obtained; the earliest runs gave higher rate constants, but after further purification of the methanol the results shown in Figure 5 were obtained. The effect of impurities initially present in the hydrocarbon gave a relatively small correction to k_3', which was always subtracted out. The pseudo-first-order rate constant k_3' increased consistently with methanol concentration to the 0.6 power over a 13-fold range in concentrations. The hexane solutions could not be studied at methanol concentrations over 5×10^{-3} M because the electron current then became too small to measure. Because the Hudson method measures the ratio of the trapping rate to the mobility of the electron, we went to 2,2,4-trimethylpentane, in which the electron mobility is some 75 times greater than in *n*-hexane. At low methanol concentrations then, we again saw the rate increasing with the 0.6 power of the concentration; but above 0.03 M, where aggregation begins to set in, the rate began to show a marked increase. In the solvent of still higher mobility, tetramethylsilane, again at low concentrations the rate appeared to increase with a power of concentration less than unity. This effect cannot be due to reaction with the electron of molecules of ordinary impurities in the methanol, for then the rate would increase with the first power of the methanol concentration.

We have considered and tested various hypotheses for this anomaly. If the impurity that reacts with the electron is formaldehyde, it could be present in equilibrium with the methanol to give a less reactive hemiacetal, which reaction could result in a square-root concentration dependence. However, addition of traces of formaldehyde to the solutions showed a reaction with electrons which was proportional to the aldehyde and independent of the methanol. Colorimetric analysis showed that the methanol contained <0.2 ppm H_2CO.

Since the experimental measurement gives the ratio of the electron reactivity to the mobility, with the calculations assuming mobility independent of methanol, the whole effect could be ascribed to an effect of methanol on the electron mobility, though this seemed unlikely on theoretical grounds. However, experiments in this laboratory by N. Cipollini, in which the electron mobility in tetramethylsilane was measured by a direct time-of-flight method, showed that addition of 10^{-3} M methanol had no effect on the mobility.

A more plausible idea ascribes the effect to reaction of the electrons with positive ions, supposed to be present in equilibrium with the methanol or with impurities in the methanol. Addition of methanol is known to increase the

very low background conductivity of purified hydrocarbons. The rate constant for electron decay in the presence of a concentration c_+ moles per liter of positive ions is[4] $5 \times 10^{13} c_+ \ s^{-1}$. We find however that 3×10^{-3} M methanol in hexane has a specific conductance $\sigma < 10^{-15}$ $\Omega^{-1}\ cm^{-1}$, while k_3' for this solution was found (Figure 5) to be 5×10^5, giving $c_+ = 1 \times 10^{-8}$ M. Since the observed conductivity is due to both positive and negative ions in equal numbers, we have $N\sigma/F = 6.24 \times 10^{18}\sigma = 2c_+(\mu_+ + \mu_-)$, where the μ's are the mobilities of the ions present. Thus for molecular ions with $\mu_+ + \mu_- > 10^{-4}$, $c_+ = 3 \times 10^7$ cm^{-3} or 5×10^{-14} M, which is about 2×10^5 times too small to account for the rate of electron disappearance.

We have no good explanation for our results in highly dilute methanol solutions. A possible though improbable cause would be the stabilization by methanol in hydrocarbon of positively charged low-mobility colloidal particles of glass, similar to the stabilization of platinum sols in ether by traces of water.[11] Such particles are known to form in large numbers[12] when water is poured into glass containers.

In agreement with our results, Baxendale and Sharpe[13] find that methanol in 2,2,4-trimethylpentane has little effect on the conductivity induced by a radiation pulse at methanol concentrations up to 0.04 M, but gives a large reduction at higher concentrations. Ethanol[14] and propanol,[13] however, are reported to show considerable effect at 0.01 M. These effects are consistent with our finding, in agreement with others,[9,15] that methanol does not form stable dimers in hydrocarbon solution; but ethanol and higher alcohols do form such dimers[16] and hence build up electron-trapping hydrogen-bonded aggregates at lower concentrations than methanol.

Discussion

The present results show that hydrogen-bonded aggregates of five or more methanol molecules in a nonpolar solvent readily trap electrons. Most of the resulting negatively charged pentamers are sufficiently unstable to lose the electron back to the solvent in a few microseconds; larger aggregates (of 10 or more molecules) seem to retain the electron indefinitely. Whether other aggregates exist that retain the electrons only over much shorter times cannot be said from our experiments. The methanol aggregates exist in significant amount only when the methanol concentration exceeds 0.02 M.

The equilibrium constant K for the reversible reaction 3 is k_1'/k_2 divided by the concentration of the species A_n. A completely accurate evaluation of K is not possible since what was measured by the IR technique was total polymer of which A_n may only be a part. However, in the case of 2,2,4-trimethylpentane the ratio k_1'/k_2 increases with methanol concentration in much the same way that the concentration of polymer does (Figure 6). Thus we assume that [polymer] = $[A_n]$ and find $K = 1.4 \times 10^5$ at 21 °C and 5.0×10^5 at −1 °C for 2,2,4-trimethylpentane. These values are constant to ±20% over the concentration range studied. If only a small fraction of the polymer is active, the true equilibrium constants with respect to the polymer fraction actually participating would be as large as 10^7. This introduces some uncertainty into the free energy of trapping: $-RT \ln K = \Delta G_{tr} \simeq -8 \pm 2$ kcal mol^{-1}. In reactions of this type there is a large decrease in entropy,[7] which for molecules of comparable size is between −20 and −30 cal deg^{-1} mol^{-1}. Thus $T\Delta S_{tr}$ is approximately -7.5 ± 1.5 kcal mol^{-1} and $\Delta H_{tr} \simeq -15 \pm 3$ kcal mol^{-1}, or -0.65 ± 0.15 eV. These results are consistent with a recent semicontinuum model calculation by Fueki et al.[17] They find for an electron surrounded by a shell of four methanol molecules in alkane solvents that the heat of solution is −1.2 eV. However when a second solvation shell of methanol is added to the cluster the heat of solution is −1.64 eV. The added stability of the larger cluster is in agreement with our conclusion that the electron reacts irreversibly with large ($n \approx 10$) aggregates. For a shell of five molecules the heat of solution should be a little less, about −1.1 eV. The heat of solution of the electron in 2,2,4-trimethylpentane is −0.4 eV. The enthalpy of trapping, or ΔH, for reaction 3 is the difference between these two values or −0.7 eV, very close to the observed value (−0.65 eV).

In tetramethylsilane the reversible reaction is observed at higher methanol concentrations, and consequently higher polymer concentrations. As can be seen in Figure 6, k_1'/k_2 is not proportional to polymer concentration. If total polymer is used as a measure of $[A_n]$, K_3 is found to increase with concentration. This precludes quantitative analysis but the fact that the reversible reaction is observed at higher polymer concentrations is consistent with previous studies. The equilibrium constants for the reaction of the electron with CO_2[6] and with aromatic compounds[7] are several orders of magnitude less in tetramethylsilane than in 2,2,4-trimethylpentane due to the greater stability of the electron in the former. Thus higher concentrations of the aggregates, A_n, are required to shift the equilibrium to the right. Considering this and the manner in which polymer is growing in suggests that here the electrons are retained only by aggregates which are larger than average.

Now, it is reported[13] that the peak of the absorption spectrum of electrons in methanol–n-hexane solutions shifts suddenly from some value above 1600 nm in 0.038 M methanol to 800 nm in 0.062 M. Further additions of methanol result in a gradual blue shift in the spectrum toward 660 nm.[18] This strongly suggests that the charged aggregates in the hydrocarbon solutions are very similar to the solvated electron in polar solvents. If this is so, there may exist in neat alcohols a class of more weakly solvated electrons, corresponding to those that give up their electron in the dilute solution. As electrons are solvated in a polar medium some shallow traps may be formed, and as the system relaxes toward equilibrium the absorption maximum shifts toward shorter wavelengths, as has been observed in many laboratories.[19]

Relaxation times are reported as 1×10^{-11} s in methanol and 3×10^{-11} s in propanol at room temperature.[19] In our solutions the time required at 20 °C for a pentamer anion to detach an electron is about 10^{-6} s in 2,2,4-trimethylpentane and about 2×10^{-8} s in tetramethylsilane. Autodetachment occurs long after dipole relaxation, which is very fast.[20] The higher rate in tetramethylsilane is attributed to a lower electron energy level in this solvent. Thus the rate of detachment differs for each solvent depending on the electron level. In a polar medium such as methanol the role of polarization in stabilizing the charged cluster would also affect the rate.

To summarize, we have shown that electrons react with aggregates of methanol molecules. Reaction with large aggregates is irreversible. Electrons escape readily from shallow traps (−0.65 eV), return to the solvent, and rapidly react with another aggregate. That is, the electron "hunts" and sooner or later finds a deep trap. The rate of escape from the traps depends on temperature, solvent, and presumably also on aggregate size.

Acknowledgment. The authors thank N. Cipollini for his assistance in the mobility measurements and M. Tachiya for the solution of eq 5 and 6. This research was carried out at Brookhaven National Laboratory under contract with the U.S. Energy Research and Development

Administration and supported by its Division of Physical Research.

References and Notes

(1) B. J. Brown, N. T. Barker, and D. F. Sangster, *J. Phys. Chem.*, **75**, 3639 (1971); *Austr. J. Chem.*, **26**, 2089 (1973).
(2) J. H. Baxendale and E. J. Rasburn, *J. Chem. Soc., Faraday Trans. 1*, **70**, 705 (1974).
(3) J. R. Brandon and R. F. Firestone, *J. Phys. Chem.*, **78**, 792 (1974).
(4) A. O. Allen and R. A. Holroyd, *J. Phys. Chem.*, **78**, 796 (1974).
(5) A. O. Allen, T. E. Gangwer, and R. A. Holroyd, *J. Phys. Chem.*, **79**, 25 (1975).
(6) R. A. Holroyd, T. E. Gangwer, and A. O. Allen, *Chem. Phys. Lett.*, **31**, 520 (1975).
(7) R. A. Holroyd, *Ber. Bunsenges. Phys. Chem.*, **81**, 298 (1977).
(8) M. Tachiya, private communication.
(9) A. N. Fletcher and C. A. Heller, *J. Phys. Chem.*, **71**, 3742 (1967).
(10) Results in 2,2,4-trimethylpentane and tetramethylsilane obtained with different preparations on different days were not as reproducible as might be hoped. Several preparations of tetramethylsilane solutions were used, and electron rates at a given methanol concentration are seen to differ by as much as a factor of 4. This trouble must be attributed to the effects of trace impurities, the great bugbear in all studies of electron behavior in dielectric liquids.
(11) S. Glasstone, "Textbook of Physical Chemistry", 2nd ed, Van Nostrand, New York, N.Y., 1946, p 1270.
(12) F. O. Rice and M. L. Kilpatrick, *J. Phys. Chem.*, **31**, 1507 (1927).
(13) J. H. Baxendale and P. H. G. Sharpe, *Chem. Phys. Lett.*, **41**, 440 (1976).
(14) G. Beck and J. K. Thomas, *J. Chem. Phys.*, **57**, 3649 (1972).
(15) E. E. Tucker, S. B. Farnham, and S. D. Christian, *J. Phys. Chem.*, **73**, 3820 (1969).
(16) W. C. Coburn, Jr., and E. Grunwald, *J. Am. Chem. Soc.*, **80**, 1318 (1958).
(17) K. Fueki, P. A. Narayama, and L. Kevan, *J. Chem. Phys.*, **64**, 4571 (1976).
(18) L. B. Magnusson, J. T. Richards, and J. K. Thomas, *Int. J. Radiat. Phys. Chem.*, 3, 295 (1971).
(19) A thorough review of the electron solvation process in polar liquids is given by J. W. Hunt, *Adv. Radiat. Chem.*, **5**, 185 (1976).
(20) K. Fueki, D-F. Feng, and L. Kevan, *J. Phys. Chem.*, **80**, 1381 (1976).

On the Calculation of the Electrostatic Lattice Energies of α-, β-, and γ-Glycine

J. L. Derissen,* P. H. Smit, and J. Voogd

Structural Chemistry Group, University of Utrecht, Padualaan 8, Utrecht, The Netherlands *(Received December 28, 1976)*

Publication costs assisted by the University of Utrecht

The calculated difference of 13 kcal/mol for the electrostatic lattice energies of β- and γ-glycine reported in the literature is not due to special structural features of γ-glycine, but is caused by poor convergence of the electrostatic lattice sum. This may generally be expected to occur in noncentrosymmetric space groups, especially when the resulting cell dipole moment is large. This problem of convergence may be avoided by application of well-known convergence acceleration methods.

Introduction

The lattice energy of a molecular crystal can be calculated by means of a summation of interatomic pair potentials.[1,2] Momany, Carruthers, and Scheraga[3] (MCS) have made such calculations on the three known polymorphs of glycine. They found a difference of 1.5 kcal/mol between the lattice energies of α- and β-glycine, and a difference of 13 kcal/mol between those of β- and γ-glycine. This latter large difference arises from the calculated electrostatic energy, the other contributions (attractive, repulsive, and hydrogen bond energies) being neary equal for α-, β-, and γ-glycine. The molecular, zwitterionic structure hardly differs in the three crystalline modifications.[4-6]

The origin of this large difference in electrostatic energy was not understood, but MCS tentatively ascribed it to the special surrounding of the nitrogen atom by five closely neighboring negatively charged oxygen atoms in γ-glycine. However, as MCS already noted, the enthalpy difference for the $\gamma \rightarrow \alpha$ transition was found to be only 0.6 kcal/mol,[6] within an order of magnitude that is usually measured for a heat of transition between polymorphs of a molecular crystal.

As it lies in our immediate field of interest,[7] we decided to perform a closer investigation of the origin of this remarkable energy difference in the glycines.

Calculation of the Electrostatic Lattice Energy

The electrostatic part of the lattice energy in the atom–atom potential method is evaluated as[1,2]

$$E_{pc} = {}^1/_2 \sum_i \sum_j 332.05 q_i q_j r_{ij}^{-1} \qquad (1)$$

TABLE I

	a, Å	b, Å	c, Å	β or γ, deg	Z	Space group
α-Glycine	5.105	11.969	5.465	111.7	4	$P2_1/n$
β-Glycine	5.077	6.268	5.380	113.2	2	$P2_1$
γ-Glycine	7.037	7.037	5.483	120	3	$P3_2$

Here r_{ij} is the distance between the atoms i and j in angstroms, the q's are the atomic point charges in electrons, and the constant 332.05 is a conversion factor to obtain E_{pc} in kilocalories per mole. The summation index i runs over all atoms of a reference molecule and j runs over all atoms of the surrounding molecules in the crystal. Usually the sum is truncated at a particular distance at which it is assumed to have converged. For molecular crystals a value of about 25 Å is often chosen for this electrostatic summation limit. Care must be taken that electroneutrality is preserved on truncating the sum.

We truncated the lattice sum in two ways. First, we constructed a crystal block around the reference unit cell extending certain numbers of cells along the three crystallographic axes, the exact numbers depending on the axes ratios. All molecules in such a block, generated by the crystal symmetry operations, were included in the sum.

Secondly, we defined a molecular origin half-way along the C–C bond and we included in the sum all molecules with their origins within a sphere of specified radius from the origin of the reference molecule.

In our calculations we used the same crystal geometries as MCS did for α-, β-, and γ-glycine.[4-6] Some relevant crystal data are collected in Table I. We calculated the atomic point charges from gross Mulliken populations

TABLE II: Atomic Charges for the Atoms in Glycine (in electrons)[a]

Method	N	O_1	O_2	C_1	C_2	H_1	H_2	H_3	H_4	H_5
CNDO/2	0.022	−0.526	−0.483	0.374	−0.021	0.164	0.208	0.199	0.033	0.030
CNDO/2 ON[b]	−0.292	−0.500	−0.500	0.500	−0.120	0.264	0.264	0.264	0.060	0.060
Ab initio[c]	−0.75	−0.70	−0.66	0.72	−0.33	0.38	0.41	0.41	0.26	0.26

[a] The CNDO/2 charges in the table are those calculated for α-glycine. For β- and γ-glycine they were also calculated, but as they are only very slightly different they are not shown here. For numbering of the atoms see ref 9. [b] Reference 3. [c] Reference 9.

TABLE III: Electrostatic Lattice Energy of Glycine (in kcal/mol) for Three Different Types of Point Charges Calculated by Direct Summation and by the Convergence Acceleration Method[a]

		Direct summation			Convergence accelerated summation		
	n, l, m	CNDO/2	Ab initio	CNDO/2 ON	CNDO/2	Ab initio	CNDO/2 ON
α-Glycine	6, 3, 6	−34.32	−48.86	−29.79	−34.40	−48.94	−29.86
β-Glycine	6, 5, 6	−32.88	−47.13	−28.54	−34.50	−47.90	−29.90
γ-Glycine	5, 5, 6	+1.69	+2.69	+0.38	−33.60	−46.28	−28.85

[a] *n, l, m* are the numbers of cells the crystal block extends in the ±*a*, ±*b*, ±*c* directions, respectively. For summation limits see also Table IV.

TABLE IV: Effect of Summation Limits on the Electrostatic Lattice Energy[a]

	n, l, m	Sum	*n, l, m*	Sum	*n, l, m*	Sum	*n, l, m*	Sum
				Direct Summation				
α-Glycine	2, 1, 2	−33.81	3, 1, 3	−34.05	5, 2, 5	−34.27	11, 5, 10	−34.37
β-Glycine	2, 2, 2	−32.63	3, 2, 3	−32.33	5, 4, 5	−32.79	11, 9, 10	−32.94
γ-Glycine	2, 2, 2	+8.58	2, 2, 3	−4.45	4, 4, 5	+0.43	8, 8, 10	−0.04

Convergence Accelerated Summation

	Direct limit	Recipr limit	Sum	Direct limit	Recipr limit	Sum	Direct limit	Recipr limit	Sum
α-Glycine	5.0	0.5	−33.48	10.0	1.0	−34.40	15.0	1.5	−34.40
β-Glycine	5.0	0.5	−34.62	10.0	1.0	−34.50	15.0	1.5	−34.50
γ-Glycine	5.0	0.5	−33.61	10.0	1.0	−33.60	15.0	1.5	−33.60

[a] For definition of *n, l, m* see Table III. The direct limit is in Å, the reciprocal limit in $Å^{-1}$.

obtained from CNDO/2 wave functions.[8]

For comparison we also used the CNDO/2 ON charges of MCS and Almlöf's[9] ab initio point charges obtained for the α-glycine molecule. See Table II.

Using formula 1 we calculated the electrostatic lattice energies of α-, β-, and γ-glycine for a summation limit of approximately 30 Å for the three types of point charges. The results are shown in Table III. Truncation was done according to the first method, but we verified that truncation with respect to molecular origins led to only very slightly differing results. It is seen that the electrostatic energies for α- and β-glycine are nearly equal, while the γ-glycine energy differs very much and is even slightly positive. The results are also highly dependent on the type of charges used.

Increasing the summation limit, we found for γ-glycine fluctuating energy values (see Table IV). Clearly the lattice sum for γ-glycine has not converged. For β-glycine convergence is also rather slow, while for α-glycine convergence of the lattice sum is already obtained at about 25 Å.

We then applied the convergence acceleration method described by Williams.[10] In this method the lattice sum is transformed, and part of it is evaluated in reciprocal space. We now obtained, for a summation limit of 10 Å in direct space and 1.0 $Å^{-1}$ in reciprocal space, for all three glycines a value for the electrostatic energy of about −34 kcal/mol using CNDO/2 charges. See also Table III.

Variation of the summation limits now showed that convergence had been obtained (Table IV). Variation of the convergence constant K from 0.2 to 0.5 had no influence on the calculated energies.

The poor convergence of the electrostatic lattice sum of γ-glycine is understood when the electrostatic energy is described by multipole interactions and space group symmetry is considered. As the space group of α-glycine is centrosymmetric, all odd *cell* multipole moments, starting with the dipole moment, vanish.[11] For β- and γ-glycine, which both have a noncentrosymmetric space group, these moments do not disappear by symmetry. The resulting cell dipole moment depends on the magnitudes and orientations of the zwitterion dipoles in the cell. It is zero for α-glycine, $2\mu_b$ for β-glcyine, and $3\mu_c$ for γ-glycine. Here μ_b and μ_c are the dipole components in the crystallographic b and c directions, respectively. From the CNDO/2 charges we calculated $2\mu_b$ = 4.1 D for β-glycine and $3\mu_c$ = 28.9 D for γ-glycine.

It is well known that dipole–dipole lattice sums may suffer from poor convergence, and that convergence acceleration methods should be applied to avoid termination errors.[10,12-15] As the dipole–dipole energy is proportional to the square of the dipole moment, we would expect this effect to be largest for γ-glycine.

Conclusion

We may conclude that the unexpected result of MCS[3] for the electrostatic lattice energy of γ-glycine is due to lack of convergence of the direct lattice sum. This may be expected to occur in molecular crystals with noncentrosymmetric space groups, especially when the resulting cell dipole moment is large. In these cases it is better to avoid the slowly converging direct lattice summation completely, and to apply a convergence acceleration method.[10,13] This has the additional advantage of being

much cheaper in computing time.

Acknowledgment. We thank the Netherlands Organisation for the Advancement of Pure Research (ZWO) for support.

References and Notes

(1) A. I. Kitajgorodskij, "Molecular Crystals and Molecules", Academic Press, New York, N.Y., 1973, Chapter II.
(2) R. F. McGuire, G. Vanderkooi, F. A. Momany, R. T. Ingwall, G. M. Crippen, N. Lotan, R. W. Tuttle, K. L. Kashuba, and H. A. Scheraga, *Macromolecules*, **4**, 112–124 (1971).
(3) F. A. Momany, L. M. Carruthers, and H. A. Scheraga, *J. Phys. Chem.*, **78**, 1621–1630 (1974).
(4) P-G. Jönsson and Å. Kvick, *Acta Crystallogr., Sect. B*, **28**, 1827–1833 (1972).
(5) Y. Iitaka, *Acta Crystallogr.*, **13**, 35–45 (1960).
(6) Y. Iitaka, *Acta Crystallogr.*, **14**, 1–10 (1961).
(7) P. H. Smit, J. L. Derissen, F. B. van Duijenveldt, *J. Chem. Phys.* in press.
(8) P. A. Dobosh, Quantum Chemistry Progam Exchange, Bloomington, Ind., Catalog 1973, No. QCPE 142.
(9) J. Almlöf, Å. Kvick, and J. O. Thomas, *J. Chem. Phys.*, **59**, 3901–3906 (1973).
(10) D. E. Williams, *Acta Crystallogr., Sect. A*, 27, 452–455 (1971).
(11) A. D. Buckingham in "Physical Chemistry, An Advanced Treatise", Part IV, D. Henderson, Ed., Academic Press, New York, N.Y., 1970, p 349.
(12) F. E. Harris, *Theor. Chem. Adv. Perspect.* **1**, 147–218 (1975).
(13) P. G. Cummins and D. A. Dunmur, *Acta Crystallogr., Sect. A*, **32**, 847–853 (1976).
(14) J. W. Weenk, Dissertation, State University of Utrecht, The Netherlands, 1976.
(15) D. J. Adams and I. R. McDonald, *Mol. Phys.*, **32**, 931–947 (1976).

The Influence of Ion Pairing on the Electroreduction of Nitromesitylene in Aprotic Solvents. 1. Thermodynamic Aspects

B. G. Chauhan, W. R. Fawcett,* and A. Lasia†

Quelph-Waterloo Centre for Graduate Work in Chemistry (Guelph Campus), Department of Chemistry, University of Guelph, Guelph, Ontario, Canada *(Received March 8, 1977)*

Association constants between nitromesitylene anion radical, formed by reduction of the parent molecule at a mercury electrode, and the alkali metal cations and tetraethylammonium cation have been determined by studying the variation in the half-wave potential for the reduction process with solution composition in both acetonitrile and dimethylformamide., The association constant was observed to increase with decrease in the crystallographic radius of the cation and on going from dimethylformamide to acetonitrile. The association constants are much smaller than the corresponding data for nitrobenzene anion radical; this observation is attributed to a large steric effect from the ortho-substituted methyl groups in nitromesitylene. It is shown that the logarithm of the association constant is a linear function of the free energy of solvation of the cation. The variation in association constant with cation and solvent is discussed with respect to the Denison–Ramsey model for ion pairing and the Fawcett–Krygowski model for solvent effects.

Introduction

The reaction mechanism for the electroreduction of organic molecules in aprotic solvents normally involves an initial one-electron transfer to form a stable anion radical.[1] From the point of view of electron transfer theory,[2,3] the initial reaction is often simple so that a study of the kinetics of electron transfer should provide data for testing the various models developed for the electron transfer rate constant. In addition, the total charge on the reactant and product is small so that discreteness-of-charge effects in the double layer are not expected to be large.[4] On the other hand, the reduction reaction sometimes involves an ion pairing step. Thus, the first reduction wave for aromatic nitro[5–7] and carbonyl compounds[6,8–10] and quinones[11–13] is shifted to more positive potentials when metal cations are added to the nonaqueous system. As a result, the thermodynamic and kinetic descriptions of these processes are very dependent on the nature of the cation in solution.

The purpose of the present investigation was to make a detailed quantitative study of the effect of the electrolyte cation on the kinetics of electron transfer to an organic molecule in two aprotic solvents, namely, acetonitrile (AN) and dimethylformamide (DMF). Nitromesitylene was chosen as reactant since its rate constant for anion radical formation falls in a range[14] where reasonably precise kinetic data may be obtained. Association constants for the ion pairing equilibria were also measured and are reported in the present paper. The kinetic results are presented in part II.

Experimental Section and Method of Data Analysis

The apparatus for obtaining the current potential data consisted of a PAR Model 174A polarographic analyzer with a 10-in. strip chart recorder connected to the output and a Hewlett-Packard Model 3465 A digital multimeter for monitoring the potential difference between the dropping mercury electrode and the reference electrode. The experiments were conducted in a simple pyrex glass cell with separate working and reference electrode compartments connected by a partially open stopcock. Platinum foil was used as a counterelectrode. The reference electrode system in DMF was Ag|Ag$^+$ as used by Ryan and Evans;[10] in AN, it was Ag|AgCl as described previously.[15] When ion pairing equilibria were studied in solutions of varying ionic strength, the cell configuration was such that any variation in liquid junction potential between the working and reference compartments could be estimated by the Henderson equation for the simple

* To whom correspondence should be addressed.
† On leave from the Department of Chemistry, University of Warsaw, Warsaw, Poland.

TABLE I: Limiting Ionic Conductivities and Stokes' Radii for Several Monovalent Ions in Acetonitrile and Dimethylformamide

	Acetonitrile		Dimethylformamide	
Ion	Limiting Ionic conductance λ_0, m^2 Ω^{-1} $equiv^{-1}$	Stokes' radius r_s, nm	Limiting Ionic conductance λ_0, m^2 Ω^{-1} $equiv^{-1}$	Stokes' radius r_s, nm
Li^+	0.00693	0.344	0.00250	0.412
Na^+	0.00769	0.310	0.00299	0.344
K^+	0.00836	0.285	0.00308	0.334
Cs^+	0.00873	0.273	0.00345	0.298
TEA^+	0.00852	0.280	0.00356	0.290
ClO_4^-	0.01037	0.230	0.00524	0.196

case of different concentrations of the same electrolyte on either side of the junction. Spectroquality DMF (Matheson Coleman and Bell) was dried with calcium hydride and stored over 4A molecular sieves. It was distilled at reduced pressure (1–2 mmHg) under a nitrogen atmosphere before use. Spectroquality AN (Matheson Coleman and Bell) was used without further purification, the sealed container being opened in a controlled atmosphere chamber (Vacuum Atmospheres) containing purified nitrogen. Tetraethylammonium perchlorate (Eastman Kodak) was recrystallized three times from triply distilled water and dried over P_2O_5 in vacuo at 50 °C. Alkali metal perchlorates were recrystallized from triply distilled water and dried in vacuo over P_2O_5 at 140 °C. All measurements were made in the controlled atmosphere chamber at 25.0 ± 0.2 °C.

Current–potential data were obtained by stepping the potential by fixed increments and determining the current at the end of drop life. The best values of the half-wave potential, $E_{1/2}$, and slope of the plot of log $[(i_d - i)/i]$ against potential, where i_d is the diffusion limited current, were determined using the appropriate linear regression method.

Unfortunately, the necessary activity coefficient and transport number data for the electrolyte solutions used are not available at present. Following the suggestion of Coetzee and Campion,[16] rational activity coefficients were estimated from the extended Debye–Hückel equation, the ion size parameter $\mathring{a}$ being set equal to the sum of the Stokes radii for the two ions in the given 1–1 electrolyte. Accordingly

$$\log f_\pm = -A\mu^{1/2}/(1 + B\mathring{a}\mu^{1/2}) \quad (1)$$

where $f_\pm$ is the mean rational activity coefficient, μ is the ionic strength, $A = 1.8246 \times 10^6/(\epsilon T)^{3/2}$, and $B = 50.29 \times 10^8/(\epsilon T)^{1/2}$, ϵ being the dielectric constant of the solvent and T the absolute temperature. The transport numbers were estimated from the limiting equivalent conductivities of the ions involved at infinite dilution. Values of the limiting equivalent conductivities taken from the compilations of Reid and Vincent[17] and Springer et al.[18] and the corresponding Stokes' radii are summarized in Table I. Finally, the diffusion potential across a liquid/liquid junction of the form

x M KA ‖ y M KA

where KA represents a simple 1–1 electrolyte was estimated from the Henderson equation

$$\phi_x - \phi_y = \frac{\lambda_K - \lambda_A}{\lambda_K + \lambda_A}\frac{RT}{F}\ln\left[\frac{a_\pm(y)}{a_\pm(x)}\right] \quad (2)$$

where ϕ_i is the inner potential in solution i, and $a_\pm$(i) the corresponding mean salt activity. Since the appropriate data are not available, the equivalent conductances were replaced by their values in the limit of infinite dilution. In that the conductivities enter eq 2 as a ratio, the latter approximation is not anticipated to introduce serious error.

Results

The reversibility of the anion radical formation reaction

$$R + e^- \rightleftharpoons R^{\cdot-} \quad (3)$$

for nitromesitylene in various electrolyte solutions was determined by cyclic voltammetry at a hanging mercury drop electrode. Current–potential curves with equal peak currents in the cathodic and anodic sweeps were obtained for 0.5 mM nitromesitylene in 0.1 M $LiClO_4$, $NaClO_4$, $KClO_4$, $CsClO_4$, and TEAP solutions in DMF confirming that the reaction is chemically reversible (TEAP represents tetraethylammonium perchlorate). The peak potential for the reduction shifted in a positive direction as the crystallographic radius of the cation decreased indicating an increase in ion pairing of the anion radical $R^{\cdot-}$ with the cation in solution in the order $TEA^+ < Cs^+ < K^+ < Na^+ < Li^+$. A second electron transfer step, ascribed to reduction of the anion radical to the dianion

$$R^{\cdot-} + e^- \rightarrow R^{2-} \quad (4)$$

which reacts irreversibly by extracting at least one proton from a proton donor in the system,[19] occurred at more negative potentials. In 0.1 M TEAP the separation between the first and second waves was approximately 300 mV; in addition, the effect of the supporting electrolyte cation in shifting the reduction potentials to more positive potentials was stronger for the second step than for the first. Similar observations have been made for the two waves observed for the reduction of quinones in the presence of various alkali metal cations.[11,12] Because of lower solubility of alkali metal perchlorate salts in AN, the same experiments were carried out with a supporting electrolyte concentration of 0.01 M. In this solvent, the results were qualitatively similar except that the potential shifts at the same electrolyte concentration were larger indicating that ion pairing is stronger in AN than in DMF. However, the limiting current for the first reduction step in both 0.01 M $LiClO_4$ and $NaClO_4$ was significantly higher than for other electrolytes. This result is attributed to a catalytic disproportionation reaction in which the dianions and the parent molecule are produced from the anion radical.[21,22] Thus, ion pairing equilibria could not be studied in these systems by the present technique.

Having established that the anion radical formation reaction is chemically reversible dc polarographic data were examined to determine whether the current–voltage curves were affected by the rate of electron transfer. In all cases, the slope of plots of electrode potential E against log $[(i_d - i)/i]$ was 59 ± 2 mV indicating that the polarographic wave could be described as due to a one electron process, the concentrations of R and $R^{\cdot-}$ at the electrode being controlled by mass transfer only. Then, assuming equal diffusion coefficients for R and $R^{\cdot-}$, the half-wave potential is equal to the formal potential for reaction 3.

Ion pair formation was first investigated for TEA^+ by determining $E_{1/2}$ in TEAP solutions of varying ionic strength. The cell configuration in DMF was

Hg|R, x M TEAP‖0.1 M TEAP‖0.05 M $AgNO_3$|Ag (5)

For variation in TEAP concentration from 0.01 to 0.1 M, $E_{1/2}$ for nitromesitylene reduction changed from −1.917 to −1.887 V. This is attributed both to ion pairing of the anion radical with TEA^+ and to change in the diffusion

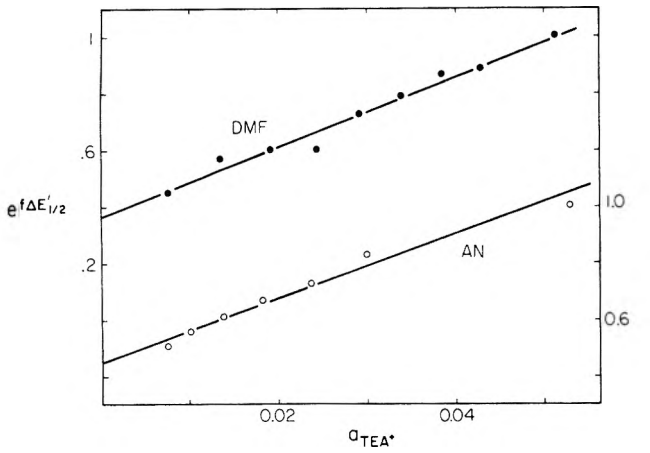

Figure 1. Plot of $e^{f\Delta E'_{1/2}}$ against activity of tetraethylammonium ion for solutions of varying ionic strength in dimethylformamide (DMF) and acetonitrile (AN) according to eq 9. $\Delta E'_{1/2}$ is the shift in the half-wave potential for reduction of nitromesitylene from that observed in 0.1 M tetraethylammonium perchlorate (TEAP) after correction for the estimated liquid–liquid junction potential change in cells 5 and 6 and $f = F/RT$. the left-hand ordinate scale applies to DMF, and the right-hand scale to AN.

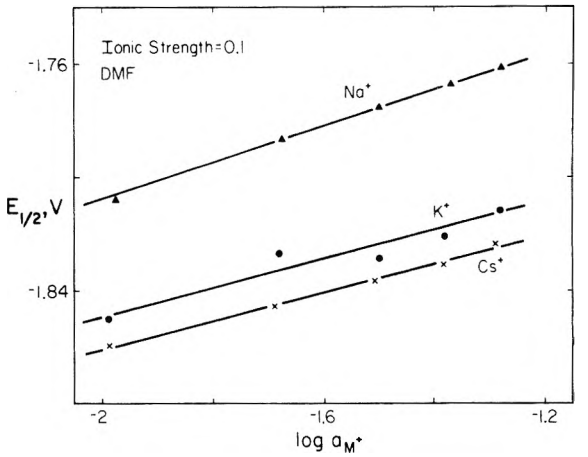

Figure 2. Plot of half-wave potential for the reduction of nitromesitylene in the presence of cations which form ion pairs with the anion radical $E_{1/2}$ against the logarithm of cation activity at constant ionic strength for solutions containing an alkali metal perchlorate and TEAP in DMF.

potential across the first liquid–liquid junction in cell 5. Since ClO_4^- is more mobile than TEA^+ in DMF (Table I), the potential in the working solution will be more negative than that in the reference compartment when the concentration of TEAP is less than 0.1 M. On the basis of eq 2 using activity coefficients estimated by eq 1, the diffusion potential between 0.01 and 0.1 M TEAP is −9.5 mV. Thus, only 20.5 mV of the observed 30 mV shift of $E_{1/2}$ in the positive direction is attributed to ion pairing. In the following anaylses all observed half-wave potentials have been corrected for the estimated diffusion potential in cell 5. A similar cell configuration was used in AN:

$$\text{Hg|R, } x \text{ M TEAP}\|0.1 \text{ M TEAP|AgCl|Ag} \qquad (6)$$

In this case a small amount of AgCl dissolves in AN to establish the reference half-reaction.[23]

When the anion radical formation reaction is followed by rapid ion pair formation

$$R^{-}\cdot + M^+ \rightleftharpoons M^+\cdots R^{-}\cdot \qquad (7)$$

it can easily be shown[24] from the Nernst equation that

$$E_{1/2} = E_0 + \frac{RT}{F} \ln [1 + K_M a_{M^+}] \qquad (8)$$

where E_0 is the standard potential for reaction 3, K_M, the association constant for ion pair formation, and a_{M^+}, the activity of the metal ion. The assumptions made in deriving eq 8 are (i) that the metal ion concentration is much larger than that of the organic reactant, so that the metal ion concentration at the electrode surface if equal to its concentration in the bulk; (ii) the diffusion coefficients of the anion radical and ion pair are the same.[25] In the present analysis, it was assumed that the metal ion activity is given by $f_{\pm}c_M$, c_{M^+} being the corresponding metal ion concentration. Defining $\Delta E'_{1/2}$ as $E_{1/2} - E^r_{1/2}$ where $E^r_{1/2}$ is the half-wave potential in a 0.10 M TEAP solution, eq 8 may be rewritten

$$e^{f\Delta E'_{1/2}} = e^{f\Delta E'_0}[1 + K_M a_{M^+}] \qquad (9)$$

where $\Delta E'_0 = E_0 - E^r_{1/2}$ and $f = F/RT$. Plots of $e^{f\Delta E'_{1/2}}$ against a_{TEA^+} for data obtained in both DMF and AN solutions are presented in Figure 1. It is apparent that a good linear relationship holds between these quantities, the best straight line being calculated by standard regression techniques. The values K_M and E_0 calculated from the slope and intercept were 36 L mol^{-1} and −1.913 V, respectively, in DMF; in AN, the corresponding values are 33 L mol^{-1} and −1.494 V. Considering the uncertainty in the correction for liquid junction potential and in the estimation of activity coefficients, the association constants cannot be regarded as more than order of magnitude estimates.

Ion pairing constants with alkali metal ions were determined at constant ionic strength by adding the corresponding perchlorate salt to the working electrode compartment of cells 5 and 6, TEAP being used to maintain the ionic strength with varying alkali metal perchlorate concentration. In the case that two cations enter into ion pairing equilibria with the anion radical, eq 8 becomes

$$E_{1/2} = E_0 + \frac{RT}{F} \ln [1 + K_M a_{M^+} + K_N a_{N^+}] \qquad (10)$$

where a_{N^+} is the activity of the second cation N^+ and K_N, its association constant with the anion radical. Assuming that ion pairing with the alkali metal cation is much stronger than that with TEA^+, one may assume that $K_N a_{N^+} \gg (1 + K_M a_{M^+})$. If this assumption is valid, plots of $E_{1/2}$ against log a_{N^+} should be linear with a slope of 59 mV. The data obtained in DMF at an ionic strength of 0.1 are presented in this form in Figure 2. In the case of Na^+, the slope is 62 mV, whereas for K^+ and Cs^+, it is approximately 50 mV. These results are taken as evidence that the coordination number for ion pair formation is indeed one as was assumed in deriving eq 10. The lower slope in the case of the K^+ and Cs^+ systems is attributed to neglect of the terms $1 + K_M a_{M^+}$. A more careful analysis was carried out using the standard potential determined from the data obtained in the presence of TEA^+ ion only and taking into account the contribution to the potential shift from ion pairing with TEA^+ ion. Equation 10 can be rewritten as

$$y = e^{f\Delta E_{1/2}} - 1 - K_M a_{M^+} = K_N a_{N^+} \qquad (11)$$

where $\Delta E_{1/2} = E_{1/2} - E_0$. Values of K_N were then determined from one parameter fits between values of y estimated from the experimental data and the alkali metal cation activity a_{N^+}. The resulting values of the association constants from experiments in both DMF and AN are summarized in Table II. It is apparent that ion pairing is considerably stronger in AN and that it increases in strength with decrease in the crystallographic radius of the

TABLE II: Crystallographic Radii and Association Constants for Ion Pair Formation between Nitromesitylene Anion Radical and the Same Cations in Dimethylformamide (DMF) and Acetonitrile (AN)

Cation	Crystallographic radius r_M, Å	Association constant K_M, L mol^{-1} DMF	AN
TEA$^+$	3.23	36	33
Cs$^+$	1.65	410	1100
K$^+$	1.33	660	4900
Na$^+$	0.95	4800	
Li$^+$	0.60	14100	

cation. The latter observation suggests that "tight" ion pairs are formed because the solvated radii of the cations considered increase with decrease in crystallographic radii. The variation in association constant with solvent can be attributed to weaker solvation of cations in AN.[26,27] On the basis of generally accepted solvent acidity and basicity scales,[27] DMF and AN are of approximately equal acidity so that anions are solvated to approximately the same extent in these solvents. On the other hand, AN is a poorer Lewis base than DMF so that cations are more weakly solvated and, therefore, associate more readily with anions in AN.

Discussion

The present results are in agreement with the trends observed in previously published association constants for polar anion radicals[7,9-11,13,28,29] in that the degree of ion pairing increases with decrease in the crystallographic radius of the cation involved and with decrease in solvent basicity. The association constants are larger than those reported for carbonyl compounds and quinones[10] but considerably less than those found for nitrobenzene in DMF.[7] In fact, Krygowski et al.[7] have obtained evidence that more than one cation is associated with a nitrobenzene anion radical in the case of Li$^+$ and Na$^+$ in DMF. Comparison of the present results with those obtained for nitrobenzene is particularly interesting because the data provide clear evidence that both polar and steric effects must be considered in ion pairing phenomena. ESR studies of the corresponding anion radicals in both AN[30] and DMF[31] have shown that the electron density on the nitro group increases in going from nitrobenzene to nitromesitylene. This observation can be attributed to both the inductive effect of the methyl groups which push charge density into the ring and also to the steric effect of the ortho-substituted groups which prevents the nitro group from being coplanar with the benzene ring and thus greatly reduces interaction between the π systems on the substituent and the ring.[30] Thus, on the basis of polar effects alone, one would expect stronger ion pairing between nitromesitylene anion radical and alkali metal cations. However, the ortho substituents also sterically hinder ion pair formation by preventing the cation from approaching the anion radical as closely as it does in the case of nitrobenzene. Thus, the magnitude of the association constant is considerably smaller for nitromesitylene.

As pointed out by Avaca and Bewick,[32] the relative strength of ion pairing in the presence of different cations depends both on the charge density on the anion radical and on the solvating ability of the solvent. In the case that the charge density is highly localized and the ion pairs are chiefly "tight", that is, of the nonsolvent separated variety, the change in ion association with solvent can be related to the relative ability of the given solvents to act as Lewis acids and bases.[26,27] Thus, although the solvents DMF, AN, dimethyl sulfoxide (Me_2SO), and hexamethylphosphoramide (HMPA) are all solvents of intermediate dielectric constant, they possess varying degrees of basicity according to well-accepted basicity scales such as the Gutmann donor number DN[33] or the Koppel–Palm parameter B.[34] Thus, the degree of ion pairing decreases from the least basic solvent AN to the most basic HMPA where cations are most strongly solvated. More detailed analysis of these effects on the basis of polarographic data for the reduction of 1,2-naphthoquinone in five aprotic solvents[12] has shown that solvent acidity must also be considered not only because it will be the important factor in anion solvation but also because solvent acidity is often directly related to the degree of solvent structure, another factor which plays a role in ion–ion interactions.[26] Finally, in the case of anions with nonlocalized charge such as anthracene anion radical, the degree of ion pairing decreases with increase in solvated cation size;[32] this observation is interpreted as evidence of solvent separated or "loose" ion pairs. In this case, insufficient data are available to discuss the ion pairing phenomena in terms of solvent acidity and basicity.

An alternative method for determining the half-wave potential for a given anion radical formation reaction in the absence of ion pairing was proposed by Kalinowski[8] and used to interpret data for the electroreduction of carbonyl compounds,[6,8] quinones,[13] and nitro compounds.[6,7] Accordingly, the half-wave potential is related to that in the absence of the ion pairing $E^0_{1/2}$ by the equation

$$E_{1/2} = E^0_{1/2} + m\Phi \tag{12}$$

where Φ is the ionic potential of the cation[35] and m is a correlation coefficient. The ionic potential is assumed to equal the charge on the cation divided by either its crystallographic radius[6,13] or the modified radius[7] defined on the basis of the free energy of ion solvation.[36] According to the Born equation, the free energy of ion solvation, $\mu^0_{i,s}$ is

$$\mu^0_{i,s} = \frac{-N_0(z_i e_0)^2}{2(r_i + \delta_s)}\left[1 - \frac{1}{\epsilon_s}\right] \tag{13}$$

where N_0 is Avogadro's number, e_0, unit charge, z_i, the valence of ion i, r_i, its crystallographic radius, δ_s, the correction used to define the modified radius in the given solvent, and ϵ_s, the dielectric constant of the solvent. Kalinowski obtained linear plots of $E_{1/2}$ determined at constant metal ion concentration against Φ defined on the basis of crystallographic radii for the reduction of nitrobenzene[6] and benzaldehyde;[6] on the other hand, a plot with two linear sections was obtained in the cases of fluorenone[8] and benzophenone.[8] On comparing eq 8 and 12, it is apparent that, when $K_M a_{M^+} >> 1$, eq 12 implies the assumption that ln K_M is a linear function of $1/r_i$ or $1/(r + \delta_s)$. The departure from linearity observed for cations associating weakly with fluorenone and benzophenone anion radicals can then be attributed to a failure of the condition $K_M a_{M^+} \gg 1$. For this reason, use of eq 12 to obtain values of the half-wave potential in the absence of ion pairing will lead to serious overestimation of ion pairing associations constants since the estimated value of $E^0_{1/2}$ will be too negative.

According to the simple model for ion pair association constants derived by Ramsey et al.,[37,38] the association equilibrium constant is given by

$$RT \ln K_M = RT \ln K^0_M - \frac{N_0 z_M z_X e_0^2}{(r_M + r_X)\epsilon_s} \tag{14}$$

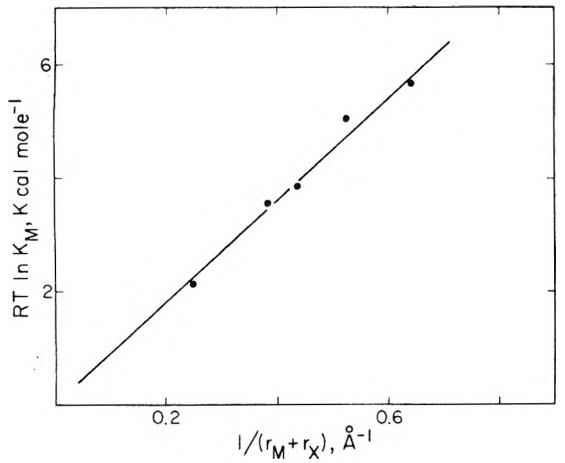

Figure 3. A plot of $RT \ln K_M$ where K_M is the association constant estimated for a given monovalent cation–anion radical ion pair in DMF, against $1/(r_M + r_X)$ where r_M is the crystallographic radius of the cation and r_X the effective solvation radius of the anion radical (assumed to be 0.96 Å).

where K^0_M is the association constant for the two uncharged species in solution,[38] z_M and z_X are the charges on the cation and anion radical, respectively, and r_M and r_X, their effective radii in the ion pair when that species is modeled as two contiguous hard spheres. It seems reasonable to assume that r_M is approximately equal to the crystallographic radius of the cation. Equation 14 was fitted to the data obtained in DMF by an iterative technique which involved choosing a value for r_X and then determining $RT \ln K^0_M$ and $N_0e_0^2/\epsilon_s$ by a least-squares fit of $RT \ln K_M$ to $1/(r_M + r_X)$. The best value of r_X was chosen by requiring that the slope of the resulting linear plot be equal to 9.05×10^8 kcal cm mol^{-1}, the value of $N_0e_0^2/\epsilon_s$ for DMF. Accordingly, it was found that $r_X = 0.96$ Å, and $RT \ln K^0_M = 0.03$ kcal mol^{-1}, the correlation coefficient for the linear fit being 0.992 (Figure 3). Considering the crude nature of the model, the success of this procedure is rather surprising. The value of r_X is much smaller than one would expect considering the actual size of the nitromesitylene anion radical; it suggests that solvation of the radical anion is localized at the reaction site, in the present case, at the nitro group. The appropriate radius for the anion radical in a hard sphere model may then be much smaller than that used when the charge density is uniformly distributed over the anion. The polarizability of these species is expected to be high so one may regard the negative charge as being virtually localized at a site close to the position of the cation in the ion pair. In this case, the effective radius of the anion radical may well be less than that of the cation. However, the approximations made in the Denison–Ramsey derivation[37] of eq 14 should be kept in mind in assessing the above parameters. In particular, their assumption that the effective radii for solvation of the free cation and anion are the same as those for solvation of these species in the ion pair is undoubtedly incorrect. Thus, eq 14 does not give an accurate account of the dependence of K_M on cation nature. The success of the Kalinowski equation[8] and the modified version of Krygowski et al.[7] for similar systems can be attributed to the fact that r_X falls in the range of r_M on the basis of the Denison–Ramsey model. Insufficient data are available to warrent determination of the equivalent quantities in acetonitrile.

Some support for the above conclusions may be obtained from the calculations of the ion–ion association energy (for similar ion pairs) made by Krygowski et al.[39] These authors used a modified version of HMO theory[40,41] to determine the most probable site for cation interaction with the anion radical and to estimate the relative change in association energy with cation size. On the basis of their calculations, the most likely site for interaction of alkali metal cations with nitrobenzene anion radical is at a point over the oxygen atoms in the nitro group, equidistant from each atom, and at a distance determined by the sum of the crystallographic radius of the cation and the van der Waals radius of the oxygen atom (1.4 Å). A considerable decrease in interaction energy was observed if the interaction site was assumed to be over the benzene ring. Krygowski et al.[39] showed that a linear relationship exists between ln K_M and the interaction energy calculated for various alkali metal cations and tetraethylammonium ion. When the same calculations are carried out for nitromesitylene, it is again found that the most favorable site for ion–ion interaction is directly over the center of a line drawn through the oxygen atoms. It was also found that ln K_M is a linear function of the association energy when variation in the distance of the metal ion from the oxygen atom is determined by the crystallographic radius of the cation. Thus, these calculations can be considered to justify somewhat the low value of the effective radius for the anion radical obtained from the Denison–Ramsey analysis.

Acknowledgment. Helpful suggestions and discussions with T. M. Krygowski are gratefully acknowledged. The research was supported by a grant from the National Research Council of Canada.

References and Notes

(1) C. K. Mann and K. K. Barnes, "Electrochemical Reactions in Nonaqueous Systems", Marcel Dekker, New York, N.Y., 1970.
(2) R. R. Dogonadze in "Reactions of Molecules at Electrodes", N. S. Hush, Ed., Wiley-Interscience, New York, N.Y., 1971, Chapter 3.
(3) P. P. Schmidt in "Electrochemistry, Specialist Periodical Reports", Vol. 5, H. R. Thirsk, Ed., The Chemical Society, London, 1975, Chapter 2.
(4) W. R. Fawcett and S. Levine, *J. Electroanal. Chem.*, **43**, 175 (1973).
(5) L. Holleck and D. Becher, *J. Electroanal. Chem.*, **4**, 321 (1962).
(6) M. K. Kalinowski, *Chem. Phys. Lett.*, **8**, 378 (1971).
(7) T. M. Krygowski, M. Lipsztajn, and Z. Galus, *J. Electroanal. Chem.*, **42**, 261 (1973).
(8) M. K. Kalinowski, *Chem. Phys. Lett.*, **7**, 55 (1970).
(9) A. Lasia and M. K. Kalinowski, *J. Electroanal. Chem.*, **36**, 511 (1972).
(10) M. D. Ryan and D. H. Evans, *J. Electroanal. Chem.*, **67**, 333 (1976).
(11) M. E. Peover and J. D. Davies, *J. Electroanal. Chem.*, **6**, 46 (1963).
(12) T. Fujinaja, K. Izutsu and T. Nomura, *J. Electroanal. Chem.*, **29**, 203 (1971).
(13) M. K. Kalinowski and B. Tenderende-Guminska, *J. Electroanal. Chem.*, **55**, 277 (1974).
(14) M. E. Peover and J. S. Powell, *J. Electroanal. Chem.*, **20**, 427 (1969).
(15) W. R. Fawcett and R. O. Loutfy, *Can. J. Chem.*, **51**, 230 (1973).
(16) J. F. Coetzee and J. J. Campion, *J. Am. Chem. Soc.*, **89**, 2513 (1967).
(17) D. S. Reid and C. A. Vincent, *J. Electroanal. Chem.*, **18**, 427 (1968).
(18) C. H. Springer, J. F. Coetzee, and J. J. Campion, *J. Phys. Chem.*, **73**, 471 (1969).
(19) Jensen and Parker[20,21] have attributed the irreversibility of the second step to trace impurities in the solvent which are not removed by conventional purification procedures. They showed that this step becomes reversible when neutral alumina is suspended in the working solution.
(20) B. S. Jensen and V. D. Parker, *J. Chem. Soc., Chem. Commun.*, 367 (1974).
(21) B. S. Jensen and V. D. Parker, *J. Am. Chem. Soc.*, **97**, 5211 (1975).
(22) M. Szwarc, *Acc. Chem. Res.*, **5**, 169 (1972).
(23) D. C. Luehrs, R. T. Iwamoto, and J. Kleinberg, *Inorg. Chem.*, **5**, 201 (1966).
(24) Z. Galus, "Fundamentals of Electrochemical Analysis", Ellis Horwood, Chichester, 1976, Chapter 14.
(25) More general versions of eq 8 have been given by Krygowski et al.[7] for the case that more than one metal ion pairs with one radical anion, and by Lasia and Kalinowski[9] for the case that more than one radical anion pairs with one metal ion. Examination of the present data confirmed that neither of those more complex ion pairing equilibria needed to be considered.
(26) T. M. Krygowski and W. R. Fawcett, *J. Am. Chem. Soc.*, **97**, 2143 (1975).
(27) W. R. Fawcett and T. M. Krygowski, *Can. J. Chem.*, **54**, 3283 (1976).

(28) M. D. Ryan and D. H. Evans, *J. Electrochem. Soc.*, **121**, 881 (1974).
(29) M. J. Hazelrigg, Jr., and A. J. Bard, *J. Electrochem. Soc.*, **122**, 211 (1975).
(30) D. H. Geske, J. L. Ragle, M. A. Bambenek, and A. L. Balch, *J. Am. Chem. Soc.*, **86**, 987 (1964).
(31) R. D. Allendoerfer and P. H. Rieger, *J. Am. Chem. Soc.*, **88**, 3711 (1966).
(32) L. A. Avaca and A. Bewick, *J. Electroanal. Chem.*, **41**, 405 (1973).
(33) V. Gutmann and R. Schmid, *Coord. Chem. Rev.*, **12**, 263 (1974).
(34) I. A. Koppel and V. A. Palm in "Advances in Linear Free Energy Relationships", N. B. Chapman and J. Shorter, Ed., Plenum Press, New York, N.Y., 1972, Chapter 5.
(35) G. H. Cartledge, *J. Am. Chem. Soc.*, **50**, 2855 (1928).
(36) W. W. Latimer, K. S. Pitzer, and C. M. Slansky, *J. Chem. Phys.*, **7**, 108 (1939).
(37) J. T. Denison and J. B. Ramsey, *J. Am. Chem. Soc.*, **77**, 2615 (1955).
(38) Y. H. Inami, H. K. Bodensch, and J. B. Ramsey, *J. Am. Chem. Soc.*, **83**, 4745 (1961).
(39) T. M. Krygowski, M. Lipsztajn, and P. Radzikowski, *J. Mol. Struct.* **28**, 163 (1975).
(40) B. J. McClelland, *Trans. Faraday Soc.*, **57**, 1458 (1961).
(41) I. B. Goldberg and J. R. Bolton, *J. Phys. Chem.*, **74**, 1965 (1970).

A Mass Spectral Study of the Kinetics of Carbon Monoxide Displacement from a Nickel Surface

L. A. Burchfield,[1] L. D. Neff, and L. I. Bone*

Department of Chemistry, East Texas State University, Commerce, Texas 75428 *(Received February 24, 1977)*

Publication costs assisted by the Robert A. Welch Foundation

We have measured the rate at which thiophene replaces CO on a Ni surface using a quadrupole mass spectrometer especially designed for this purpose. A cell containing the active surface is mounted at the ion source of the mass spectrometer after the molecular leak. A Ni film is evaporated on the inside surface of a glass tube, and CO is adsorbed. A mixture containing thiophene, an inert dilution gas, and a trace of a reference gas is flowed over the surface at a controlled rate, directly into the source of the mass spectrometer. The intensity of the CO peak is proportional to the rate of the replacement: rate = $k_1[Ni_I]^0e^{-k_1t} + k_2[Ni_{II}]^0e^{-k_2t}$, where $[Ni_I]^0$ and $[Ni_{II}]^0$ are the initial concentrations of CO on different types of Ni sites, and k_1 and k_2 are relative rate constants for the desorption process including the steady state concentration of thiophene at the surface. Our results show that a plot of ln rate vs. time can be deconvoluted into two straight lines indicating at least two different kinds of CO–Ni sites. The relative concentrations of the two sites are 5/1 with the least abundant type being replaced by thiophene 7 times faster.

Introduction

Many investigators[2,3] have studied the chemisorption of carbon monoxide on different transition metals. The bulk of the work has concerned itself with the carbon monoxide–nickel system with only a few investigations using the other metals. Because carbon monoxide bonds to transition metals in an unusual manner, it has been suggested[4] that it could be used as an effective probe of the adsorbent surface. Blyholder[4] proposed that the strength of the adsorbate–adsorbent bond is related to the position of the corresponding carbon monoxide adsorption band in the infrared. Using synergic bonding arguments, he concluded that as the energy required to excite the carbon–oxygen stretching vibrations decreased (as reflected by a shift of the corresponding spectral bands toward lower energy) the strength of the carbon–metal bond increased. This is supported by molecular orbital calculations[4-6] which show that the metal–carbon π bonding orbital ($d\pi$–$p\pi$) is simultaneously antibonding for the carbon–oxygen π orbital. Thus as the electron density increases in the metal–carbon π bond (and therefore an increase in the strength of the bond), it decreases the overall bond order of the carbon–oxygen bond thereby weakening it; hence a shift is observed in the spectra.

Spectra of carbon monoxide chemisorbed on nickel exhibit two major bands at about 2040 and 1920 cm^{-1}. The peak at 2040 cm^{-1} is highly symmetric, but the band at 1920 cm^{-1} is asymmetric and can be considered to be a composite of several absorptions. For evaporated films of nickel, additions of a mercaptan or thiophene results in the subsequent displacement of the carbon monoxide.[7] As the concentration of the mercaptan is increased, the position of the two absorption maxima are shifted toward lower energy and the more weakly held material is displaced first. Therefore, the nickel adsorbents appear to exhibit a variety of surface sites having different free valencies. Eischens et al.[8] attributed the two bands to the presence of two distinctly different surface species, characterized as linear and bridge bonded carbon monoxide. The linear structures result from the formation of a single carbon–nickel bond, whereas the bridge bonded species is envisioned to involve the carbon atom bonded to two different nickel atoms. Other workers[9,10] have explained the spectra in terms of a single structure (the linear structure) located at different points on the surface.

This study reports the usefulness of mass spectrometrically following displacement of a chemisorbed species in a flow apparatus. We have assembled an instrument in which we pass a gaseous mixture containing thiophene over a Ni surface saturated with chemisorbed carbon monoxide. The gas then passes directly into the source of the mass spectrometer allowing a direct determination of the concentration of CO displaced as a function of time, flow rate, and composition of the displacing mixture. Using this technique two types of CO–Ni sites have been detected. Also, the relative concentration, and the relative rate of displacement from each site were determined.

Experimental Section

The mass spectrometer and associated experimental apparatus used in this study were assembled especially for this investigation. Since the system has not been described

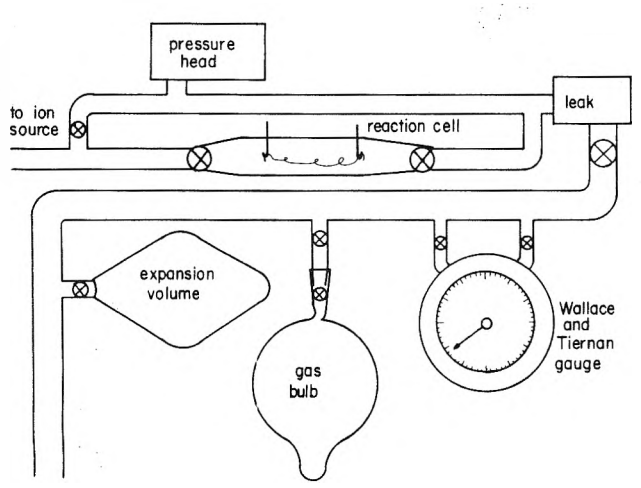

Figure 1. Diagram of gas inlet system.

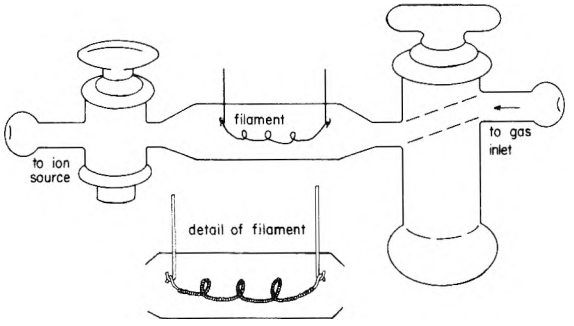

Figure 2. Reaction cell for evaporated nickel samples.

previously, it will be discussed in some detail.

The system consists of a Welch turbo-molecular pumping station with a speed of 140 L/s. The mass spectrometer is enclosed in a vacuum chamber constructed from 8-in. stainless steel pipe with a volume of nearly 0.75 ft^3. The interior of the chamber is easily accessed through a $7^1/_3$-in. i.d. port. The mass spectrometer consists of a du Pont Model 21-440 quadrupole mass filter and a locally constructed source of a conventional design. The detector consists of a 13 stage Cu–Be multiplier, a dc amplifier, and a Honeywell Model 90613 recording oscillograph.

The stainless steel gas inlet system is shown in Figure 1. A MKS Baratron capacitance manometer with a 0–10 Torr pressure sensing head is used with a Granville-Phillips motor driven leak to automatically maintain the gas flow rate into the source at a preset value. Displacement gas mixtures can be prepared in the inlet using the Wallace and Tiernan gauge and stored in a 3-L glass bulb. The reaction cell which is shown in Figure 2 is mounted in the inlet system using 18/9 ball joints. The cell is constructed of 30-mm pyrex glass and has a 6-mm bore stopcock on each end.

A nickel film is evaporated onto the inside wall of the glass reaction cell from a hot filament. The filament is made by wrapping 0.010-in. diameter nickel wire (99.95% pure) around a 0.20-in. diameter tungsten wire (99.99% pure). This filament is suspended from the tungsten electrodes in the reaction cell as shown in Figure 2. While pumping on the cell, the filament is electrically heated to a dull red color. When the filament has been hot for 2–3 min the voltage across the filament is removed. After the filament has cooled, 5–10 Torr of helium is introduced into the cell. A voltage is again applied across the filament to heat it to a red color. At this stage the voltage is rapidly increased, heating the filament to a white heat and evaporating a thin film of nickel onto the inside surface of the cell. The helium is then pumped out of the cell and carbon monoxide is introduced. The CO is allowed to stay in the cell for about 1 min and is then pumped out. The cell is isolated from the rest of the system to await displacement.

A gaseous mixture consisting of 4–10 mol % thiophene, 1 mol % methane, and 89–95 mol % argon is used to displace CO from the metal surface. The relatively low concentration of thiophene results from a trade off between instrument sensitivity and reaction rate. At higher concentration the reaction was too fast for our experimental technique; at lower concentrations the sensitivity of the instrument for CO was too low. Since the absolute sensitivity of the instrument fluctuates somewhat with time, methane was used as an internal standard. All peak heights are measured relative to the m/e 15 peak from methane.

Experimental data are collected by first observing the spectrum of the displacing gas by passing it through the bypass and into the ion source at the same pressure at which the run is to be made. While the gas is flowing and the mass spectrum is repeatedly scanned and recorded, the path of the displacing gas is then diverted through the cell. As the gas flows over the nickel surface, CO is displaced and is detected by the mass spectrometer.

Since these are flow experiments, the height of the CO peak (m/e 28) is proportional to the rate of its displacement. Each scan lasts 30 s and repeats immediately allowing us to measure the rate of CO displacement at 30-s intervals.

Results and Discussion

Infrared evidence indicates there are at least two different kinds of surface structures for CO chemisorbed on nickel. These structures represent different adsorbent–adsorbate bonding considerations. Thus, two chemical equations may be written to represent the desorption reactions which take place when CO is displaced by some other species:

$$D + (Ni\text{-}CO)_I \xrightarrow{k_1} CO + Ni\text{-}D \quad (1)$$

$$D + (Ni\text{-}CO)_{II} \xrightarrow{k_2} CO + Ni\text{-}D \quad (2)$$

where D is the displacing species, $(Ni\text{–}CO)_I$ and $(Ni\text{–}CO)_{II}$ are the two kinds of complexes of CO chemisorbed on nickel, Ni–D is the complex of the displacing species chemisorbed on nickel, and k_1 and k_2 are the rate constants. Now, if both of these processes produce CO simultaneously, a rate equation of the form

$$d(CO)/dt = k_1(Ni\text{-}CO)_I(D) + k_2(Ni\text{-}CO)_{II}(D) \quad (3)$$

may be written. In a flow system where D is continuously passed over the surface, its concentration may be held constant allowing the rate equation to be simplified to

$$d(CO)/dt = k_1'(Ni\text{-}CO)_I + k_2'(Ni\text{-}CO)_{II} \quad (4)$$

If each reaction is pseudo-first order in D

$$(Ni\text{-}CO)_I = (Ni\text{-}CO)_I^0 e^{-k_1' t} \quad (5)$$

and

$$(Ni\text{-}CO)_{II} = (Ni\text{-}CO)_{II}^0 e^{-k_2' t} \quad (6)$$

where $(Ni\text{–}CO)_I^0$ and $(Ni\text{–}CO)_{II}^0$ are the initial concentrations of CO chemisorbed on sites of types I and II. The rate equation may now be written

$$d(CO)/dt = k_1'(Ni\text{-}CO)_I^0 e^{-k_1' t} + k_2'(Ni\text{-}CO)_{II}^0 e^{-k_2' t} \quad (7)$$

TABLE I: Rate Constants for Displacement of CO by Thiophene

Run	Cell pressure, Torr	Slope 10^3 k_1', s^{-1}	Slope 10^3 k_2', s^{-1}	Mole % thiophene	Pressure × mole fraction, Torr	Slope 10^2 k_1,[a] Torr	Slope 10^2 k_2,[a] Torr
A	1.8	35 ± 8.0	5.4 ± 0.6	10.0	0.180	19 ± 5	3.0 ± 0.3
B	0.9	5.4 ± 0.5	0.9 ± 0.1	4.2	0.038	14 ± 2	2.3 ± 0.3
C	1.7	9.8 ± 1.8		4.2	0.071	14 ± 2.0	
D	1.0	9.6 ± 1.5	1.1 ± 0.1	4.2	0.042	23 ± 3	2.7 ± 0.3
E	1.0	9.8 ± 1.6	0.7 ± 0.1	4.2	0.042	23 ± 3	1.6 ± 0.2
F	1.6	14 ± 2.0	1.7 ± 0.2	6.0	0.096	15 ± 2	2.8 ± 0.3
						Av 18	2.5

[a] Slope/(pressure × mole fraction).

TABLE II: Relative Quantities of $(Ni\text{-}CO)_I^0$ and $(Ni\text{-}CO)_{II}^0$

Run	Slope 10^3 k_1', s^{-1}	Slope 10^3 k_2', s^{-1}	Intercept k_1'' (arbitrary units)	Intercept k_2'' (arbitrary units)	Ratio of $(Ni\text{-}CO)_I^0/(Ni\text{-}CO)_{II}^0$
A	35 ± 8.0	5.4 ± 0.6	200 ± 80	30 ± 3	1.0 ± 0.8
B	5.4 ± 0.5	0.9 ± 0.1	5.5 ± 0.5	3.9 ± 0.5	0.23 ± 0.2
D	9.6 ± 1.5	1.1 ± 0.1	11 ± 1	7.6 ± 1	0.17 ± 0.2
E	9.8 ± 1.6	0.7 ± 0.1	23 ± 8	9 ± 2	0.18 ± 0.6
F	14 ± 2.0	1.7 ± 0.2	7.2 ± 0.7	3.4 ± 0.5	0.25 ± 0.2

However, since $(Ni\text{-}CO)_I^0$ and $(Ni\text{-}CO)_{II}^0$ are constants, they may also be incorporated into the rate constants. The equation simplifies to

$$d(CO)/dt = k_1''e^{-k_1't} + k_2''e^{-k_2't} \quad (8)$$

When k_2'' and k_1'' are comparable but different, a plot of ln rate vs. time will give a curve which can be deconvoluted into two straight lines by a standard analytical technique. From the slope and intercept of the two resulting lines k_1', k_2', k_1'', k_2'', $(Ni\text{-}CO)_I^0$, and $(Ni\text{-}CO)_{II}^0$ can be calculated. In each case, the slope of ln rate vs. time is k' or $k(D)$. However since the steady state concentration of thiophene is the product of pressure X mole fraction of thiophene, the quotient, slope/(pressure X mole fraction of thiophene), gives relative rate constants for each process.

Results of two representative experiments at different flow rates and thiophene concentrations are shown in Figures 3 and 4. The units on the abscissa are seconds but the units on the ordinate are arbitrary since the rate is expressed as a ratio of the peak heights of CO in millimeters to the peak heights of a reference peak in millimeters. Table I summarizes the slopes from five separate ln rate vs. time plots along with pertinent experimental parameters. The values recorded in the "pressure" column refer to the pressure of the displacing gas mixture at the entrance to the cell and represent a measure of the rate of flow of the displacing gas mixture.

The slopes of the two deconvoluted lines which are equal to k_1' and k_2' are recorded in the next two columns in units of $(second)^{-1}$. The percentage listed in the "mole percent of thiophene" column gives the concentration of thiophene in the displacing gas mixture. Both the rate of flow of the displacing gas and the concentration of thiophene in the gas mixture directly govern how much thiophene is made available at the nickel surface to displace CO. Therefore, a relative measure of the concentration of thiophene delivered to the surface is given by the product of the flow times the concentration of thiophene in the gas mixture. As discussed earlier, the rate of flow is measured by the pressure of the displacing gas mixture at the entrance of the reaction cell. The "pressure X mole fraction of thiophene" column is proportional to the concentration of thiophene at the surface. If the rate constants k_1' and k_2' are divided by this measure of the thiophene concentration, relative values of the rate constants k_1 and k_2 are obtained. These are given in the last column of Table I.

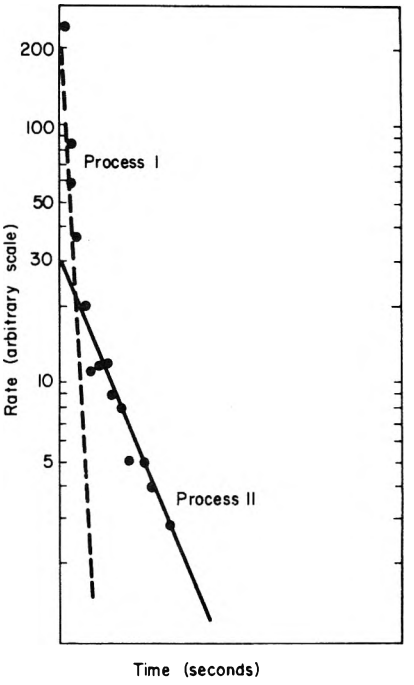

Figure 3. In rate of CO desorption vs. time for run A.

The intercepts of the deconvoluted lines from a plot of ln rate vs. time give a measure of k_1'' and k_2''. Since

$$k_1'' = k_1'(Ni\text{-}CO)_I^0 \quad (9)$$

and

$$k_2'' = k_2'(Ni\text{-}CO)_{II}^0 \quad (10)$$

the ratio of CO molecules on type I sites to those on type II sites is given by

$$\frac{(Ni\text{-}CO)_I^0}{(Ni\text{-}CO)_{II}^0} = \frac{(k_1'')(k_2')}{(k_2'')(k_1')} \quad (11)$$

This ratio and the pertinent information used to calculate it is given in Table II. Run C is not tabulated as it did not resolve into two lines.

These results clearly indicate that there are at least two different types of desorption processes with different rates.

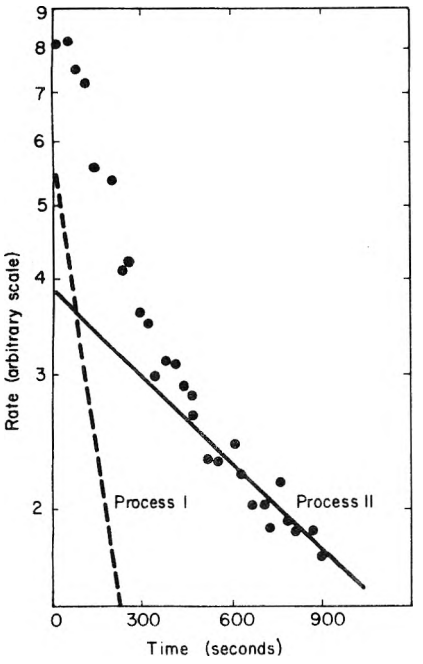

Figure 4. In rate of CO desorption vs. time for run B.

Suggesting that there are at least two kinds of metal–CO bonds involved which undoubtedly have different bond energies and that their approximate ratio is 5/1, the type of site greatest in quantity being that which bonds most strongly with CO. There may be other types of sites or these two kinds may actually include subtypes which have bond energies so close as to be indistinguishable by this experimental technique.

Since the room temperature rate constant for displacement for process I is about 7 times greater than that for process II, the activation energy for process II must be 1200 cal greater than that for process I. This suggests that the CO displaced in process II might be bonded to the metal 1200 cal more strongly than that which is displaced in process I. This deduction is highly speculative, however, since when a more strongly bonded CO is displaced, the displacing molecule may also be bonded more strongly and this could have considerable influence on the activation energy for the process. At best, it is probably reasonable to assume that the process II corresponds to desorption of a more strongly bonded CO.

Runs B, D, E, and F of Table II indicate that CO on a Ni site of type I is only about 0.2 as abundant as CO on a Ni site of type II. There is considerable reason to believe that the relative abundance of the two types of sites is probably a strong function of the technique used in the evaporation and the agreement found in this work is actually somewhat surprising considering that each run was carried out on an individually prepared surface.

Note Added in Proof. One experiment was conducted to determine if argon alone would remove CO from an evaporated Ni surface. Ni was evaporated on a salt plate in the infrared cell,[11] CO was adsorbed, the spectrum was recorded, and the system was purged with argon. No change in the spectrum could be observed.

Acknowledgment. This work was supported by the Faculty Research Committee of East Texas State University and the Robert A. Welch Foundation.

References and Notes

(1) Present Adress: Department of Chemistry, Texas A&M University, College Station, Tex. 77843.
(2) L. H. Little, "Infrared Spectra of Adsorbed Species", Academic Press, New York, N.Y., 1966, Chapter 3.
(3) M. L. Hair, "Infrared Spectroscopy in Surface Chemistry", Marcel Dekker, New York, N.Y., 1967, Chapter 6.
(4) G. D. Blyholder, *J. Phys. Chem.*, **68**, 2772 (1964).
(5) G. D. Blyholder and C. A. Coulson, *Trans. Faraday Soc.*, **63**, 1782 (1967).
(6) P. Politzer and S. D. Kasten, *J. Phys. Chem.*, **80**, 385 (1976).
(7) J. L. Wallace, Honors Thesis, East Texas State University, Commerce, Tex., 1972.
(8) R. P. Eischens, S. A. Francis, and W. A. Pliskin, *J. Phys. Chem.*, **60**, 194 (1956).
(9) G. D. Blyholder, *Proc. Int. Congr. Catal., 3rd, 1964*, 657 (1965).
(10) R. Van Hardeveld and F. Hartog, *Adv. Catal.*, **22**, 75 (1972).
(11) L. D. Neff and S. Kitching, *J. Phys. Chem.*, **78**, 1648 (1974).

Heterogeneous Photocatalytic Oxidation of Cyanide and Sulfite in Aqueous Solutions at Semiconductor Powders

Steven N. Frank and Allen J. Bard*

Department of Chemistry, The University of Texas at Austin, Austin, Texas 78712 *(Received February 14, 1977)*

Publication costs assisted by The University of Texas at Austin

The photocatalytic oxidations of CN^- and SO_3^{2-} were studied at several semiconductor powders including TiO_2, ZnO, CdS, Fe_2O_3, and WO_3 using a xenon light source. TiO_2, ZnO, and CdS were active photocatalysts for cyanide oxidation, while no oxidation was seen for Fe_2O_3 and WO_3. The catalyzed oxidation of CN^- at TiO_2 using sunlight was also investigated. The rate constant for CN^- oxidation at TiO_2 in sunlight was 3.1×10^{-5} mol day^{-1} cm^{-2} illuminated surface. The product of the oxidation of CN^- at TiO_2 was quantitatively determined to be OCN^-. TiO_2, ZnO, CdS, and Fe_2O_3 photocatalyzed the oxidation of SO_3^{2-}. The order of the catalytic activity was $Fe_2O_3 \sim ZnO \sim CdS > TiO_2$. The rates of the photocatalytic oxidations were greater for SO_3^{2-} than for CN^- in the cases of TiO_2, ZnO, and CdS. The chemical and photochemical stabilities for the most active catalysis were determined.

Introduction

The study of semiconductor materials as electrodes in electrochemical solar cells is currently a subject of much interest.[1] Less attention has been directed toward exploiting the photoelectrochemical properties of semiconductors for other purposes, however, e.g., as photocatalysts for bulk synthesis and for the conversion of pollutants in waste streams to less harmful forms. In electrochemical devices such as solar cells[2] the n-type semiconductor functions as a photoanode and a metal or

carbon counterelectrode functions as the cathode (for example, in the TiO_2|NaOH|Pt cell, oxygen is photogenerated at the n-TiO_2 and is reduced at the Pt cathode). However, under certain conditions both reduction and oxidation can occur simultaneously at an illuminated semiconductor.[3-5] This process, called heterogeneous photocatalysis, bears the same relation to photoelectrochemical cells as corrosion processes relate to galvanic cells. A number of solution studies of the photocatalyzed reactions at semiconductor powders have been carried out.[3] These studies have usually involved organic reducing agents and have mainly been concerned with the production of H_2O_2 by reduction of the O_2 present in the solution. Little effort has been directed to larger scale experiments and to carrying the chemical processes to completion.

In a previous communication we reported the photocatalyzed oxidation of CN^- in aqueous solutions at TiO_2 powders.[4] Here we extend these studies to the photocatalyzed oxidation of CN^- at other semiconductors such as ZnO, CdS, and Fe_2O_3. We also studied the oxidation of CN^- at TiO_2 under solar radiation at concentrations and solution volumes which would be useful in gauging the applicability of this reaction to large scale processes. The effect of varying the solution redox level was explored by measuring the rate of the photocatalyzed oxidation of sulfite ion (SO_3^{2-}) at the same semiconductor materials.

Experimental Section

The following were the sources of the semiconductor powders: TiO_2 [anatase, Matheson Coleman and Bell (MCB)]; ZnO (Fischer); α-Fe_2O_3 (MCB); all were used without further pretreatment. Two samples of CdS powder were used. One was prepared in this lab by precipitating CdS by heating a solution of $Cd(NO_3)_2$ and thioacetamide. The other was a commercial powder of unknown origin. Electron micrographs showed that the particle size of all of the powders was less than 1 μm. Other chemicals were of reagent grade. Solutions were prepared with low conductivity water.

Typical experiments consisted of illuminating 10-mL aliquots of CN^- or SO_3^{2-} in quartz tubes containing 0.1 g of semiconductor powder (except where noted) kept in suspension by bubbling O_2 through the solution. These tubes were positioned in a standard fashion in order to maintain a constant photon flux from run to run. The light source was a 450-W xenon lamp (Oriel, Stamford, Conn.) powered with an Oriel Model 6242 arc lamp power supply.

Polarographic analysis was carried out with a PAR Model 170 electrochemistry system (Princeton Applied Research, Princeton, N.J.) at a dropping mercury electrode utilizing a PAR 172 drop knocker.

Unreacted CN^- was determined by potentiometric titration with $AgNO_3$, cyanate, by spectrophotometry,[6] and SO_3^{2-}, by titration with iodine to a starch endpoint. In some determinations, such as SO_3^{2-} in the presence of CdS, the semiconductor interfered with the titration with iodine. In these cases the semiconductor powder was removed by centrifugation before the determination.

Results

Photocatalyzed Oxidation of Cyanide at TiO_2. The photocatalyzed oxidation of CN^- at TiO_2 was reported previously.[4] Since the most active form of TiO_2 was found to be the undoped anatase, all work reported here used this material. In the previous report the rate of CN^- oxidation as a function of concentration was investigated in the range of 1 mM to 0.1 M. In this range the rate of oxidation (i.e., the moles of CN^- removed per second at a given irradiation intensity) was nearly independent of the CN^- concentration. We extended these measurements to lower concentrations, since these could be of significance in the removal of CN^- from waste streams to sub parts per million levels. The number of mol of CN^- removed as a function of time from 10 mL of a solution initially containing 1 mM CN^- illuminated with a 450-W xenon lamp is shown in Figure 1. Note that the oxidation rate decreased by about one-half when the CN^- concentration fell below ca. 0.5 mM. A similar conclusion is reached by comparing the results for removal of CN^- from 1 and 3 mM solutions at TiO_2 (Table I), where significantly less CN^- was removed from the 1 mM solution than from the 3 mM solution during the same length of time, 1 h. At shorter times, when less CN^- is removed and the concentration of CN^- is higher, the rates were more nearly the same (e.g., for 60 min, 7.7

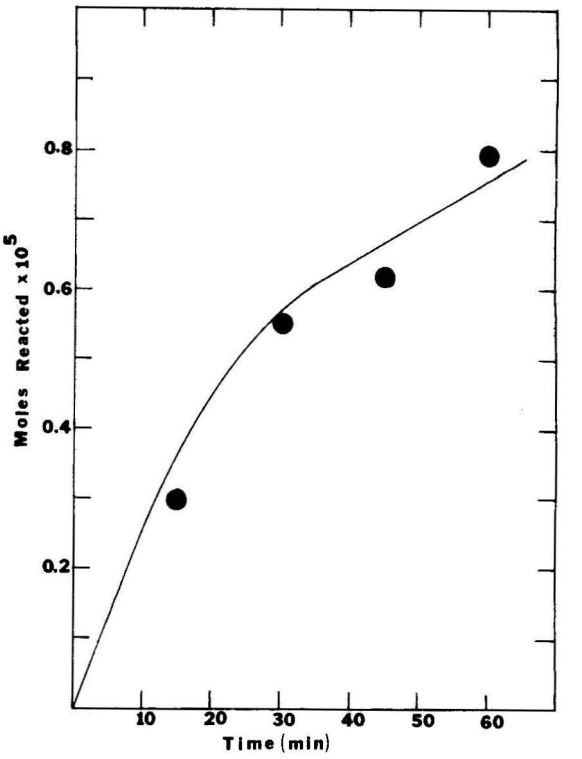

Figure 1. Number of mol of CN^- that reacted following irradiation with 450-W xenon lamp while bubbling O_2. Solution initially 1 mM CN^-. 0.1 M KOH electrolyte containing 0.1 g of anatase TiO_2. Solution volume 10 mL.

TABLE I: Removal of CN^- Under Irradiation in the Presence of Several Semiconductor Powders[a]

μmol of CN^- reacted	Initial CN^- concn, mM	illumination time, min	Semiconductor powder
7.7	1	60	TiO_2 (anatase)
6.3	1	45	TiO_2 (anatase)
5.5	1	30	TiO_2 (anatase)
9.5	1	60	ZnO
7.8	1	30	ZnO
<0.1	1	30	Fe_2O_3
<0.3	1	45	WO_3
0.6	3	60	CdS
<0.1	3	60	Fe_2O_3
15.8	3	60	TiO_2
22.5	3	60	ZnO

[a] The solution was 10 mL of 0.1 M KOH containing the indicated amount of KCN and 0.1 g of semiconductors contained in a quartz tube, illuminated with a 450-W Xe lamp with continuous O_2 bubbling.

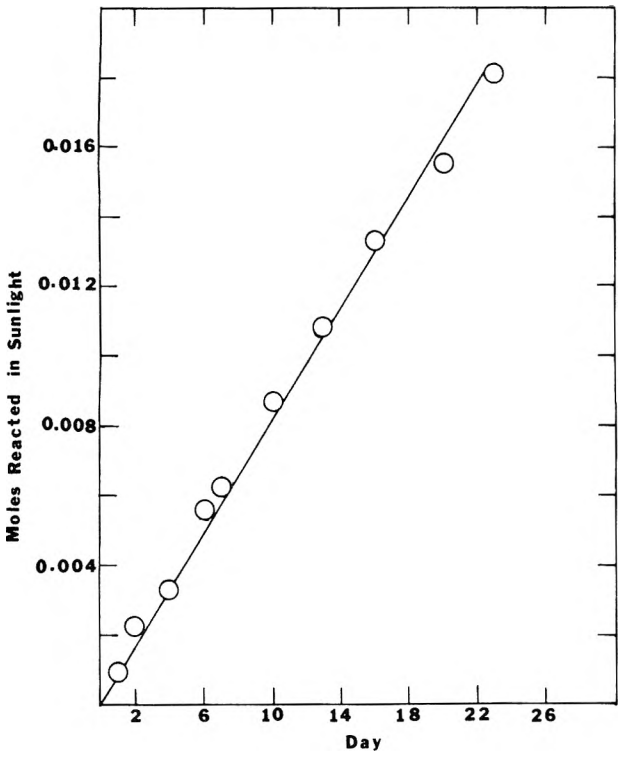

Figure 2. Number of mol of CN^- that reacted in 750 mL of a 30 mM KCN solution (0.1 M KOH) containing 7.5 g of anatase TiO_2 illuminated with unfocused sunlight. The solution was unstirred.

$\times 10^{-6}$ mol vs. 15.8×10^{-6} mol and for 30 min 5.5×10^{-6} mol vs. 7.9×10^{-6} mol removed from the 1 mM vs. 3 mM solutions, respectively). The vigorous solution agitation and relatively long times employed suggest that the decrease in rate at low CN^- concentrations cannot be attributed to difference in the rate of mass transfer of CN^- to the catalyst particles. It probably represents a decrease in efficiency of CN^- oxidation with respect to electron–hole recombination (see Discussion) at low concentrations.[8]

Product of the Oxidation of CN^- at TiO_2. In the previous investigation[4] we reported that a spot test indicated that OCN^- was one of the products of CN^- oxidation. In order to determine quantitatively the final oxidation product of CN^- at TiO_2, we measured the amount of OCN^- in a 20 mM CN^- solution containing TiO_2 following 10 h of illumination with a 450-W xenon lamp by spectrophotometry by measuring the absorbance of the copper(II)–pyridine–OCN^- complex following extraction with chloroform.[6] The analysis showed that at least 90% of the CN^- decomposed to form OCN^- as a stable final product of the oxidation.

The photocatalyzed oxidation of CN^- at TiO_2 in sunlight was also reinvestigated. In this experiment 750 mL of a 30 mM KCN solution was placed in a large crystallizing dish so that the solution depth was about 3 cm and the area about 254 cm^2. A quantity of TiO_2 (7.5 g) sufficient to cover the bottom of the crystallizing dish with a thin layer of powder was added and the top of the crystallizing dish was covered with Saran Wrap, which is transparent to UV radiation in the range where TiO has a high absorbance. The amount of CN^- removed when the crystallizing dish was placed on the roof where it was exposed to sunlight for most of the day, with the solution unstirred, is shown in Figure 2. The experiment was carried out from late September through October. About 65% of the days were clear to partly cloudy. The remainder of the days were cloudy, some with rain. The variation in the weather was such, however, that there was no significant nonlinearity in the plot due to a number of cloudy days in succession. For a control prepared in exactly the same way, but not containing TiO_2, which was placed beside the first dish, no loss of CN^- was observed. From the slope of the plot in Figure 2 the rate of CN^- removal was 3.1×10^{-6} mol day^{-1} cm^{-2} irradiated surface.

Oxidation of Cyanide at Other Semiconductors. The amount CN^- that reacted in 1 mM solutions at several other semiconductors under irradiation with the Xe lamp is given in Table I. Several experiments were attempted with $SrTiO_3$, $FeTiO_3$, $BaTiO_3$, and Eu_2O_3 as catalysts but no evidence of any reaction was found with these. Of the semiconductors listed in Table I, ZnO was the most active and only a small amount of catalytic activity was seen with both forms of CdS. No reaction of CN^- was detected with either Fe_2O_3 or WO_3. No reactions were observed with any of the powders listed in Table I in the dark, or in the absence of catalyst or oxygen. The results were independent of the amount of powder over a considerable range as long as all the light that impinged on the sample tube was absorbed (i.e., opaque solutions).

The photocatalyzed oxidation of CN^- at ZnO has been reported previously.[7] The greater activity of ZnO as compared to TiO_2 cannot be explained by absorption of more light quanta since the band gap of ZnO (3.2 eV) is greater than that of TiO_2 (3.0 eV). At TiO_2 the quantum efficiency for the oxidation of CN^- was estimated to be about 0.06.[4] A similar estimate for ZnO could not be made, since data on the quantum efficiency and current–potential curve of a single crystal ZnO electrode for the xenon lamp used in these experiments were not available. However, the quantum efficiency of the ZnO powder must be significantly larger than that of the TiO_2 powder. Efficiencies higher than 0.06 have been reported for ZnO[3] as well as for TiO_2[9] with other reducing agents. The much lower catalytic activity for the smaller band gap CdS suggests a quantum efficiency much less than 0.06 for this material.

A decrease in the rate of CN^- removal was found with ZnO just as with TiO_2 at lower concentrations of CN^- (Table I). The 60-min result for ZnO in Table I corresponds to nearly complete removal of CN^- from solution so that it cannot be compared to the 60-min TiO_2 result. However comparison of rates at shorter times or higher CN^- concentrations shows that the catalytic activity of TiO_2 is about 0.7 that of ZnO at all concentrations.

Dissolution of Semiconductor Powders. For single crystal semiconductor electrodes dissolution of the semiconductor lattice is an important reaction path in the absence and often even in the presence of reducing agents[10] when the semiconductor is illuminated with band gap radiation. The instability of the semiconductor material when illuminated or when exposed to certain chemicals even in the dark is a potential complication to the interpretation of the experimental results and in the application of these reactions in practical systems. TiO_2 is well known to be stable under a wide variety of conditions,[11] although decomposition in H_2SO_4 solutions under irradiation has been reported.[12] ZnO and CdS are known to decompose as photoanodes under some conditions, so their stability in the presence of 0.1 M KOH with and without CN^- in the dark and following illumination with the xenon lamp was investigated. These experiments were carried out by treating the ZnO or CdS with the solutions for different time periods and then removing the powders by centrifugation, deaerating, and analyzing the resulting solution for Zn or Cd using polarographic methods.[13] Some dissolution of the ZnO powder was noted after stirring with 0.1 M KOH in the dark for several minutes yielding an equilibrium concentration of ZnO_2^{2-} of about 0.2 mM. The

same concentration was found when the ZnO was illuminated.

When 5 mM KCN was present, the dark dissolution of ZnO increased and a total Zn(II) solution concentration of about 1 mM resulted. When the ZnO suspension in this solution was illuminated by the xenon lamp, no increase in the Zn(II) concentration was detected but a much larger wave attributable to H_2O_2 reduction was observed. H_2O_2 is known to be the product of oxygen reduction at the ZnO powder. Thus in these solutions ZnO is photochemically stable but is subject to some chemical attack. No chemical attack was observed for the CdS in the dark. When CdS in a CN^- solution was illuminated and the resulting solution analyzed, a H_2O_2 reduction wave, smaller than the one seen with ZnO, was observed. A shoulder on the rising portion of this wave was seen. Although the location of this wave is not the same as that found for a solution containing Cd^{2+} and CN^-, the photochemical stability of CdS in the presence of CN^- is still suspect.

Photocatalyzed Oxidation of Sulfite. A study of the photocatalytic oxidation of SO_3^{2-} in acidic solutions was undertaken to investigate the effect of location of the solution species energy levels on the reaction rate for the different semiconductor powders. The standard electrode potential, $E°$, of the $OCN^-|CN^-$ couple in base is −1.21 V vs. SCE, while that for the $SO_4^{2-}|SO_3^{2-}$ couple in acid is −0.07 V vs. SCE.[14] Taking into account the variation of the flat band potential, V_{fb}, with pH, there is at least a 0.4 V difference between the relative locations of the standard potentials of the CN^- and SO_3^{2-} systems and the location of the conduction band edges of the semiconductors. Significantly different interactions between CN^- and SO_3^{2-} with the semiconductor surfaces is also expected.

The solution conditions for the SO_3^{2-} experiments (10 mM acetic acid) were selected to mimimize solution losses of SO_3^{2-} due to spontaneous oxidation of sulfite by oxygen and to volatilization as SO_2. At this level of acid all of the semiconductors, except ZnO, were stable; some dissolution of ZnO with subsequent neutralization of the solution occurred. However, the duration of the experiments with ZnO was sufficiently short that significant spontaneous oxidation of SO_3^{2-} did not occur. Blank experiments showed significant (i.e., up to 30%) losses of SO_3^{2-} from ZnO- and CdS-containing solutions in the dark. This loss was greatest for the first few seconds following addition of catalyst powder and was larger for the CdS prepared in this laboratory, which seemed to have a larger surface area (i.e., a smaller particle size was found by scanning electron micrography) than the commercial CdS. The time dependence and apparent surface area effect suggests a possible irreversible adsorption of SO_3^{2-} onto the semiconductor surfaces, perhaps forming adsorbed SO_4^{2-}. Although this effect was not studied, all results under illumination were corrected for the relatively large initial loss of SO_3^{2-} with ZnO and CdS. No dark reaction of SO_3^{2-} with TiO_2 or Fe_2O_3 was found.

The results of the photocatalyzed oxidation of SO_3^{2-} at TiO_2, ZnO, CdS (both sources), and Fe_2O_3 is shown in Figure 3. The rates of oxidation of SO_3^{2-} at illuminated ZnO, Fe_2O_3, and CdS (lab prepared) were highest and about the same. The bending over of the curves for Fe_2O_3 and CdS presumably result from a depletion of SO_3^{2-} from the solution. This occurs for CdS after less SO_3^{2-} has photoreacted than for Fe_2O_3 because of the initial dark loss of SO_3^{2-} discussed above that occurred with CdS. The reason for the different catalytic behavior of the two CdS samples is not known. However, significantly different photon efficiencies have been noted for CdS[15] depending upon the method of preparation.

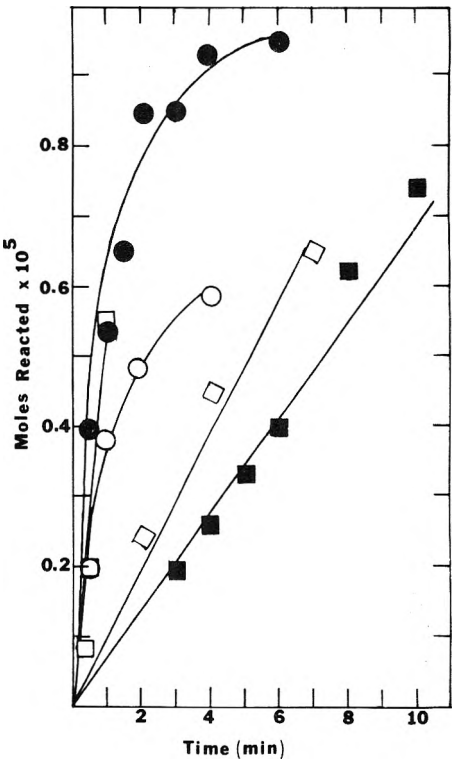

Figure 3. Number of mol of SO_3^{2-} that reacted in 10 mL of 1 mM Na_2SO_3 (also 10 mM acetic acid) following illumination with 450-W xenon lamp while bubbling O_2. Solution also contained (●) 0.1 g of Fe_2O_3 powder, (□) 0.1 g of ZnO powder, (○) 0.1 g of CdS powder prepared in this lab, (◇) 0.1 g of CdS powder, commercial, (■) 0.1 g of anatase TiO_2 powder.

The quantum efficiency for SO_3^{2-} removal with the TiO_2 can be estimated by the same method as that used with CN^{2-} to be about 0.16. The quantum efficiency of ZnO on the basis of the TiO_2 results is greater than 1. Polarographic analysis of the solutions following illumination in the presence of SO_3^{2-} showed no reduction wave for H_2O_2 for any of the semiconductors. The likely fate of any H_2O_2 would be the reaction of SO_3^{2-}.

Discussion

The mechanism for the photocatalytic oxidation of compounds by oxygen at semiconductors has been discussed.[3] Irradiation of a semiconductor with band gap light results in creation of holes in the semiconductor valence band by excitation of an electron to the conduction band. The valence band hole is scavenged by solution species before electron–hole recombination can occur within the semiconductor. Electroneutrality within the semiconductor is maintained by reduction of dissolved oxygen or other solution species by the conduction band electron. The process is repeated until the solution oxygen or reducing agents are exhausted.

Thus the process for removal of CN^- can be represented as follows:

$$(TiO_2) + 2h\nu \rightarrow (TiO_2) + 2p^+ + 2e^- \quad (1)$$

$$CN^- + 2OH^- + 2p^+ \rightarrow OCN^- + H_2O \quad (2)$$

$$O_2 + 2e^- + 2H_2O \rightarrow H_2O_2 + 2OH^- \quad (3a)$$

or

$$^1/_2O_2 + 2e^- + H_2O \rightarrow 2OH^- \quad (3b)$$

The rate of the photocatalysis is determined by several factors. Among these are the competitive rates of recombination of photogenerated electron–hole pairs within

the semiconductor and the scavenging of holes and electrons by oxygen and reducing agents such as CN^- and SO_3^{2-}.[1] Electron–hole recombination will depend on the degree of band bending within the semiconductor and the presence of any electron and hole traps at the particle surface and the space-charge region. Since the degree of band bending is expected to be less in the individual particles of a powder than can be induced in a semiconductor electrode, the separation of electrons and holes should be less efficient in the powder and recombination should play a more important role than in a semiconductor electrode. Accordingly, the quantum efficiencies should be considerably less than the near unity efficiencies seen with electrodes held at sufficiently positive potentials.[2a,11,16] The presence of surface states at energies within the band gap region can either decrease or increase the lifetime of electrons and holes depending upon whether these energy levels function as efficient recombination centers or as surface traps which prolong the life of a hole and an electron. The difference in photocatalytic activity between the anatase and rutile forms of TiO_2 was in part explained by possible trapping of electrons in the anatase form at the surface where they can more easily react with oxygen.[4] The existence of these levels seem well established by electroluminescence and other experiments.[17]

If H_2O_2 is produced and can react with a reductant in solution, more efficient removal of the reductant will be observed. Thus, for example, for the photocatalyzed oxidation of SO_3^{2-} at ZnO two modes of SO_3^{2-} removal are possible: direct oxidation of sulfite at the illuminated part of the particle and reaction of SO_3^{2-} with H_2O_2 produced by reduction of O_2 in the dark reaction. The overall reaction scheme (without implying mechanistic details) is

$$(ZnO) + 2h\nu \rightarrow (ZnO) + 2p^+ + 2e^- \quad (4)$$

$$SO_3^{2-} + 2p^+ + H_2O \rightarrow SO_4^{2-} + 2H^+ \quad (5)$$

$$O_2 + 2e^- + 2H^+ \rightarrow H_2O_2 \quad (6)$$

$$H_2O_2 + SO_3^{2-} \rightarrow SO_4^{2-} + H_2O \quad (7)$$

$$2h\nu + 2SO_3^{2-} + O_2 \rightarrow 2SO_4^{2-} \quad (8)$$

This could explain the anomalously high quantum efficiency (calculated by assuming only oxidation by holes was the cause of SO_3^{2-} removal) observed with ZnO.

The photocatalytic behavior displayed by semiconductors could be of technological significance. Thus processes related to those observed here may be responsible for the degradation and "chalking" observed in TiO_2- and ZnO-based paints.[18] The addition of the proper semiconductor powder to a waste stream could be used to purify it of selected impurities by using solar energy irradiation. Similarly, the same type of processes could be used for synthetic purposes. Of the semiconductors investigated here, TiO_2 is the most satisfactory from the standpoint of its chemical and photochemical stability under a wide variety of conditions. The biggest disadvantage of TiO_2 is that it absorbs such a small fraction of the solar spectrum. However, even with its low absorbance and low absolute quantum efficiency (0.06 for CN^-), TiO_2 may be worth considering in industrial processes. We have previously mentioned the common industrial methods for removing cyanide from industrial waste streams and the high capital and operating costs of these methods.[4] One method gaining some popularity is oxidation of CN^- in an electrochemical reactor.[19] If one assumes a typical reactor is capable of processing 81 000 mol of CN^- (7.8 tons of NaCN) per year, the same amount of cyanide could be processed by a TiO_2 solar reactor 85 m on a side and 3 cm deep containing sufficient TiO_2 to just cover the bottom of the reactor, assuming the rate of cyanide oxidation determined in Figure 2 as an average.

Acknowledgment. The support of this research by the Robert A. Welch Foundation and the National Science Foundation (MPS 74-23210) is gratefully acknowledged.

References and Notes

(1) (a) H. Gerischer, *J. Electroanal. Chem.*, **58**, 263 (1975); (b) J. Manassen, D. Cahen, and G. Hodes, *Nature (London)*, **263**, 97 (1976); (c) M. D. Archer, *J. Appl. Electrochem.*, **5**, 17 (1975), and references therein.
(2) (a) D. Laser and A. J. Bard, *J. Electrochem. Soc.*, **123**, 1027 (1976); (b) K. L. Hardee and A. J. Bard, *ibid.*, **124**, 215 (1977).
(3) T. Freund and W. P. Gomes, *Catal. Rev.*, **3**, 1 (1969).
(4) S. N. Frank and A. J. Bard, *J. Am. Chem. Soc.*, **99**, 303 (1977).
(5) M. S. Wrighton, P. T. Wolczanski, and A. B. Ellis, *J. Solid State Chem.*, in press.
(6) E. L. Martin and G. McClelland, *Anal. Chem.*, **23**, 1519 (1951).
(7) M. C. Markham, J. C. Kuriacose, J. DeMarco, and C. Giaquinto, *J. Phys. Chem.*, **66**, 932 (1962).
(8) S. N. Frank and A. J. Bard, submitted for publication.
(9) R. B. Cundall, R. Rudham, and M. S. Salim, *J. Chem. Soc., Faraday Trans. 1*, 1642 (1976).
(10) H. Gerischer and W. Mindt, *Electrochim. Acta*, **13**, 132 (1968).
(11) M. S. Wrighton, D. S. Ginley, P. T. Wolczanski, A. B. Ellis, D. J. Morse, and A. Linz, *Proc. Natl. Acad. Sci. U.S.A.*, **72**, 1518 (1975).
(12) L. A. Harris and R. H. Wilson, *J. Electrochem. Soc.*, **123**, 1010 (1976).
(13) I. M. Kolthoff and J. J. Lingane, "Polarography", 2nd ed, Interscience, New York, N.Y., 1952.
(14) W. M. Latimer, "Oxidation Potentials", 2nd ed, Prentice-Hall, Englewood Cliffs, N.J., 1952.
(15) R. E. Stephens, B. Ke, and D. Trivich, *J. Phys. Chem.*, **59**, 966 (1955).
(16) T. Ohnishi, Y. Nakato, and H. Tsubomura, *Ber. Bunsenges. Phys. Chem.*, **76**, 523 (1975).
(17) (a) B. Pettinger, H. R. Schöppel, and H. Gerischer, *Ber. Bunsenges. Phys. Chem.*, **80**, 849 (1976); (b) R. Noufi, P. Kohl, S. N. Frank, and A. J. Bard, manuscript in preparation; (c) S. N. Frank and A. J. Bard, *J. Am. Chem. Soc.*, **97**, 7427 (1975).
(18) W. F. Sullivan, *Prog. Org. Coat.*, **1**, 157 (1972).
(19) Q. D. Mehrkam, *Met. Prog.*, **108**, 103 (1975).

Determination of Equilibrium Constants for Electron Donor–Acceptor Complexes by Resonance Raman Spectroscopy[1]

Kirk H. Michaelian,[2] Klaus E. Rieckhoff, and Eva-Maria Voigt*

Departments of Chemistry and Physics, Simon Fraser University, Burnaby, British Columbia, Canada V5A 1S6 *(Received August 9, 1976; Revised Manuscript Received May 16, 1977)*

Publication costs assisted by the National Research Council of Canada

We describe a new method for the measurement of equilibrium constants for electron donor–acceptor complexes in solution which makes quantitative use of resonance Raman intensity effects in one of the components of the complex. This procedure was evaluated through its application to tetracyanoethylene complexes having methylbenzenes and methoxybenzenes as electron donors. The equilibrium constants calculated from resonance Raman intensities agree well with published data obtained by previously established methods, where comparative data are available, thus confirming the usefulness of the new method.

Introduction

We present in this paper a new method for the determination of equilibrium constants (K_c^{AD}) for the formation of electron donor–acceptor (EDA) complexes in solution. In this technique, relative intensities in the Raman spectra of EDA complexes are used to calculate the degree of complexation of one of the components in solutions where initial concentrations are known; once the intensity changes with complexation have been determined for the component under consideration, each solution which is analyzed yields a value for K_c^{AD}.

The change in the relative intensities of the C=C and C≡N stretching bands in the Raman spectrum of tetracyanoethylene (TCNE) on complexation with aromatic electron donors,[3,4] which is a consequence of preresonance or resonance Raman (RR) scattering,[5,6] arises from the proximity of the Raman excitation frequencies to the charge transfer absorption bands. TCNE EDA complexes having methyl or methoxy substituted benzenes as electron donors display large intensity changes in the TCNE $\nu_{C=C}$ and $\nu_{C\equiv N}$ bands with complexation when an argon laser is used for excitation; these bands are also red-shifted up to 20 cm^{-1} with respect to their positions in the spectrum of uncomplexed TCNE.[3] Since the intensity changes are more easily related to the degree of complexation of TCNE, they were chosen as the basis for the Raman determination of K_c^{AD}. TCNE complexes which have comparatively small equilibrium constants and show smaller intensity effects upon complexation (e.g., benzene–TCNE) were not examined, since the uncertainties in the K_c^{AD} for such complexes as calculated from the Raman spectra are of the same order of magnitude as the equilibrium constants themselves.

The principal solvent used for the Raman determination of K_c^{AD} was CH_2Cl_2; the reasons for selection of this solvent are given in the Results section. Other solvents used for the Raman determination of K_c^{AD}, dibromomethane and 1,2-dichloroethane, were chosen for similar reasons. Equilibrium constants for TCNE complexes in nonpolar solvents were not included in the present study, because of circumstances described below.

Experimental Section

Raman spectra were measured in the $\nu_{C=C}$ (about 1560 cm^{-1}) and $\nu_{C\equiv N}$ (about 2230 cm^{-1}) regions for the TCNE EDA complexes in solution; all measurements were made at room temperature. The argon ion laser lines at 457.9, 476.5, 488.0, and 514.5 nm were used for excitation of the spectra. Excitation power was kept below 250 mW to avoid heating the solutions and affecting the equilibrium constants. Experimental equipment was the same as previously described.[6]

Solutions which were used for K_c^{AD} determination had a total TCNE concentration of about 0.05 M. The concentration of *complexed* TCNE was generally between 5×10^{-4} and 5×10^{-3} M, i.e., about 1–10% of the acceptor was complexed in each solution. This meant that the intensity ratio of the $\nu_{C=C}$ band with respect to the $\nu_{C\equiv N}$ band for each sample was intermediate between the complexed value and the uncomplexed value, and could be used to calculate the fraction of TCNE present which was complexed (see below). Solutions were prepared with concentrations [D] ~ [A] in order to keep the occurrence of termolecular complexes to a minimum.

The intensity ratios which appear in eq 2 were obtained as follows: I_{2u}/I_{1u} came from the spectrum of uncomplexed TCNE, the subscripts 1 and 2 referring to the $\nu_{C=C}$ and $\nu_{C\equiv N}$ vibrations, respectively. I_{2c}/I_{1c} was obtained for each complex by examining solutions which contained a large excess of donor, and thus had most of the TCNE complexed; I_{2c}/I_{1c} in general depends on donor and on excitation wavelength, so it was measured with all of the above-mentioned laser lines for every donor used. The other ratios were calculated as the products $I_{2u}/I_{1c} = (I_{2u}/I_{1u})(I_{1u}/I_{1c})$ and $I_{2c}/I_{1u} = (I_{2c}/I_{1c})(I_{1c}/I_{1u})$, where I_{1c}/I_{1u} is the relative increase in $\nu_{C=C}$ intensity on complexation. This intensity increase was determined by comparison of the $\nu_{C=C}$ intensity with that of a strong solvent band for a TCNE solution before and after the addition of sufficient donor to cause complexation of virtually all of the TCNE present. This use of a solvent band as internal standard compensated for the loss in overall intensity resulting from the absorption of the excitation light by the EDA complex formed in this process. The intensities of the bands were measured as peak heights. Representative data of measured and calculated intensity ratios and their dependence on excitation wavelength described above are shown in Table I.

Results

The complexation of TCNE results in an increase in the intensity ratio $I(\nu_{C=C})/I(\nu_{C\equiv N})$ from the value for uncomplexed TCNE (about 0.5) to a larger value characteristic of the complex and of the excitation frequency

TABLE I: Intensity Ratios Used for the Calculation of K_c^{AD} for TCNE EDA Complexes in CH_2Cl_2 Solutions[a,b]

Donor	Excitation wavelength, nm	I_{2c}/I_{1c}	I_{2u}/I_{1c}	I_{2c}/I_{1u}	I_{1c}/I_{1u}
Durene	488.0	0.26	0.031	15	59
	514.5	0.23	0.019	22	96
Isodurene	488.0	0.33	0.043	14	43
	514.5	0.30	0.032	17	58
Pentamethylbenzene	488.0	0.31	0.016	36	115
	514.5	0.32	0.010	61	188
Hexamethylbenzene	488.0	0.41	0.012	62	150
	514.5	0.41	0.0068	110	275

[a] Uncertainties in the intensity ratios are less than 10% of their magnitudes. [b] Subscripts 1 and 2 signify TCNE $\nu_{C=C}$ and a_g $\nu_{C\equiv N}$ bands, respectively; c and u denote complexed and uncomplexed TCNE, respectively.

used.[3,6] In a solution where a small fraction y of the TCNE is complexed, the $\nu_{C=C}$ and $\nu_{C\equiv N}$ intensities originate both from complexed and from uncomplexed TCNE and an intensity ratio somewhere between the two limiting values occurs. This fraction is given by the ratio $y = [AD]/[A]_0$, where [AD] is the equilibrium concentration of the complex and $[A]_0$ is the initial acceptor concentration. For the TCNE $\nu_{C=C}$ and a_g $\nu_{C\equiv N}$ intensities we thus have

$$I_1 = yI_{1c} + (1 - y)I_{1u} \tag{1a}$$

$$I_2 = yI_{2c} + (1 - y)I_{2u} \tag{1b}$$

$$\frac{I_1}{I_2} = \frac{y}{y(I_{2c}/I_{1c}) + (1 - y)(I_{2u}/I_{1c})} + \frac{1 - y}{y(I_{2c}/I_{1u}) + (1 - y)(I_{2u}/I_{1u})} \tag{2}$$

where I_{1c} and I_{2c} are intensities per mole of complexed TCNE, and I_{1u} and I_{2u} are intensities per mole of uncomplexed TCNE.

The equilibrium constant for the formation of the complex according to the relation D + A $\rightleftharpoons$ AD can be written

$$K_c^{AD} = \frac{[AD]}{([D]_0 - [AD])([A]_0 - [AD])} = \frac{y}{([D]_0 - y[A]_0)(1 - y)} \tag{3}$$

where $[D]_0$ is the initial donor concentration. When y is much less than 1, eq 3 reduces to $y \approx K_c^{AD}[D]_0$.

The solvents used for Raman studies of EDA complexes must be chosen so that they satisfy certain criteria. The most important of these are the following: that the solvent dissolve both of the components of the complex in sufficient concentration that the Raman bands of interest are of reasonable intensity over a range of concentrations; that the solvent does not have Raman bands which interfere with the component bands to be analyzed; and finally; that the solvent does not interact strongly with either of the components. Since dichloromethane meets all the above criteria, it was chosen as the principal solvent for this investigation; moreover, equilibrium constants determined by other methods have been reported for many TCNE EDA complexes in CH_2Cl_2, so that a comparison of some of the Raman results with other published results is possible.

In Figure 1 the dependence of I_1/I_2 on $[D]_0/[A]_0$ for several different TCNE EDA complexes is shown. The figure shows that for low donor concentrations I_1/I_2 increases linearly with relative concentration, which follows from eq 2 and 3 when $y \ll 1$. The figure also illustrates the expected dependence of I_1/I_2 on the magnitudes of K_c^{AD} and of I_{1c}/I_{1u}; for mesitylene–TCNE, I_{1c}/I_{1u} is greater with 514.5-nm excitation than with 488.0-nm excitation and the slope of I_1/I_2 vs. $[D]_0/[A]_0$ is steeper for the former case.

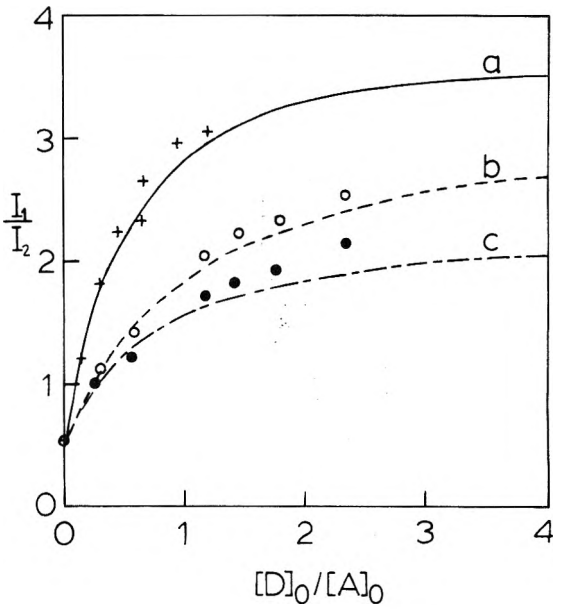

Figure 1. Intensity ratio of TCNE $\nu_{C=C}$ and $\nu_{C\equiv N}$ bands as a function of relative donor concentration for durene (+) and mesitylene (O and ●). The uncertainty in the observed I_1/I_2 is ±0.2 or less. The excitation wavelength was 514.5 nm (+ and O) or 488.0 nm (●). The curves show I_1/I_2 calculated from eq 2 and 3 for the following conditions: (a) $K_c^{AD} = 3.3$, excitation at 514.5 nm; (b) $K_c^{AD} = 1.6$, excitation at 514.5 nm; (c) $K_c^{AD} = 1.6$, excitation at 488.0 nm.

TABLE II: Equilibrium Constants for TCNE EDA Complexes in CH_2Cl_2 Solutions at Room Temperature (~21 °C)

Donor	K_c^{AD}, M^{-1}	I_{1c}/I_{1u}[a,b]
o-Xylene	0.42 ± 0.15	75 ± 25
m-Xylene	0.50 ± 0.18	75 ± 25
p-Xylene	0.52 ± 0.19	75 ± 25
Mesitylene	1.6 ± 0.6	75 ± 25
Durene	3.3 ± 0.4	96
Isodurene	4.7 ± 0.7	58
Pentamethylbenzene	7.4 ± 0.6	188
Hexamethylbenzene	17 ± 2	275
Anisole	0.52 ± 0.14	20 ± 5
o-Dimethoxybenzene	1.0 ± 0.3	12 ± 3
m-Dimethoxybenzene	1.0 ± 0.3	30 ± 10
p-Dimethoxybenzene	1.0 ± 0.3	9 ± 3
1,2,3-Trimethoxybenzene	0.84 ± 0.30	30 ± 10
1,2,4-Trimethoxybenzene	1.2 ± 0.3	12 ± 3
1,3,5-Trimethoxybenzene	1.3 ± 0.3	45 ± 10

[a] Intensity increase of the TCNE $\nu_{C=C}$ band on complexation; excitation wavelength 514.5 nm. [b] Values quoted with uncertainties are estimated (see text).

TABLE III: Equilibrium Constants for TCNE EDA Complexes in Solvents Other Than CH_2Cl_2 at Room Temperature (~21 °C)

Donor	Solvent	K_c^{AD}, M^{-1}	I_{1c}/I_{1u}[a]
p-Dimethoxybenzene	CH_2Br_2	1.0 ± 0.3	9 ± 3[b]
Hexamethylbenzene	CH_2Br_2	23 ± 2	206
Hexamethylbenzene	$C_2H_4Cl_2$	19 ± 3	153

[a] Intensity increase of the TCNE $\nu_{C=C}$ band on complexation; excitation wavelength 514.5 nm. [b] Estimated value (see text).

The K_c^{AD} calculated from eq 2 and 3 and from such data as shown in Table I are summarized for the TCNE complexes in CH_2Cl_2 solutions in Table II and for the CH_2Br_2 and dichloroethane solutions in Table III. The comparison of these results with previously published K_c^{AD} is described in the Discussion section. It should be noted that the equilibrium constant for the CH_2Cl_2–TCNE EDA complex[7,8] is less than about 0.2 M^{-1}, i.e., it is considerably smaller than any of the K_c^{AD} in Table II.

The equilibrium constants in Table II are based on I_1/I_2 measured at several excitation wavelengths between 457.9 and 514.5 nm. Since I_1/I_2 for a solution in general depends on excitation wavelength, each intensity ratio was analyzed by substituting into eq 2 constants applicable for that laser line and donor. The results showed that for a particular solution the value of y was independent of excitation wavelength. Therefore for each solution, the average y obtained using data for all of the excitation wavelengths was substituted into eq 3 in order to calculate K_c^{AD}. K_c^{AD} was evaluated in this manner for a number of solutions (5 to 15) of various concentrations for each complex, averaged for that complex, and entered in Table II. Only one or two excitation wavelengths were used to calculate the K_c^{AD} summarized in Table III, since the results for the CH_2Cl_2 solutions showed that by using a wider range of laser lines no further information is obtained.

In addition to the calculated equilibrium constants, Tables II and III contain the $\nu_{C=C}$ intensity enhancements on complexation, as observed with 514.5-nm excitation. From eq 2 it can be seen that the determination of K_c^{AD} using Raman intensity ratios is only as accurate as are the measured I_{1c}/I_{1u}. Thus for completeness, both K_c^{AD} and I_{1c}/I_{1u} are entered in the tables. Comparison of these ratios with the preresonance Raman intensity enhancements of TCNE EDA complexes[5] shows that the RR intensity increases are in most cases an order of magnitude larger than the preresonance Raman ratios. For this reason, the K_c^{AD} were obtained only for TCNE complexes in which the RR effect occurs with argon laser excitation.

One limitation of the intensity ratio method is the inaccessibility of accurate I_{1c}/I_{1u} ratios for complexes having small K_c^{AD}. For such complexes the addition of even a large excess of the donor to a TCNE solution does not bring about the complexation of most of the TCNE. Attempts to measure I_{1c}/I_{1u} for these complexes yielded artifically low results, because the concentration of TCNE responsible for the band with intensity I_{1c} is less than the concentration which produces intensity I_{1u}. (This does not occur for complexes with higher K_c^{AD}, where an excess of donor ensures the complexation of virtually all of the TCNE.) If a large amount of donor is added to a solution in an attempt to complex all of the TCNE, a concentration gradient sometimes develops within the cuvet, further complicating the results.

Because of these considerations, the I_{1c}/I_{1u} observed for the weaker complexes are used only as a basis for the estimate of the true ratios. The I_{1c}/I_{1u} in Tables II and III which are estimated are those for which uncertainties are quoted. For example, mesitylene or one of the xylenes produces an intensification in the TCNE $\nu_{C=C}$ band by a factor between perhaps 50 and 100 when added to a TCNE solution; for one of these complexes, I_{1c}/I_{1u} is therefore about 75 ± 25. These fairly wide limits were derived from the results of a number of attempts to measure the ratios for these complexes, and from the estimate that about 0.3 to 0.7 of the acceptor was actually complexed in each solution. Obviously, the K_c^{AD} calculated using estimated I_{1c}/I_{1u} are not as reliable as those calculated for complexes in which I_{1c}/I_{1u} is known more accurately.

TABLE IV: Comparison of Equilibrium Constants for TCNE EDA Complexes in CH_2Cl_2 Solutions Obtained by Different Methods

Donor	Raman K_c^{AD},[a] M^{-1}	Absorption K_c^{AD}, M^{-1}
o-Xylene	0.42 ± 0.15	0.45[b]
m-Xylene	0.50 ± 0.18	0.38[b]
p-Xylene	0.52 ± 0.19	0.49[b]
Mesitylene	1.6 ± 0.6	1.1;[b] 1.5[c]
Durene	3.3 ± 0.4	3.4[b]
Pentamethylbenzene	7.4 ± 0.6	7.9[b]
Hexamethylbenzene	17 ± 2	16.8;[b] 21.6[c]
Anisole	0.52 ± 0.14	0.28[d]

[a] Room temperature (~21 °C). [b] Reference 7; based on data in ref 8, measured at 22 °C. [c] Reference 7; measured at 25 °C. [d] Calculated from the K_x^{AD} value in ref 8, measured at 22 °C.

The Raman method of determining K_c^{AD} of EDA complexes was successfully applied to TCNE complexes in the solvents CH_2Cl_2, CH_2Br_2, and dichloroethane (Tables II and III). Readily available conventional nonpolar solvents could not be used, partly because of the limited solubility of TCNE in these solvents, and partly because of interfering solvent bands. Solvents such as cyclohexane and CCl_4 were tried, but in order to dissolve sufficient TCNE in one of them to produce a reliable Raman spectrum, an excess of the electron donor had to be added. In that case, however, the resulting solution was not suitable for equilibrium constant determination by the Raman intensity ratio method, since it had much more than 1/10 of the dissolved TCNE complexed (see above). Because of this, the Raman method was not applied to TCNE complexes in such solvents, despite the desirability of such data for comparison with results in solvents such as CH_2Cl_2.

Discussion

In Table IV, the K_c^{AD} for CH_2Cl_2 solutions as determined from the Raman intensity ratios are compared with published K_c^{AD} obtained by absorption spectroscopy. The results of the Raman spectra agree very well with those of the absorption method, showing that the application of Raman spectroscopy for the measurement of K_c^{AD} of EDA complexes is viable. For solvents other than CH_2Cl_2, the hexamethylbenzene–TCNE K_c^{AD} determined from the Raman spectra (Table III) are equal, within experimental uncertainty, to the values obtained from absorption spectra.[9,10] The results of the Raman *and* absorption methods for obtaining K_c^{AD} are greatly at variance with those derived from a calorimetric method.[11]

The equilibrium constants calculated from the Raman spectra, for solutions with [D] ~ [A] (column 2, Table IV) agree well with those obtained from absorption spectra for solutions have [D] ≫ [A] (column 3). Since only 1:1 complexes are likely to occur when the donor concentration is comparable to that of the acceptor and the overall concentration is low, the consistency of these results affirms the assumption that only 1:1 complexes occur under the condition [D] ≫ [A] for the complexes studied. Thus we conclude that the K_c^{AD} calculated from the Raman intensity ratios are the true equilibrium constants for the 1:1 complexes.

Further comment on the accuracy of the K_c^{AD} determined from Raman spectra is possible in view of the results of NMR measurements of K_c^{AD} for π–π EDA complexes using, however, acceptors other than TCNE. The K_c^{AD} calculated from absorption spectra for solutions with [D] = [A] agree well with the NMR results, which are inde-

pendent of the relative concentration [D]/[A].[12] The lack of relative concentration dependence in the NMR data implies that the same kind of complex is detected in each solution; by inference, that is the 1:1 complex. This indicates that the K_c^{AD} determined by absorption spectroscopy for solutions with [D] = [A] are accurate equilibrium constants for the formation of 1:1 complexes. Since the absorption and Raman results tend to agree, the Raman intensity ratio method is thus supported by the NMR method as well.

Since the Raman method for K_c^{AD} determination was not applied to TCNE complexes in nonpolar solvents (see above), we are unable to extend further the comparison of Raman results with published K_c^{AD}. On the basis of the good results which we obtained for the TCNE complexes in CH_2Cl_2 and similar solvents, we expect the Raman intensity ratio method to also prove successful for EDA complexes in nonpolar solvents. A verification of this prediction should be the next test of the Raman method for measuring equilibrium constants.

References and Notes

(1) This research was supported by grants from the National Research Council of Canada to K. E. Rieckhoff and E. M. Voigt.
(2) Present address: Department of Chemistry. University of Toronto, Toronto, Ontario, Canada M5S 1A1.
(3) K. H. Michaelian, K. E. Rieckhoff, and E. M. Voigt, *Chem. Phys. Lett.*, **23**, 5 (1973).
(4) The bands in the Raman spectra of TCNE EDA complexes which in ref 3 were described as shifted or new donor bands have recently been found to be experimental artifacts.
(5) K. H. Michaelian, K. E. Rieckhoff, and E. M. Voigt, *Chem. Phys. Lett.*, **30**, 480 (1975).
(6) K. H. Michaelian, K. E. Rieckhoff, and E. M. Voigt, *Proc. Natl. Acad. Sci. U.S.A.*, **72**, 4196 (1975).
(7) R. X. Ewall and A. J. Sonnessa, *J. Am. Chem. Soc.*, **92**, 2845 (1970).
(8) R. E. Merrifield and W. D. Phillips, *J. Am. Chem. Soc.*, **80**, 2778 (1958).
(9) P. J. Trotter and D. A. Yphantis, *J. Phys. Chem.*, **74**, 1399 (1970).
(10) R. Foster and I. B. C. Matheson, *Spectrochim. Acta, Part A*, **23**, 2037 (1967).
(11) W. C. Herndon, J. Feuer, and R. E. Mitchell, *Chem. Commun.*, 435 (1971).
(12) R. Foster, "Organic Charge Transfer Complexes", Academic Press, London, 1969.

Raman Measurements of Temperature Effects on Self-Association in Glycerol

Jerry E. Solomon

Department of Physics, San Diego State University, San Diego, California 92182

(Received March 11, 1977)

Publication costs assisted by the Department of Physics, San Diego State University

The effect of temperature on intermolecular hydrogen bonding in glycerol is studied by use of the OH Raman stretching band. The value of $\partial\nu_s/\partial T$ for glycerol is found to be 3.4 ± 0.3 cm^{-1}/K as compared to 0.63 ± 0.08 cm^{-1}/K for methanol. The results are discussed in terms of the functionality of various alcohols and their relative glass-forming tendencies. An interpretation of the results is presented based on the "configurational entropy" theory of glass formation.

I. Introduction

The glycerol system represents an important class of hydrogen bonded glass formers, and we are currently carrying out measurements aimed at elucidating the role of hydrogen bonding in the glass formation process. Although the monofunctional alcohols such as methanol and ethanol form glasses fairly readily, there appears to be a significant difference in the glass-forming tendency of these simple alcohols and polyfunctional alcohols such as glycerol. In fact, glycerol forms a glass so readily that it is extremely difficult to crystallize this substance. As is well known,[1,2] the OH stretching band, which appears in the infrared and Raman spectra of systems containing OH groups, is an extremely useful indicator in studies of hydrogen bonding, and our current studies utilize measurements of the shift in the peak of the OH stretching band, ν_s, as a function of temperature to probe the role of hydrogen bonding in glass formation. In this article we wish to report some early results which we feel lend support to the notion that there are readily measurable quantitative differences in the glass-forming tendencies of mono-, di-, and polyfunctional alcohols.[3]

II. Experimental Section

The measurements reported here were made in the standard 90° Raman scattering geometry using a Spectra-Physics argon-ion laser as the excitation source, and a Spex 1704 1-m monochromator. Both photon-counting and dc anode current measurements with an ITT FW130 photomultiplier tube were used in detecting the Raman signals. The samples are contained in a 1-cm diameter tubing cross which is fused inside a dewar and cooled by flowing cold nitrogen gas. The glycerol samples were prepared by filtering and distillation to remove particulates and H_2O. The sample temperature was measured using a copper–constantan thermocouple and a digital voltmeter. The temperature measurement accuracy of the data presented here is ±2 K. The Raman spectra obtained with this system were wavelength calibrated using a low-pressure mercury discharge source, and wavenumber calibrated against standard spectra of spectroquality dimethyl sulfoxide (DMSO), CCl_4, and benzene.

III. Results and Discussion

The results which we wish to report are shown in Figure 1, where we have plotted ν_s as a function of temperature for both glycerol and methanol. Although infrared results for methanol have been reported previously,[4] we felt it necessary to have a comparison based on samples run in the same system under the same conditions. The striking difference in behavior of the two systems is readily apparent from the figure. From our data we find the temperature dependence of ν_s, $\partial\nu_s/\partial T$, to be 0.63 ± 0.08 cm^{-1}/K for methanol and 3.4 ± 0.3 cm^{-1}/K for glycerol. In contrast with these results, Fishman and Chen[5] find

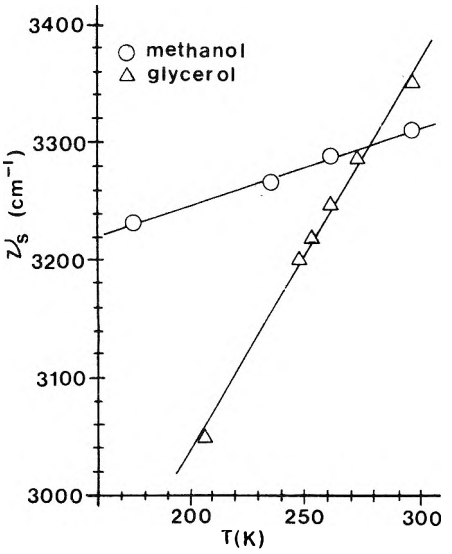

Figure 1. Temperature dependence of ν_s for methanol and glycerol.

very little difference between $\partial\nu/\partial T$ for the monofunctional alcohols and series of difunctional alcohols, butanediols, which they studied. These authors report $\partial\nu_s/\partial T$ values for the butanediols in the range of 0.73 to 0.8 cm^{-1}/K.

The lack of a significant difference between the temperature dependence of ν_s in monofunctional alcohols as compared to the butanediols can be understood physically in terms of conformation. The conformations of the butanediols studied by Fishman and Chen all involve intramolecular hydrogen bonded rings, and thus the number of effective donor/acceptor sites per molecule available for intermolecular association is significantly reduced. Therefore, in effect, the butanediols look like monofunctional alcohols from the standpoint of their ability to form intermolecular hydrogen bonds. Since the temperature sensitivity of ν_s depends on the number and complexity of intermolecular hydrogen bond sites available to the system,[1,2] it is not too surprising that $\partial\nu_s/\partial T$ is about the same in butanediols as it is in monofunctional alcohols such as methanol and ethanol. In the case of glycerol there is some evidence from NMR data[6] to suggest that the molecule has a conformation involving a six-membered hydrogen bonded ring. However, even if this ring conformation is the most favorable one for glycerol, the system contains three OH groups and thus there are still two donor and two acceptor sites per molecule which are free to participate in intermolecular hydrogen bonding. This availability of donor/acceptor sites leads to the possibility of forming large and complex polymer groups in the pure liquid. We believe that it is this ability to form large polymer groups that gives rise to the large temperature dependence of ν_s in the glycerol system.

If we adopt the view that the temperature dependence of ν_s in the pure liquid is attributable to the formation of different polymeric species,[1] then the results and discussion above can be correlated with the bulk glass-forming tendencies of self-associated liquids. In those alcohols that are *effectively* monofunctional the degree and complexity of polymerization is limited and thus the number of bond rearrangements required for crystal growth are fewer than for truly polyfunctional systems which are capable of a much higher degree and complexity of polymerization. Furthermore, the interpretation that increasing values of $\partial\nu_s/\partial T$ represent an increase in the degree of polymerization present in the system can be justified in terms of the "configurational entropy" theory of glass formation which has been developed principally by Gibbs, et al.[7] Indeed, it is the growth of polymerization with falling temperature that is responsible for the decrease in configurational entropy attendent to the glass transition.

We are presently extending our study of the glycerol system to include a careful series of measurements of ν_s vs. temperature in the region of the glass transition temperature. We are also investigating the effect of cooling rate on the observed values for $\partial\nu_s/\partial T$, an effect one would expect to be present based on the kinetics of the supercooled system. We are hopeful that this study, and others like it, will aid in our quantitative understanding of the glass formation process.

Acknowledgment. The author thanks Professor Lowell J. Burnett for stimulating discussions regarding various aspects of this work, and Mr. Bruce Rising for assistance in taking some of the data.

References and Notes

(1) G. C. Pimentel and A. L. McClellan, "The Hydrogen Bond", W. H. Freeman, San Francisco, Calif., 1960, Chapters 3 and 5.
(2) M. D. Joesten and L. J. Schaad, "Hydrogen Bonding", Marcel Dekker, New York, N.Y., 1974.
(3) D. Turnbull and M. H. Cohen in "Modern Aspects of the Vitreous State", J. D. Mackenzie, Ed., Butterworths, London, 1960.
(4) U. Liddel and E. D. Becker, *Spectrochim. Acta*, **10**, 70 (1957).
(5) E. Fishman and T. L. Chen, *Spectrochim. Acta, Part A*, **25**, 1231 (1969).
(6) L. J. Burnett and S. B. W. Roeder, *J. Chem. Phys.*, **60**, 2420 (1974).
(7) J. H. Gibbs in "Modern Aspects of the Vitreous State", J. D. Mackenzie, Ed., Butterworths, London, 1960; J. M. Gordon, J. H. Gibbs, and P. D. Fleming, *J. Chem. Phys.*, **65**, 2771 (1976).

Microwave Study of Perchlorylbenzene

Walther Caminati, Rinaldo Cervellati, and Bruno Lunelli*

Istituto "G. Ciamician", Università di Bologna, I-40126 Bologna, Italy and Laboratorio di Spettroscopia Molecolare del C.N.R., I-40126 Bologna, Italy *(Received February 2, 1977)*

The study of the spectra of $C_6H_5{}^{35}ClO_3$, $C_6H_5{}^{37}ClO_3$, $C_6D_5{}^{35}ClO_3$, and $C_6D_5{}^{37}ClO_3$ demonstrates that the perchlorylbenzene molecule is composed of a C_{3v} perchloryl group, attached by the chlorine atom to the phenyl ring. There is a low barrier to internal rotation of the perchloryl group with respect to the phenyl ring around an axis coincident with the CCl bond connecting the two moieties. The experimental (B + C) and the distance from the center of mass of the chlorine atom determined from the chlorine isotopic molecules indicate a very long CCl distance and a remarkable deformation of the phenyl ring.

Introduction

In the course of a comprehensive study directed to the elucidation of the physicochemical properties associated with the presence of the perchloryl (ClO_3) group in organic molecules, we decided to carry out a microwave study of perchlorylbenzene (PB) to date one of the simplest and most interesting organic compounds containing the perchloryl group.[1]

Such a study will first allow the determination with certainty of the symmetry of the title compound, which should follow unambiguously from the microwave spectral pattern. The literature suggests a C_6H_5–ClO_3 structure for PB[2] and an x-ray investigation establishes such a structure for the *m*-nitro derivative of PB[3] (henceforth referred to as NPB). However, the discussion in ref 2a seems to give plausible, rather than clear-cut, support to the above structure, and nitration of PB takes place with very active reagents, which might promote also a contemporary isomerization from a possible C_6H_5–$OClO_2$ structure. Furthermore, we should also obtain the C–Cl and Cl–O distances on the basis of quite reasonable assumptions.

The third goal of this work concerns the type and height of the barrier to internal rotation of the heavy ClO_3 top with respect to the C_6H_5 frame.

Experimental Section

PB and perchlorylbenzene-d_5 (PBD) have been prepared and purified as reported in ref 2b. The spectra were recorded in the 8–40-GHz range using a Hewlett-Packard 8400 C-type spectrometer. The measurements were carried out at room temperature, where PB and PBD display a vapor pressure of about 0.050 Torr. We performed both low and high (time constant up to 10 s) resolution measurements to obtain the band and line spectra, respectively.

Results and Discussion

The spectra of the examined isotopic species PB–^{35}Cl, PB–^{37}Cl, PBD–^{35}Cl, and PBD–^{37}Cl display intense and narrow bands, and a lack of intense lines between the bands, Figures 1 and 2. Such a pattern is a characterizing feature of the rotational spectra of molecules with a sixfold low barrier to internal rotation, due to the pile up of the lines corresponding to higher values of the torsional number *m* (see below) and to the near prolate value of the rotational asymmetry parameter κ (–0.96) because in this case *A* refers only to the frame. These facts establish a C_{3v} symmetry for the top and consequently the structure C_6H_5–ClO_3 for PB. Analogous results for PBD confirm this view.[4]

PB is thus a molecule with a V_6 potential barrier and heavy top. To date in only a few molecules of this type have the rotational spectrum been analyzed in detail: CF_3–NO_2,[5] SiF_3–BF_2,[6] and C_6H_5–CF_3.[7]

Since the PB molecule is quite similar to C_6H_5–CF_3, we thought it possible to undertake a detailed study of its internal rotation, taking also into account that the zero value of the oxygen nuclear spin quantum number implies the absence of torsional levels with $m \neq 3n$ (n = 0, 1, 2, . . ., ∞), and consequently a simplified and more intense spectral pattern.

To calculate the energy levels, we used two different approaches. The first uses as unperturbed basis set for the building of the energy matrix the functions $\psi_{JKM}e^{im\alpha}$, which are those appropriate for the study of the free internal rotation of molecules with both top and frame symmetrical rotors. The rotational asymmetry and the barrier to internal rotation are considered as perturbations and give rise to corresponding off-diagonal terms.[8] As reported in ref 5, we obtain four submatrices, all of infinite order, indicated by β, where β takes the values 0, 1, 2, 3. For PB, we need to consider only the submatrices corresponding to β = 0 and β = 3 because the levels corresponding to the others are missing owing to the zero value of the oxygen nuclear spin.[9] The two submatrices with β = 0 and β = 3 have been factorized using Wang's procedure, obtaining four further submatrices for each.

When the barrier for internal rotation is of the V_6 type, the energy difference between torsional levels connected by nonzero matrix elements is approximately $[F(36 + 12m)]$, where *F* is the reduced rotational constant. For PB, *F* is quite low (about 9300 MHz), so the difference in energy between torsional levels becomes much larger (an order of magnitude) than that between rotational levels only for rather high ($\gtrsim$20) values of *m*. Thus for $m > \sim 20$ (m = 18, 24, 30, . . . for β = 0; m = 15, 21, 27, . . . for β = 3) we applied the Van Vleck transformation to the parts of matrices containing the blocks *m* and (*m* + 6), causing a truncation of the energy matrix to the value of *m* considered and addition of a term $(V_6)^2/\{192[A_z' K - F(m + 3)]\}$ (where A_z' is the rotational constant of the frame) to the diagonal elements of block *m*.

The second approach[7,8] takes as starting functions for setting up the energy matrix the $\psi_{JKM}\gamma_{Kv\sigma}$, where ψ_{JKM} are the symmetric rotor functions and $\gamma_{Kv\sigma}$ are the solutions of the torsional equation including also the rototorsional interaction term. The rotational asymmetry is taken as the perturbation.

A computer program based on the latter approach and supplied by Ogata[7] gave values of the energy levels practically coincident with those obtained by a program written by us following the former approach. Systematic variation of the suitable parameters resulted in an ex-

TABLE I: Experimental Center Band Frequencies (MHz) and $(B + C)$ Values for the Four Isotopic Species of PB

$J \leftarrow J + 1$	$C_6H_5{}^{35}ClO_3$	$C_6H_5{}^{37}ClO_3$	$C_6D_5{}^{35}ClO_3$	$C_6D_5{}^{37}ClO_3$
17 ← 16	27343	27178		
18 ← 17	28954	28768		
19 ← 18	30562	30376	28610	28431
20 ← 19	32176	31968	30112	29926
21 ← 20	33774	33573	31607	31409
22 ← 21	35389	35173	33125	32918
23 ← 22	37001	36770	34638	
24 ← 23	38608	38364	36136	35903
25 ← 24			37643	37408
$(B + C)$	1608.6 ± 0.2	1598.6 ± 0.2	1505.6 ± 0.2	1496.2 ± 0.2

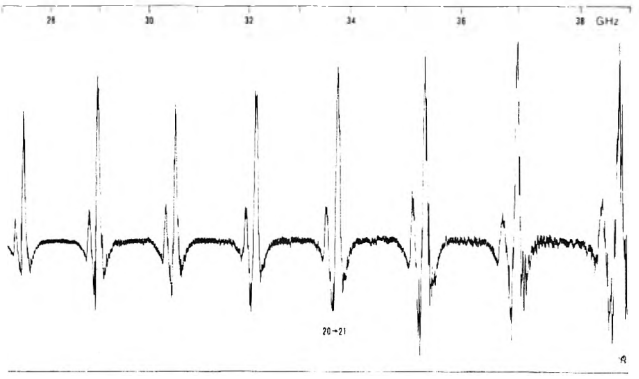

Figure 1. Low resolution (time constant 0.1 s) microwave spectrum of the natural isotopic mixture perchlorylbenzene-^{35}Cl–perchlorylbenzene-^{37}Cl.

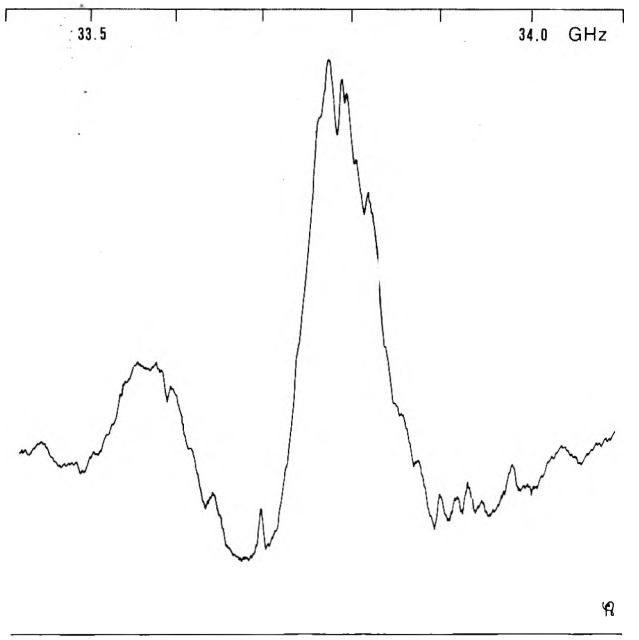

Figure 2. High resolution (time constant 3 s) microwave spectrum of the 21 ← 20 bands of the natural isotopic mixture perchlorylbenzene-^{35}Cl–perchlorylbenzene-^{37}Cl.

tended set of spectral predictions, on the basis of which we tried a spectral assignment, which would have permitted the determination of the barrier height. However, in spite of careful experimentation, carried out at borderline sensitivity of the available instrument, we did not succeed in the assignment. This is due to the fact that the intensities of the interesting PB lines are much lower than that of trifluoromethylbenzene because in our case (i) two isotopic species PB–^{35}Cl and PB^{37}Cl are present; (ii) quadrupole broadening occurs; and (iii) the value of the dipole moment is presumably substantially lower than that of trifluoromethylbenzene. Furthermore, the vapor pressure of PB did not allow measurements below room temperature.

TABLE II: Dependence of the r^0 CCl Distance on the ∠CClO Angle and Phenyl Ring Structure

Phenyl ring structure	∠CClO, deg	a^0_{CCl}, Å PB	a^0_{CCl}, Å PBP	CCl distance, Å
Regular hexagon[a]	105	1.41	1.47	1.73
	107	1.38	1.45	1.70
	109	1.35	1.42	1.67
Distorted I[b]	105	1.41	1.48	1.79
	107	1.38	1.45	1.76
	109	1.36	1.42	1.73
Distorted II[c]	105	1.41	1.48	1.79
	107	1.38	1.45	1.76
	109	1.36	1.42	1.73

a^s_{CCl} = 1.41 ± 0.02 for PB; 1.46 ± 0.02 for PBD

[a] CC distance 1.396 Å, CH distance 1.084 Å, all angles 120°. [b] Reference 14. [c] Obtained from I by pushing C_1 toward the center until ∠$C_6C_1C_2$ was 126°.

Table I lists the values of the measured band centers for the four isotopic species examined, and the average $(B + C)$ values. From these $(B + C)$ values for ^{35}Cl– and ^{37}Cl–PB and ^{35}Cl– and ^{37}Cl–PBD we obtained the a^s_{Cl} (the coordinate along the a axis of the Cl atom in the principal axis system) by subtracting from the equation

$$a^2 = (2/\mu)(I'_{BC} - I_{BC}) \quad (1)$$

where I_{BC} (amu Å^2) = 505379/$(B + C)_{exptl}$ (MHz), a correction term D

$$D = a^2(I_B - I_C)^2/(I_B + I_C)^2 \quad (2)$$

for the error implied in the use of the I_{BC}s instead of the experimentally unavailable I_Bs or I_Cs. The latter were estimated from the assumed structure. For PB, $D \simeq 0.5\%$.

Practically coincident values of the a^s_{Cl} were calculated from the formula

$$a^2 = \mu^{-1}(I'_{BC} - I_{BC})(I_B{}^{-1} + I_C{}^{-1})^2/(I_B{}^{-2} + I_C{}^{-2}) \quad (3)$$

which was suggested by a referee.

Both (2) and (3) were obtained by neglecting μa^2 with respect to $I_B + I_C$.

Several least-squares calculations were performed in order to fit the C–Cl distance (r_{CCl}) to the four experimental $(B + C)$ values. Changing the ClO distance (with the ∠CClO angle at 105°, the value which makes a^0_{Cl} the nearest to a^s_{Cl}) has only a slight effect on the CCl distance.[10] Much more influential are the ∠CClO angle and the ring geometry, the effects of which are shown in Table II together with the data (the a^s_{Cl}) obtained from substitution analysis.

The values in Table II show that a^0_{Cl} approaches a^s_{Cl} if we decrease the ∠CClO angle. We do not expect this angle, nor the ClO distance to take values smaller than in NPB, because of the tendency of both these quantities to increase along with a decrease of the electron-withdrawing properties of the molecular fragment attached to the ClO_3 group.[3,11,12] However, the experimental uncertainties prevent considering this difference as significant.

A regular hexagon phenyl ring (cf. note *b* of Table II) was considered as a reference geometry, although it appears improbable on the basis of the following considerations. In mono-substituted benzenes, distortion of the phenyl ring appears to affect mainly the $\angle C_6C_1C_2$ angle and the C_1C_2, C_1C_6 bond distances[3,13,14] preserving the ring planarity. The amount and direction of such ring distortion has been correlated to the polar effect of the substituent[13-15] and to the parameter σ_I,[16] which is defined as a polar effect scale.[15a] The polar effect for the perchloryl group was reported to be larger than that of the nitro group;[17] σ_I and σ_R for $-ClO_3$ can be evaluated as 0.80 and 0.27, respectively.[15,17] These values are not consistent with the *p*-fluorine delta shift, also reported,[17] but the direction of the discrepancy does not suggest decreasing the σ_I value. Thus, the C_1 atom should probably be pushed toward the ring center[13,14] equally or more than in nitrobenzene, with a corresponding increase of the $\angle C_2C_1C_6$ angle and decrease of the C_1C_2, C_1C_6 bond lengths. This is also suggested by the x-ray structure analysis of NPB.[3]

Thus we took as a further ring structure that reported for nitrobenzene.[14] From Table II (distorted I) it appears that, with this geometry, the values of the a^0_{Cl} are in good agreement with a^s_{Cl} when the angle is about 106°. Correspondingly, the C–Cl distance is about 1.78 Å, one of the longest known CCl bond lengths, as occurs for NPB in the solid state.[3]

Since in NPB the ring angle at $-NO_2$ is the same as in nitrobenzene,[14] we thought that the same might be true of the ring angle at the $-ClO_3$. We thus took for the ring a further geometry obtained from that of nitrobenzene pushing the C_1 atom toward the center until the angle $\angle C_6C_1C_2$ was 126°. As Table II shows, no significant change of the CCl distance results.

It follows that our experimental data, i.e., the values of $(B + C)$ and the a^s_{Cl}, can best be accounted for when a ring structure essentially equal to that of nitrobenzene and a CCl distance of 1.78 Å are assumed.

References and Notes

(1) The effects of electron impact on PB and PB-d_5 have been discussed by A. G. Giumanini and B. Lunelli, *Org. Mass. Spectrom.*, **11**, 569 (1976); investigations on the vibrational, electronic, and electrochemical behavior are in progress.

(2) (a) C. E. Inman, R. E. Oesterling, and E. A. Tyczkowski, *J. Am. Chem. Soc.*, **80**, 5286 (1958); (b) B. Lunelli, *Ind. Eng. Chem., Prod. Des. Develop.*, **15**, 278 (1976).

(3) G. J. Palenik, J. Donohue, and K. N. Trueblood, *Acta Crystallogr., Sect. B*, **24**, 1139 (1968).

(4) We carried out the calculation of the $(B + C)$ and of the a^0_{Cl} values also for three C_6H_5–O–ClO_2 structures, that is for the two terminal oxygen atoms (i) symmetrically farthest, (ii) symmetrically nearest, and (iii) one farthest and one nearest to the center of the phenyl ring. The $-OClO_2$ structure was assumed identical with that of $FClO_2$, cf. C. R. Parent and M. C. L. Gerry, *J. Mol. Spectrosc.*, **49**, 343 (1974). It turned out that either the $(B + C)$ or a^s_{Cl} value or both do not fit the corresponding experimental value.

(5) W. M. Tolies, E. T. Handelman, and W. D. Gwinn, *J. Chem. Phys.*, **43**, 3019 (1965).

(6) T. Ogata, A. P. Cox, D. L. Smith, and P. L. Timms, *Chem. Phys. Lett.*, **26**, 186 (1974).

(7) T. Ogata and A. P. Cox, *J. Mol. Spectrosc.*, **61**, 265 (1976).

(8) E. B. Wilson, Jr., C. C. Lin, and D. R. Lide, *J. Chem. Phys.*, **23**, 136 (1955).

(9) The presence in the PB molecule of an even number of couples of equivalent fermions implies that the overall wavefunction must be a symmetrical one. In terms of the symmetry classes of the D_{3h} point group (H. C. Longuet-Higgins, *Mol. Phys.*, **6**, 445 (1963))

$$(A_1') \times (A_1'A_1'') \times (A_1'A_1'' - A_2'A_2'') \times (A_1'E'E''A_1'' + A_2'' \cdots) = A_1' \text{ or } A_2'$$

top spin function	frame spin functions	rotational functions	torsional functions	overall function

From the D_{3h} multiplication table it follows that if the torsional functions belong to the E' or E'' species, the overall function cannot be of A_1' or A_2' species; consequently such torsional levels cannot exist.

(10) Taking for the phenyl ring the distorted I geometry (Table II), the ∠CClO angle as 105°, and the ClO distance as 1.44, 1.45, and 1.46 Å, we obtained for the CCl distance 1.79_2, 1.78_9, and 1.78_4, or, to our approximation, a value of about 1.79 Å.

(11) A. D. Walsh, *J. Chem. Soc.*, 2301 (1953).

(12) (a) A. H. Clark, B. Beagley, D. W. J. Cruickshank, and T. G. Hewitt, *J. Chem. Soc. A*, 872 (1970); (b) *ibid.*, 1613 (1970).

(13) J. Casado, L. Nygaard, and G. O. Soerensen, *J. Mol. Struct.*, **8**, 211 (1971).

(14) J. H. Hoeg, Thesis, Copenhagen, 1971.

(15) (a) R. N. Taft, Jr., *J. Am. Chem. Soc.*, **79**, 1046 (1957); (b) R. T. C. Brownlee and R. W. Taft, *ibid.*, **92**, 7007 (1971).

(16) D. Christen, D. G. Lister, and J. Sheridan, *J. Chem. Soc., Faraday Trans. 2*, **70**, 1953 (1974).

(17) D. M. Gardner, R. E. Oesterling, and F. L. Scott, *J. Org. Chem.*, **28**, 2650 (1963).

Donor Energy Effects on the Triplet-Sensitized Isomerization of 11-*cis*-Retinal

T. Rosenfeld, O. Kalisky, and M. Ottolenghi*

Department of Physical Chemistry, Hebrew University, Jerusalem, Israel

(Received January 5, 1977)

The photosensitized isomerization of 11-*cis*-retinal was investigated over a range of donors with varying triplet energy (E_T). The photoisomerization yield (ϕ^T_{iso}) for each retinal triplet produced by energy transfer was determined using continuous and pulsed-laser excitation methods. The marked dependence of ϕ^T_{iso} on E_T sets an upper limit of ~0.1 to the isomerization yield in the thermally relaxed T_1 state. The data are interpreted in terms of an efficient isomerization path involving higher vibronic triplet levels.

The mechanism of photochemical cis–trans isomerization in retinals and derivatives, which bears on the primary photoprocess in visual pigments,[1] has been investigated using direct and triplet-sensitized excitation methods.[2-7] In the present study we carried out a set of experiments in which the photosensitized isomerization of 11-*cis*-retinal (the isomer present in the visual chromophore, rhodopsin) was studied as function of the excess energy in the sensitizers. Special attention was paid to monitoring the isomerization yield for each triplet molecule

TABLE I: 11-*cis* → *all-trans*-Retinal (Triplet-Sensitized) Isomerization Yields as a Function of the Donor's Energy[a]

Sensitizer	E_T,[b] kcal/mol	$10^{-9}k_{ET}$, s^{-1} mol^{-1}	ϕ_{iso}^T
Benzophenone	69	3.0	0.16 ± 0.05
Biphenyl	65	3.0	0.12 ± 0.05
Phenanthrene	62		0.13 ± 0.05
Biacetyl	55	3.0	0.15 ± 0.05
1,2:5,6-Dibenzanthracene	52	9.5	0.5 ± 0.1
Pyrene	49	6.5	0.3 ± 0.1
1,2-Benzanthracene	46	5.0	0.56 ± 0.1
Anthracene	42	2.5	0.85 ± 0.15
3,4-Benzpyrene	42	4.1	1.0 ± 0.15

[a] Excitation was carried out at 253.7 nm, except in the cases of biphenyl (λ_{exc} 313 nm) and biacetyl (438 nm). [b] Data reproduced from J. B. Birks, "Photophysics of Aromatic Molecules", Wiley-Interscience, New York, N.Y., 1970.

produced by energy transfer. In this respect it should be recalled that in the pioneering investigations of Hammond and co-workers in stilbene and related systems, the dependence of the photostationary cis–trans composition on the energy of the donor was interpreted in terms of energy effects on the rates of energy transfer to either cis or trans ground state acceptors.[8] A constant isomerization probability (independent of the donor's energy), after energy transfer, was assumed. The validity of such an assumption in the 11-*cis*-retinal system is now being questioned.

The energy transfer reaction (eq 1) from a triplet donor ($^3D^*$) to 11-*cis*-retinal (R) was followed using previously

$$^3D^* + R \rightarrow {}^3R^* + D \qquad (1)$$

described pulsed N_2 laser photolysis methods[3,5,6] in which the decay of $^3D^*$, as well as the matching growing in of the retinal triplet state, are directly observable. The 11-cis → all-trans yields (ϕ_{iso}^T) (molecules photoisomerized for each $^3R^*$ produced in reaction 1 with a quantum yield ϕ_T^R) were determined from continuous excitation experiments (λ_{exc} 313 or 254 nm), using the expression $\phi_{iso}^T = \Delta D_i/\Delta\epsilon t I \phi_T^R$, where $\Delta\epsilon = 2.1 \times 10^4$ cm^{-1} M^{-1} is the difference in extinction coefficients between the 11-cis and all-trans isomers at 365 nm, ΔD_i is the (initial) increase in absorbance at 365 nm after time t due to the 11-cis → all-trans reaction, and I is the light intensity at the sample cell (usually of the order of $I = 10^{-2}$ einstein L^{-1} cm^{-1} min^{-1}). ΔD_i values were recorded from the initially linear slope of the ΔD vs. t plots, where the 11-cis → all-trans conversion does not exceed ~15%. This allows neglecting the back photoreaction from *all-trans*-retinal to cis isomers.

For the determination of ϕ_{iso}^T, the values of ϕ_T^R were evaluated using the expression

$$\phi_T^R = \phi_T^D \phi_{ET} = \phi_T^D \{k_{ET}[R]/(k_{ET}[R] + k_d)\} \qquad (I)$$

where ϕ_T^D is the donor's intersystem crossing yield and ϕ_{ET} denotes the yield of energy transfer. ϕ_{ET} is a function of the retinal concentration [R] and of the rate constant for energy transfer (k_{ET}), as well as of that of the decay of the unquenched donor triplet (k_d). To avoid interference with accurate measurements of ΔD_i, the initial absorbance of the solution at the 365-nm monitoring wavelength had to be kept below ~1.5, so that $[R] \lesssim 5 \times 10^{-5}$ M. This implies incomplete energy transfer ($\phi_{ET} < 1$), requiring an exact determination of ϕ_T^R or ϕ_{ET} in each experiment. Such values were obtained using various alternative procedures[3,6] based on pulsed laser photolysis, involving the direct determination of absorbance changes associated with the formation of $^3R^*$ via reaction 1, as well as of the rate constant for the decay of $^3D^*$.

Sensitizers were selected, subject to the following requirements: (a) The absence of reactions between $^3D^*$ and R other than reaction 1. (b) The absence of processes in the excited (singlet or triplet) donor leading to photoproducts, such as, e.g., free radicals, capable of catalyzing the isomerization of R, thus leading to erroneous ϕ_{iso}^T values. (c) The lack of any detectable effects of R on the fluorescence quantum yield of the donor, thus excluding complications due to interactions between $^1D^*$ and R. (d) Identity of the superimposed absorption spectra of separated solutions of R and D with those of the corresponding mixtures used in the photosensitization experiments, which could be indicative of ground-state interactions between donor and acceptor. (e) Independence of the intrinsic lifetime of $^3D^*$ on [D], in order to avoid complications due to self-quenching of the donor's triplet. The values obtained for ϕ_{iso}^T, using a series of different triplet sensitizers, with varying triplet energy (E_T), are presented in Table I. No detectable transfer or photoinduced isomerization was observed in the case of the naphthacene triplet (E_T = 29 kcal/mol) which lies considerably below that of 11-*cis*-retinal (see below).

The systematic dependence of ϕ_{iso}^T on ΔE_T (rather than on specific molecular properties of the donor such as ionization potential, electron affinity, etc.) shows that the excess energy in the donor plays an important role in determining the isomerization efficiency following triplet energy transfer. The minimum value observed for ϕ_{iso}^T (for high energy sensitizers) indicates that the isomerization yield in the lowest thermalized triplet of 11-*cis*-retinal is below ~12%. Moreover, the data of Table I demonstrate the existence of an efficient isomerization path taking place via thermally or electronically unrelaxed levels of $^3R^*$. Should isomerization take place exclusively via the quantitative population of a single equilibrated lowest (triplet) state (as it has been recently postulated for rhodopsin in its singlet manifold[1]), the value of ϕ_{iso}^T would be independent of ΔE_T. (For each of the sensitizers, one retinal triplet is produced for each $^3D^*$ quenched.) Such conclusions not only indicate a fundamental difference between the behavior of singlet excited rhodopsin and triplet 11-*cis*-retinal, but they also bear on the general problem of donor energy effects on the efficiency of triplet-sensitized reactions. It is evident that, in some systems, not only the efficiency of energy transfer, but also the probability for the reaction to occur after transfer, may be markedly affected by the excess energy in the donor.

At present it is difficult to account quantitatively for the above effects in terms of a detailed model. However, a plausible explanation for the inefficiency of an activated isomerization process in the thermalized T_1 state ($\tau_{1/2} \simeq 10$ μs) involves the assumption of a substantial barrier ($\Delta E > 5$–10 kcal) along the 11–12 coordinate of T_1. The high isomerization yield observed with a low energy sensitizer such as anthracene may be explained by assuming that in this case energy is transferred to a higher triplet (e.g., T_2), characterized by a barrierless curve along the 11–12 co-

ordinate. In view of the difference between E_T(anthracene) = 42 kcal/mol and E_T(11-*cis*-retinal) $\lesssim$ 38 kcal/mol,[9] this would imply a relatively small gap (ΔE_T = 4–6 kcal/mol) between (11-cis) T_1 and T_2. Unfortunately, it is difficult to test quantitatively such conclusions in terms of the published theoretical calculations of retinal triplet energy levels.[10,11] These very substantially in the spacings between the T_i states and, more significantly, in the sign and size of their 11–12 rotational barrier. Qualitatively in keeping with the above interpretation is the prediction[11] of four triplet levels (T_1–T_4) within the ΔE_T range covered by the sensitizers of the present study.

A more difficult task is that of suggesting a model accounting for the observed systematic decrease in ϕ_{iso}^T at higher ΔE_T. It is possible that the population of higher vibronic levels in the triplet manifold leads to geometrical changes along other coordinates which prevent that corresponding to the 11–12 tortional motion. Such changes provide a deactivation path, back to the original 11-cis molecule, without leading to any net photochemical transformation. This approach seems also to provide the best explanation for the inefficiency of the reverse trans → cis photoreaction. Thus, although the direct-excitation quantum yields of the all-trans → (cis isomers) process are comparable to those of the 11-cis → (all-trans) photoreaction (0.1 and 0.12 correspondingly, using 313-nm excitation), the photosensitized isomerization yields of the all-trans molecule measured by us with biphenyl (ϕ_{iso} < 0.01) or 1,2-benzanthracene (ϕ_{iso}^T = 0.02) as sensitizers are extremely low. Here too, the triplet sensitized photochemistry of the retinal model compound markedly differs from that following direct excitation of the corresponding (transoid) visual pigment, bathorhodopsin.[1]

Acknowledgment. The authors are grateful to Professors R. Gerber, R. D. Levine, and B. Honig for valuable discussions.

References and Notes

(1) T. Rosenfeld, B. Honig, M. Ottolenghi, J. Hurley, and T. G. Ebrey, VII, *J. Pure. Appl. Chem.*, in press (IUPAC Symposium on Photochemistry, Aix-en-Provence, France, July, 1976).
(2) R. Hubbard, *J. Am. Chem. Soc.*, **78**, 4662 (1956); A. Kropf and R. Hubbard, *Photochem. Photobiol.*, **12**, 249 (1970).
(3) T. Rosenfeld, A. Alchalel, and M. Ottolenghi, *J. Phys. Chem.*, **78**, 366 (1974).
(4) R. A. Raubach and A. V. Guzzo, *J. Phys. Chem.*, **77**, 889 (1973).
(5) T. Rosenfeld, A. Alchalel, and M. Ottolenghi in "Excited States of Biological Molecules", J. Birks and S. P. McGlynn, Ed., Wiley-Interscience Monographs in Chemical Physics, New York, N.Y., 1976, p 540.
(6) T. Rosenfeld, A. Alchalel, and M. Ottolenghi, *Photochem. Photobiol.*, **20**, 121 (1974); A. Alchalel, B. Honig, M. Ottolenghi, and T. Rosenfeld, *J. Am. Chem. Soc.*, **97**, 2161 (1975).
(7) E. L. Menger and D. S. Kliger, *J. Am. Chem. Soc.*, **98**, 3975 (1976).
(8) See, for example, G. S. Hammond et al., *J. Am. Chem. Soc.*, **86**, 3197 (1964).
(9) The latter value is established by our observation that the 11-*cis*-retinal triplet does not transfer energy to azulene (E_T = 38 kcal/mol), and is consistent with previously published estimates for the all-trans isomer (E_T = 36–38 kcal/mol, see ref 4 and A. Guzzo and G. L. Pool, *J. Phys. Chem.*, **73**, 2512 (1969)).
(10) J. R. Weisenfeld and E. W. Abrahamson, *Photochem. Photobiol.*, **8**, 487 (1968); J. Langlet, B. Pullman, and H. Berthod, *J. Chim. Phys.*, **66**, (1969); H. Suzuki, N. Takizawa, and T. Komatsu, *Prog. Theor. Phys. Suppl.*, **46**, 16 (1970); R. S. Becker, K. Inuzaka, J. King, and D. E. Balke, *J. Am. Chem. Soc.*, **93**, 43 (1971).
(11) L. J. Weimann, G. M. Maggiora, and P. E. Blatz, *Int. J. Quantum Chem.*, QBS2 9 (1975).

Second Moment Studies of the Electron Spin Resonance Line Shape of Trapped Electrons in Sodium–Ice Condensates. Relation to the Molecular Structure Around Trapped Electrons

D. P. Lin† and Larry Kevan*

Department of Chemistry, Wayne State University, Detroit, Michigan 48202 *(Received December 8, 1976)*

The second moment of the ESR line shape of trapped electrons produced by codeposition of sodium and water vapor at 77 K has been measured in H_2O and D_2O at both 9 and 35 GHz microwave frequencies. The sodium concentration is less than 0.01 M in this matrix. By analyzing the difference in the second moments in the protiated matrix at 9 and 35 GHz the isotropic and anisotropic hyperfine constants for n nearest equivalent interacting protons are obtained. The structural results found are similar to those obtained previously for trapped electrons in 10 M NaOH glassy ice by analysis of second moment and electron spin echo data. Since the trapped electron solvation structure seems independent of the solute concentration, we suggest that this solvation structure is also characteristic of solvated electrons in liquid water.

Introduction

Solvated electrons are perhaps the most important reactive intermediates in the radiolysis of condensed systems.[1] In the past 12 years much has been learned of their reaction rates with a host of compounds, but their geometrical structure is only now being elucidated. Pulse radiolysis and 4 K radiolysis studies suggest that trapped electrons in organic and aqueous glassy matrices reorient their surrounding solvent molecules at 77 K to reach an equilibrium solvated state. The most detailed picture of the arrangement of solvent molecules around a solvated electron has been obtained for electrons trapped at 77 K in a glassy ice composed of 10 M NaOH.[2-4] It is found that six H_2O molecules are arranged equivalently (i.e., octahedrally) around the excess electron with one OH bond from each H_2O molecule oriented toward the electron. The nearest neighbor electron–proton distance is 2.1 ± 0.1 Å. This geometrical model has been obtained through a combination of electron spin resonance (ESR) techniques involving analysis of electron spin echo modulation

† Present Address: Edward Waters College, Jacksonville, Fl.

patterns[3] and second moment ESR line shape analyses.[2,4]

It has been suggested that the structure deduced for the solvated electron in the 10 M NaOH glassy ice matrix is also applicable to the solvated electron in water.[4] The spin echo results show that the electron in 10 M NaOH ice does have nearest neighbor water molecules and that the Na^+ ions are at least 5 Å away. However, the high ion concentration in 10 M NaOH may impose structural constraints and it is desirable to study the geometrical structure of the electron in a less concentrated aqueous matrix. One cannot simply lower the NaOH concentration much because below about 5 M the glassy state is no longer produced by rapid freezing and the trapped electron yield drops concommitantly. However, Bennett et al.[5] found that trapped electrons in reasonably high yield can be produced by codeposition of water vapor and sodium vapor at 77 K. With this technique the Na concentration is less than 0.01 M.

In the present work we have studied the second moment ESR line shape of trapped electrons produced by codeposition of sodium and water vapor at 77 K in order to assess if the geometrical structure of this electron is significantly different from that produced in 10 M NaOH ice. Although the experimental uncertainty is larger than desirable, we find little significant difference between the solvated electron structure in these two matrices.

Experimental Section

Bennett et al.[5] used a complex rotating cryostat arrangement for codeposition of sodium and water vapor. However Froben and Willard[6] codeposited sodium and 3-methylpentane directly onto a pyrex cold finger and appeared to achieve a well-mixed, uniform deposit. We have used this latter, simpler method as adapted by Raitsimring et al.[7] Water and purified sodium metal were contained in separate reservoirs attached to an evacuated flask containing a 8-mm o.d. pyrex cold finger. The cold finger was filled with liquid nitrogen and could be removed from the flask by a ground glass joint. During deposition the sodium was gently heated and the water reservoir stopcock was opened; the total deposition time was 40–60 min. As deposition proceeds the matrix becomes blue and finally blue-black indicating spontaneous ionization of the sodium to produce trapped electrons.[5] After deposition the cold finger is quickly removed from the flask and the blue color fades somewhat. The deposit is scraped off under liquid nitrogen and is transferred under liquid nitrogen into an ESR insertion dewar for X-band studies or directly into the ESR cavity for Q-band studies. Based on Bennett et al.[5] we estimate that the Na concentration in our samples is less than 0.01 M.

The ESR measurements were performed on a Varian V-line spectrometer at X-band and on a Varian E-line spectrometer at Q-band. The Q-band cavity was immersed in a cold gas flow dewar for temperature control. Most measurements were made at 100 K at Q-band and at 77 K at X-band. Warm-up measurements at X-band were made by depositing the sample on a 3-mm o.d. Suprasil quartz cold finger which was then inserted into a flow dewar. Temperatures were measured with copper–constantan thermocouples with direct read out. ESR spectra were obtained with 100-kHz field modulation at a microwave power of about 20 μW at X-band and about 100 μW at Q-band. Based on earlier measurements these powers are low enough to exclude saturation broadening.

Results

1. *Spectral Characteristics.* The X-band ESR spectra of the Na–ice condensates are shown in Figures 1 and 2

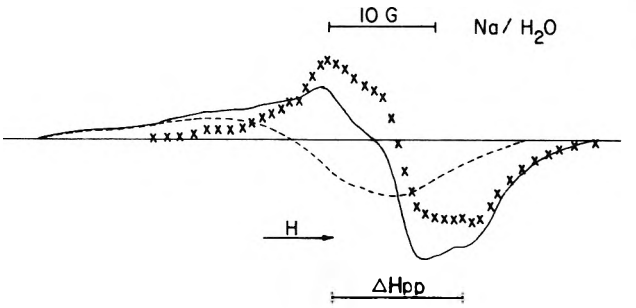

Figure 1. X-band ESR spectra of a Na–H_2O condensate at 77 K before (—) and after (---) bleaching with visible light. The difference spectrum (XXX) corresponding to the bleachable component is also shown.

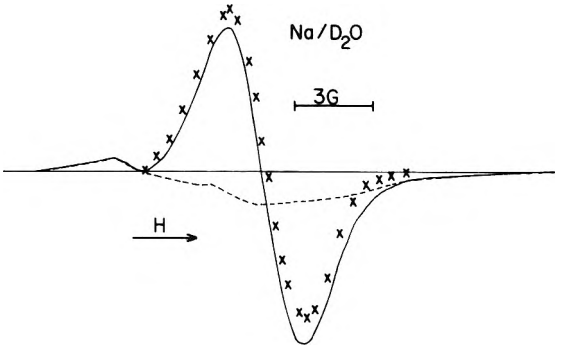

Figure 2. X-band ESR spectra of a Na–D_2O condensate at 77 K before (—) and after (---) bleaching with visible light. The difference spectrum (XXX) corresponding to the bleachable component is also shown.

for H_2O and D_2O matrices, respectively. The solid lines represent the observed spectra, with care being taken not to expose the sample to bright room lights. The H_2O spectrum is quite asymmetric. The reason for the asymmetry is revealed by visible bleaching. The dashed line is the spectrum observed after 30 s bleaching by a 500-W slide projector. At this point the sample is opaque white so we assume that all trapped electrons (e_t^-) have been optically bleached. The difference spectrum is shown by the crosses; it is fairly symmetric and is attributed to trapped electrons.

Bennett et al.[5] did not report any background spectrum after optical bleaching and their original spectra are symmetric. Our background spectra are characterized by $g = 2.007$ and peak-to-peak line widths (ΔH_{pp}) of 17 G in H_2O and 5.5 G in D_2O. At present we are unsure of the identity of our background spectra, however, this is not critical since our main focus in this paper will be on the trapped electrons.

The difference spectrum in H_2O clearly shows some structure and is similar to that reported by Bennett et al.[5] They were able to improve their resolution quite considerably by thermal annealing at 173 K. In one early experiment we were also able to improve the resolution in this manner, although not nearly as dramatically as shown by Bennett et al. However, in all subsequent experiments on a different apparatus, thermal annealing only led to electron decay and loss of color by the sample. This is the behavior Bennett et al. found for 10-fold lower Na concentrations (<0.001 M) so we believe our Na concentrations are quite low. We suspect that the relative rates of deposition of the sodium and water vapor as well as the sodium concentration sensitively affect the annealing properties of the matrix.

The line width and second moment of our difference spectra at X-band assigned to trapped electrons are summarized in Table I. The errors are relatively large for the H_2O matrix because of the large background spectrum.

TABLE I: ESR Line Shape Parameters for Trapped Electrons in Sodium-Ice Condensates

	X-band (9.2 GHz)		Q-band (~35 GHz)	
	Na/H_2O	Na/D_2O	Na/H_2O	Na/D_2O
ΔH_{pp}	(12 ± 1 G)[a]	2.9 ± 0.2 G	9 ± 1 G	2.4 ± 0.3 G
$\langle H^2 \rangle$	36 ± 5 G^2	2.4 ± 0.3 G^2	20 ± 4 G^2	2.1 ± 0.3 G^2

[a] Line shape shows structure so that line width is not well defined; see Figure 1.

The line width in H_2O is measured symmetrically about the center of the spectrum as shown in Figure 1. We note that the line width is not well defined because the line shape shows structure and the structure is not always exactly symmetric. Bennett et al. report a smaller line width (ΔH_{pp} = 9.2 ± 0.5 G) but it is not clear from where they measured it. Their reported line width appears to correspond to ΔH_{pp} for our original asymmetric spectrum, but given the unresolved structure and the asymmetry this does not seem to be an appropriate measure. Our line widths in the D_2O matrix, where there are no complications from partially resolved structure, agree well with those of Bennett et al.

It seems clear that sodium in vapor condensed ice at 77 K spontaneously ionizes and that recombination of Na^+ and e^- is prevented by solvation of at least the electron. We note in less polar matrices such as 3-methylpentane that sodium does not spontaneously ionize, presumably because the electron solvation process is less energetic and/or slower. It thus appears that vapor condensed ice at 77 K should trap electrons produced by γ irradiation. However, when we took an identically prepared sample without the sodium and γ irradiated it to doses between 0.1 to 1 Mrad at 77 K, we found no trapped electrons.

Q-band spectra were also obtained for Na in H_2O and D_2O but they were always much noisier. It is tricky to obtain these spectra because small pieces of the Na/H_2O preparation must be put into the small Q-band cavity under liquid nitrogen in dim light. The filling factor of the cavity seems poor for such samples. At Q-band the spectra in both H_2O and D_2O are fairly symmetric with no indication of partially resolved structure. The lack of structure suggests that the structure observed in H_2O samples at X-band is not due to purely isotropic hyperfine interaction. At Q-band there is little interference from the background spectrum because it has a higher g factor than e_t^- and is shifted downfield. The line shape parmeters for the e_t^- at Q-band are also given in Table I. The same sample preparations were examined at both X- and Q-band to provide the best comparison; these are the values given in Table I.

In previous Q-band studies of e_t^- in γ-irradiated 10 M NaOH glassy ice proton spin-flip satellites were resolved at high gain.[8] In the present studies a careful search was made for these satellites but none could be observed. The signal-to-noise level was not as high as in the 10 M NaOH samples so we feel that the satellites were simply below our detection threshold. It is also possible that the satellite lines are broader in the sodium–ice condensation due to a less ordered first solvation shell around e_t^-.

2. *Second Moment Analysis.* Second moments of the e_t^- ESR lines on an enlarged field scale were determined by both even moment and odd moment methods[9] with comparable results. The accuracy of the second moment determinations depends rather sensitively on properly including the wings of the spectra. For e_t^- in H_2O at X-band the background spectrum produces a large correction to the low field wings of the e_t^- spectrum. Accordingly, more weight was placed on the high field wings in measuring this second moment. At X-band both allowed and forbidden ESR transitions contribute to the spectral shape and are included in the second moment.[4] However, at Q-band for e_t^- in H_2O the proton spin–flip satellites due to the forbidden transitions occur at about ±20 G from the center of the main allowed transition and should not contribute to the observed ESR line and second moment. Our sensitivity does not appear high enough to observe these satellite lines, but we have approximated their positions and have slightly cut off the spectral wings so as to only include the second moment associated with the main allowed transition. This, of course, increases our error.

For e_t^- in 10 M NaOH glass we have shown that the total second moment including both allowed and forbidden transitions is independent of microwave frequency.[4] This is verified here for e_t^- in D_2O; the second moments at X- and Q-band are equal within experimental error. In D_2O the deuterium satellite lines occur near ±3 G from the main line and are not expected to be resolved at Q-band. Thus the second moment for e_t^- in D_2O includes both main and satellite lines at both X- and Q-band. In contrast, the second moment for e_t^- in H_2O is definitely larger at X-band than at Q-band. Thus we interpret the second moment for e_t^- in H_2O at Q-band as due only to main, allowed transitions.

In terms of hyperfine parameters the second moment for a system described by an isotropic g factor with only Zeeman and hyperfine terms in its Hamiltonian is given by[10]

$$\langle H^2 \rangle = (n/4)(a^2 + b^2) + S_{p_{nn}} + S_0 \qquad (1)$$

where n is the number of equivalent nearest neighbor protons with an isotropic hyperfine constant a and a dipolar hyperfine constant b. $S_{p_{nn}}$ is the second moment due to nonnearest neighbor protons given by eq 11 in ref 10, and S_0 is due to all other broadening sources. Our objective is to determine values of n, a, and b that describe the solvation structure of e_t^- in the Na–ice condensates. For the type of system we are considering we have shown that nonnearest neighbor proton broadening may be neglected (i.e., $S_{p_{nn}} = 0$).[10] S_0 can be determined from the second moments in H_2O and D_2O at X-band by the expression[10]

$$S_0 = [\langle H^2 \rangle^X_{D_2O} - \alpha \langle H^2 \rangle^X_{H_2O}](1 - \alpha)^{-1} \qquad (2)$$

where α = 0.0628 is the ratio of the deuteron to proton dipolar contributions to the second moment. We find S_0 = 0.2 G^2 for e_t^- in Na–ice condensates.

We have recently demonstrated that the isotropic and dipolar hyperfine constants can be separated in a second moment analysis if measurement can be made at two microwave frequencies of which one frequency is high enough to partially separate or resolve the main and satellite lines.[4] For proton interactions measurements at X- and Q-band suffice. Thus we may determine nb^2 from

$$\langle H^2 \rangle^X - \langle H^2 \rangle^Q = (3/20)nb^2 \qquad (3)$$

which is valid in the high field approximation. The dipolar coupling b is related to the nearest neighbor proton distance r by

$$|b| = \sqrt{2} g \beta g_n \beta_n r^{-3} \text{ or } r(\text{Å}) = (39.8/b)^{1/3} \qquad (4)$$

where b is in gauss. The isotropic coupling constant a can then be determined from

$$\langle H^2 \rangle^X_{H_2O} - S_0 = (n/4)(a^2 + b^2) \qquad (5)$$

By assuming a value for n, corresponding values of a, b, and r may be found from eq 3–5. Table II summarizes

TABLE II: Hyperfine Coupling Parameters of e_t^- and Effective Distances between e_t^- and Nearest Protons in Sodium–Ice Condensates

n	b, G	a, G	r, Å
4	5.2 ± 1.2	3.0 ± 1.4	2.0 ± 0.2
6	4.2 ± 1.1	2.5 ± 1.1	2.1 ± 0.2
	(4.8 ± 0.6)[a]	(1 ± 3)[a]	(2.0 ± 0.1)[a]
8	3.6 ± 1.0	2.1 ± 1.0	2.2 ± 0.2

[a] Values determined previously from second moment analysis for e_t^- in 10 M NaOH at 77 K.[4]

the results for the range of values for n thought to be possible for solvated electrons in aqueous systems.

Discussion

The hyperfine coupling parameters for e_t^- in Na–ice condensates in Table II agree within experimental error with the similar parameters found by a second moment analysis for e_t^- in 10 M NaOH glassy ice.[4] See the comparison for $n = 6$ in Table II. This suggests that the geometrical structure of surrounding water molecules is the same for e_t^- formed in both the concentrated and dilute alkaline ice matrices. If anything, the isotropic hyperfine coupling may be somewhat larger for e_t^- in the Na–ice condensate; this may imply that the e_t^- wavefunction is a little more diffuse in the dilute compared to the concentrated alkaline ice matrix.

Although the second moment analysis indicates a similar geometrical structure for e_t^- in Na–H_2O and in 10 M NaOH their ESR spectra at X-band are distinctly different. Structure is observed in the Na–H_2O ESR spectrum but not in the 10 M NaOH spectrum. We suspect that this difference is due to additional broadening by Na^+ dipolar interactions in 10 M NaOH. This is supported by the S_0 values in both matrices; $S_0 = 10$ G^2 for 10 M NaOH samples[10] but $S_0 = 0.2$ G^2 for Na–H_2O samples. We do not know the Na concentration in our Na–H_2O samples, but based on Bennett et al.'s data[5] it appears to be less than 0.01 M.

Since the Na–H_2O spectra at Q-band do not show partially resolved hyperfine structure, the structure at X-band is apparently not due to purely isotropic hyperfine coupling as suggested originally.[5] Furthermore, the partially resolved structure at X-band seems periodic at about 5.6 G and this seems too large an isotropic coupling to be compatible with the second moment analysis of the same spectrum. We suspect that the structure at X-band in Na–H_2O samples is due to proton spin–flip transitions. Such transitions would be periodic near 5.6 G at X-band for multiple proton spin–flips and, based on the satellite intensities observed at Q-band for e_t^- in 10 M NaOH,[8] would be expected to be nearly as intense as the main transition at X-band. Normally, forbidden satellite transitions can be distinguished from allowed main transitions by differential saturation effects[11] as is the case for trapped hydrogen atoms.[12] However, when the dipolar interaction is sufficiently strong the distinction between allowed and forbidden transitions becomes blurred and the differential saturation effects are small. We find that the partially resolved structure for e_t^- in Na–H_2O samples at X-band does not show significant differential saturation; this seems compatible with the above comments. We conclude that the partially resolved structure for e_t^- in Na–H_2O condensates is not compatible with isotropic coupling, but is compatible with nearly allowed proton spin–flip transitions.

The number of equivalent nearest neighbor interacting protons around e_t^- cannot be determined from a second moment analysis alone. However, we have shown that n can be found from an analysis of the electron spin echo modulation pattern.[3] The spin echo results for e_t^- in 10 M NaOH give $n = 6$, $a = 2.1$ G, $b = 4.4$ G, and $r = 2.1$ Å. These results are in excellent agreement with the values for $n = 6$ in Table II. Furthermore, electron spin echo modulation patterns for e_t^- in Na–D_2O condensates have been cursorily examined and appear essentially identical with those for e_t^- in 10 M NaOD.[13] The spin echo results lend further support that the solvation structures of e_t^- in Na–H_2O condensates and in 10 M NaOH ice are essentially identical.

We conclude that trapped, solvated electrons in disordered frozen aqueous systems with <0.01 M ionic impurities have the same solvation structure as in more concentrated aqueous systems (10 M). Since the solvation structure seems independent of a 10^3-fold change in Na^+ concentration we suggest that this solvation structure is also characteristic of solvated electrons in liquid water.

Acknowledgment. This research was partially supported by the U.S. Energy Research and Development Administration under Contract No. E(11-1)-2086. L. K. thanks the US–USSR Scientific Exchange Program for supporting a visit to Novosibirsk where preliminary experiments were performed and Dr. A. M. Raitsimring, Dr. Yu. D. Tsvetkov, and R. Samoilova for their help and discussions. We thank Dr. S. Schlick for initial experiments at Wayne State University. L. K. thanks Professor K. Fueki of Nagoya University and the Japanese Society for the Promotion of Science for their support while this manuscript was being completed.

References and Notes

(1) L. Kevan, *Adv. Radiat. Chem.*, **4**, 181 (1974).
(2) S. Schlick, P. A. Narayana, and L. Kevan, *J. Chem. Phys.*, **64**, 3153 (1976).
(3) P. A. Narayana, M. K. Bowman, L. Kevan, V. F. Yudanov, and Yu. D. Tsvetkov, *J. Chem. Phys.*, **63**, 3365 (1975).
(4) B. L. Bales, M. K. Bowman, L. Kevan, and R. N. Schwartz, *J. Chem. Phys.*, **63**, 3008 (1975).
(5) J. E. Bennett, B. Mile, and A. Thomas, *J. Chem. Soc. A*, 1502 (1969).
(6) F. W. Froben and J. E. Willard, *J. Phys. Chem.*, **75**, 35 (1971).
(7) A. Raitsimring, R. Samoilova, and Yu. D. Tsvetkov, private communication.
(8) M. Bowman, L. Kevan, R. N. Schwartz, and B. L. Bales, *Chem. Phys. Lett.*, **22**, 19 (1973).
(9) C. P. Poole, Jr., "Electron Spin Resonance", Wiley-Interscience, New York, N.Y., 1967, Chapter 20.
(10) B. L. Bales, J. Helbert, and L. Kevan, *J. Phys. Chem.*, **78**, 221 (1974).
(11) S. Schlick and L. Kevan, *J. Magn. Reson.*, **22**, 171 (1976).
(12) A. Plonka and L. Kevan, *Chem. Phys. Lett.*, **43**, 489 (1976).
(13) V. F. Yudanov, private communication.

Electron Spin Resonance Studies of Superoxide Ions Produced by Radiolysis in Alcoholic Media

George W. Eastland[†] and Martyn C. R. Symons*

Department of Chemistry, The University, Leicester, LE1 7RH, England *(Received April 19, 1976; Revised Manuscript Received May 3, 1977)*

Air or oxygen saturated alcohols or aqueous alcohols gave O_2^- on exposure to ^{60}Co γ rays at 77 K. These radicals were characterised by low-field parallel ESR features whose g values were solvent dependent. The shift of $g_\parallel$ from 2.0023 was least for aqueous methanol and greatest for cyclohexanol. In some cases slight annealing above 77 K gave an increase in yield and a small shift in $g_\parallel$ toward 2.0023. Dissolution of NaO_2 in these solvents gave well-defined spectra of O_2^- with $g_\parallel$ values identical with the limiting values obtained by radiolysis. On annealing the irradiated glasses the $g_\parallel$ features for O_2^- decayed simultaneously with the growth of features assigned to $HO_2\cdot$ (or $DO_2\cdot$). In some cases $RO_2\cdot$ radicals were also detected. Since the magnitude of $g_\parallel$ is controlled by the strength and direction of the hydrogen bonds, and since the parent dioxygen molecules are not hydrogen bonded, we conclude that solvation is almost completely developed at 77 K in these media within <60 s.

Introduction

The ESR spectrum for the superoxide ion, O_2^-, was measured many years ago by studying commercial sodium peroxide, which often contains NaO_2 as an impurity.[1] The ion is characterised by a low-field parallel feature whose g value is controlled by the magnitude of the crystal-field from the cations. The perpendicular feature is shifted slightly to high field of the free-spin value because of the effect of orbital angular momentum about the z axis.[2]

Oxygen is known to be an extremely efficient electron scavenger, and O_2^-, detected by its ultraviolet absorption, is a well-established transient in pulse-radiolysis studies.[3] However, although peroxy radicals are sometimes detected by ESR spectroscopy in solids containing dissolved oxygen after irradiation, the superoxide ion is not generally reported as a significant radiation product in solid-state studies, and removel of oxygen is not usually thought to be important unless accurate yields are required. It has, however, been previously observed in various protic solvents and the solid-state ESR spectra recorded.[4] Where they overlap, our results agree satisfactorily with these.

We had previously assumed that features for O_2^- were not detected because the perpendicular part of the spectrum would be concealed by intense features from other radicals in the free-spin region, while the parallel feature would be at very low fields and too poorly defined to be detectable. This was because we envisaged O_2^- in the environment of the parent dioxygen molecules rather than in its equilibrium environment. However, the results for trapped electrons (e_t^-) in protic solvents show that, although this would be true at 4.2 K,[15] it is not true at 77 K, at which temperature e_t^- is apparently solvated in a manner similar to that in field solutions.[5-7] On warming above 4.2 K the spectra changed gradually, but the change was complete at ca. 40 K for e_t^- in ethanol.[6]

It therefore seemed probable that O_2^- ions would similarly achieve their normal solvation in rigid protic media, and our results confirm that this is nearly correct. In order to discover the correct values for $g_\parallel$ in the solvents used, we have cooled solutions containing NaO_2 to 77 K.

Experimental Section

Solvents were of the highest grade available, and since traces of water had no effect on the results, they were generally used as supplied. Oxygen was removed either by freeze–pump–thaw sequences or by flushing with pure nitrogen gas.

Superoxide solutions were prepared by adding commercial sodium peroxide (containing some superoxide) to the rigid solvent at 77 K and warming until sufficient had dissolved to give good ESR spectra for O_2^- at 77 K.

Samples were irradiated as small spherical beads or in evacuated quartz tubes at 77 K in a Vickrad ^{60}Co γ ray source for ca. 0.5–1.0 h at a dose rate of 1.7 Mrad h^{-1}.

ESR spectra were measured with a Varian E3 spectrometer at 77 K. Samples were annealed either using a Varian variable temperature accessory, or by allowing the samples to warm above 77 K in the empty insert Dewar, while the spectra were continuously monitored in the region of interest. They were recooled to 77 K whenever significant spectral changes were observed.

Results and Discussion

Values for $g_\parallel$ derived for O_2^- in γ irradiated solvents and for O_2^- obtained from NaO_2 dissolved in the same solvents are listed in Table I. Only in the latter cases could we estimate $g_\perp$, which was always close to 2.002. Typical spectra are given in Figure 1. Both for irradiated methanol and for aqueous methanol at 77 K, $g_\parallel$ was equal to the equilibrium value, but the features were slightly broadened (Table I). On annealing to ca. 90 K they narrowed to the equilibrium widths (16 G). However, the higher alcohols, and especially cyclohexanol, gave parallel features that were shifted down field from the equilibrium position and greatly broadened. Annealing to ca. 100 K resulted in a shift and narrowing to give the equilibrium result.

We found that after scrupulous deoxygenation these parallel features were lost, but that normal procedures still left a small residual peak. Thus this is a fairly sensitive method for testing for oxygen, which is clearly a most efficient scavenger in rigid solvents. However, oxygen saturated ethers gave no trace of O_2^- features under these conditions. We have no doubt that O_2^- is formed readily from dissolved O_2. That it captures electrons in aprotic solvents is well known from pulse radiolysis studies.[3] Our present studies show that there is an induction of several minutes in the growth of the e_t^- signal in the presence, but not the absence, of oxygen, thus confirming that O_2 scavenges electrons in these media. We conclude that well-defined hydrogen bonding is needed to give clear $g_\parallel$ features from trapped O_2^-.

[†] Department of Chemistry, Saginaw Valley State College, University Center, Mich. 48710.

TABLE I: ESR Parameters for O_2^-, HO_2, and $RO_2\cdot$ Radicals in Alcohol Glasses and in Na_2O_2

Radical	Medium	$g_{\|\|}$ (i)[b]	$(g_z)^a$ (ii)[b]	(iii)[b]	$\Delta H(^1/_2)$, G (±1.0 G) (i)[b]	(ii)[b]	(iii)[b]
O_2^-	NaO_2			*ca.* 2.180			*ca.* 60
O_2^-	CD_3OD or CH_3OH	2.075	2.075	2.075	18	16	16
O_2^-	$CD_3OD + D_2O$	2.065	2.065	2.065	19	18	18
O_2^-	CH_3CH_2OH or CD_3CD_2OD	2.080	2.077	2.077	25	15	15
O_2^-	$(CH_3)_2CHOH$	2.089	2.078	2.078	*ca.* 34	22	22
O_2^-	Cyclohexanol	2.092	2.078	*e*	*ca.* 29	24	*e*
O_2^-	Neopentyl alcohol	2.090	2.082	*e*	25	16	*e*
O_2^-	1,4-Butanediol	2.090	2.080	*e*	23	19	*e*
O_2^-	β-D-Glucose	2.088	2.080		25	19	
O_2^-	Glycerol	~2.10	2.072	2.072	*ca.* 50	26	26
O_2^-	Glycol	~2.093	2.075	2.075	*ca.* 35	18	18
RO_2	$(CD_3)_3COD$		2.0332 (av 2.0126)			6	
HO_2	CD_3OH		2.0345[c]			8	
DO_2	CD_3OD		2.0345			8	
HO_2	$SrCl_2\cdot 6H_2O$[f]		2.0355[d]				

[a] $g_\perp$ close to 2.002 for all NaO_2 solutions. (In radiolyses this feature was hidden beneath those for other radicals.) [b] (i) γ radiolysis at 77 K prior to annealing. (ii) After annealing: the changes were usually rapid in the 90-100-K region. (iii) From dilute solutions of NaO_2. [c] $A(^1H)_{\|\|} = 15.5$ G. [d] $A_z(^1H) = 17.2$ G. [e] Insoluble. [f] Reference 10.

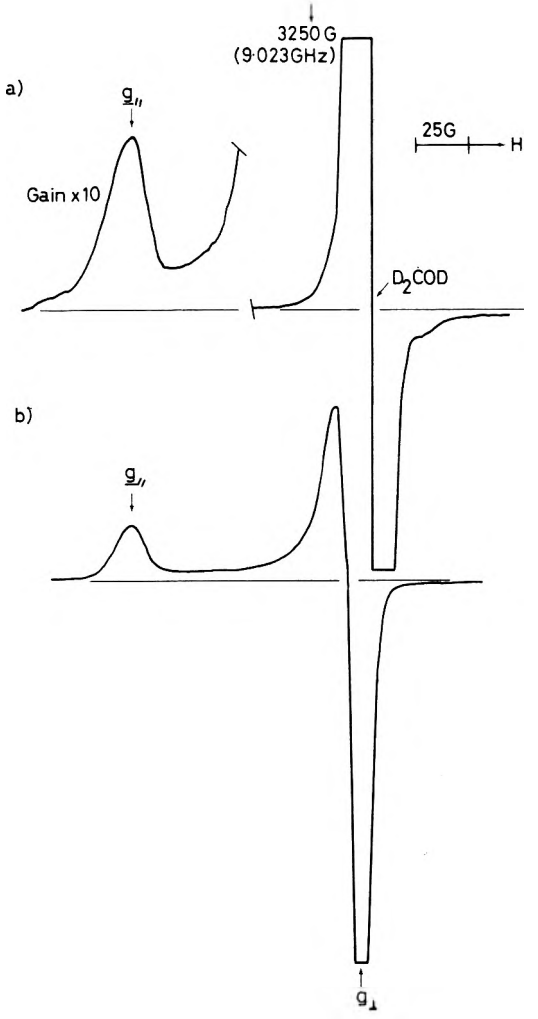

Figure 1. First derivative X-band (ν = 9.023 GHz) ESR spectra for O_2^- in CD_3OD at 77 K; (a) after exposure of $CD_3OD + O_2$ to ^{60}Co γ rays, and (b) from NaO_2 dissolved in CD_3OD.

The superoxide ion has a π^{*3} configuration and would have g values of zero and 4 in the absence of any solvent perturbation. As solvents (or cations) quench the orbital angular momentum, $g_{\|}$ (g_z) should fall from 4 toward 2, while $g_\perp$ should rise from zero toward 2. One way in which solvation can achieve this via hydrogen bonding is shown in I, the configuration being $\pi_y^{*2}\pi_x^{*1}$. Thus, for a spectrum to be detected in the free-spin region there must be strong

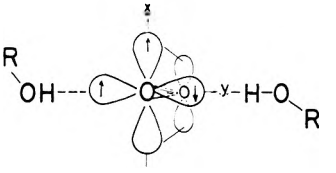

I

asymmetric solvation. An analogous situation is postulated for the stabilization of ·OH radicals in ice.[8]

In addition to the fact that solvation is clearly "switched on" rapidly at 77 K despite the rigidity of the glassy solvents, two other aspects are noteworthy. One is the narrowness of the parallel (z) features. In our experience a half-width of ca. 15 G is not unusual for glasses of this type even when the g values are determined by the molecule and not by the solvent. This suggests a uniform precision in solvation. Since it is often stated that ions have a range of solvation states in the liquid phase, our results are significant, especially since the value of $g_{\|}$ (g_z) depends not only on the precise strength and number of the hydrogen bonds, but also on the symmetry. That is to say that the difference between x and y bonding must also be precise (see I). The other noteworthy aspect is the magnitude of $g_{\|}$ (g_z) compared with that for O_2^- in NaO_2 (see Table I). The shift for NaO_2 is controlled by the differential crystal field from neighboring sodium ions, and this comparison supports the contention that hydrogen bonds can have a stronger effect than cations on the electronic properties of basic molecules or ions, probably because of their highly directional character.

The solvent dependence of $g_{\|}$ follows expectation, with aqueous glasses giving the strongest overall bonding and the bulky alcohols giving the weakest. Since the strengths of individual hydrogen bonds formed by alcohols do not vary greatly,[9] this effect is probably a steric reduction in the number of hydrogen bonds to O_2^- formed at equilibrium.

On annealing, in addition to solvation changes, three chemical reactions involving dioxygen or O_2^- can be anticipated:

$$O_2 + e_t^- \rightarrow O_2^- \quad (1)$$

$$O_2 + R\cdot \rightarrow RO_2\cdot \quad (2)$$

$$O_2^- + ROH \rightleftharpoons HO_2 + RO^- \quad (3)$$

Reactions 1 and 2 will occur when the reactants become mobile, provided complete conversion to O_2^- has not al-

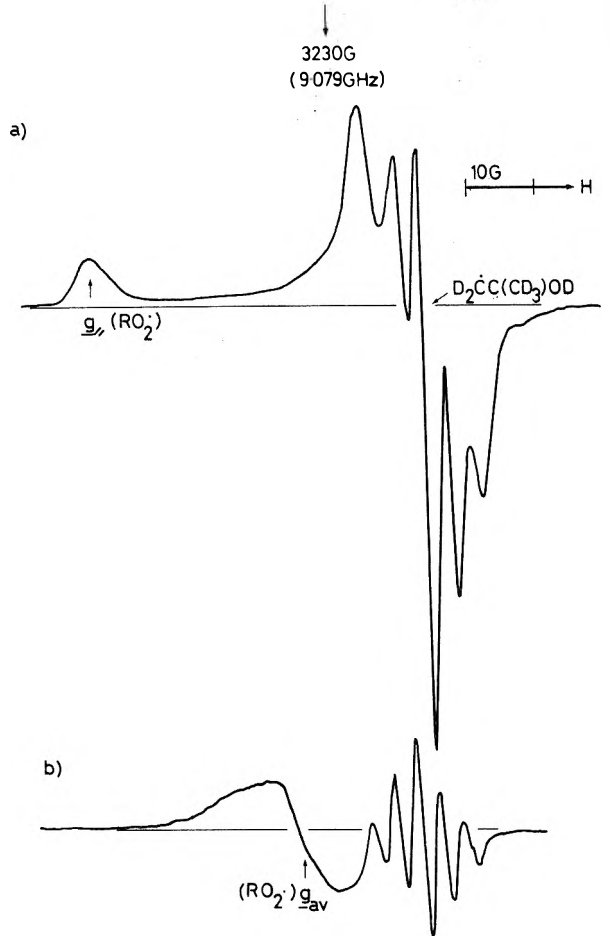

Figure 2. First derivative X-band (ν = 9.079 GHz) ESR spectra for $(CD_3)_3CO_2$· radicals in irradiated $(CD_3)_3COD$ (a) at 77 K, showing the parallel component and (b) at ca. 150 K, showing the absorption for rotating peroxy radicals. The features in the free-spin region are for $D_2\dot{C}$–$C(CD_3)_2OD$ radicals.

ready occurred. We stress that O_2^- formation competes with e_t^- formation in the solid state and e_t^- is not a necessary intermediate. Reaction 1 is unlikely to be a direct tunneling process since we found that the $[O_2^-]$ was independent of time at 77 K even though there were increases as great as a factor of 2 during the annealing process, after allowance had been made for any shift and narrowing. (Indeed, in most instances, reaction 1 occurred only at temperatures 10–20° above those needed to give equilibrium solvation.)

Reaction 2 competes with reaction 1, and when $[O_2]$ was low and the γ-ray dose high, reaction 2 was suppressed. In contrast, when $[O_2]$ was high and the dose relatively low, annealing gave good spectra for RO_2· radicals (Figure 2). These had well-defined $g_{\parallel}$ (g_z) features in the 2.033 region, close to those previously reported.[10] Once formed, these were stable, and during the annealing broad features for the rotating radicals could often be observed, as shown in Figure 2b.

Reaction 3 was difficult to observe unless RO_2· formation was inhibited as described above. Proof that HO_2· rather than RO_2· was then formed comes from the observation of ^1H ($M_I = \pm 1/2$) hyperfine features on the low-field component (Figure 3). Use of ROD solvent removed this splitting, thus confirming that it stems from the transferred proton. The splitting of 15.5 G is close to that reported for HO_2· in a strontium chloride matrix (17.2 G),[11] as is the value for $g_{\parallel}$ (g_z) (Table I). The signals for HO_2· and DO_2· decayed at temperatures below the softening

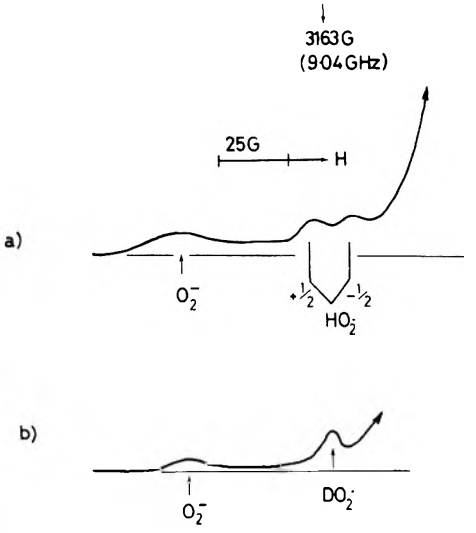

Figure 3. First derivative X-band (ν = 9.04 GHz) ESR spectra for methanol and water (50/50 v/v) after exposure to ^{60}Co γ rays at 77 K and partial annealing (a) for $CD_3OH + H_2O$ showing parallel features for O_2^- and HO_2· and (b) for $CD_3OD + D_2O$, showing parallel features for O_2^- and DO_2·. Central features, not shown, are for ·OH and $D_2\dot{C}OH$ radicals.

point of the glasses in contrast with those for RO_2·. Also, we were unable to detect them in the absence of strong parallel features for O_2^-, suggesting that equilibrium 3 is incomplete under our conditions.

Other Radicals

In all cases, except *tert*-butyl alcohol, central features characteristic of $R_2\dot{C}OH$ radicals were obtained. These have been well characterized in previous studies.[12] Methanol gave the 125-G doublet for $H\dot{C}O$ radicals,[13] but the use of CD_3OD removed these interfering features. For *tert*-butyl alcohol, $H_2\dot{C}C(CH_3)_2OH$ and $(CH_3)_3\dot{C}$ radicals were detected,[14] but again, use of the perdeuterated alcohol removed these features which obscured the features from RO_2· radicals.

Acknowledgment. We thank the Saginaw Valley State College for granting leave of absence to G.W.E., and a referee for helpful comments.

References and Notes

(1) J. E. Bennett, D. J. E. Ingram, M. C. R. Symons, P. George, and J. S. Griffith, *Phil. Mag.*, **46**, 443 (1955).
(2) W. Känzig and M. H. Cohen, *Phys. Rev. Lett.*, **3**, 509 (1959).
(3) E. J. Hart and M. Anbar, "The Hydrated Electron", Wiley-Interscience, New York, N.Y., 1970.
(4) J. E. Bennett, B. Mile, and A. Thomas, *Trans. Faraday Soc.*, **64**, 3200 (1968); D. S. Gorbenko-Germanov and I. V. Kozlova, *Zh. Fiz. Khim.*, **48**, 166 (1974).
(5) M. J. Blandamer, L. Shields, and M. C. R. Symons, *J. Chem. Soc.*, 1127 (1965).
(6) H. Hase, M. Noda, and T. Higashimura, *J. Chem. Phys.*, **54**, 2975 (1971); H. Hase, T. Warashina, M. Noda, A. Namiki, and T. Higashimura, *Ibid.*, **57**, 1039 (1972).
(7) F. S. Dainton, *Chem. Soc. Rev.*, **4**, 323 (1975).
(8) J. A. Brivati, M. C. R. Symons, D. J. A. Tinling, H. O. Wardale, and D. O. Williams, *Trans. Faraday Soc.*, **63**, 2112 (1967).
(9) A. A. Lipovskii and T. A. Dem'yanova, *Radiokhimiya*, **8**, 112 (1966).
(10) See, for example, D. W. Overnall, *J. Phys. Chem. Solids*, **26**, 81 (1965); J. W. Searl, R. C. Smith, and S. J. Wyard, *Proc. Phys. Soc.*, **74**, 1174 (1954); H. Fisher, K. H. Hellvege, and P. Neudörfl, *J. Polym. Sci., Part A*, **1**, 2109 (1963).
(11) R. C. Catton and M. C. R. Symons, *J. Chem. Soc. A*, 1393 (1969).
(12) J. F. Gibson, D. J. E. Ingram, M. C. R. Symons, and M. G. Townsend, *Trans. Faraday Soc.*, **53**, 914 (1957); J. F. Gibson, M. C. R. Symons, and M. G. Townsend, *J. Chem. Soc.*, **2**, 69 (1959).
(13) J. A. Brivati, N. Keen, and M. C. R. Symons, *J. Chem. Soc.*, 237 (1962).
(14) K. V. S. Rao and M. C. R. Symons, *Chem. Phys. Lett.*, **20**, 555 (1973).
(15) Note Added in Proof. We have now established that after exposure to β rays at 4.2 K no O_2^- resonance was observed at this temperature.

Factors Affecting the Conformation of Aromatic Nitro Groups

James R. Holden* and Charles Dickinson

Naval Surface Weapons Center, White Oak Laboratory, Silver Spring, Maryland 20910 *(Received December 15, 1976)*

Publication costs assisted by the Naval Surface Weapons Center

Examination of the conformations of 104 aromatic nitro groups from 43 crystal structure determinations indicates that nitro groups tend to be coplanar with the aromatic ring, but that there is no relationship between the interplanar angle and the length of the C–N bond. Nitro groups have longer C–N bonds than aromatic amine groups. The ring bonds adjacent to a nitro group tend to be shorter than those in unsubstituted benzene, whereas those adjacent to an amine group tend to be longer. An adequate empirical explanation for the observed nitro group positions was attained with a potential energy function which rises 9.0 kcal/mol as a nitro group rotates 84° about its C–N bond from coplanarity with the ring. The agreement between the observed rotation angles and those of minimum calculated energy was further improved by adjustment of the repulsive terms of a reported set of interatomic potential functions. Empirical treatment of the angular distortion functions indicates that at "equilibrium" the O–N–O angle of an aromatic nitro group is 126.4°; the two C–N–O angles are equal; and the two C–C–N angles are equal. Parameters for the energy functions are given.

Introduction

The overall objective of this work was to determine the factors which control the conformation of aromatic nitro groups by intercomparison of the atom positions found by crystal structure determinations. For steric factors, a further objective was to determine empirical force functions for the interaction of nonbonded atoms, distortion of bond angles, and rotation of groups of atoms around single bonds. The present work is limited to nitro groups attached to benzene rings and to compounds containing only carbon, hydrogen, nitrogen, and oxygen. The data are further limited to crystal structure determinations with reported agreement factors (R values) of less than 0.1, and in which all hydrogen atom positions were included in the final refinement.

As has been pointed out, nitro groups have different effects on the benzene ring than other substituent groups where a trigonal nitrogen atom is attached to the ring, e.g., amines. The interior angle at a carbon to which a nitro group is attached is always larger than the nominal 120°.[1,2] This has been attributed to electron withdrawal by the nitro group changing the hybridization of the carbon atom.[2] No such effect is observed with an amine group.

Electron withdrawal by nitro groups situated ortho or para to an amine substituent appears to enhance resonance interaction between the amine and the aromatic ring.[3] There is an inverse correlation between the length of the amine C–N bond and the average length of the adjacent C–C bonds in the ring. The C–N bond is shorter (and the C–C bonds longer) if nitro groups are present at ortho or para positions.[3]

Aromatic nitro groups tend to lie in or near the aromatic plane unless prevented by steric effects. Those with hydrogen atoms at both ortho positions are, on the average, rotated to a smaller angle with the ring plane than those with one nonhydrogen ortho substituent which in turn are rotated less than those with other groups at both ortho positions.[4] Primary amines in ortho positions do not have this effect, probably due to the formation of intramolecular hydrogen bonds.[4] Large rotation angles observed for nitro groups which are not sterically hindered intramolecularly can often be explained by the steric effect of a neighboring molecule in the crystal.[3]

Resonance interaction between the nitro group and the atomatic ring is often cited as the reason for the tendency for nitro groups to assume a coplanar configuration.[5,6] Nagakura, Kojima, and Maruyama[7] have reported spectroscopic evidence for such resonance in nitrobenzene and give 8.4 kcal/mol as the potential energy difference between the coplanar and perpendicular configurations. Trotter[5] estimated that the resonance interaction energy would diminish as the square of the cosine of the angle between the nitro and aromatic group planes, and gave 6.5 kcal/mol as the potential energy difference. Stated in terms of energy increase with nitro group rotation, this function would have the form

$$E_R = C_R(1 - \cos^2 \theta) \tag{1}$$

where θ is the angle of rotation (interplanar dihedral angle) and C_R has the value 6.5 kcal/mol according to Trotter[5] or 8.4 kcal/mol according to Nagakura et al.[7] Dashevsky, Struchkov, and Akopyan[8] proposed $C_R(1 - \cos \theta)$ as the form of the potential energy function and 11 kcal/mol as the value of C_R. However, later Kitaigorodsky and Dashevsky[9] revised the form of the function to $C_R(1 - \cos 2\theta)/2$ which is equivalent to the function given as (1). In this paper an attempt is made to evaluate the magnitude and shape of this potential energy function and determine whether one such expression can adequately account for the observed nitro group rotation angles in the crystal structures of all (or most) nitroaromatic compounds.

In addition to rotation about the C–N bond, the other sterically controlled distortions which must be considered in explaining the conformations of aromatic nitro groups are "wag" of the group about the carbon atom and "wag" of the oxygen atoms about the nitrogen atom. In this paper, "wag" is defined as rotation of an atom around the center of another atom to which it is covalently bonded. If other atoms are also covalently bonded to the atom in motion, they move with it through the same angle in the same direction. The direction of a "wag" is specified by giving component angles in directions specified by the positions of other atoms covalently bonded to the "fulcrum" atom.

Dashevsky et al.[8] proposed the following types of potential energy functions to apply to the components of "wag" motions of the atoms of an aromatic nitro group:

$$E_A = C_A(A_0 - A)^2 \tag{2}$$

$$E_p = C_p \sin^2 B \tag{3}$$

where C_A is a Hooke's law constant associated with a

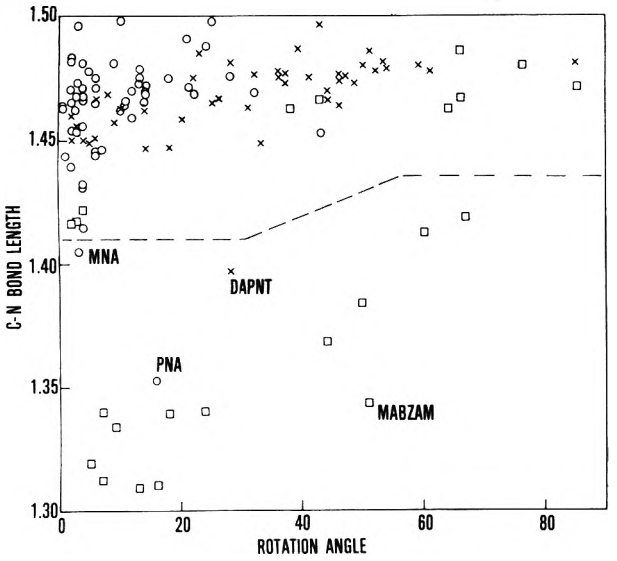

Figure 1. C–N bond length (angstrom units) vs. rotation angle from coplanarity (degrees) for aromatic nitro groups (above dashed line) and amine groups (below dashed line); data from Table I. Circles represent groups with hydrogen at both ortho positions, crosses with hydrogen at one ortho position, and squares with atoms other than hydrogen at both ortho positions.

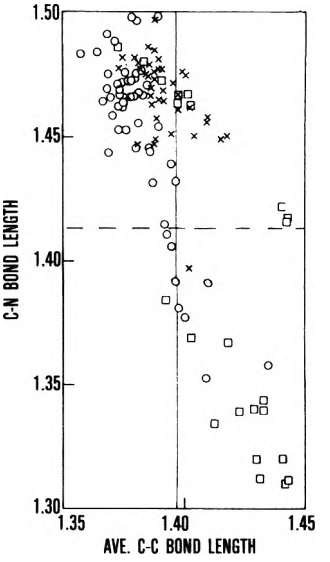

Figure 2. C–N bond length vs. average C–C bond length in adjacent ring bonds (angstrom units) for aromatic nitro groups (above dashed line) and amine groups (below dashed line); data from compounds in Table I. Vertical line is at bond distance reported for benzene (ref 52). Circles, crosses, and squares as in Figure 1.

restoring force on bond angle A toward its ideal value A_0. Values of 52 and 30 kcal/mol·rad were given for C_A for carbon and nitrogen and the A_0 value for all angles was assumed to be 120°. E_p is a potential energy term associated with an assumed force on substituent atoms tending to keep them in the aromatic ring plane. For a nitro group, B is the angle between the C–N bond and the plane of the ring bonds of the carbon atom to which it is attached. A value of 64 kcal/mol was given for C_p.

The other required potential energy functions are those which account for interaction between nonbonded atoms. The energy associated with the strongest attractive force, the van der Waals force, is generally approximated by a term of the type C_{D1}/D^6 where D is the distance between the centers of the atoms. Two types of terms have often been used to account for the repulsive force between atoms at short distances; the Lennard-Jones[10] type, C_{D2}/D^{12}, and the Buckingham[11] type, $C_{D2}\exp(-C_{D3}D)$. Different values of C_{D1}, C_{D2}, and C_{D3} are required for each pair of atom types: e.g., C to C, C to H, C to N, C to O, etc. Several sets of constants have been published. However, the set which served the purposes of this study best was that published by Giglio[12] which uses a combined form of the repulsive force term such that the atomic interaction potential energy function is given as

$$V(r) = a\exp(-br)/r^d - c/r^6 \qquad (4)$$

where r is the distance between atom centers.

Table I contains a list of the crystal structure determinations which have been used in this study. All have the following characteristics: (1) The molecule contains at least one nitro group attached to a benzene ring. (2) The crystal contains only carbon, hydrogen, nitrogen, and oxygen atoms. (3) The positions of all atoms (including hydrogen) were determined and included in the refinement. (4) The structure does not contain a significant amount of disorder. (5) The agreement factor (R value) for the structure determination is less than 0.1. No claim is made that all such structures have been included. Some large molecules containing only one nitro group were omitted intentionally; others have undoubtedly been omitted due to oversight.

Bond Length Correlations

If the observed tendency for aromatic nitro groups to be coplanar with the ring plane is due to resonance interaction, one might expect a correlation between the length of the C–N bond and the angle of rotation of the nitro group out of the ring plane. However, Figure 1 indicates that no such correlation exists. All the points in this plot above the dashed line refer to nitro groups in the compounds listed in Table I. The only obvious observation which might be drawn is that all the shortest C–N bonds are to groups with small angles of rotation. However, the converse is not true; all the small angles of rotation do not correspond to groups with short C–N bonds. The points shown as circles are groups with hydrogen atoms at both ortho positions; those with crosses have one non-hydrogen group at an ortho position; and those with squares have non-hydrogen groups at both ortho positions. As expected[4], most of the circles fall at small angles of rotation and most of the squares fall at large angles of rotation. The three squares at small angles refer to the nitro groups of TATB where amine groups are at both ortho positions.

The points below the dashed line in Figure 1 refer to aromatic amines; that is, other groups where a nitrogen atom is bonded to the benzene ring. These include *N*-methyl-2,4,6-trinitroacetanilide and 1,3-diaziridinyl-2,4,6-trinitrobenzene. The circles, crosses, and squares have the same meaning as with the nitro groups. As had been observed,[3] the presence of nitro groups in ortho or para positions to a primary amine group tends to shorten the C–N bond to the amine. All of the points except those for MNA, PNA, DAPNT, and MABZAM refer to amines with nitro groups in both the ortho and para positions. These points seem to follow a trend of increasing bond length with increasing rotation angle. All of the primary amines have rotation angles less than 20°, the secondary amine from IPRTNA has a rotation angle of 24°, and the tertiary amines have rotation angles greater than 40°. Perhaps steric effects inhibit the resonance interaction of the secondary and tertiary amines with the aromatic ring.

Figure 2 is a plot of the C–N bond lengths for amine groups and nitro groups vs. the average length of the adjacent C–C bonds in the ring. The circles, crosses, and

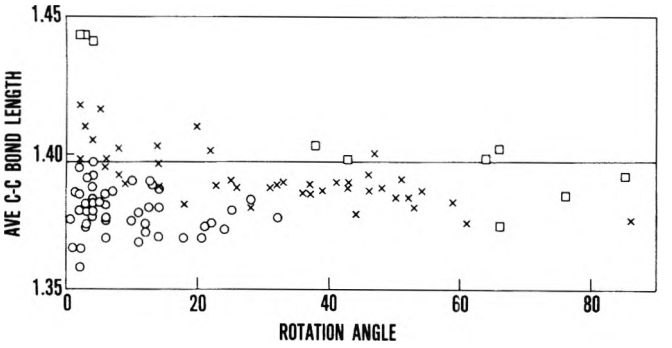

Figure 3. Average C–C bond length of adjacent ring bonds (angstrom units) vs. rotation angle from coplanarity (degrees) for aromatic nitro groups; data from compounds in Table I. Horizonal line at bond length for benzene (ref 52). Circles, crosses, and squares as in Figure 1.

squares have the same meaning as in Figure 1 and again the points for nitro groups are above the dashed line and amine groups below. This, in itself, illustrates the most obvious difference; nitro groups have longer C–N bond lengths than amine groups even though both are bonds between sp^2 carbon atoms and sp^2 nitrogen atoms. The points for the amine groups show the same trend as had been previously noted;[3] that is, increasing C–C length with decreasing C–N length. Here, secondary and tertiary amines are also included. The further relationship to be noted is that the points for the nitro groups (especially those without ortho substituents) appear to form an extention of this trend.

The vertical line in Figure 2 is at 1.397 Å, the bond length which has been given[52] for benzene. Note that most of the average bond lengths adjacent to amine groups are longer than 1.397 Å and most of the average lengths adjacent to nitro groups are shorter. This is also shown in Figure 3 where the horizonal line is drawn at 1.397 Å. Thirteen of the eighteen nitro groups for which the average adjacent C–C bond length is greater than 1.397 Å have one or two amine groups in ortho positions. For these, any tendency of the nitro group to shorten adjacent ring bonds would be counteracted by the tendency of the amine group to lengthen them. The other point illustrated by Figure 3 is that there is no apparent correlation between the rotation angle of the nitro group and the average length of the adjacent ring bonds.

Conformation Calculations

The formation of a crystal involves the attainment of the lowest energy configuration of the molecules consistent with the thermal motion associated with the prevailing temperature. The positions of the atoms are those of lowest potential energy not only for the crystal as a whole, but locally for parts of the molecule as well. For example, if the oxygen atoms of an aromatic nitro group could attain positions of lower potential energy by rotation of the group about the C–N bond, the group would have so rotated during crystal formation. Therefore, the atoms of a crystal are in positions of minimum potential energy with respect to all possible types of movement such as group rotation about a bond or wag of an atom or group of atoms about the atom to which it is attached.

Of course, the atoms and molecules of a crystal undergo all types of thermal motion, but the atomic positions found by means of x-ray or neutron diffraction are time-average locations and should be close to the positions of minimum potential energy. With this premise, it should be possible to derive empirical potential energy functions for the forces which determine the positions of the atoms by comparison of the structures of a number of similar molecules. The best set of functions is that from which potential energy minima are calculated closest to the positions where atoms are actually found by crystal structure determinations.

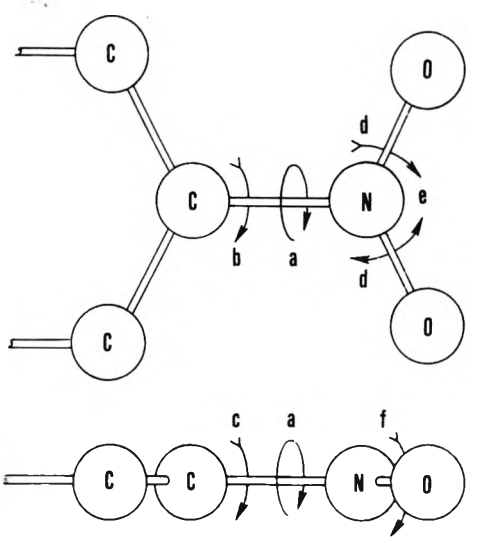

Figure 4. Motions of the aromatic nitro group for which the energy has been minimized: (a) rotation around the C–N bond; (b) wag of the nitro group in the C–C–C plane; (c) perpendicular to the C–C–C plane; (d) concerted wag of the O atoms in the O–N–O plane; (e) opposing wag of the O atoms in the O–N–O plane; (f) wag of the O atoms perpendicular to the O–N–O plane.

The aromatic nitro group is a logical atomic configuration to which to apply this empirical treatment, because the crystal structures of many compounds containing this group have been accurately determined. The 43 structure determinations listed in Table I contain 104 crystallographicly independent nitro groups. Figure 4 illustrates the motions of the nitro group for which potential energy functions have been derived. The way in which the possible motions have been grouped implies assumptions which will be discussed regarding "equilibrium" bond angles and restoring forces counteracting deviations from these angles.

All of the motions listed produce changes in the distances of the atoms of the nitro group from other atoms in the molecule and adjacent molecules in the crystal lattice. Therefore, estimation of the change of the potential energy requires a set of interatomic potential functions. In the interest of calculation speed and simplicity, we chose not to use Giglio's interatomic potential function (eq 4) but rather the following:

$$E_D = C_{d1}/D^6 + C_{d2}/D^{12} + C_{d3}/D^{18} \quad (5)$$

where D is the distance between atom centers. For interactions not involving hydrogen, this is equivalent to Giglio's form if we set $C_{d1} = -c$ and $C_{d3} = 0$ since Giglio assumes $b = 0.0$ and $d = 12$ for these atoms. For interactions involving hydrogen, the coefficients, C_{d2} and C_{d3}, were obtained by least-squares fits of the first derivative of eq 5 (with the first derivative of eq 4) at distances from 2.5 to 4.0 Å at intervals of 0.05 Å. The root-mean-square difference in the first derivatives calculated from the two functions was less than 0.012 kcal/mol·Å for all atom type combinations.

Table II lists the interatomic potential function parameters given by Giglio[12] as adapted to eq 5. All C_{d1} terms are Giglio's "c" with the sign changed. For interactions not involving hydrogen, C_{d2} is Giglio's "a". For interactions involving hydrogen, C_{d2} and C_{d3} were derived from Giglio's data as described above.

In the motions for which the potential energy is minimized in this study, the lengths of all covalent bonds

TABLE I: Nitro Group-Benzene Ring Interplanar Angles for Crystal Structures Used in This Study

Abbrev		Ref	Ring position	Obsd angle	Calcd angle	Rotation angle
ANBPH	4-Acetyl-2′-nitrobiphenyl	13	2	46	41	−5
APNBZM	α-*p*-Nitrobenzaldoxime	14	4	4	4	0
APNPHL	α-*p*-Nitrophenol	15	4	1	5	−6
BPNPCI	Bis(*p*-nitrophenyl)carbodiimide	16	4	12	12	0
			4′	4	4	−4
BPNPHL	β-*p*-Nitrophenol	17	4	7	5	−2
DAPNT	2,6-Diamino-4-nitrotoluene	18	4	(0)		
DIPAM	3,3′-Diamino-2,2′,4,4′,6,6′-hexanitrobiphenyl	19	2	38	38	0
			4	25	28	3
			6	14	13	−1
			2′	66	69	3
			4′	8	2	−6
			6′	9	10	1
DIZI	1,3-Diaziridinyl-2,4,6-trinitrobenzene	20	2	64	63	−1
			4	33	36	3
			6	44	46	2
DNBZWP	3,5-Dinitrobenzoate ester of pyrocalciferol	21	3	13	12	−1
			5	25	24	−1
DNBZPY	2-(2,4-Dinitrobenzyl)pyridine	22	2	32	29	−3
			4	12	6	−6
DNEBZM	2,4-Dinitro-5-ethyleneiminobenzamide	23	2	26	26	0
			4	14	11	−3
DPNPHE	1,1-Di-(*p*-nitrophenyl)ethylene	24	4	14	10	−4
GUPICH	Guanine picrate monohydrate	25	2	5	3	−4
HNABI	2,2′,4,4′,6,6′-Hexanitroazobenzene (form I)	26	2	51	51	0
			4	14	9	−5
			6	39	35	−4
HNABII	2,2′,4,4′,6,6′-Hexanitroazobenzene (form II)	26	2	86	83	11
			4	2	2	0
			6	28	23	−5
			2′	53	54	1
			4′	21	25	4
			6′	37	34	−3
HNCNMT	Methyl 4-hydroxy-3-nitro-*trans*-cinnamate	27	3	6	4	−2
HNSA	2,2′,4,4′,6,6′-Hexanitrostilbene (molecule A)	28	2	48	44	−4
			4	18	18	0
			6	6	11	5
HNSB	(molecule B)		2	14	19	5
			4	21	22	1
			6	43	37	−6
IPRTNA	*N*-Isopropyl-2,4,6-trinitroaniline	19	2	20	27	7
			4	3	5	−6
			6	47	45	−2
MABZAM	*N*-methyl-2-(*N*-methylamino)-3,5-dinitrobenzamide	29	3	3	9	6
			5	4	4	0
MNA	3-Nitroaniline	30	3	2	2	−4
ONBZAM	2-Nitrobenzamide	31	2	46	48	2
OODNT	2,6-Dinitrotoluene	32	2	37	33	−4
			6	52	52	0
PNA	4-Nitroaniline	33	4	2	8	6
PNACPN	4-Nitroacetophenone	34	4	4	4	0
PNBPHN	4-Nitrobiphenyl	35	4	2	2	0
PNBZA	4-Nitrobenzoic acid	36	4	13	11	−2
PNBZIM	*syn*-4-Nitrobenzaldoxime	37	4	4	3	−1
PNDZAB	4-Nitrodiazoaminobenzene	38	4	4	2	−5
PNPACA	4-Nitrophenyl acetate (molecule A)	39	4	3	5	2
PNPACB	(molecule B)		4	11	9	−2
PNPPDZ	1-*p*-Nitrophenyl-3-methylperhydro-2,9-pyridoxazine	40	4	3	5	2
TATB	1,3,5-Triamino-2,4,6-trinitrobenzene	41	2	3	3	−5
			4	2	3	1
			6	4	4	1
TCDDNP	Tetracyclo[5.2.1.$0^{2,6}$,$0^{4,9}$]decan-3-one 2,4-dinitrophenylhydrazone	42	2	4	9	5
			4	4	10	6
TENA	2,3,4,6-Tetranitroaniline	43	2	43	44	1
			3	66	68	2
			4	18	17	−1
			6	2	2	−1
TETRYL	*N*-Methyl-*N*,2,4,6-tetranitroaniline	44	2	23	22	−1
			4	24	25	1
			6	43	38	−5
TNA	2,4,6-Trinitroaniline	3	2	22	20	−2
			4	4	3	−1
			6	8	9	1
TNACTD	*N*-Methyl-2,4,6-trinitroacetanilide	45	2	54	53	−1
			4	4	5	1
			6	36	32	−4

TABLE I: *(Continued)*

Abbrev		Ref	Ring position	Obsd angle	Calcd angle	Rotation angle
TNB A	1,3,5-Trinitrobenzene (molecule A)	46	1	3	8	5
			3	28	22	−6
			5	3	6	−7
TNB B	(molecule B)		1	9	13	4
			3	10	2	−8
			5	6	9	4
TNBBZD	Benzidine 1,3,5-trinitrobenzene molecular complex	47	1	2	4	2
			3	14	2	−12
TNBPYR	Pyrene 1,3,5-trinitrobenzene molecular complex	48	1	6	5	−1
			3	2	2	0
			5	6	3	−3
TNBTAB	1,3,5-Triaminobenzene 1,3,5-trinitrobenzene molecular complex	49	1	10	10	0
			3	0	0	0
			5	6	12	6
TNMX	2,4,6-Trinitro-*m*-xylene	50	2	76	80	4
			4	36	36	0
TNPHTL	2,4,6-Trinitrophenetole	51	2	31	33	2
			4	3	1	−2
			6	61	58	−3
TNTAA	2,4,6-Trinitrotoluene (phase A, molecule A)	28	2	59	58	−1
			4	32	30	−2
			6	41	41	0
TNTAB	(molecule B)		2	46	47	1
			4	22	22	0
			6	50	52	2
		Av rotation				2.9
		Rms rotation				3.8

TABLE II: Interatomic Function Parameters (Giglio,[a] Modified)

Interaction	C_{d_1}, kcal · Å^6/mol	$C_{d_2} \times 10^{-3}$, kcal · Å^{12}/mol	$C_{d_3} \times 10^{-5}$, kcal · Å^{18}/mol
C-C	−327.2	301.0	
C-H	−125.0	77.5	−25.8
C-N	−340.0	340.0	
C-O	−342.3	279.0	
H-H	−49.2	17.4	−7.9
H-N	−132.0	90.1	−30.0
H-O	−132.7	71.4	−21.7
N-N	−354.0	387.0	
N-O	−356.0	316.0	
O-O	−358.5	259.0	

[a] Reference 12.

remain constant. Kitaigorodsky terms this procedure "conformational analysis".[53] No terms are entered into the energy calculation for interactions between bonded atoms. We have made the procedural decision also to exclude terms for "1–3" interactions, interactions between two atoms which are covalently bonded to a common third atom. There is evidence[54] that the effective size of some atoms changes with the angle between the interatomic vector and the covalent bond and these are extreme cases with the "back sides" of the atoms facing one another. Pauling[55] pointed out that the effective radii of atoms are smaller in this direction; therefore the isotropic functions used for intermolecular and other intramolecular interactions would not apply. The 1–3 interatomic forces would essentially parallel those associated with bond angle distortion. By excluding them, we are actually treating their effect as part of the bond angle distortion energy. It should be noted that results derived from nitro group rotation are not affected by this decision because no bond angles or "1–3" distances are changed by this motion.

Giglio[12] introduces another function to account for hydrogen bonds. However, we have used the same type of function as for other atomic interactions but treat "hydrogen bonding hydrogen atoms" (those attached to nitrogen or oxygen; amines or hydroxyl groups) as a different type of atom. At one time we introduced terms to account for the directional character of these interactions but later abandoned them. This is discussed in Appendix A, available as supplementary material.[56] In like manner, we treat nitro group oxygen atoms as a different type atom than the other oxygen atoms of the molecules. The rationale here is that these oxygen atoms carry a partial negative charge due to the internal resonance of the nitro group depicted in Figure 5.

Figure 5. Resonance forms of the nitro group.

A. *Rotation of a Nitro Group About Its C–N Bond.* First it was established that a restoring force toward nitro group coplanarity with the ring plane is required to explain the observed positions of nitro groups. In order to avoid the complication of hydrogen bonding, those compounds containing hydrogen atoms attached to nitrogen or oxygen (amine and hydroxyl groups) were omitted from this part of the study. The interatomic potential parameters listed in Table II were used to calculate the potential energy for each molecule with the nitro groups positioned as found by the crystal structure determination. Each nitro group was then rotated in steps of 1° about its C–N bond until the position of minimum calculated potential energy was found (motion a, Figure 4). The average angle through which a group rotated was 14.9°; the root-mean-square angle was 18.0°. For 52 of the 60 nitro groups treated, the rotation was to a larger angle with the ring plane; that is, a motion which would have been counteracted by a force function acting toward coplanarity. These calculations were performed with a computer code which we named MOLCON, molecular conformation. (See Appendix B.[56])

TABLE III: Interatomic and Rotation Function Parameters Derived without Hydrogen Bonds

Interaction	C_{d_1}, kcal · Å^6/mol	$C_{d_2} \times 10^{-3}$, kcal · Å^{12}/mol	$C_{d_2} \times 10^{-3}$, kcal · Å^{12}/mol
C-O	−342.3	362.7	362.7
H-O	−132.7	24.1	23.5
N-O	−356.0	296.2	295.7
O-O	−358.5	369.7	367.9
Rotation		C_R, kcal/mol	C_R, kcal/mol
NO_2		(8.40)	8.27

The next step was to determine whether this tendency could be corrected by adjustment of the repulsive terms of the interatomic potential functions (C_{d2} and C_{d3} of eq 5). For this operation, we used a second computer code named CONREF, constant refinement. (See Appendix C.[56]) CONREF estimated an angular error (the difference between the true position and the position of minimum calculated energy) for each nitro group by interpolation between calculated positions, and determined the root-mean-square error for all of the nitro groups. The parameters were then adjusted by a steepest-descents procedure to minimize the rms error.

Using the parameters listed in Table II, the rms error estimated by CONREF was 11.7°. Adjustment of the C_{d2} and C_{d3} parameters lowered the estimated rms error to 8.0°, but unrealistic values of these repulsion parameters were produced.

A potential energy function of the type given in eq 1, with a value of C_R of 8.4 kcal/mol, as estimated by Nagakura et al. for nitrobenzene,[7] was then entered into the calculation. With this rotation function and the interatomic parameters from Table II, CONREF gave an estimated rms error angle of 6.2°. Minimization of this error by changing only the value of C_R gave a rms angle of 6.1° with a value of 9.7 kcal/mol for C_R. When the value of C_R was held at 8.4 kcal/mol and the repulsion parameters for the functions involving oxygen were varied, the value of the estimated rms error angle was lowered to 3.65°. When both the rotation and interatomic function parameters were allowed to vary together, the estimated rms angle remained 3.65° because the rotation parameter, C_R, was only changed to 8.27 kcal/mol. These parameters are listed in Table III.

The calculations described above established the fact that a restoring force toward aromatic nitro group coplanarity with the ring is required to explain the nitro group positions which are found in structure determinations. Compounds in which strong hydrogen bonding might be expected were excluded. We then determined whether a simple, nondirectional function for hydrogen bond interactions would allow the positions of the nitro groups of hydrogen bonded molecules to be explained to a comparable degree.

Using all the compounds listed in Table I and the interatomic and rotational parameters listed in Table III, the estimated rms angle between the observed nitro group positions and those of minimum calculated energy was 7.0°. When the hydrogen atoms attached to nitrogen or oxygen were treated as a different atom type "HB" and the separate C_{d2} parameter for the O–HB interactions was refined, the rms angle was lowered to 4.00°. Refinement of all the interatomic and rotational parameters together then lowered the rms angle to 3.91°. This angle, a measure of the agreement between the angles of rotation predicted by the energy calculations and those actually observed, is slightly larger than that obtained for compounds without hydrogen bonds (3.65°). However, since almost twice as many nitro groups were included with the introduction of only one additional parameter, the use of the simple isotropic energy function for hydrogen bonds was considered about as valid as the other assumptions which had been made.

TABLE IV: Interatomic and Rotation Function Parameters Derived from All Structures

Interaction	C_{d_1}, kcal·Å^6/mol	$C_{d_2} \times 10^{-3}$, kcal·Å^{12}/mol
C-O	−342.3	423.4
H-O	−132.7	25.0
HB-O	−132.7	1.45
N-O	−356.0	274.8
O-O	−358.5	365.6
O-OX	−358.5	475.3

Rotation	C_{r_1}[a]	C_{r_2}[a]	C_{r_3}[a]	C_{r_4}[a]
Nitro	1.928	−9.100	0.001	−1.718

[a] In units of kcal/mol.

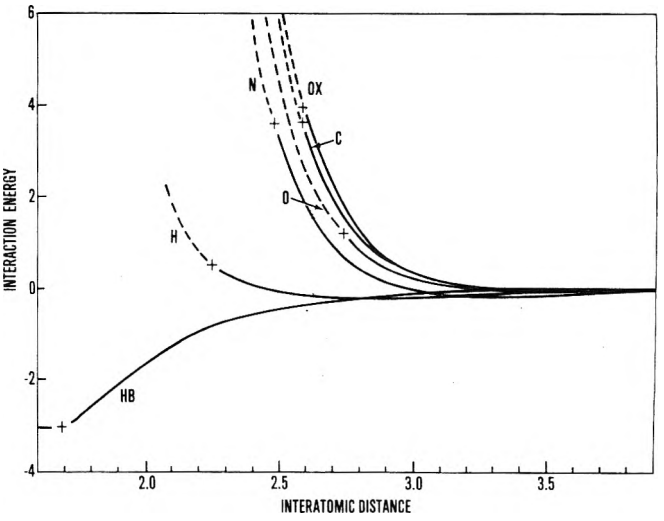

Figure 6. Potential energy (kcal/mol) vs. interatomic distance (angstrom units) for interactions between nitro group oxygen atoms and carbon (C), nitrogen (N), hydrogen bonded to carbon (H), hydrogen bonded to oxygen or nitrogen (HB), nitro oxygen (O), and other oxygen (OX). Crosses mark the shortest distances found in the structures listed in Table I.

Next, the shape of the rotational energy function was examined. To this point we had used the form proposed by Trotter and others,[5,9] eq 1. The following arbitrary generalization of this form was introduced which allows flexibility of the shape while still permitting rapid energy calculation by the computer and parameter adjustment in the same manner used for the other parameters:

$$E_R = -\Sigma C_{ri} + \Sigma C_{ri} \cos^i \theta \qquad (6)$$

The parameter, C_{r2} of eq 6 is equivalent to $-C_R$ of eq 1. Inclusion of three additional parameters in the refinement, C_{r1}, C_{r3}, and C_{r4}, lowered the estimated rms error angle from 3.91 to 3.66°.

The oxygen atoms of a nitro group carry a partial negative charge, because they are involved in the intragroup resonance depicted in Figure 5. Therefore, they might be expected to have different interatomic potential properties than other oxygen atoms. When an additional C_{d2} parameter was added to the calculation to allow the nitro oxygens to be treated as a separate atom type, the estimated rms error angle was lowered to 3.63°. The values obtained from this refinement are listed in Table IV, the interatomic potential functions are plotted in Figure 6, and

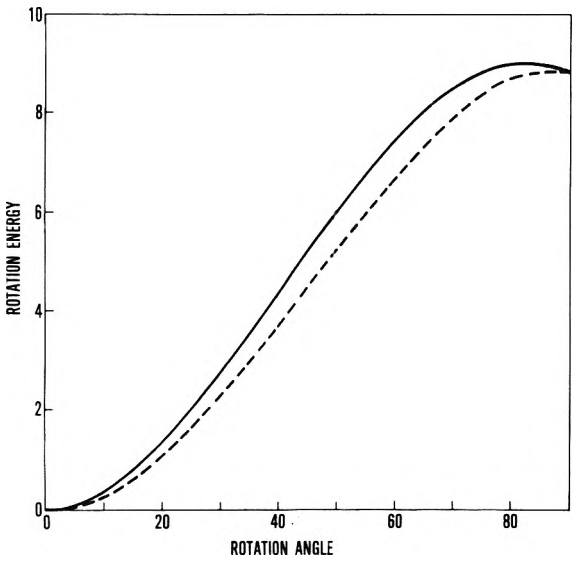

Figure 7. Potential energy of rotation (kcal/mol) vs. rotation angle (degrees) for aromatic nitro groups (solid line). The dashed line is the $(1 - \cos^2 \theta)$ function with the same value at 90°.

the potential energy function for nitro group rotation about the C–N bond is plotted in Figure 7. The $(1 - \cos^2 \theta)$ function is shown as a dashed line in Figure 7 for comparison.

It should be pointed out that the procedure by which the parameters listed in Table IV were obtained only establishes their magnitudes relative to one another and not their absolute magnitudes. The overall scale of the parameters has been set indirectly by using the values of the attractive interatomic potential terms (C_{d1} terms) given by Giglio.[12] The conformation of minimum calculated potential energy for a crystal structure always depends upon a balance between forces and, therefore, is independent of the overall scale of the parameters.

Figure 6 is a plot of the potential energy vs. distance functions for the interactions between nitro group oxygen atoms and the other types of atoms present in the compounds listed in Table I. As explained above, "hydrogen bonding hydrogen atoms", those attached to nitrogen or oxygen, were treated as a different atom type than those attached to carbon. Since nitro group oxygen atoms are hydrogen bond acceptors, the curve for the hydrogen bonding interactions, labeled HB, is very different than the one for the hydrogen atoms attached to carbon, labeled H. The oxygen atoms which were not in nitro groups were also treated as a different atom type. The curve for these atoms is labeled OX. It does not differ greatly from that for interactions to other nitro group oxygens, labeled O. This division produced only a small improvement in the agreement between calculated and observed rotation angles and may not represent physical reality.

The crosses in the curves in Figure 6 mark the shortest interatomic distances between atoms of the designated types found in the structures of the compounds listed in Table I. The empirical method by which these curves were obtained would indicate that hydrogen bonding interactions to nitro oxygens are attractive over the entire observed interatomic distance range. Predicted hydrogen bond lengths are determined by the balance between the O–HB attraction and the repulsive force between the nitro group oxygen and the atom to which the HB is bonded (N or OX) plus other nearby atoms of the molecule.

Comparison of Table IV with Table II indicates that empirical adjustment of the C_{d2} repulsive parameters (see eq 5), to improve the agreement between the calculated and observed nitro group rotation positions, increased the C_{d2} values for carbon and oxygen and decreased those for nitrogen and hydrogen. Figure 6 shows that this reverses the relative effective atomic radii of nitrogen and oxygen from the order given by Pauling.[55] Pauling gives 1.40 Å as the atomic radius of oxygen and 1.50 Å as that of nitrogen which would give 2.80 and 2.90 Å as the contact distances for the O–O and N–O interactions. However, the N–O curve in Figure 6 rises at a shorter interatomic distance than either that for O–O or O–OX. This ordering is not caused by compensation to account for hydrogen bonding since the parameters listed in Table III, obtained from compounds with no hydrogen bonds, show the same effect.

The potential energy function for rotation of a nitro group about its C–N bond as shown in Figure 7 was calculated from the parameters listed in Table IV. The curve reaches a maximum of 8.99 kcal/mol at 84° then declines to 8.89 kcal/mol at 90°. This shallow minimum at 90° is smaller than the accuracy of the derivation and an artifact of the way in which the function was obtained. An adequate description of the results of this determination of the energy associated with the rotation of an aromatic nitro group is that the total potential energy increase on rotation is about 9.0 kcal/mol and that the energy rises rapidly as the group is rotated from coplanarity and reaches its maximum at about 84°.

The final columns of Table I indicate the degree to which the parameters listed in Table IV explain the interplanar angles between the nitro groups and the benzene rings observed in the crystal structure determinations. The first column is the ring position as the compound is named, not necessarily as given in the reference. The second column is the interplanar dihedral angle to the nearest degree between the plane of the nitrogen and oxygen atoms and that of the three carbon atoms as calculated from the atom positions given in the reference. The third column is the dihedral angle after the nitro group is rotated in 1° steps around the C–N bond to the position of minimum calculated energy. The last column is the angle of rotation (minus means toward coplanarity). This may not equal the difference between the preceeding columns when the bonds to nitrogen are not coplanar or when the group has been rotated through 0 or 90°. As indicated, the average rotation angle was 2.9°; the root-mean-square angle was 3.8°.

B. *Distortion of the Bond Angles Associated with the Nitro Group.* As mentioned above, no energy terms were entered for interaction between pairs of atoms covalently bonded to the same third atom, and any effects of such an interaction are included in terms associated with the bond angle between them. It has also been pointed out that the C–C–C angle at a ring atom bearing a nitro group is always greater than 120° possibly due to a change of hybridization caused by the inductive effect of the nitro group. It should also be noted that the O–N–O angles of nitro groups are nearly always greater than 120°. This could be caused by repulsion between the oxygen atoms, or, again, by a change of hybridization of the orbitals of the nitrogen atom. In any case, treatment of the angles at both the carbon and nitrogen atoms requires greater flexibility than would be afforded by eq 2.

It would appear that the equilibrium value for the O–N–O angle is greater than the 120° which would be predicted for trigonal (sp^2) hybridization of the nitrogen atom. In this context, "equilibrium" is the angle which the group would assume if no steric forces were acting on any of its atoms. Actually, each nitro group probably has

its own equilibrium value due to the electronic effects of the other atoms of the molecule. The application of the treatment to be described makes the assumption that these values do not differ so widely that an average value is not an adequate approximation. There is a strong tendency for the nitrogen atom of a nitro group to lie in the plane of the three atoms bonded to it. Therefore, establishment of an "equilibrium" value for the O–N–O angle, A_{ONO}, would also establish "equilibrium" values for the two C–N–O angles, A_{CNO}. That is, $A_{CNO} = {}^1/_2(360 - A_{ONO})$. Energy terms of the type given in eq 2 could be used for all three angles to account for displacement of the oxygen atoms in the nitro group plane. However, an alternate approach was taken. An energy term of this type was used for the O–N–O angle, but it was assumed that the "equilibrium" condition for the two C–N–O angles was when they were equal to one another. It was further assumed that the displacement energy increased with the square of the difference between the C–N–O angles. An additional term of the type of eq 3 was included for nonplanar distortion of the three bonds of the nitro group. The complete energy function for the angles of the nitrogen atom is then

$$E_A = C_{n1}(A_{ONO0} - A_{ONO})^2 + C_{n2}(A_{CNO1} - A_{CNO2})^2 + C_{n3}\sin^2 B_C \quad (7)$$

where A_{ONO0} is the "equilibrium" value of the O–N–O angle, A_{ONO} is its observed value, A_{CNO1} and A_{CNO2} are the two observed C–N–O angles, and B_C is the angle between the C–N bond and the plane of the nitrogen and oxygen atoms.

The bond angles at the ring carbon atom to which a nitro group is attached were treated in a similar way. It was assumed that the "equilibrium" position of the nitro group was with the nitrogen atom in the plane of the three carbon atoms of the ring and with the two C–C–N angles equal to one another. The corresponding energy terms are independent of the value of the C–C–C angle within the benzene ring. No attempt was made in this study to explain the shapes of the benzene rings; therefore, no energy term was included for distortion of the C–C–C angle. The energy function for the angles of the carbon atom is then

$$E_A = C_{c1}(A_{CCN1} - A_{CCN2})^2 + C_{c2}\sin^2 B_N \quad (8)$$

where A_{CCN1} and A_{CCN2} are the C–C–N angles and B_N is the angle between the C–N bond and the plane of the three carbon atoms.

As has been pointed out, a basic assumption of this study is that the atomic positions found by a crystal structure determination are positions of minimum potential energy with respect to any type of motion by parts of the molecule. Therefore, types of motion were chosen to single out the various angle parameters for adjustment (see Figure 4). A value of C_{c1} was derived by CONREF to minimize the sum of the squares of the angles between the observed nitrogen positions and those of minimum calculated energy (motion b, Figure 4). In like manner, C_{c2} was chosen to minimize the error angles for motion c, Figure 4. In both cases, parameters from Table IV were used for interactions involving oxygen and parameters from Table II were used for other interactions involving nitrogen. Results are given in Table V.

The C_{n1}, A_{ONO0}, and C_{n2} parameters for the bond angles of nitrogen (see eq 7) were derived by CONREF by minimizing the error angles for motions d and e in Figure 4. Concerted wags change the difference between the C–N–O angles without changing the O–N–O angle. Opposing wags change the O–N–O angle without changing the difference between the C–N–O angles. The C_{n3} parameter was obtained by minimizing the error angles for motion f, Figure 4. All of these parameters are listed in Table V along with the estimated rms angles between the calculated and observed atom positions when moved in the way used to derive each parameter.

TABLE V: Bond Angle Distortion Function Parameters

Central atom	Angle	Symbol	Value	Rms error, deg
C	C-C-N	C_{c1}	81 kcal/mol · rad	0.69
	C-N-plane	C_{c2}	107 kcal/mol	1.23
N	O-N-O	A_0	126.4°	
		C_{n1}	134 kcal/mol · rad²	0.61
	C-N-O	C_{n2}	307 kcal/mol · rad²	0.47
	N-C-plane	C_{n3}	230 kcal/mol	1.58

C. *Rotation of Primary Aromatic Amine Groups About the C–N Bond.* The group of crystal structures listed in Table I was assembled for the study of aromatic nitro groups. However, these structures contain 10 crystallographicly independent primary aromatic amine groups. As with the nitro group, rotation of an amine group about its C–N bond involves no bond angle changes and all the interatomic separation changes involve one type of atom, hydrogen. Using the C–H, H–H, and N–H interatomic function parameters from Table II and the O–HB parameters from Table IV, MOLCON was used to find the rotation angles from the observed hydrogen positions to those of minimum calculated potential energy. Eight of the 10 amine groups were rotated to larger interplanar angles with the benzene ring, and the average angle of rotation was 32°. (The root-mean-square rotation angle was 41°.) Introduction of the same rotational function as that found for the nitro group lowered the rms error angle as estimated by CONREF to 7.4°.

Adjustment of the magnitude of the energy of rotation but not the shape of the function by means of CONREF gave a value of 9.6 kcal/mol (as compared to 8.99 kcal/mol for the nitro group) with no significant change in the rms error angle. Refinement of the C_{d2} interatomic parameters (see eq 5) for the C–H, H–H, and N–H interactions along with the magnitude of the rotation energy lowered the estimated rms angle to 5.6°. The values found were 90 300, 686, and 38 000 kcal Å^{12}/mol and 7.0 kcal/mol. However, since these were obtained from only 10 amine groups, they are much less reliable than the values listed in Table IV. The fact that the rms error angle for the amine groups is larger than that obtained for the nitro groups might be caused by two factors: (1) The positions of hydrogen atoms are not determined as accurately by x-ray diffraction as those of oxygen atoms. (2) The energy required to rotate an amine group may depend more on the other groups present on the benzene ring than the energy required to rotate a nitro group. Figure 2 shows that there is a wider variation in the lengths of the C–N bonds.

D. *Rotation of Phenyl Groups About a Biphenyl Linkage.* Three of the compounds listed in Table I contain the biphenyl linkage. These provide six crystallographicly independent phenyl groups from which to assess the energetic effect of rotation of such a group about the C–C bond with another phenyl group. Using the interatomic parameters listed in Table IV, and those in Table II for the interactions not treated in this study, the estimated

rms rotation angle from the observed positions to those of minimum calculated energy was only 2.1°. This error angle was only lowered to 2.0° by including a rotation function with a magnitude of 1.8 kcal/mol. Therefore, based on this limited data, it would appear that no rotation energy function is required to explain the interplanar angles found in biphenyl compounds.

In a conformational study of biphenyl, Dashevsky and Kitaigorodsky[57] use $9(1 - \cos\theta)$ kcal/mol as the energy function for rotation about the central bond. However, they state that 9 is an "assumed" value. Adrian[58] uses 4 kcal/mol as the energy difference between the coplanar and perpendicular conformations, a value which he attributes to Wheland.[59] Any definite statement about the energy involved in such rotations must be based on far more data than contained in Table I.

Summary

The C–N bond lengths for aromatic nitro groups are longer than the C–N bond lengths for aromatic amines. There is no correlation between the C–N bond length for a nitro group and the interplanar angle between the plane of the nitro group and that of the aromatic ring. However, there appears to be such a correlation for amine groups which have nitro groups at their ortho and para positions. The average length of the C–C bonds in the aromatic ring on either side of a nitro group is usually shorter than 1.4 Å. The average length of the bonds adjacent to an amine group is usually longer than 1.4 Å. There is an inverse correlation between the C–N bond length of an amine group and the average length of the adjacent ring bonds. Nitro groups with hydrogen atoms at their ortho positions appear to fall on an extention of this trend line.

A potential energy function which rises with nitro group rotation out of the aromatic plane is required to explain the positions found for aromatic nitro groups in crystal structure determinations. The shape of this function which best explains the observed positions rises more sharply at small angles of rotation than the suggested $(1 - \cos^2\theta)$, and reaches its maximum at about 84°. The conventional "6–12" atomic interaction functions are adequate to explain the nitro group positions. Adjustment of the repulsive terms, for the best fit between calculated and observed nitro group rotations indicates that, contrary to the usually accepted van der Waals radii, the O–N effective contact distance is shorter than the O–O contact distance.

The usual Hooke's law treatment of bond angle distortion is adequate to explain the nitro group conformations. The "equilibrium" value of the O–N–O angle of the nitro group was found to be 126.4°. The C–C–N and C–N–O angles were considered to be in their equilibrium condition when the two equivalent angles for a nitro group were equal to one another.

The potential energy increase involved in rotation of an aromatic amine group out of the aromatic plane appears to be about the same as for a nitro group. However, limited data from three compounds in Table I indicate that no such energy is involved in rotation about the central bond of a biphenyl compound.

Acknowledgment. The authors gratefully acknowledge the Independent Research Fund, Task IR-144, of the Naval Surface Weapons Center for financial support of this work.

Supplementary Material Available: Appendices A, B, and C containing a description of calculation considerations, the molecular conformation program, and the constants refinement program (8 pages). Ordering information is available on any current masthead page.

References and Notes

(1) A. S. Bailey and C. K. Prout, *J. Chem. Soc.*, 4867 (1965).
(2) O. L. Carter, A. T. McPhail, and G. A. Sim, *J. Chem. Soc. A*, 822 (1966).
(3) J. R. Holden, C. Dickinson, and C. M. Bock, *J. Phys. Chem.*, **76**, 3597 (1972).
(4) J. R. Holden and C. Dickinson, *J. Phys. Chem.*, **73**, 1199 (1969).
(5) J. Trotter, *Can. J. Chem.*, **37**, 905 (1959).
(6) J. Trotter, *Tetrahedron*, **8**, 13, (1960).
(7) S. Nagakura, M. Kojima, and Y. Maruyama, *J. Mol. Spectrosc.*, **13**, 174 (1964).
(8) V. G. Dashevsky, Yu. T. Struchkov, and Z. A. Akopyan, *Zh. Struk. Khim.*, **7**, 594 (1966).
(9) A. I. Kitaigorodsky and V. G. Dashevsky, *Tetrahedron*, **24**, 5917 (1968).
(10) J. E. Lennard-Jones, *Physica*, **4**, 941 (1937).
(11) R. A. Buckingham, *Proc. Roy. Soc. London, Ser. A*, **168**, 264 (1938).
(12) E. Giglio, *Nature (London)*, **222**, 339 (1969).
(13) H. H. Sutherland, J. H. C. Hogg, and D. J. Williams, *Acta Crystallogr., Sect. B*, **30**, 1562 (1974).
(14) F. Bachechi and L. Zambonelli, *Acta Crystallogr., Sect. B*, **29**, 2598 (1973).
(15) P. Coppens and G. M. J. Schmidt, *Acta Crystallogr., Sect. B*, **18**, 62 (1965).
(16) A. T. Vincent and P. J. Wheatley, *J. Chem. Soc., Perkin Trans. 2*, 1567 (1972).
(17) P. Coppens and G. M. J. Schmidt, *Acta Crystallogr.*, **18**, 654 (1965).
(18) J. R. Holden and C. W. Dickinson, to be published.
(19) C. Dickinson and J. R. Holden, to be published.
(20) C. Dickinson and J. R. Holden, unpublished results.
(21) A. J. de Kok and C. Romers, *Acta Crystallogr., Sect. B*, **31**, 1535 (1975).
(22) K. Seff and K. N. Trueblood, *Acta Crystallogr., Sect. B*, **24**, 1406 (1968).
(23) J. Iball, S. N. Scrimgeour, and B. C. Williams, *Acta Crystallogr., Sect. B*, **31**, 1121 (1975).
(24) G. Casalone and M. Simonetta, *J. Chem. Soc. B*, 1180 (1971).
(25) C. E. Bugg and U. Thewalt, *Acta Crystallogr., Sect. B*, **31**, 121 (1975).
(26) E. J. Graeber and B. Morosin, *Acta Crystallogr., Sect. B*, **30**, 310 (1974).
(27) A. W. Hanson, *Acta Crystallogr., Sect. B*, **31**, 1963 (1975).
(28) J. R. C. Duke, unpublished results.
(29) M. Mathew and G. J. Palenik, *Acta Crystallogr., Sect. B*, **30**, 2381 (1974).
(30) A. C. Skapski and J. L. Stevenson, *J. Chem. Soc., Perkin Trans. 2*, 1197 (1973).
(31) K. Fujimori, T. Tsukihara, Y. Katsube, and J. Yamamoto, *Bull. Chem. Soc. Jpn.*, **45**, 1564 (1972).
(32) C. Dickinson and J. R. Holden, to be published.
(33) K. N. Trueblood, E. Goldish, and J. Donohue, *Acta Crystallogr.*, **14**, 1009 (1961).
(34) J. K. S. Kim, E. R. Boyko, and G. B. Carpenter, *Acta Crystallogr., Sect. B*, **29**, 1141 (1973).
(35) G. Casalone, A. Gavezzotti, and M. Simonetta, *J. Chem. Soc., Perkin Trans. 2*, 342 (1973).
(36) S. S. Tavale and L. M. Pant, *Acta Crystallogr., Sect. B*, **27**, 1479 (1971).
(37) L. Brehm and K. J. Watson, *Acta Crystallogr., Sect. B*, **28**, 3646 (1972).
(38) Yu. D. Kondrashev, *Zh. Struk. Khim.*, **15**, 517 (1974).
(39) R. Guttormson and B. E. Robertson, *Acta Crystallogr., Sect. B*, **28**, 2702 (1972).
(40) C. S. Huber, *Acta Crystallogr., Sect. B*, **28**, 37 (1972).
(41) H. H. Cady and A. C. Larson, *Acta Crystallogr.*, **18**, 485 (1965).
(42) J. Potenza, D. Mastropaolo, D. Gallaher, and T. Henderson, *Acta Crystallogr., Sect. B*, **31**, 1975 (1975).
(43) C. Dickinson, J. M. Stewart, and J. R. Holden, *Acta Crystallogr.*, **21**, 663 (1966).
(44) H. H. Cady, *Acta Crystallogr.*, **23**, 601 (1967).
(45) G. G. Christoph and E. B. Fleischer, *Acta Crystallogr., Sect. B*, **29**, 121 (1973).
(46) C. S. Choi and J. E. Abel, *Acta Crystallogr., Sect. B*, **28**, 193 (1972).
(47) N. Tachikawa, K. Yakushi, and H. Kuroda, *Acta Crystallogr., Sect. B*, **30**, 2770 (1974).
(48) C. K. Prout and I. J. Tickle, *J. Chem. Soc., Perkin Trans. 2*, 734 (1973).
(49) F. Iwasaki and Y. Saito, *Acta Crystallogr., Sect. B*, **26**, 251 (1970).
(50) J. H. Bryden, *Acta Crystallogr., Sect. B*, **28**, 1395 (1972).
(51) C. M. Gramaccioli, R. Destro, and M. Simonetta, *Acta Crystallogr., Sect. B*, **24**, 129 (1968).
(52) A. Langseth and B. P. Stoicheff, *Can. J. Phys.*, **34**, 350 (1956).
(53) A. I. Kitaigorodsky, "Molecular Crystals and Molecules", Academic Press, New York, N.Y., 1973.
(54) S. C. Nyburg and J. T. Szymanski, *Chem. Commun.*, 669 (1968).

(55) L. Pauling, "Nature of the Chemical Bond", 3rd ed, Cornell University Press, Ithaca, N.Y., 1960.
(56) See paragraph at end of text regarding supplementary material.
(57) V. G. Dashevsky and A. I. Kitaigorodsky, *Theor., Eksp. Khim.*, **3**, 43 (1967).
(58) F. J. Adrian, *J. Chem. Phys.*, **28**, 608 (1958).
(59) G. W. Wheland, "Resonance in Organic Chemistry", Wiley, New York, N.Y., 1955, p 132.

Ionic and Electrical Conductances in Polyelectrolyte Solutions

A. Schmitt,* R. Varoqui, and J. P. Meullenet

CNRS, Centre de Recherches sur les Macromolécules, 6, rue Boussingault, Strasbourg, France *(Received June 28, 1976; Revised Manuscript Received May 18, 1977)*

Publication costs assisted by Centre de Recherches sur les Macromolecules

A phenomenological theory of electrical transport in polyelectrolyte-plus-salt solutions is developed. The treatment is based on linear force–flux relationships by using binary frictional coefficients within the framework of linear nonequilibrium thermodynamics. Correlations between conductances and reduced self-diffusion coefficients of counterions and coions are established without taking recourse to an explicit model, and former theories on the subject are generalized. In particular, it is shown that the "intrinsic conductivity" of a polyelectrolyte in excess-of-salt solutions may be related in a simple way to the electrophoretic mobility of the polyion, the transport parameters of small ions in pure salt solutions, and to the lowering of the self-diffusion coefficient of small ions in the presence of the polyelectrolyte. A comparison with recent experimental results displays semiquantitative agreement.

I. Introduction

The study of the correlation between electrophoretic and self-diffusion ionic mobilities in polyelectrolyte, salt-free, solutions started with the pioneering work of Huizenga, Grieger, and Wall,[1] who proposed a simple equation to interrelate their experimental data. Manning[2] was the first to establish the HGW equation on theoretical grounds and to discuss its physical significance by considering a model polyelectrolyte solution. His result was later generalized by Schmitt and Varoqui,[3] using a phenomenological approach.

When a low-molecular-weight salt is present, a great variety of experiments, ranging from the salt-free to the excess-of-salt conditions, is in principle available. However, not many extensive results have been published to enable the same kind of interrelations to be made. It is the purpose of the present paper to establish general equations interrelating ionic mobilities, and to propose some guidelines for a more systematic experimental investigation. A comparison is made with the recent work of Devore and Manning[4] who extended the results of the Manning theory.

II. Theory

(1) *The Polyelectrolyte Solution.* Let us consider an aqueous solution containing a monodisperse polyelectrolyte and a low-molecular-weight salt of concentrations c_p and c_σ, respectively.

The valences (z) of the mutual counterion (1), coion (2), and polyelectrolyte (3) are z_1, z_2, and z_{3s}, respectively. The conditions of electroneutrality are

$$z_1\nu_s + z_{3s}\nu_3 = 0 \tag{1}$$

$$z_1\nu_1 + z_2\nu_2 = 0 \tag{2}$$

where ν_1 and ν_2 are the number of counterions and coions, respectively, per salt molecule and ν_s and ν_3 are the number of counterions and polyions per polyelectrolyte molecule ($\nu_3 = 1$). From a thermodynamic point of view,[3,5] some counterions might have to be considered as part of the polyion. The effective valence of the polyion is then z_3 ($z_3 \leq z_{3s}$), and the number of free counterions per polyelectrolyte molecule ν, so that the fraction f of free counterions per polyelectrolyte molecule is

$$f = \nu/\nu_s = z_3/z_{3s} \tag{3}$$

Finally, we express the stoichiometric fraction, x, of counterions belonging to the polyelectrolyte

$$x = \nu_s c_p/(\nu_s c_p + \nu_1 c_\sigma) \tag{4}$$

x ranges from 0 (excess-of-salt limit) to 1 (salt-free solution).

(2) *Correlation of Ionic Conductances.* (a) *Basic Equations.* When a uniform and constant electric field is applied to a homogeneous ionic solution, the algebraic ionic diffusion fluxes, J_i, are proportional to the applied field strength, ϵ, in the linear approximation[6]

$$J_i = c_i v_i = c_i u_i \epsilon \qquad (i = 1, 2, 3) \tag{5}$$

v_i and u_i are the mean algebraic velocity and mobility of ionic species i, with respect to the solvent.

If f differs from unity, we suppose that the bound ions move with the polyion, so that the stoichiometric counterion flux, J_{1s}, is expressed as

$$J_{1s} = J_1 + J_3(\nu_s - \nu) \tag{6}$$

With eq 3, 4, and 6, the relation between measured and effective counterion mobilities is

$$u_{1s} = [1 - x(1 - f)]u_1 + x(1 - f)u_3 \tag{7}$$

Let us finally define the ionic equivalent conductances (positive quantities) by

$$\lambda_i = \frac{z_i}{|z_i|}\mathfrak{F}u_i \qquad (i = 1, 1s, 2, 3) \tag{8}$$

$\mathfrak{F}$ is the Faraday constant.

(b) *Equivalent Conductance of the Coion.* Correlations between the various ionic mobilities are easily obtained through the friction coefficient formalism. Under the conditions stated in section II 2(a), it expresses that the electrical force applied to 1 mol of an ion is balanced by the frictional forces with other mobile species. As applied to the coion, the multicomponent equation gives[7]

$$z_2\mathcal{F}\epsilon = f_{21}(v_2 - v_1) + f_{23}(v_2 - v_3) + f_{2w}v_2 \qquad (9)$$

where f_{ij} is the molar friction coefficient between substance i and substance j and where the subscript w signifies the component water. We can thus calculate the coion mobility[9]

$$u_2 = (1/f_2)(z_2\mathcal{F} + u_1 f_{21} + u_3 f_{23}) \qquad (10)$$

where f_2 is the total friction coefficient of the coion with its environment, i.e.

$$f_2 = f_{2w} + f_{21} + f_{23} \qquad (11)$$

Let us now make a perturbation approximation and suppose that, for small values of x, f_{2w} and f_{21} have the same values as those in a pure salt solution of concentration c_σ. Thus, the frictional interaction between the coions and the polyion appears only through the f_{23} coefficient.

We denote with superscript σ quantities relative to a pure salt solution of concentration c_σ, so that

$$f_2 \simeq f_2^\sigma + f_{23} = f_{21}^\sigma + f_{2w}^\sigma + f_{23} \qquad (12)$$

After some rearrangement, eq 10 can be rewritten in the form

$$\lambda_2 = \lambda_2^\sigma\rho_2 + \lambda_3(1 - \rho_2) - (\lambda_1 - \lambda_1^\sigma)\rho_2(f_{21}^\sigma/f_2^\sigma) \qquad (13)$$

where ρ_2 is the reduced self-diffusion coefficient of the coion due to the presence of polyion.[10]

$$\rho_2 = f_2^\sigma/f_2 = D_2/D_2^\sigma \qquad (14)$$

D_2 and D_2^σ are the diffusion coefficients of coions in polyelectrolyte and in pure salt solution, respectively.

(c) *Equivalent Conductance of the Counterion.* Using the same method and symbols as before, an equation similar to (13) is obtained for the effective ionic conductance of counterions:

$$\lambda_1 = \lambda_1^\sigma\rho_1 - \lambda_3(1 - \rho_1) - (\lambda_2 - \lambda_2^\sigma)\rho_1(f_{12}^\sigma/f_1) \qquad (15)$$

However, when some counterions are bound to the polyion, λ_1 cannot be measured, but only the stoichiometric value λ_{1s} can be obtained. Let us use the following relation between ρ_1 and ρ_{1s}:[5]

$$\rho_{1s} = \rho_1[1 - x(1 - f)] \qquad (16)$$

which is valid if the self-diffusion mobility of the polyion is negligible compared to that of the free ion. Using eq 7, 15, and 16, we obtain

$$\lambda_{1s} = \lambda_1^\sigma\rho_{1s} - \lambda_3(1 - \rho_{1s}) - (\lambda_2 - \lambda_2^\sigma)\rho_{1s}(f_{12}^\sigma/f_1^\sigma) \qquad (17)$$

(d) *Electrical Conductance of the Polyelectrolyte Solution.* The electrical conductance of the homogeneous solution is defined by

$$K = \frac{I}{\epsilon} = \frac{\mathcal{F}}{\epsilon}\sum_i z_i J_i \qquad (i = 1s, 2, 3) \qquad (18)$$

which, with eq 5, 7, and 8 can be rearranged to

$$K = |z_1|[c_\sigma\nu_1(\lambda_{1s} + \lambda_2) + c_p\nu_s(\lambda_{1s} + \lambda_3)] \qquad (19)$$

If K^σ is the electrical conductance of a pure salt solution, of the same concentration c_σ, the difference in the electrical conductances of the two solutions can be written as

$$K - K^\sigma = |z_1|c_p\nu_s\left[\frac{1 - x}{x}(\lambda_{1s} - \lambda_1^\sigma + \lambda_2 - \lambda_2^\sigma) + \lambda_{1s} + \lambda_3\right] \qquad (20)$$

This equation will be useful in studying the limiting behavior when an excess of salt is present, as we will now see.

(e) *Conductances in the Excess-of-Salt Limit.* The excess-of-salt limit is characterized by $x << 1$. The reduced diffusion coefficients, ρ_i, can be expanded in a power series of x and, if we limit ourselves to first-order terms, we may write

$$\rho_i = 1 - k_i x + O(x^2) \qquad (i = 1, 1s, 2) \qquad (21)$$

If we replace these expressions in eq 13, 17, and 20, we can obtain the slope, s, of the conductance vs. x curve, in the limit of small x and obtain to a good approximation:[12]

$$s_{1s} = \lim\left(\frac{\lambda_{1s} - \lambda_1^\sigma}{x}\right) = -\left[k_{1s}(\lambda_1^\sigma + \lambda_3) - k_2\frac{f_{12}^\sigma}{f_1^\sigma}(\lambda_2^\sigma - \lambda_3)\right] \qquad (22a)$$

$$s_2 = \lim\left(\frac{\lambda_2 - \lambda_2^\sigma}{x}\right) = -\left[k_2(\lambda_2^\sigma - \lambda_3) - k_1\frac{f_{21}^\sigma}{f_2^\sigma}(\lambda_1^\sigma + \lambda_3)\right] \qquad (22b)$$

$$s_K = \lim\left(\frac{K - K^\sigma}{|z_1|c_p\nu_s}\right) = \left[\lambda_1^\sigma\left(1 - k_{1s} + k_1\frac{f_{21}^\sigma}{f_2^\sigma}\right) + \lambda_2^\sigma k_2\left(\frac{f_{12}^\sigma}{f_1^\sigma} - 1\right) + \lambda_3\left(1 + k_2 - k_{1s} + k_1\frac{f_{21}^\sigma}{f_2^\sigma} - k_1\frac{f_{12}^\sigma}{f_1^\sigma}\right)\right] \qquad (22c)$$

III. Discussion

Our main interest is study the excess-of-salt limit, for two reasons. First, we know that our approach is strictly valid in this limit, and so are the self-diffusion theories we would like to test. Second, our aim is to study the limiting transport coefficients characterizing the polyion and we showed that, in addition to the polyion's hydrodynamic friction coefficient, f_{3w}, the ionic friction coefficients f_{3i} (i = 1, 2) might play an important role if self-diffusion theories are correct.[13,14] However, since a direct experimental test of these theories appears to be problematic in the excess-of-salt limit, because of accuracy problems, the indirect test via the more precisely obtained s_K parameter seems to be appropriate.

1. *Comparison with the Manning–Devore Theory.* If we neglect the last terms on the right-hand side of eq 13 and 17, by setting $f_{ij} = 0$, our formulas are formally similar to the ones obtained by Devore and Manning.[4] Thus it appears, as stated by these authors, that the DM theory is strictly valid in the limit of vanishing salt concentration. However, as c_σ increases in the polyelectrolyte solution, two differences appear with regards to their formulation: (1) the λ_i^σ conductances are no longer limiting ones, but correspond to a pure salt solution of concentration c_σ, a correction suggested by Devore and Manning on empirical

TABLE I: Variation of a, b, and c Coefficients (See Eq 24) with Salt Concentration c_σ (mol L^{-1}) for a Sodium Chloride Solution at 25 °C

c_σ	a	b	c
0	0.833	0.167	1.00
0.01	0.840	0.163	1.00
0.10	0.850	0.156	1.01
1.00	0.865	0.148	1.01

grounds; we will call it a primary salt correction; (2) a secondary salt correction appears (last term on the right-hand side of eq 13 and 17) whose numerical value increases with c_σ, but it is often negligible as we will see later.

The difference between our phenomenological approach and the DM molecular theory originates from the fact that in the latter model, kinetic interactions between simple ion fluxes are disregarded, the aim being to compute the perturbation of the ionic motion due to the presence of the polyion.

Let us make use of analytical expressions for the k_i coefficients, calculated by Manning in his self-diffusion theory for the rodlike model.[5] In this theory, the central parameter is the dimensionless linear charge density ξ, whose effective value cannot be greater than $|z_1|^{-1}$, because of counterion condensation. Since we will limit ourselves to a mono-monovalent salt in this paragraph, we have, according to Manning

$$k_{1s} = k_1 = k_2 = \xi/6 \quad \text{if } \xi \leqslant 1 \tag{23a}$$

$$\left.\begin{aligned} k_1 &= k_2 = \xi^{-1}/6 \\ k_{1s} &= 1 - 5\xi^{-1}/6 \end{aligned}\right\} \text{ if } \xi \geqslant 1 \tag{23b}$$

By substitution of these formulas into eq 22, one obtains expressions for s_{1s}, s_2, and s_K given in Appendix I. The parameters entering these expressions are ξ, λ_3, and transport coefficients characterizing the pure salt solution. These latter coefficients can easily be computed from literature data, as explained in Appendix II.

We now focus our attention on the formula giving s_K, for the rodlike model when $\xi \geq 1$, and compare our result with the one recently published by Manning:[15]

$$s_K = \xi^{-1}(a\lambda_1{}^\sigma - b\lambda_2{}^\sigma + c\lambda_3) \tag{24}$$

The numerical values of a, b, and c are given in Table I, for an aqueous sodium chloride solution at 25 °C, at different concentrations c_σ. The predictions of the Manning theory correspond to $c_\sigma = 0$.

It is seen that the so-called secondary salt correction can to a first approximation be neglected, unless the deviation between theory and experiment becomes small, which is obviously not the case, as we will now see.

2. *Comparison with Experimental Data.* Recently, van der Drift[16] published a set of experimental results where s_K and λ_3 values were measured under various experimental conditions, at 25 °C. The polyelectrolyte was polymethacrylic acid, neutralized to different degrees, α, and for most of the data the ordinary salt was sodium bromide, whose transport coefficients are given in Appendix II. We compare in Table II the measured and calculated values of the slope s_K for the cylinder model. To calculate ξ, we chose a length per monomer of 2.35 Å, as suggested by van der Drift, because of the polymer's tacticity, so that $\xi = 3.03\alpha$.

It is seen that experimental and theoretical values of s_K show the same trend of variation, but there is a significant discrepancy which cannot be explained by a lack of experimental precision. As a matter of fact, the difference between the theoretical and experimental values is systematic and increases with low α and c_σ values. The quantitative predictions of the Manning self-diffusion theory[5] might thus be questioned, especially at low ionization degrees, as it already appears in polyelectrolyte salt-free solutions.[3] However, we emphasize the need for more data to draw positive conclusions.

We also computed theoretical s_2 values and found a proper order of magnitude, since the mean value proposed by van der Drift is −6 ohm^{-1} cm^2 equiv^{-1}. To illustrate the

TABLE II: Comparison of Calculated with Observed Limiting Slopes for the Conductance vs. Equivalent Polyion Concentration Curves

α	c_σ, mol L^{-1}	λ_3 ohm^{-1} cm^2 equiv^{-1}	s_K, ohm^{-1} cm^2 equiv^{-1} theory	s_K, ohm^{-1} cm^2 equiv^{-1} expt	$-s_2$, ohm^{-1} cm^2 equiv^{-1} theory	Δ, %
0.3	0.003	35.0	64.5	44.3	5.8	6.3
0.3	0.01	30.6	59.2	38.3	5.9	7.8
0.5	0.001	47.0	49.5	39.1	3.1	6.6
0.5	0.003	41.3	45.5	36.1	3.5	8.0
0.5	0.01	36.0	41.5	33.0	3.7	11.9
0.5	0.03	32.3	38.4	31.5	3.7	15.0
0.5	0.10	23.4	31.5	27.4	4.0	17.8
0.7	0.003	39.5	31.7	29.0	2.6	7.5
0.7	0.01	37.0	30.1	24.6	2.6	12.5

TABLE III: Ionic Friction Coefficients and Equivalent Conductances in Sodium Bromide and Sodium Chloride Aqueous Solutions at 25 °C

c_σ, mol L^{-1}	$10^{-15}f_{12}{}^\sigma$ (cgs)	$10^{-15}f_{1w}{}^\sigma$ (cgs)	$10^{-15}f_{2w}{}^\sigma$ (cgs)	$\lambda_1{}^\sigma$, ohm^{-1} cm^2 mol^{-1}	$\lambda_2{}^\sigma$, ohm^{-1} cm^2 mol^{-1}
		Sodium Bromide			
0.001	0.024	1.84	1.14	48.6	76.9
0.003	0.037	1.84	1.14	47.8	75.7
0.01	0.068	1.85	1.15	46.0	74.0
0.03	0.096	1.86	1.15	44.1	71.4
0.10	0.16	1.89	1.14	40.7	67.8
		Sodium Chloride			
0.01	0.048	1.88	1.20	46.8	71.7
0.10	0.146	1.88	1.18	41.8	64.9
1.00	0.326	2.01	1.21	31.6	54.2

relative importance of the corrective term in the equation for s_2 (see eq A1a in Appendix I), we define the quantity Δ by

$$\Delta = 100\frac{\lambda_1^\sigma + \lambda_3}{\lambda_2^\sigma - \lambda_3}\left(\frac{f_{21}^\sigma}{f_2^\sigma}\right) \quad (25)$$

At high salt concentrations ($c_\sigma \geq 0.01$ mol L^{-1}), Δ is obviously not negligible, which is opposite to what happens with the corresponding quantity for the counterion. However, this secondary salt correction will remain formal as long as it cannot be substantiated by well-established experimental arguments.

Another comment is in order. One might be tempted, owing to the low value of s_2, to state that the coion flux is almost not coupled with the polyion flux. This is erronous, as can already be seen from eq 13. There is a compensation between "lowering" and "enhancing" factors in the conductance equation (see also ref 4).

Finally, let us point out that an exhaustive set of experimental data should include, for each pair of c_σ and α values, the measurement of s_K, s_{1s}, s_2, and λ_3, so that the equation

$$s_K = (s_{1s} + s_2 + \lambda_1^\sigma + \lambda_3) \quad (26)$$

could be used at the same time to test experimental precision.

IV. Conclusion

It has been shown elsewhere[13,14] that the understanding of interactions between small ions and polyions is of prime interest to interpret the molecular transport parameters characterizing the polyelectrolyte in the limits of dilute polymer solutions and excess-of-salt conditions. In this respect, we wanted to emphasize in the present paper, the fundamental interest of experiments extending to a wider range of situations the work first developed by Wall and his co-workers. We have established equations which interrelate electrical transport parameters and small ion reduced self-diffusion coefficients. It enabled us to corroborate and discuss the Manning–Devore conductance equations, showing that they are not model dependent. In addition we checked, using recent experimental data, the Manning self-diffusion theory, but no quantitative agreement was reached.

Acknowledgment. The authors are pleased to acknowledge several useful conversations with Dr. J. B. Craig of Aberdeen University. Thanks are also due to Dr. W. P. J. T. van der Drift, Rijksuniversiteit Utrecht, who kindly allowed us to make use of his experimental results.

Appendix I

When no condensation is present we obtain, according to the cylinder model, for a mono-monovalent salt, the following slopes:

$$s_2 = -(\xi/6)[(\lambda_2^\sigma - \lambda_3) - (f_{21}^\sigma/f_2^\sigma)(\lambda_1^\sigma + \lambda_3)] \quad (A1a)$$

$$s_{1s} = -(\xi/6)[(\lambda_1^\sigma + \lambda_3) - (f_{12}^\sigma/f_1^\sigma)(\lambda_2^\sigma - \lambda_3)] \quad (A1b)$$

$$s_K = \left\{\lambda_1^\sigma\left[1 + (\xi/6)\left(\frac{f_{21}^\sigma}{f_2^\sigma} - 1\right)\right] + \lambda_2^\sigma(\xi/6)\left(\frac{f_{12}^\sigma}{f_1^\sigma} - 1\right) + \lambda_3\left[1 + (\xi/6)\left(\frac{f_{21}^\sigma}{f_2^\sigma} - \frac{f_{12}^\sigma}{f_1^\sigma}\right)\right]\right\} \quad (A1c)$$

When the reduced charge parameter is greater than unity, condensation is present and the equations become:

$$s_2 = -(\xi^{-1}/6)[(\lambda_2^\sigma - \lambda_3) - (f_{21}^\sigma/f_2^\sigma)(\lambda_1^\sigma + \lambda_3)] \quad (A2a)$$

$$s_{1s} = -(\xi^{-1}/6)[(6\xi - 5)(\lambda_1^\sigma + \lambda_3) - (f_{12}^\sigma/f_1^\sigma)(\lambda_2^\sigma - \lambda_3)] \quad (A2b)$$

$$s_K = (\xi^{-1}/6)\left\{\lambda_1^\sigma\left(5 + \frac{f_{21}^\sigma}{f_2^\sigma}\right) + \lambda_2^\sigma\left(\frac{f_{12}^\sigma}{f_1^\sigma} - 1\right) + \lambda_3\left[6 + \left(\frac{f_{21}^\sigma}{f_2^\sigma} - \frac{f_{12}^\sigma}{f_1^\sigma}\right)\right]\right\} \quad (A2c)$$

Appendix II

Phenomenological conductivity coefficients L_{ij} are obtainable for a given salt solution, at a given concentration, through a knowledge of electrical and diffusional transport parameters.[6] Friction coefficients can then be computed for a mono-monovalent salt according to the relations

$$f_{12}^\sigma = f_{21}^\sigma = (c_\sigma/\delta)L_{12} \quad (A3a)$$

$$f_{1w}^\sigma = (c_\sigma/\delta)(L_{22} - L_{12}) \quad (A3b)$$

$$f_{2w}^\sigma = (c_\sigma/\delta)(L_{11} - L_{12}) \quad (A3c)$$

$$\delta = L_{11}L_{22} - L_{12}^2 \quad (A3d)$$

We collected from the literature[17–19] useful data for aqueous sodium bromide and sodium chloride solutions at 25 °C, and the results of our calculations are summarized in Table III.

Notation

c_p	concentration of polyelectrolyte
c_σ	concentration of low-molecular-weight salt
c_i	concentration of ions (i = 1, 2, 3)
D_i, D_i^σ	self-diffusion coefficient of a small ion in the polyelectrolyte solution and in pure salt solution, respectively
$\mathfrak{F}$	Faraday constant
f	fraction of free counterions per polyelectrolyte molecule
f_{ij}, f_{ij}^σ	binary molar friction coefficient, in polyelectrolyte solution and in pure salt solution, respectively
f_i, f_i^σ	total molar friction coefficient, of an ion with its environment, in polyelectrolyte solution and in pure salt solution, respectively
I	electrical current density
J_i	molar ionic flux, in the reference frame of the solvent
J_{1s}	stoichiometric molar counterion flux, same reference frame
K, K^σ	electrical conductance of polyelectrolyte solution and pure salt solution, respectively
k_i	first-order coefficient in the expansion of ρ_i
L_{ij}	phenomenological conductivity coefficient
s_K	limiting slope of "excess" electrical conductance vs. equivalent polyion concentration
s_i	limiting slope of "excess" ionic conductance vs. x
u_i	algebraic ionic Hittorf mobility of ions
v_i	algebraic ionic Hittorf drift velocity of ions
x	stoichiometric fraction of counterions belonging to the polyelectrolyte
z_1	valence of mutual counterion
z_2	valence of coion
z_{3s}	stoichiometric valence of polyion
z_3	effective valence of polyion

α	degree of neutralization of polyelectrolyte acid
Δ, δ	defined in text
ϵ	algebraic electrical field strength
λ_i	ionic equivalent conductance of ions
ν_s, ν	stoichiometric and effective number of counterions per polyelectrolyte molecule, respectively
ν_1	number of counterions per salt molecule
ν_2	number of coions per salt molecule
ξ	dimensionless linear charge density parameter
ρ_i	reduced self-diffusion coefficient of small ions

References and Notes

(1) J. R. Huizenga, P. F. Grieger, and F. T. Wall, *J. Am. Chem. Soc.*, **72**, 2636, 4228 (1950).
(2) G. S. Manning, *J. Chem. Phys.*, **47**, 2010 (1967).
(3) A. Schmitt and R. Varoqui, *J. Chem. Soc., Faraday Trans. 2*, **69**, 1087 (1973).
(4) D. I. Devore and G. S. Manning, *J. Phys. Chem.*, **78**, 1242 (1974).
(5) G. S. Manning, *J. Chem. Phys.*, **51**, 923, 934 (1969).
(6) A. Katchalsky and P. F. Curran, "Nonequilibrium Thermodynamics in Biophysics", Harvard University Press, Cambridge, Mass., 1967.
(7) Laity[8] was the first to show that this formulation is an alternate way to write the usual linear force–flux relationships of irreversible thermodynamics.
(8) R. W. Laity, *J. Phys. Chem.*, **63**, 80 (1959); *J. Chem. Phys.*, **30**, 682 (1959).
(9) We consider here only frictional interactions with free counterions in order that the friction coefficients maintain their intrinsic significance. For a more detailed discussion, see ref 3.
(10) Strictly speaking, the reduced self-diffusion coefficient should include the f_{ii} coefficient. However, it can be shown that, for an aqueous sodium chloride solution up to 1 M concentration, such a coefficient is apparently negligible.[11]
(11) A. Schmitt, Thèse, University Louis Pasteur, Strasbourg, 1972.
(12) In these formulas, we neglected a coefficient $\epsilon = (f_{12}^{\sigma} f_{21}^{\sigma})/(f_{1w}^{\sigma} f_{2w}^{\sigma})$, which is always much less than one, as it can be seen from data in Appendix II or in ref 11.
(13) R. Varoqui and A. Schmitt, *Biopolymers*, **11**, 1119 (1972).
(14) A. Schmitt and R. Varoqui, *Eur. Polym. J.*, **11**, 1, 9 (1974).
(15) G. S. Manning, *Biopolymers*, **14**, 1991 (1975).
(16) W. P. J. T. van der Drift, Thesis, Rijksuniversiteit, Utrecht, 1975.
(17) R. A. Robinson and R. H. Stokes, "Electrolytes", Academic Press, New York, N.Y., 1955.
(18) H. S. Harned and B. B. Owen, "The Physical Chemistry of Electrolytic Solutions", 3rd ed, Rheinhold, New York, N.Y., 1958.
(19) T. W. Chapman, Ph.D. Thesis, University of California, Berkeley, 1967.

Isotope Effect in Diffusion of Perdeuteriobenzene and Benzene in a Series of Normal Hydrocarbons at 25 °C

Ian R. Shankland, Pawittar S. Arora, and Peter J. Dunlop*

Department of Physical and Inorganic Chemistry, University of Adelaide, Adelaide, South Australia, 5001

(Received February 22, 1977)

Binary diffusion coefficients have been measured for benzene and perdeuteriobenzene diffusing in *n*-pentane, *n*-hexane, *n*-heptane, and *n*-hexadecane at 25 °C, and used to study the isotope effect in these systems. The isotope effect is not proportional to the square root of the molecular weight of the isotopic species, and appears to be related to the viscosity of the solvent as suggested by Aoyagi and Albright.

In a number of recent papers[1-7] limiting binary diffusion coefficients, D^0, and corresponding *tracer* diffusion coefficients, D_T, have been reported for various isotopically labeled benzenes diffusing in various solvents at 25 °C. In most cases the data indicated a very slight linear dependence on the mass of the tracer species in concordance with the theoretical predictions of Friedman.[8] However the tracer diffusion coefficients were not inversely proportional to the square root of the mass of the tracer, as has sometimes been suggested,[2] or to the reduced mass of the system. The purpose of this paper is to report binary diffusion coefficients for liquid systems containing benzene (C_6H_6) or perdeuteriobenzene (C_6D_6) with the solvents *n*-pentane, *n*-hexane, *n*-heptane, and *n*-hexadecane, which have been extrapolated to yield limiting mutual (or tracer) diffusion coefficients for both C_6H_6 and C_6D_6. These solvents were chosen to complete a series of similar studies undertaken in this laboratory,[1,3-5] in order to investigate how the mass dependence of tracer diffusion in liquids varies with the nature of the solvent.

Experimental Section and Discussion

All binary diffusion coefficients were measured with a Gouy diffusiometer[10] and a special diffusion cell which have been described elsewhere,[11,12] as have also the experimental techniques and computations that are necessary to obtain the diffusion coefficients. As pentane and hexane are highly volatile solvents, the volumes above the solutions in the diffusion cell were kept saturated with vapor from reservoirs containing mixtures at the same concentrations. This precaution was necessary to minimize the effects of evaporation which would alter the relative concentrations of the two components during an experiment. All liquids used were analyzed by GPC and found to contain less than 0.05% impurity except the C_6D_6 which contained less than 0.4% impurity. The *n*-pentane, *n*-hexane, and *n*-hexadecane were obtained from Fluka, Switzerland; the *n*-heptane from Aldrich, Wisc.; the perdeuteriobenzene from ICN Pharmaceuticals, Calif. The latter material was stated by the manufacturers to contain 99.65% deuterium. It is believed that the binary diffusion data, summarized in Table I (see paragraph at end of text regarding supplementary material), are accurate to ap-

TABLE II: Values of Extrapolated Mutual Diffusion Coefficients

	$10^9 D^0(m^2 s^{-1})$	10^{11} error
C_6H_6 + *n*-pentane	6.023	1.0
C_6H_6 + *n*-hexane	4.758	0.8
C_6H_6 + *n*-heptane	3.858	0.7
C_6H_6 + *n*-hexadecane	0.8860	0.1
	$10^9 D_T(m^2 s^{-1})$	10^{11} error
C_6D_6 + *n*-pentane	5.951	1.0
C_6D_6 + *n*-hexane	4.724	0.8
C_6D_6 + *n*-heptane	3.833	0.7
C_6D_6 + *n*-hexadecane	0.8848	0.1

TABLE III: Values of A/D^0 and $f_T\Delta K$ for Benzenes Diffusing into Various Solvents

Solvent	$(A/D^0) \times 10^3$ (mol g^{-1})[a]	$f_T\Delta K$	Ref
n-Pentane	2.0	0.31	*b*
n-Hexane	1.12	0.18	*b*
n-Hexane	1.14	0.22	8
n-Heptane	1.11	0.17	*b*
n-Heptane	1.15	0.24	4
n-Octane	1.11	0.17	6
n-Dodecane	0.52	0.081	8
n-Hexadecane	0.22	0.035	*b*
n-Hexadecane	0.44	0.069	8
Cyclohexane	0.98	0.15	6
Cyclohexane	1.11	0.17	8
Chlorobenzene	0.53	0.083	6
Benzene	0.53	0.084	3
Benzene	0.00	0.00	7

[a] D^0 is the limiting value of D. [b] This work.

proximately 0.2%. Limiting binary diffusion coefficients were obtained by extrapolating the experimental data to $\bar{x} = 0$, where $\bar{x}$ is the mean mole fraction of C_6H_6 (C_6D_6) (see Table II) used in an experiment. In both these cases the coefficients obtained in this way are limiting binary coefficients, D^0; in the case of C_6D_6, however, the coefficient obtained is *also* the tracer diffusion coefficient, D_T, of the isotope of benzene.

As reported previously[6] the tracer diffusion coefficients of ^{14}C-substituted and perdeuterated benzenes in a number of organic solvents can be represented by an equation of the form

$$(D_T/D^0) = 1 - \frac{A}{D^0}(M_T - M_0) \quad (1)$$

where D^0 and M_0 are the limiting tracer diffusion coefficient of C_6H_6 and the molecular weight of C_6H_6, respectively, M_T is the molecular weight of the tracer species, and A is a constant for a particular system. The value of (A/D^0) (Table III) is indicative of the magnitude of the isotope effect for tracer diffusion and a comparison between solvents can be made on this basis.

Equations describing the mass dependence of tracer diffusion in solids[13-15] have recently been applied to tracer diffusion in some liquid systems; one[6] of these relations can be written as

$$D_T = D^0 - \frac{D^0 f_T \Delta K}{2M_0}(M_T - M_0) \quad (2)$$

In this equation f_T is a *correlation* factor which for impurity diffusion is not a geometrical factor since it depends on the *relative* jump frequencies of tracer and host, and ΔK is the fraction of the total kinetic energy, associated with the decomposition of a saddle point configuration, which resides in the migrating labeled species. This equation only applies to the situation where *one molecule is relocated*. When $f_T\Delta K = 1$ the tracer diffusion coefficient is inversely proportional to the square root of the molecular mass. Comparison of 1 and 2 shows that

$$(A/D^0) = (f_T\Delta K/2M_0) \quad (3)$$

(the values of the product $f_T\Delta K$ are given in Table II). An estimation of ΔK can be made by *assuming* the approximate result[15]

$$f_T = 1 - (2/Z) \quad (4)$$

where Z is the coordination number. If $Z \sim 10$ (a reasonable choice for the liquids studied) then $f_T = 0.8$ and the corresponding values of ΔK are all quite small, so only a small fraction of the kinetic energy associated with the jump is retained by the migrating molecule. Thus as mentioned before[6] a small value of ΔK may indicate that during the migration process momentum is transferred to the surrounding molecules, suggesting that the mass effect for tracer diffusion in liquids may possibly be related to the viscosity of the solvent.

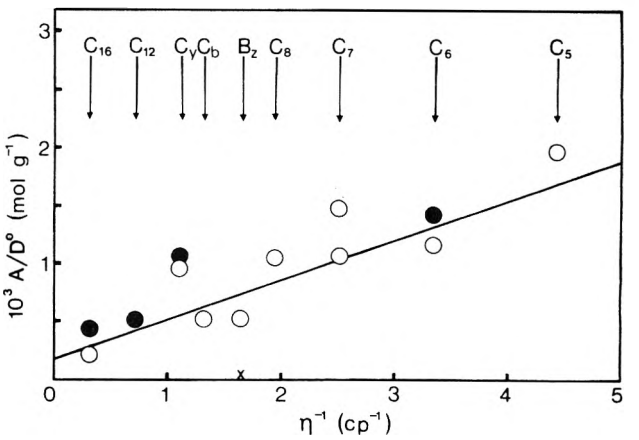

Figure 1. (A/D^0) vs. reciprocal of solvent viscosity, η, obtained from ref 16 and 17: O, this laboratory[3,4,6]; ●, Albright and Aoyagi;[8] ×, Mills.[7] *n*-Alkanes are indicated by C_i; cyclohexane, C_y; chlorobenzene, C_b; benzene, B_z.

The values of (A/D^0) are plotted against the reciprocal of the solvent viscosity, η, in Figure 1, where one can see that (within the experimental error of 10–50%) the isotope effect decreases with increasing solvent viscosity. The data can be represented by the least-squares line

$$(A/D^0) = 1.9 \times 10^{-4} + 3.4 \times 10^{-4}\eta^{-1} \quad (5)$$

with an average deviation of 3×10^{-4}. The standard deviations of the intercept and slope were 2×10^{-4} and 8×10^{-5}, respectively. This *linear* relationship may be fortuitous as other functions of viscosity (e.g., η^{-2}, η^{-3}) can also be used. Albright and Aoyagi[8] have also suggested a correlation between solvent viscosity and the isotope effect for tracer diffusion in different solvents.

Acknowledgment. This work was supported in part by a grant from the Australian Research Grants Committee.

Supplementary Material Available: Table I containing the mutual diffusion coefficients at 25 °C for C_6H_6 and C_6D_6 in various solvents (2 pages). Ordering information is available on any current masthead page.

References and Notes

(1) K. R. Harris, C. K. N. Pua, and P. J. Dunlop, *J. Phys. Chem.*, **74**, 3518 (1970).
(2) L. B. Eppstein and J. G. Albright, *J. Phys. Chem.*, **75**, 1315 (1971).
(3) G. G. Allen and P. J. Dunlop, *Phys. Rev. Lett.*, **30**, 316 (1973).
(4) S. J. Thornton and P. J. Dunlop, *J. Phys. Chem.*, **78**, 346 (1974).
(5) I. R. Shankland and P. J. Dunlop, *J. Phys. Chem.*, **79**, 1319 (1975).
(6) I. R. Shankland, P. J. Dunlop, and L. W. Barr, *Phys. Rev. B*, **12**, 2249 (1975).
(7) R. Mills, *J. Phys. Chem.*, **79**, 852 (1975).
(8) K. Aoyagi and J. G. Albright, *J. Chem. Phys.*, **64**, 81 (1976).
(9) H. L. Friedman in "Molecular Motions in Liquids", J. Lascombe, Ed., Reidel Publishing Co., Dordrecht, Netherlands, 1974.
(10) J. Kegeles and L. J. Gosting, *J. Am. Chem. Soc.*, **69**, 2516 (1947).
(11) H. D. Ellerton, G. Reinfelds, D. E. Mulcahy, and P. J. Dunlop, *J. Phys. Chem.*, **68**, 403 (1964).
(12) G. R. Staker and P. J. Dunlop, *J. Chem. Eng. Data*, **18**, 61 (1973).
(13) A. H. Schoen, *Phys. Rev. Lett.*, **1**, 138 (1958).
(14) A. D. LeClaire, *Phil. Mag.*, **14**, 1271 (1966).
(15) A. D. LeClaire in "Physical Chemistry", Vol. X, H. Eyring, H. Henderson, and W. Jost, Ed., Academic Press, New York, N.Y., 1970.
(16) F. D. Rossini et al., "Selected Values of Physical and Thermodynamic Properties of Hydrocarbons and Related Compounds", Carnegie Press, Pittsburgh, Pa., 1953. A.P.I. Research Project 44.
(17) J. Timmermans, "Physico Chemical Constants of Pure Organic Compounds", Elsevier, Amsterdam, 1950.

Solvent Dielectric Attenuation of Substituent Effects. Field Transmission in Partially Occluded Cavities[1]

S. Ehrenson

Chemistry Department, Brookhaven National Laboratory, Upton, New York 11973 *(Received March 23, 1977)*

Publication costs assisted by Brookhaven National Laboratory

Some ramifications of severe cavity shape alteration upon polar effect transmission within the Bjerrum–Kirkwood–Westheimer electrostatic work model are explored. Significant dependencies of the effective dielectric constants computed are shown to exist not only upon the relative positioning of the interacting sites within the cavity and the dielectric properties of the surrounding medium, but, potentially overwhelmingly, on the curvature of the cavity boundaries nearby. Previously recognized and newly revealed effective dielectric constant anomalies are rationalized in terms of refractions of the field lines emanating from point sources as they pass through these boundaries.

Introduction

Dielectric continuum models representing solvent influence on transmission of substituent effects have occupied considerable attention in the chemical physics literature over the past 40 years, despite recognition of the serious limitations they embody. Kirkwood's formulations for multipole interactions at a distance,[2,3] within cavities of simple shape, have been adopted to rationalize bulk effects in a number of interesting chemical reactivity systems.[4] Most of these systems unfortunately involve production or neutralization of ionic centers at peripheral (and hence unshielded from the solvent) sites in the molecule where the bulk effects might be of secondary importance to those exercised by individual solvent molecules in specific configurations. Models which combine features of specific interaction with nearest or nearby solvent moieties and a continuum of solvent further out, including such sources of anomaly in the bulk effect near cavity edges as electrical saturation and electrostriction, should provide satisfactory representation of most solvation phenomena and may now be practicable.[6]

Optimum utility of such combination models depends upon maximum understanding of the workings and limitations of their components. In the present preliminary investigation, details of extreme cavity shape modifications as they apply to the effective dielectric constants experienced by molecules contained within are examined. The implications of this study to strategies for evaluation of bulk effects in cavities of arbitrary shape, for systems of separated poles upon approach, and reasons for apparent anomalies in effective dielectrics in cavities of simple shapes are also explored.

Method and Rationale

Electrostatics and Cavity Shapes Considered. Computation of the electrostatic work accompanying formation or destruction of an ion in the presence of an electric field within the Kirkwood–Westheimer procedure[3] depends upon solution of Laplace's equation for the system, subject to the appropriate boundary conditions, i.e., for the multipoles representing the molecular species within the cavities they are pictured to occupy. To date, solutions for only a few quite regular cavity shapes have been obtained,[3,5,12] mainly because of the approximate nature of the model and the difficulty of solving the Laplacian potentials problem for other than these shapes. Interacting polar sites located within the cavities considered thus far always "see" each other directly; that is, the shortest paths between them lie entirely within the cavity and hence only pass through regions of low dielectric.

It seemed of interest to consider what the effect might be of interposing different dielectric media directly between the interacting sites, thereby creating situations where the shortest and numerically significant proportions of the lines of force would experience different conditions than previously explored. To this end, locating the poles within toroidal and spherical shell cavities allows direct comparison with the effects of similar positioning within uniform-medium simple-shaped (i.e., spherical) cavities of like volume, curvature, imbedding characteristics, etc. Both systems are tractable analytically, and of little greater complexity than some of the simpler shapes previously considered if location of the interacting sites are subject to some (physically realistic) constraints. Furthermore, because of mathematical requirements for separation of variables in the toroidal Laplace equation, some information concerning directional properties of the interaction paths and how they contribute to the effective dielectric is available. Previously noted anomalies in the effective dielectrics experienced at sites lying close to cavity boundaries are likewise amenable to scrutiny in the spherical shell case, leading to better understanding of their origins. Derivation of the appropriate electrostatic work equations for monopole–monopole interactions follows, most relevant for our present purposes. Extension to pole–instantaneous dipole cases could easily be obtained from limits analysis of the pole–pole results in the usual manner.

Toroidal Cavities. Laplace's equation for the toroidal coordinate system where

$$x = a_T \sinh \eta \cos \phi/(\cosh \eta - \cos \theta)$$
$$y = a_T \sinh \eta \sin \phi/(\cosh \eta - \cos \theta)$$
$$z = a_T \sin \theta/(\cosh \eta - \cos \theta)$$

has the following solutions for the potential external and internal to the toroidal surface ($\eta = \eta_0$), in the presence of charges e_k located within the cavity described by this surface[13,14] (see Figure 1)

$$V_{ext} = \pi^{-1}(\cosh \eta - \cos \theta)^{1/2} \times \sum_{m=0}^{\infty} \sum_{n=0}^{\infty} A_{nm} P_{n-1/2}^{m}(\cosh \eta) \cos n\theta \cos m\phi \quad (1)$$

$$V_{int} = \pi^{-1}(\cosh \eta - \cos \theta)^{1/2} \times \sum_{m=0}^{\infty} \sum_{n=0}^{\infty} B_{nm} Q_{n-1/2}^{m}(\cosh \eta) \cos n\theta \cos m\phi + \frac{1}{D_i} \sum_{k=1}^{\nu} \frac{e_k}{|r - r_k|} \quad (2)$$

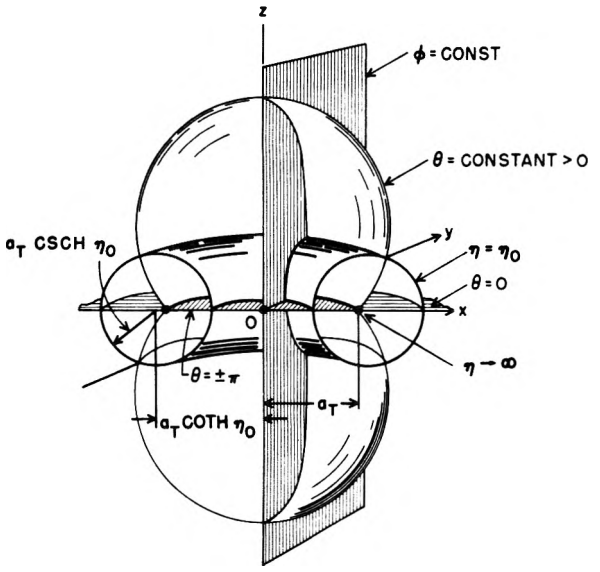

Figure 1. Toroidal cavity representation with coordinate surfaces η = constant. Other surfaces shown are spherical bowls (θ constant) and meridian planes (ϕ constant).

The last term which expresses the interacting polar site influence on the potential at any point within the cavity of dielectric D_i may be expanded as the appropriate Green's function[15]

$$D_i^{-1} \sum_{k=1}^{\nu} \frac{e_k}{|r - r_k|} = (D_i\pi)^{-1}(\cosh\eta - \cos\theta)^{1/2} \times \sum_{m=0}^{\infty}\sum_{n=0}^{\infty} \beta_{mn} P_{n-1/2}{}^{m}(\cosh\eta)\cos m\phi \cos n\theta \quad (3)$$

where

$$\beta_{mn} = \sum_{k=1}^{\nu} \frac{e_k}{a_T}(\cosh\eta_k - \cos\theta_k)^{1/2}\epsilon_m\epsilon_n(-i)^m \times \frac{\Gamma(n - m + 1/2)}{\Gamma(n + m + 1/2)} Q_{n-1/2}{}^{m} \times (\cosh\eta_k)\cos m\phi_k \cos n\theta_k \quad (4)$$

valid for all polar sites located on the x axis (θ_k, ϕ_k = 0 or π) and for $\eta_k > \eta$. The Neumann constants ϵ_j are unity for j = 0, otherwise 2 for $j \geq 1$ and Γ are the gamma functions. To assure the generality of this expansion we constrain $\eta_k = \infty$ (locus, distance a_T from the origin in the x, y plane) and follow by imposing the appropriate boundary conditions

$$V_{int}(\eta_0, \phi, \theta) = V_{ext}(\eta_0, \phi, \theta) \quad (5)$$

$$D_i(\partial V_{int}/\partial\eta)_{\eta=\eta_0} = D_s(\partial V_{ext}/\partial\eta)_{\eta=\eta_0} \quad (6)$$

where D_s is the bulk dielectric constant for the medium surrounding the torus.

Solution of the simultaneous equations provided by eq 5 and 6 yields

$$B_{nm} = \left[\frac{1}{D_s} - \frac{1}{D_i}\right]\beta_{nm}\left[\frac{P}{Q}\right]\Bigg/ \left\{1 - \frac{D_i}{D_s}\frac{P}{Q}\left[\frac{2(\cosh\eta_0 - \cos\theta)Q' + Q}{2(\cosh\eta_0 - \cos\theta)P' + P}\right]\right\} \quad (7)$$

where the superscripts, subscripts, and arguments of the half-order Legendre polynomials are temporarily suppressed and the primes indicate derivatives with respect to cosh η. (The indices are respectively m, $n - 1/2$ and the argument is cosh η_0.)

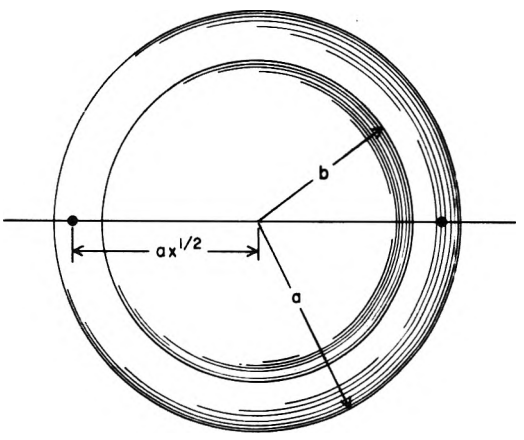

Figure 2. Spherical shell cavity representation with $r = ax^{1/2}$.

Since for location of the interacting sites a_T distant from the origin to the right and left respectively along the x axis

$$\lim_{\eta=\eta_k\to\infty} \Delta W = e^2\left\{\frac{1}{2a_T D_i} + \frac{(\cosh\eta - \cos\theta)^{1/2}}{\pi} \times \sum_{n=0}^{\infty}\sum_{m=0}^{\infty}(-1)^m B_{nm} Q_{n-1/2}{}^{m}(\cosh\eta)\cos n\theta\right\} \quad (8)$$

and one may show

$$\lim_{\eta\to\infty}(\cosh\eta - \cos\theta)^{1/2} Q_{n-1/2}{}^{m}(\cosh\eta) = (-1)^m(\pi/2)^{1/2}\Gamma(1/2 + m) \quad \text{for } n = 0$$
$$= 0 \quad \text{for } n > 0 \quad (9)$$

term combination limits which enter into evaluation of both β, eq 4, and the sum term in eq 8, we may now adopt the usual form for the electrostatic work, particularly pertinent for consecutive ionization steps

$$\Delta W = \Delta F = 2.303kT\Delta pK = e^2/RD_{eff} = e^2/(2a_T D_{eff}) \quad (10)$$

where

$$D_i/D_{eff} = 1 + \left[\frac{D_i}{D_s} - 1\right]\sum_{m=0}^{\infty}\frac{U_m}{1 - (D_i/D_s)C_m} \quad (11)$$

$$U_m = \epsilon_m(i)^m\Gamma(1/2 + m)\Gamma(1/2 - m) \times (P_{-1/2}{}^{m}/Q_{-1/2}{}^{m}) \quad (12)$$

$$C_m = \left\{G + (Q_{1/2}{}^{m}/Q_{-1/2}{}^{m})\right\}\Big/ \left\{G + (P_{1/2}{}^{m}/P_{-1/2}{}^{m})\right\} \quad (13)$$

and

$$(1 - 2m)G = (\cosh\eta_0\cos\theta - 1)/(\cosh\eta_0 - \cos\theta) \quad (14)$$

Again, the arguments of the Legendre polynomials, cosh η_0, have been suppressed. Derivation of eq 9, the relationship to remove the derivatives of P and Q from appearance in eq 13, and the means of generating the polynomials are briefly outlined in the Appendix. The directional dependence of the effective dielectric, a result of the fact that unidimensional representation of the potential is impossible in toroidal coordinates, it should be noted, resides entirely in G; θ equal π refers to interactions focused toward the interior of the torus (toward the coordinate system origin), i.e., over the shortest spatial path of interaction.

Spherical Shell Cavities. Figure 2 illustrates the special case of polar containment within spherical shell cavities

most conveniently treated and yet informative. The interacting sites are assumed to lie within the shell defined by the concentric spheres, the larger of radius a, the smaller of radius of b, but always on the common diameter, equidistant from the origin by r ($a \geq r \geq b$). Potentials in the three regions of space (inside sphere b, between spheres b and a, and outside sphere a) may be defined in terms of powers of r and Legendre function polynomial expansions, see, e.g., ref 2, particularly for definition of the central region potential for uniform fields, and the two sets of boundary conditions imposed (i.e., continuity of the potential and the dielectric displacement at both boundaries r equal a and b). Upon recognition of the appropriate limitations of the Neumann expansion for $|r - r_k|^{-1}$ in spherical coordinates pertaining to the special case under consideration or from the Green's function which has the value zero at the boundaries defined by the concentric spheres

$$|r - r_k|^{-1} = \sum_{n=0}^{\infty} \frac{r_k^n}{r^{n+1}} P_n(\cos\theta_k)P_n(\cos\theta) \qquad r_k \leq a$$

$$= \sum_{n=0}^{\infty} \frac{r^n}{r_k^{n+1}} P_n(\cos\theta_k)P_n(\cos\theta) \qquad r_k \geq b$$

$$G = R^{-1} - \sum_{n=0}^{\infty} \frac{P_n(\cos\theta_k)P_n(\cos\theta)}{a^{2n+1} - b^{2n+1}} \left\{ \frac{r_k^n}{r^{n+1}} (r^{2n+1} - b^{2n+1}) + \frac{b^{2n+1}}{(rr_k)^{n+1}} (a^{2n+1} - r^{2n+1}) \right\} \qquad (15)$$

the four simultaneous equations obtained from the potentials upon imposition of the boundary conditions are soluble and yield, again for $\Delta W = e^2/(2rD_{eff})$

$$\frac{D_i}{D_{eff}} = 1 + 2\left[\frac{D_i}{D_s} - 1\right] \times \sum_{n=0}^{\infty} (-1)^n \frac{\{(n+1)[(a/b)x^{1/2}]^{2n+1} J_n + n(x^{-1/2})^{2n+1} K_n + L_n\}}{(a/b)^{2n+1} J_n K_n - M_n} \qquad (16)$$

Here, the constraints are imposed that the dielectric of the medium to the inside and to the outside of the shell are equal (D_s), that within the shell it is D_i and

$$J_n = n + (n+1)D_i/D_s$$
$$K_n = (n+1) + nD_i/D_s$$
$$L_n = 2n(n+1)(D_i/D_s - 1)$$
$$M_n = n(n+1)(D_i/D_s - 1)^2$$
$$x = (r/a)^2 \qquad 1 \geq x \geq b/a \qquad (17)$$

Some further details on this derivation are to be found in the Appendix, particularly on the operational forms adopted for the sum in eq 16 upon approach to a variety of limiting conditions.

Results and Discussion

In Figure 3 the dependence of the effective dielectric, normalized to the internal dielectric and averaged over θ for charged sites located as previously described within toroidal cavities, is shown as a function of η_0 and of the external medium dielectric. The abscissa η_0 is, of course, simply related to relative ring thickness which provides convenient visualization of the dimensions of the system; i.e., the diameter of the ring normalized to the distance between interacting sites, $d_T/2a_T(=\Delta_T) = \text{csch } \eta_0$. See Figure 4 where log Δ_T vs. η_0 is illustrated. All D_{eff}/D_i curves appear rational to the extent that thick rings, where little

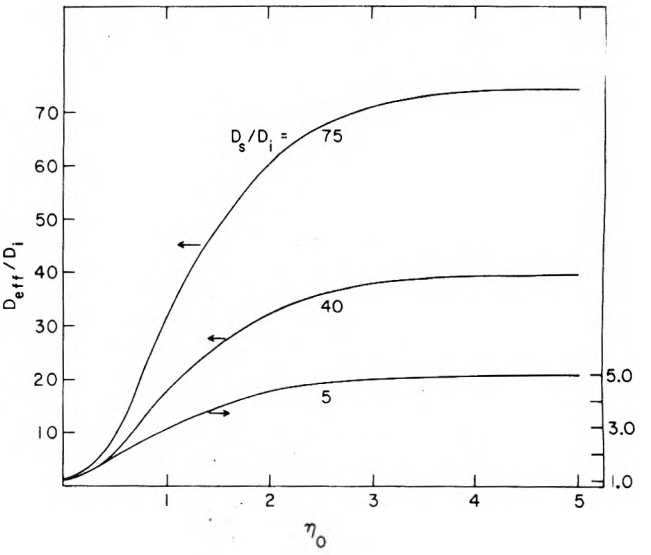

Figure 3. D_{eff}/D_i as functions of ring-size parameter, η_0, and the relative medium dielectric ratios, D_s/D_i.

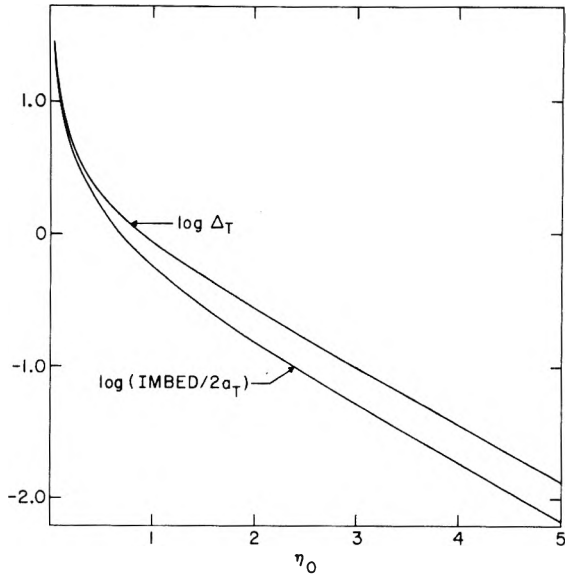

Figure 4. Dependence of relative ring thickness, Δ_T, and relative solid sphere "imbedding" factor on η_0.

high-dielectric space interposes between the interacting sites, are characterized by effective dielectric constants approximately that of the ring material and upon passage to thinner rings, η_0 increasing, D_{eff}/D_i approaches in monotonic- and eventually asymptotic-fashion the bulk dielectric of the surrounding medium. The shapes of the curves are seen to be quite similar over the range of D_s/D_i considered, rising most sharply in the η_0 region, 0.5 to 1.5.

Figure 5 presents typical results which contrast the effective dielectric constants experienced in toroidal cavities with those in solid spherical cavities of equal outside dimensions and location of interacting sites. That is, the intersite distances are $2a_T$ and the imbedding distance within the sphere is $a_T(\text{csch } \eta_0 + \coth \eta_0 - 1)$. The functional relationship of the imbedding to intersite distances is plotted in Figure 4.[16] Also shown in Figure 5 is the relatively minor effect of θ averaging, particularly for thin rings, which are of most interest as regards comparisons with the sphere. For cavities of the latter shape, it has long been recognized that location of the interacting sites progressively nearer the cavity edges is accompanied by increasing effective dielectric constants, eventually *surpassing* the dielectric of the surrounding medium by significant amounts.[3a] This is clearly shown

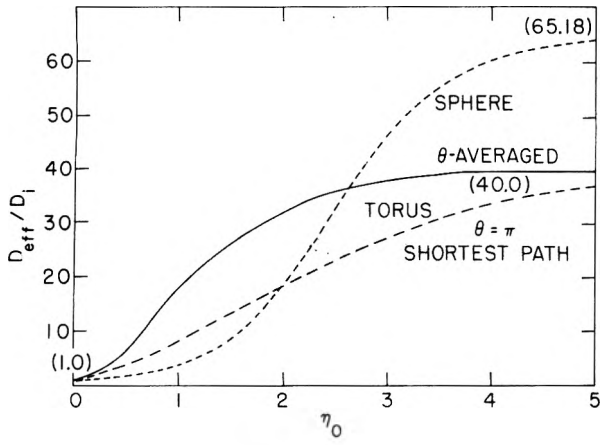

Figure 5. D_{eff}/D_i for toroidal and solid spherical cavities with interacting sites similarly disposed. Here and henceforth all figures are for $D_s/D_i = 40$, and numbers in parentheses indicate limits for η_0 of zero and infinity.

in Figure 5 where D_{eff}/D_i is greater than D_s/D_i beyond $\eta_0 = 2.75$ and approaches in the limit, for $D_s/D_i \gg 1$, $(D_e/D_i)/2(1 - \ln 2)$.

In contrast, the toroidal cavities appear to exhibit more coherent effects upon change in their dimensions and interacting site location. Only for interaction paths characterized by very small θ (not shown, initial directions away from each other site) is D_{eff}/D_i found to exceed D_s/D_i and then only substantially in middle ranges of η_0. This may be roughly deduced by the differences in the shortest path and averaged curves shown in Figure 5. Eventually the disappearance of low-dielectric volume forces the effective dielectric toward its proper limit, i.e., that of the external medium containing no cavity whatsoever. In the sphere, however, the limiting approach of the cavity edge to the sites is not accompanied by disappearance of the cavity itself (limiting sphere of radius a_T): the presence of *low* dielectric material in these limits supports a *higher* effective dielectric than of the surroundings.

We may conclude thus far, therefore, that interposing high dielectric media between interacting sites, or alternatively that restricting the density of low dielectric paths therebetween will raise the effective dielectric as one might expect (viz., in the η_0 regions 0.5 to 2.0, where these restrictions would be judged on any spatial grounds as moderate), at coherent rates and between regular limits, and that if anomalies in behavior exist they do for the simpler shaped, solid spherical cavities. Kirkwood and Westheimer in ref 3a attribute the anomalously high D_{eff}/D_i values to the form imposed by adherence to the Bjerrum charging-work treatment.[18] Whether this is the correct reason for the simple shaped cavities—it obviously does not interfere in the admittedly more stringent limiting toroidal conditions—or whether other restrictions imposed by the Laplace boundary conditions impose interaction path weighting conditions which in turn cause the anomalies may be further explored when the spherical shell cavity results are examined.

In Figure 6, the results for a number of site location and volume conditions for spherical shell cavities are shown pertaining to systems characterized by $D_s/D_i = 40$, matching the conditions for Figure 5. Since, as it should be recalled, the dielectric of the medium inside and outside the shell are equal and the interacting sites are located on the common diameter of the spheres defining the cavity, the contrasts with toroidal cavities accrue from provision of an added dimension of low-dielectric paths for site interaction (in the limit as a spherical surface compares to any one of its great circles).

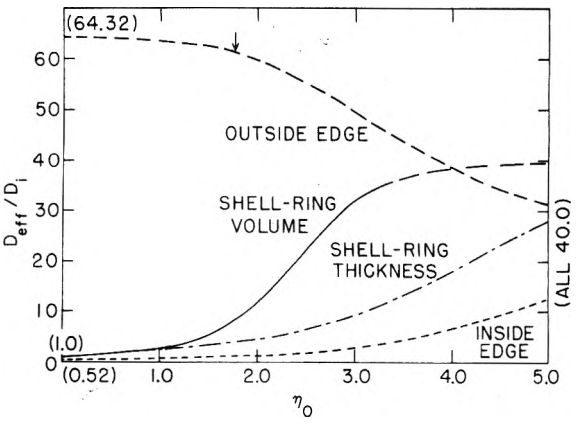

Figure 6. D_{eff}/D_i for various interacting site placements within spherical shell cavities. Arrow indicates where the "imbedding" displacement function achieves its minimum ratio (1% of shell thickness) (see text). Note, as well, $a/b = (\cosh \eta_0 + 1)/(\cosh \eta_0 - 1)$ or $\eta_0 = \ln\{[(a/b)^{1/2} + 1]/[(a/b)^{1/2} - 1]\}$.

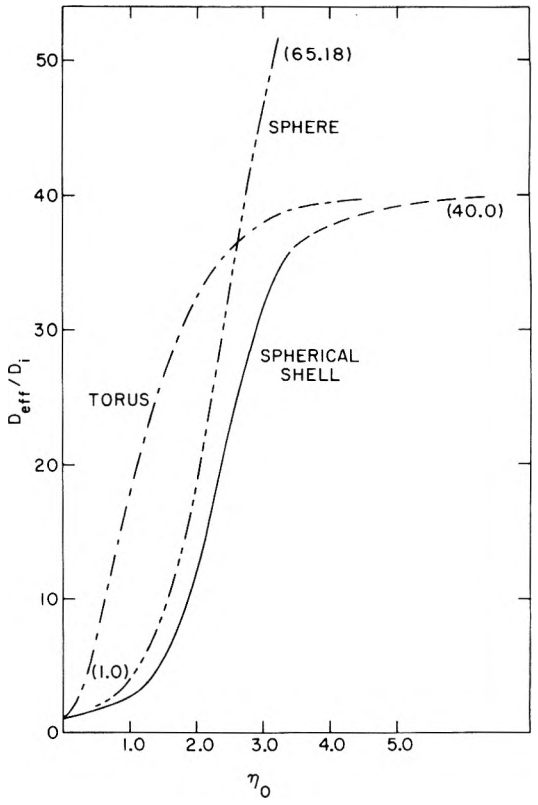

Figure 7. Contrast of D_{eff}/D_i for ring and spherical shell of equal volume and for solid spherical cavity.

The most direct and obvious comparison is where the shell diameter is matched to that of the torus with interacting sites held in the same position as in the ring. This, the second-slowest-rising curve with increasing η_0 in Figure 6, while well-behaved in the sense of exhibiting monotonic behavior between the limits of pure cavity and surrounding medium dielectric values, exhibits much more gradual approach to the high η_0 limit than does the corresponding curve for the torus. The simplest and most reasonable explanation for this difference would appear to reside in the volumes available for paths of low dielectric, that is, of the cavities, and how they change with η_0 (see the Appendix).

This effect may easily be corrected for by matching the spherical shell and torus volumes, instead of their diameters, maintaining the condition of equivalent placement with respect to the inside and outside cavity edges. The more rapidly rising curve (with increasing η_0) shown

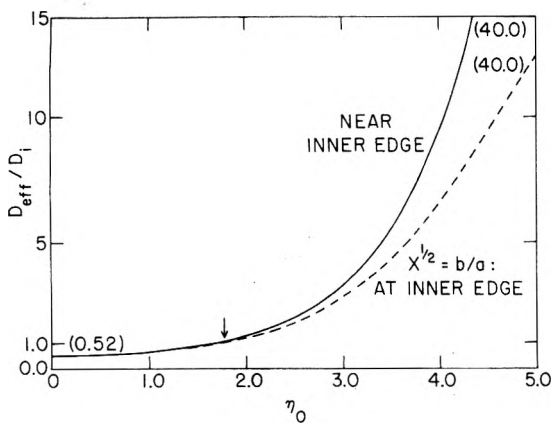

Figure 8. Difference in D_{eff}/D_i depending on site placement at or near the inner spherical shell boundary. The arrow again indicates where the minimum 1% of shell thickness for "imbedding" is reached (see text).

in Figure 6 and the direct comparison with the torus shown in Figure 7 indicate that while some differences remain, the volume effect upon thickness matching was indeed important. Inclusion of the curve for the solid sphere proves to be informative; it is of great interest to observe the similarity over much of the early η_0 range of this curve and that for the shell. What this seems to suggest is that, within limits, intrusion of low dielectric material between the interacting sites is less important a function of how great is this intrusion than the shape of the boundary made therewith. At high η_0 where the rings and shells become very thin, of course, they exhibit grossly different behavior than the solid. D_{eff}/D_i for both the former approach the limiting value D_s/D_i asymptotically, consistent with the eventual disappearance of the cavity, where for the solid sphere, as previously discussed, this external medium value is substantially exceeded.

Two other site-positioning conditions within the spherical shells are of interest in enhancing our understanding of important contributing effects of cavity shapes and sizes to effective dielectrics. These are explored as well in Figure 6. If the interacting sites are located at the inside edge of the cavity, the very slowly rising curve shown in Figure 6 and, with magnification, as the lower curve in Figure 8 pertain. In this case, anomalously low effective dielectric constants are observed in the thick shell region; D_{eff}/D_i is smaller than unity up to $\eta_0 \sim 1.7$ which corresponds to the situation where the shell thickness is approximately half the outer sphere radius (i.e., $b/a = 0.48$). That this effect persists away from this edge is shown by the other curve in Figure 8; here the interacting sites are located 1–2% of its thickness inside the cavity. For the thicker shells this displacement makes insignificant differences. Only for the thin shells where the ~1% displacement brings $x^{1/2}$ near unity is there substantial acceleration of D_{eff}/D_i to the common limiting value of D_s/D_i.[19]

If, as the other extreme, the interacting sites are located near the outer edge of the cavity (i.e., $x^{1/2} \rightarrow 1$), the upper curve in Figure 6 is obtained. The particular case plotted is with $x^{1/2} = 1 - \delta$, where δ is the greater of 0.01 and $0.02(1 - b/a)$. This means the interacting sites lie approximately 2% away from the outer edges of thick shell cavities and approaching 1% within for thinner shells. Here, a most interesting situation is encountered where anomalously high effective dielectric values, limit 64.32 (differing from the solid spere limit previously reported because $x^{1/2} = 0.98$), properly decrease with decreasing shell thickness, passing through the external medium value (40.0) but eventually to return in the limit to this value. The nonmonotonic behavior noted here is a function of the small displacement imposed; in the thin shell region, moving the sites even fractionally apparently can produce sufficient inner-edge effects to pull the effective dielectric below the external medium value. Upon further decreases of the shell thickness, of course, the vanishing cavity effect compels return to the latter value in the limit. For $x^{1/2}$ held at unity, monotonic decrease to D_s/D_i would be observed.

Conclusions

The studies described plainly indicate that bulk medium effects upon interaction of poles located within cavities of various shapes appears to depend as much upon the immediate environment of the poles as upon the overall size, shape, and relative dielectric properties of the cavity and surrounding medium. Interposition of high dielectric material directly between interacting sites may have greater or lesser effects depending upon whether it occupies spatially closer positions to these sites than the global surroundings of equal properties. Effects in both directions have been demonstrated; in the limits effective dielectric constants both higher than that of the external medium and lower than that of the cavity may be produced dependent upon the curvature of the cavity boundary being approached.

This may be most readily understood in terms of spreading or concentration of lines of force upon passage through a curved dielectric surface or boundary. We here always consider point charge fields to be located in the region of low dielectric and since the angles made by the lines of force with the normal to the surface is given by the relationship

$$D_i \cot \theta_i = D_s \cot \theta_s$$

one may easily show that in passing outward through a concave surface there is tendency toward spreading of the field, i.e., separation of the field lines, an effect which is the greater the closer is the point source brought to the surface (where the apparent curvature is greater). The same effect, it should be recognized, can be simulated by increasing the apparent external- to internal-medium dielectric ratio, keeping the point source position constant. In extreme cases there seems no reason to doubt that this effect could substantially override the diminishment in the number of lines of force in the close boundary direction, producing an overall higher effective dielectric than of the external medium. Passing through a convex boundary (as toward the inner surface of a spherical shell) produces the opposite effect, i.e., concentration of the lines of force and hence of simulation of the movement of the point source toward the boundary by a decrease in D_s/D_i value.

For nonextreme conditions, which after all characterize the chemical systems of interest, the boundary shape effects also contribute in important ways as, for example, reexamination of Figure 7 will attest. It seems reasonable here that the persistently smaller D_{eff}/D_i value for the spherical shell than toroidal cavity (of equal volumes) resides mainly in the differences in refraction the manifold of field lines experience through respectively the inner convex vs. concave boundaries. Similarly, this effect can be recognized to be roughly similar in magnitude to that accompanying adjustment of torus-to-shell thickness parity to volume parity (see Figure 6).

Finally, it should be reiterated that the intention of this study was to provide an enhanced understanding of what the contributing features of the cavity-bulk dielectric model are, and under what circumstances they would be

expected to contribute. Whether the occluded cavities of the shapes chosen for this illustration are themselves of any potential use for containment of chemical systems viewed in conventional terms is questionable. At the same time, the extreme site locations discussed should also be recognized as physically unlikely, effects such as intermolecular repulsions maintaining reasonable distances to cavity boundaries and/or electrostriction effects which would deform the boundary shape upon approach of naked charge. The results are already judged useful in interpreting the effects of shape, size, site location, and relative dielectric in cavities of more conventional shapes. They are anticipated to be all the more upon extension to irregular shaped cavities, where numerical solution of Laplace's equation is necessary.

Although not yet pursued, another and perhaps equally interesting application of the present analysis to chemical reactivity studies may be envisioned. It warrants brief mention in conclusion. To what degree, it may be asked, are the cavity models developed here, which are framework conformable upon appropriate modification and extension, capable of simulating the bond fall-off mode for transmission of substituent effects, a long standing alternative to the presently favored field model.[5,20] For example, for bridgehead disubstituted bicyclooctanes in solution, where three regions of spherical coordinate space may be distinguished, can the saturated molecular skeleton containing the atoms and intervening regions of high electron density (corresponding to the shell) be treated as a region of higher dielectric than the "emptier" interior, and different at the same time from that of the surroundings? The major objections to this model as regards approximations to physical reality, it should be recognized, are different mainly in degree but not in kind from those generally levelled at the field model. In particular, treatment of microscopic regions in bulk terms is here extended to intramolecular directional levels.

Appendix

Toroidal Cavity Analysis. The half-order Legendre polynomials are expressed in terms of hypergeometric functions[14]

$$P_{n-1/2}^{m}(\cosh\eta) = \frac{i^m\,\Gamma(n+m+1/2)}{m!\,\Gamma(n-m+1/2)}\frac{\tanh^m(\eta/2)}{\cosh^{1-2n}(\eta/2)}F(1/2-n,\ 1/2+m-n,\ m+1;\ \tanh^2(\eta/2)) \quad \text{(A1)}$$

and the direct expansion of F given in ref 21a, eq 15.1.1 is used for $\eta < 3.5$. For $\eta > 3.5$, the substitution $z = 1 - \tanh^2(\eta/2)$ is made and the more complicated hypergeometric function ref 21b, eq 15.3.11 is used.

Similarly for the polynomials of the second kind[21c]

$$Q_{n-1/2}^{m}(\cosh\eta) = \frac{(-1)^m\pi^{1/2}(1-e^{-2\eta})\Gamma(1/2+m+n)}{e^{(n+1/2)\eta}\Gamma(1+n)} \times F(1/2+m,\ 1/2+m+n,\ 1+n;\ e^{-2\eta}) \quad \text{(A2)}$$

the same direct expansion for F as above is used for $\eta > 0.15$, and the complementary expansion 15.3.12, ref 21b, is employed for η smaller than this value. Because of the similarity of forms single high- and low-argument computer routines for P and Q could be efficiently written and employed. The switchover limits between the expansions were carefully determined as functions of both the accuracy (with single precision arithmetic) and efficiency. Time requirements on CDC 7600 were generally trivial for the sums.

Equation 9 in the text it should be noted is obtained from (A2), multiplied by $(\cosh\eta - \cos\theta)^{1/2}$, in the limit, i.e.

$$\lim_{\eta\to\infty}(\cosh\eta - \cos\theta)^{1/2}Q_{n-1/2}^{m}(\cosh\eta) = \{[(e^{\eta}+e^{-\eta})/2 - \cos\theta]^{1/2}(-1)^m\pi^{1/2}(1 - e^{-2\eta})\Gamma(1/2+m+n)F/e^{(n+1/2)\eta}\Gamma(1+n)\} \quad \text{(A3)}$$

with F approaching unity in the limit. The derivatives appearing in eq 7 are most conveniently removed employing the relationships

$$\frac{dP_{\nu}^{\mu}(z)}{dz} = \frac{-(\nu+1)zP_{\nu}^{\mu}(z) + (\nu-\mu+1)P_{\nu+1}^{\mu}(z)}{(z^2-1)} \quad \text{(A4)}$$

and the similar equation obtained upon replacing P by Q. These are obtained by combining relationships for varying degree and derivative given in ref 21d.

Averaging eq 11 over θ to obtain results such as are shown in Figure 5 is straightforward when each term in the sum is recognized to be, upon arrangement, of the form

$$(f_m - g_m\cos\theta)/(1 - h_m\cos\theta) \quad \text{(A5)}$$

Since $h_m < 1$, the average terms are available directly from the definite integrals over the appropriate range of θ, solutions for which are known exactly[22]

$$\int_0^{\pi}\{(f_m - g_m\cos\theta)\,d\theta/(1 - h_m\cos\theta)\}/\int_0^{\pi}d\theta = \frac{1}{\pi}\left\{\frac{\pi}{(1-h_m^2)^{1/2}}\left[f_m + g_m\frac{(1-h_m^2)^{1/2}-1}{h_m}\right]\right\} \quad \text{(A6)}$$

Spherical Shell Analysis. By comparison, the spherical shell cases are much simpler to handle, evaluation of the effective dielectric constant proceeding through eq 16 except for the following limiting cases. For $x^{1/2}$ and/or (a/b) near unity, eq 16 only slowly converges. Division of the sum term, numerator by denominator, yields the equivalent form

$$\frac{D_i}{D_{eff}} = 1 + 2\left[\frac{D_i}{D_s} - 1\right]\sum_{n=0}^{\infty}(-1)^n\left\{\frac{(n+1)x^{n+1/2}}{K_n} + \frac{nK_n[(L_nx^{n+1/2}/2nK_n)+1]^2}{x^{n+1/2}[(a/b)^{2n+1}J_nK_n - M_n]}\right\} \quad \text{(A7)}$$

and evaluation of the first of the two sum terms, to good approximation for D_i/D_s small, by expansion of K_n^{-1} to the first order in D_i/D_s, i.e.

$$2\left[\frac{D_i}{D_s} - 1\right]\sum_{n=0}^{\infty}(-1)^n\frac{(n+1)x^{n+1/2}}{K_n} = \frac{-2x^{1/2}}{1+x} + 2\left[\frac{D_i}{D_s}\right]\left\{\frac{2x^{1/2}}{1+x} - \frac{\ln(1+x)}{x^{1/2}}\right\} \quad \text{(A8)}$$

provides the relief sought. The second term generally converges rapidly.

Cavity Volume Comparisons. The volume of the toroidal cavities considered are

$$V_T = 2\pi a_T(\coth\eta_0)(\pi[a_T\,\mathrm{csch}\,\eta_0]^2) = 2\pi^2a_T^3(\cosh\eta_0/\sinh^3\eta_0) \quad \text{(A9)}$$

and those of the spherical shells of the same thickness and interacting site separation as the rings.

$$V_{SS} = (4/3)\pi a_T^3 \left[\left[\frac{\cosh \eta_0 + 1}{\sinh \eta_0} \right]^3 - \left[\frac{\cosh \eta_0 - 1}{\sinh \eta_0} \right]^3 \right]$$
$$= (8/3)\pi a_T^3 \left[\frac{3 \cosh^2 \eta_0 + 1}{\sinh^3 \eta_0} \right] \quad \text{(A10)}$$

In the volume-matching described, relative positions of the interacting sites with respect to the boundaries were maintained by shrinking a and b by the same factor.

References and Notes

(1) Research carried out at Brookhaven National Laboratory under contract with the U.S. Energy Research and Development Administration and supported by its Division of Physical Research.
(2) J. G. Kirkwood, *J. Chem. Phys.*, 2, 351 (1934).
(3) (a) J. G. Kirkwood and F. H. Westheimer, *J. Chem. Phys.*, **6**, 506 (1938); (b) *ibid.*, **6**, 513 (1938); (c) *ibid.*, **7**, 437 (1939).
(4) A partial review of and source of references for additional applications accompanies description of a recent generalization of the prolate spheroidal cavity model.[5]
(5) S. Ehrenson, *J. Am. Chem. Soc.*, 98, 7510 (1976).
(6) Noell and Morokuma[7] review recent efforts in individual solvent molecule modeling as a prelude to presentation of their fractional charge MO model and mention simple systems (e^-,He)[8,9] where combination models of sorts are applied. Electrical saturation and electrostriction effects, generally ignored or incorrectly evaluated, were recognized classically as accompanyments to bulk dielectric effects.[3a,10,11]
(7) J. O. Noell and K. Morokuma, *J. Phys. Chem.*, 80, 2675 (1976).
(8) M. D. Newton, *J. Chem. Phys.*, 58, 5833 (1973); *J. Phys. Chem.*, 79, 2795 (1975).
(9) J. Hylton, R. E. Cristofferson, and G. G. Hall, *Chem. Phys. Lett.*, **26**, 501 (1974).
(10) C. K. Ingold, *J. Chem. Soc.*, 2179 (1931).
(11) Cf. M. Abraham and R. Becker, "Classical Electricity and Magnetism", Blackie and Son, Ltd., London, 1932; W. R. Smyth, "Static and Dynamic Electricity", McGraw-Hill, New York, N.Y., 1968, Chapter 2.
(12) (a) J. N. Sarmousakis, *J. Chem. Phys.*, **12**, 277 (1944); (b) S. W. Harrison, H.-J. Nolte, and D. L. Beveridge, *J. Phys. Chem.*, **80**, 2580 (1976).
(13) Cf. P. Moon and D. E. Spencer, "Field Theory for Engineers", D. Van Nostrand, New York, N.Y., 1961, Chapter 13, and the following reference for the uniform field representations.
(14) P. M. Morse and H. Feshbach, "Methods of Theoretical Physics", McGraw-Hill, New York, N.Y., 1953, Chapter 10.
(15) Morse and Feshbach (ref 14) give an expansion of R^{-1} (eq 10.3.81) which with several minor corrections yields eq 3 and 4.
(16) How far below the surface of spherical and ellipsoidal cavities interacting sites of contained molecular reactants should be placed in modeling their electrostatic effects and whether common distances could be chosen for families of related molecules are questions of continuing interest.[5,17]
(17) C. Tanford, *J. Am. Chem. Soc.*, 79, 5348 (1957).
(18) N. Bjerrum, *Z. Phys. Chem.*, **106**, 219 (1923).
(19) It can readily be shown that in the limit of vanishing η_0 here, with $D_s \gg D_i$, $D_{eff}/D_i = \{2[1 - D_i/D_s(1 + \ln 2)]\}^{-1}$, a quantity which is uniformly smaller than one.
(20) Cf. S. Ehrenson, *Prog. Phys. Org. Chem.*, **2**, 195 (1964).
(21) (a) M. Abramowitz and I. Stegun, "Handbook of Mathematical Functions", Dover Publications, New York, N.Y., 1965, p 556; (b) *ibid.*, pp 559–560; (c) *ibid.*, p 336, eq 8.11.3; (d) *ibid.*, p 334, eq 8.5.3 and 8.5.4.
(22) Cf. I. M. Ryshik and I. S. Gradstein, "Tables of Series, Products and Integrals", VEB Deutscher Verlag der Wissenschaften, Berlin, 1957, p 162, eq 3.451.

COMMUNICATIONS TO THE EDITOR

Hydrogen Bonding to the Charged π Clouds of the Cyclooctatetraene Dianion and Anion Radical

Publication costs assisted by the University of Puerto Rico

Sir: The fact that the existence of intermolecular hydrogen bonds has an immense effect upon the chemical and physical properties of the interacting systems (i.e., the unusual properties of water and the alcohols) has been recognized for some time.[1] More recently it has been observed that even the π cloud of electrons in aromatic hydrocarbons can serve as weak hydrogen bond acceptors.[2]

Annulenes that contain $4n$ π electrons are distorted from planarity[3] and do not possess the necessary conjugated π system to act as hydrogen bond acceptors. However, the addition of two electrons to these annulenes yields aromatic dianions,[4] which should serve as excellent proton acceptors. Further, the presence of these hydrogen bonds may severely perturb the chemistry of these dianions and the corresponding anion radicals. Here we wish to report the formation of the hydrogen bonded cyclooctatetraene (COT) anion radical (I) and dianion (II), an estimation of the relative strengths of these hydrogen bonds, and the drastic effect they have upon the comproportionation equilibrium that controls the relative concentrations of the dianion, anion radical, and neutral species in solution.

I II

Solutions of COT in hexamethylphosphoramide (HMPA) will dissolve small amounts of sodium metal to form the corresponding dianion and anion radical, which are completely free of ion pairing.[5] The concentrations of these species are controlled by the following comproportionation equilibrium:

$$COT^{2-} + COT \rightleftarrows 2COT^{-\cdot} \quad (1)$$

$$K_{free} = [COT^{-\cdot}]^2/[COT^{2-}][COT] \quad (2)$$

If the addition of a proton donor (ammonia) to this solution results in the formation of I and II it should manifest itself in a change in the comproportionation equilibrium. Since the hydrogen bond in II is stronger than that in I, the presence of small amounts of NH_3 should lead to a displacement of overall equilibrium to the left and decrease the observed equilibrium constant (K_{obsd}, eq 3). However, the presence of large amounts of proton

$$K_{obsd} = ([COT^{-\cdot} \cdots H\text{-}NH_2] + [COT^{-\cdot}])^2/([COT^{2-} \cdots H\text{-}NH_2] + [COT^{2-}])[COT] \quad (3)$$

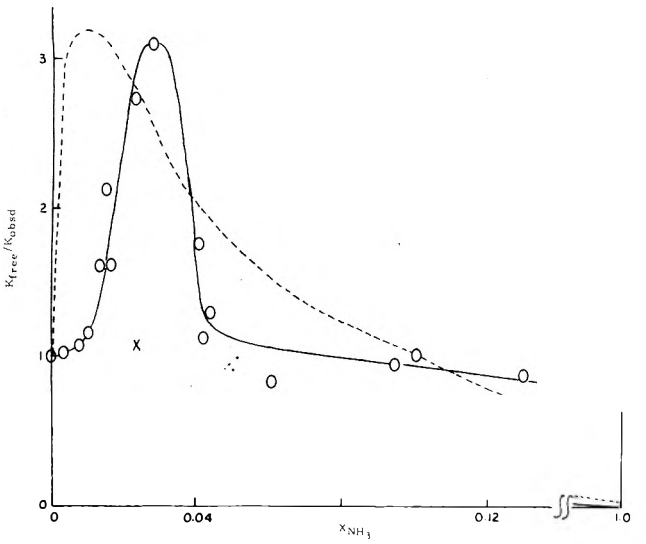

Figure 1. Plots of K_{free}/K_{obsd} vs. the mole fraction of added ammonia. The solid line represents the experimental curve and the dashed line the theoretical curve. The point marked X was taken after the addition of 0.1 M $NaClO_4$.

donor would be expected to cause an increase in K_{obsd} due to the stoichiometry of eq 1. These predictions were confirmed experimentally, Figure 1.

Successive additions of NH_3 to a solution of the COT dianion and anion radical in HMPA first results in an increase in K_{free}/K_{obsd}. This ratio reaches a maximum at about a 3×10^{-2} mole fraction of NH_3 to HMPA (0.17 M).[6] As the NH_3 concentration is further increased K_{free}/K_{obsd} falls off rapidly then more slowly approaches its value in pure ammonia of 10^{-3}.

The relative strengths of the hydrogen bonds in I and II can be determined by comparing K_1 and K_2 as defined by

$$COT^{-\cdot} + NH_3 \rightleftarrows I \quad (4)$$

$$COT^{2-} + NH_3 \rightleftarrows II \quad (5)$$

$$K_1 = [I]/[COT^{-\cdot}][NH_3] \quad (6)$$

$$K_2 = [II]/[COT^{2-}][NH_3] \quad (7)$$

Substituting eq 6 and 7 into eq 4 and 5 and rearranging yields

$$K_{free}/K_{obsd} = (1 + K_2[NH_3])/(1 + K_1[NH_3])^2 \quad (8)$$

By assuming values for K_1 and K_2, theoretical plots of K_{free}/K_{obsd} vs. the mole fraction of added proton donor can be constructed. The plot most closely resembling the experimental curve was obtained by utilizing values of $K_1 = 15$ and $K_2 = 190$.[7] The theoretical plot yields a maximum value for K_{free}/K_{obsd} close to the experimental value, but there are basic differences in the two plots. The theoretical plot rises much more rapidly than does the experimental plot. This fact may be accounted for by the formation of a complex between the solvated sodium cations and the added NH_3. Indeed, amines like ammonia have recently been observed to form complexes with alkali metal cations.[8] If this explanation is correct, the addition of extra Na^+ ions to the solution should result in an increase in the delay. Addition of various concentrations of $NaClO_4$ to the HMPA solution has the expected result. One of these experiments is ploted in Figure 1. At higher concentrations of added NH_3 the formation of ion pairs probably contributes to the deviation from the theoretical curve,[9] but this does not alter the qualitative effects of hydrogen bonding upon the comproportionation equilibrium.

The results reported here show that while the thermodynamic stability of the COT dianion is clearly enhanced by hydrogen bond formation, the solvation of the two species (anion radical and dianion) shifts the disproportionation equilibrium toward the anion radical in the presence of large amounts of proton donor. However, the opposite effect is noted in the presence of small concentrations of donor. The formation of these types of hydrogen bonded complexes is of considerable importance when considering the chemistry of aromatic anions in solution where the solvent may serve as a proton donor.

Other measurements (NMR or IR) of the hydrogen bonding to a charged π cloud are not feasible due to the masking of the effect by the proton donor–solvent interactions. Further, it is not possible to change to an inert solvent as organic dianions are not stable or soluble in this type of media. In conclusion, the free energy of disproportionation of an anion radical is a very sensitive probe into the specific interactions involving organic anions and dianions.

Acknowledgment. G.R.S. wishes to thank his gracious host (Stanford University) where he spent his sabatical year and where this manuscript was prepared. We also wish to thank the National Institutes of Health for partial support of this work.

References and Notes

(1) S. N. Vinogradov and R. H. Linnell, "Hydrogen Bonding", Van Nostrand-Reinhold, New York, N.Y., 1971, p 23.
(2) For a recent example see T. S. Pang and S. Ng, *J. Magn. Reson.*, **17**, 166 (1975).
(3) P. D. Garratt, "Aromaticity", McGraw-Hill, New York, N.Y., 1971.
(4) (a) H. L. Strauss, T. J. Katz, and G. K. Fraenkel, *J. Am. Chem. Soc.*, **85**, 2360 (1963); (b) J. F. M. Oth and G. Schroder, *J. Chem. Soc. B*, 904 (1971); (c) J. F. M. Oth, H. Bauman, J. M. Gilles, and G. Schroder, *J. Am. Chem. Soc.*, **94**, 3498 (1972).
(5) G. R. Stevenson and I. Ocasio, *J. Am. Chem. Soc.*, **98**, 890 (1976).
(6) (a) Dry ammonia (distilled from the solvated electron) was added to the HMPA solution via break seals. (b) K_{free}/K_{obsd} was measure by comparing the overmodulated ESR signal intensities of the solutions taken before and after the NH_3 addition. The relative signal intensities were measured in the dual cavity of a Varian E-9 ESR spectrometer as previously described.[5]
(7) These values for K_1 and K_2 were used to generate the theoretical plot in Figure 1. However, they can only be regarded as order of magnitude estimates of the real equilibrium constants.
(8) H. B. Flora and W. R. Gilkerson, *J. Phys. Chem.*, **80**, 679 (1976).
(9) F. J. Smentowski and G. R. Stevenson, *J. Phys. Chem.*, **73**, 340 (1969).

Department of Chemistry
University of Puerto Rico
Rio Piedras, Puerto Rico 00931

Gerald R. Stevenson*
Aurora Vassos

Received December 10, 1976

Thermochemical Decomposition of Water Catalyzed by Zeolites

Publication costs assisted by the Union Carbide Corporation

Sir: Many thermochemical reaction cycles that would effect the decomposition of water into oxygen and hydrogen have been proposed and/or demonstrated.[1] Most of the processes reported to date, however, consist of four or more reaction steps and often involve highly reactive chemicals such as alkali metal, halogen, or hydrogen halide. We wish to describe in this communication a simple two-step thermochemical cycle, the net reaction of which is the decomposition of water. Only one chemical besides water is required in this process, zeolite of appropriate type containing suitable multivalent cations introduced through

a conventional exchange process.

We reported earlier that anhydrous zeolites possess strong electrolytic or ionizing property.[2] The electrolytic property arises from irregular and extremely spacious arrangement of the charged components within the crystalline structure and the desire on the part of the crystal to create additional charged species in order to establish more uniform and closely spaced distribution of the charges. The presence of such ionization power has been evidenced in (1) dissolution of strong electrolyte, such as NaCl in its ionized state, (2) ionization of adsorbed molecules such as HX (hydrogen halide), (3) induction of electron transfer reactions between adsorbed molecules, and (4) reduction of multivalent zeolitic cations by absorbed molecules.

During an ESR (electron spin resonance) study of Cu-exchanged, mordenite-type zeolites, we observed that the intensity of the ESR signal due to the Cu^{2+} ions decreased to $\sim 1/2$ of the original intensity after vacuum activation at temperatures above 300 °C. We surmised that the reduction of Cu^{2+} to Cu^{+} by residual water in the *nearly* dehydrated zeolite must be responsible for the reduction of the ESR signal. We further observed that the Cu^{2+} ESR signal regained its original intensity when the activated zeolite was hydrated and then exposed to oxygen at room temperature. The signal remained unchanged when the activated sample was exposed to degassed water or to dry oxygen alone at room temperature. The reoxidation of Cu^{+} to Cu^{2+} by oxygen in hydrated zeolite is thus strongly suggested. Using the notation such as $[Na^{+}]$ M to represent the mordenite-type zeolite of the Na^{+} cation form, we may write:

$$[2Cu^{2+}, nH_2O]\,M \xrightarrow[T > 300\ ^\circ C]{-(n-2)H_2O} [2Cu^{2+}, 2H^{+}, 2OH^{-}]\,M \rightarrow [2Cu^{+}, 2H^{+}]\,M + H_2O\uparrow + {}^1/_2O_2\uparrow \quad (1)$$

$$[2Cu^{+}, 2H^{+}]\,M \xrightarrow[\text{room temp}]{+{}^1/_2O_2 + (n-1)H_2O} [2Cu^{2+}, nH_2O]\,M \quad (2)$$

Reaction 1 can be viewed as yet another manifestation of the electrolytic property of anhydrous zeolite, the ionization of the residual water followed by the reduction of Cu^{2+} by the hydroxide ions. The presence of residual water in activated zeolites with multivalent cations has been shown by infrared[3] and X-ray[4] studies. Reaction 2 represents an expected chemistry of Cu^{+} in an acidic, oxygenated aqueous environment.

The proposed reactions 1 and 2 constitute a cyclic process, the net effect of which is the liberation of oxygen from H_2O. The volume and mass-spectroscopic analyses of the noncondensable gaseous material evolved during activation above 300 °C indeed revealed that the gas is essentially oxygen (>90%) and corresponds in quantity to that expected from the reduction of $\sim 50\%$ of the Cu^{2+} ions present in the zeolite. In order to obtain further substantiation of the proposed mechanism a sample of Cu–mordenite was activated at 300 °C, exposed to water vapor enriched with ^{18}O (the enrichment = 10%) and normal oxygen at room temperature, and then subjected to the second activation. The oxygen evolved during the second activation contained $\sim 10\%$ $^{18}O^{16}O$. Had all the oxygen been generated from the enriched water, the concentration of $^{18}O^{16}O$ would have been 18%. The observed dilution of ^{18}O in the evolved oxygen is attributed to the water present in the initially activated zeolite and also to the water produced from normal oxygen according to the reaction 2.

It is illustrative to examine the reaction 2 in terms of the relevant reduction potentials.

$$Cu^{2+} + e^{-} \rightarrow Cu^{+} \qquad E^\circ = +0.158\ V$$

$$H^{+}\ (pH\ 7.0) + e^{-} \rightarrow {}^1/_2H_2\uparrow \qquad E^\circ = -0.414\ V$$

$$O_2 + 4H^{+}\ (pH\ 7.0) + 4e^{-} \rightarrow 2H_2O \qquad E^\circ = +0.815\ V$$

The need for both oxygen and water for the reoxidation of Cu^{+} to Cu^{2+} was thus explained. We also noted that, if one could exchange into zeolite a sufficient amount of multivalent cations M^{q+} for which the reduction potential for the half-cell reaction $M^{q+} + e^{-} \rightarrow M^{(q-1)+}$ is more negative than –0.414 V, the cations reduced by water upon activation would be oxidized by water generating hydrogen.

$$[2M^{q+}, nH_2O]\,M \xrightarrow[\Delta]{-(n-1)H_2O} [2M^{(q-1)+}, 2H^{+}]\,M + {}^1/_2O_2\uparrow \quad (3)$$

$$[2M^{(q-1)+}, 2H^{+}]\,M \xrightarrow[\text{room temp}]{+nH_2O} [2M^{q+}, nH_2O]\,M + H_2\uparrow \quad (4)$$

The reduction potential for the $Cr^{3+}|Cr^{2+}$ cell is –0.41 V. Taking cognizance of the fact that the reaction 4 would be facilitated further in an acidic environment, we prepared Cr^{3+}-exchanged mordenite starting with H^{+} zeolon. The resulting material [chemical analysis: $Cr_{0.08}{}^{3+}\ H_{0.77}{}^{+}\ (AlO_2)_{1.0}\ (SiO_2)_{9.1}$] was indeed found to undergo the reaction cycle (3) ⇄ (4), generating oxygen and hydrogen in alternate steps. A representative experiment is described below.

Fifteen grams of Cr^{3+}-exchanged H^{+} zeolon (described above) was evacuated at room temperature for 2 h and then heated to 500 °C over a period of 6 h. The gaseous product evolved during the heat-treatment was collected and analyzed by mass spectrometry and by gas chromatograph. It was found to be 5 cm^3 (stp) of oxygen indicating the reduction of $\sim 50\%$ of Cr^{3+} to Cr^{2+} according to reaction 3. The activated material was then cooled to, and maintained at 50 °C, and exposed to water vapor for 6 h. The gaseous phase in equilibrium with the rehydrated zeolite was found to contain a significant amount of hydrogen. The comparison of the observed gas chromatographic peak with that of a reference hydrogen–air mixture showed that the quantitative production of hydrogen according to the reaction scheme 4 had occurred. The cycle was repeated four times on the same sample obtaining the identical result at each cycle.

Similar results were obtained from In^{3+}-exchanged H zeolon [chemical analysis: $In_{0.16}{}^{3+}\ H_{0.53}{}^{+}\ (AlO_2)_{1.0}\ (SiO_2)_{7.7}$]. The reduction potential of the $In^{3+}|In^{2+}$ cell is –0.49 V.

For a two-step water thermolysis process consisting of an endothermic step at T_H, and an exothermic step at T_L ($T_H > T_L$), the thermodynamic efficiency requires that

$$Q\left(\frac{T_H - T_L}{T_H}\right) \geq \Delta G_{H_2O}$$

where Q is the heat absorbed at T_H and ΔG_{H_2O} is the standard free energy of formation of water. The minimum entropy change incurred during the first step is thus given by

$$\Delta S = \frac{Q}{T_H} \geq \frac{\Delta G_{H_2O}}{T_H - T_L} \simeq 120\ \text{eu}$$

where the last figure is for T_H = 800 K and T_L = 300 K. Such a large entropy change is rarely found in a single chemical reaction. The standard entropy change associated with the reaction H_2O (l) → $H_2 + {}^1/_2O_2$ is 40 eu. A large entropy change can be realized by resorting to a cycle consisting of many reaction steps or to a single reaction involving many molecules. All the processes reported to date for the thermochemical decomposition of water consist of several chemical reactions. The zeolite process

described here represents the first demonstrated example of a two-step process and resorts to a reaction involving many water molecules of hydration as given in (3).

References and Notes

(1) See, for example, a review article by R. E. Chao, *Ind. Eng. Chem., Prod. Res. Develop.*, **13**, 94 (1974).
(2) P. H. Kasai and R. J. Bishop, Jr., *J. Phys. Chem.*, **77**, 2308 (1973).
(3) J. A. Rabo, C. L. Angell, P. H. Kasai, and V. Schomaker, *Chem. Eng. Prog., Symp. Ser.*, **63**, 31 (1967).
(4) O. H. Olson, *J. Phys. Chem.*, **72**, 1400 (1968).

Union Carbide Corporation **Paul H. Kasai***
Tarrytown Technical Center **Roland J. Bishop, Jr.**
Tarrytown, New York 10591

Received March 20, 1977

Boundary Conditions for Integration of the Equation of Continuity

Sir: The writer is grateful to Professor C. Alden Mead (University of Minnesota) for an analysis which shows that the boundary condition

$$\lim (f'_{ji}/n^2) \neq \infty, \quad c \to 0 \tag{1}$$

is insufficient for the complete evaluation of A_0, a coefficient which appears in the integration[1] of the equation of continuity. The integration is reviewed below; it will be shown that $A_0 = -1$ is the limiting value of A_0 at zero concentration. Consequently, the 1975 derivation in effect contains an unstated approximation: terms of order $\varkappa^2R^2$ and higher in A_0 were omitted. These terms in A_0 would lead to additional terms of order c and higher in the conductance function $\Lambda(c)$.

The equation of continuity is

$$\mathrm{div}_1(\mathrm{f}_{ij}\mathrm{v}_{ij}) + \mathrm{div}_2(f_{ji}\mathrm{v}_{ji}) = 0 \tag{2}$$

where v_{ij} is the velocity of a j ion in an element of volume $\mathrm{d}V_2$, given the presence of an i ion in $\mathrm{d}V_1$ which is at a distance r_{21} from $\mathrm{d}V_2$. The distribution functions are defined by

$$f_{ij} = n_i n_{ij} = n_j n_{ji} = f_{ji} \tag{3}$$

where

$$n_{ij} = n_j \exp(-e_j\psi_i/kT) \tag{4}$$

gives the local concentration of j ions at $\mathrm{d}V_2$ and ψ_i is the potential at $\mathrm{d}V_2$ due to the i ion and its atmosphere, and congruently for n_{ji}. These functions give the probability of simultaneously finding a j ion in $\mathrm{d}V_2$ and an i ion in $\mathrm{d}V_1$. In the presence of an external field X

$$f_{ji} = f^0_{ji} + f'_{ji} \tag{5}$$

and

$$\psi_j = \psi^0_j + \psi'_j \tag{6}$$

where the zero-superscripted symbols refer to the spherically symmetric functions in the absence of an external field and the primed symbols represent the perturbations produced by the field. Substitution of explicit values for the velocities and rearrangement converts (2) into eq 2.12 of the 1975 paper:

$$\begin{aligned}(\Delta - \varkappa^2/2)f'_{21} = {} & \\ & - n^2 Xe\beta \exp(-\varkappa r)(1 + \varkappa r)\cos\theta/r^2\mu kT \\ & - \varkappa^2\xi(1 + \xi/2)f'_{21}/2 + \Phi(\varkappa, r, \psi'_j, f'_{21})\end{aligned} \tag{7}$$

Above, $n = n_1 = n_2$ is concentration, $e = e_1 = -e_2$ is charge, $\beta = e^2/DkT$, θ is the angle between $\mathbf{r}_{21}$ and the field direction

$$\xi = e_i\psi^0_j/kT = e_j\psi^0_i/kT \tag{8}$$

and

$$\varkappa^2 = 8\pi n\gamma e^2/DkT, \qquad n = Nc/1000 \tag{9}$$

The first term on the right of (7) is the origin of the leading term of order $c^{1/2}$ in the conductance function, the second term is from the Boltzmann factor approximated by the truncated series

$$e^\xi = 1 + \xi + \xi^2/2 \tag{10}$$

and the last term is a complicated function of the indicated quantities. Equation 7 is a second-order inhomogeneous equation, impossible to solve explicitly; it was therefore treated by the methods of successive approximations.

First, f'_{21} was separated into two parts

$$f'_{21} = Q_0(\varkappa, r)\cos\theta + G_{21} \tag{11}$$

where Q_0 is defined as the solution of

$$\begin{aligned}\partial^2 Q_0/\partial r^2 + (2/r)(\partial Q_0/\partial r) & \\ - (2/r^2 + \varkappa^2/2)Q_0 = -n^2 C\, g(\varkappa, r)\end{aligned} \tag{12}$$

In (12)

$$g(\varkappa, r) = \exp(-\varkappa r)(1 + \varkappa r)/r^2 \tag{13}$$

and

$$C = Xe\beta/\mu kT \tag{14}$$

Substitution of (11) in (7) gives

$$\begin{aligned}(\Delta - \varkappa^2/2)(Q_0\cos\theta + G_{21}) = {} & -n^2 Cg(\varkappa, r)\cos\theta \\ & + [\varkappa^2\xi(1 + \xi/2)f'_{21}/2 + \Phi(\varkappa, r, f'_{21}, \psi'_j)]\end{aligned} \tag{15}$$

Multiplying (12) by $\cos\theta$ and subtracting the result from (15) gives the partial differential equation

$$(\Delta - \varkappa^2/2)G_{21} = [(15)] \tag{16}$$

where the symbol [(15)] denotes the quantity in brackets in (15). It was shown that Q_0 is the source of the limiting relaxation term of order $c^{1/2}$ in the conductance function $\Lambda(c)$. Therefore G_{21} is the source of terms of order c and higher in $\Lambda(c)$. By using $Q_0\cos\theta$ as the first approximation for f'_{21} in [(15)] (and the corresponding part $P_0\cos\theta$ as first approximation to ψ'_j) in [(15)], we obtain

$$\begin{aligned}(\Delta - \varkappa^2/2)G_{21} = {} & (\varkappa^2\xi/2)(1 + \xi/2)Q_0\cos\theta \\ & + \Phi(\varkappa, r, Q_0, P_0, \cos\theta)\end{aligned} \tag{17}$$

where explicit (rather than unknown) functions now appear in the inhomogeneous term on the right. Solution of (17) gives the first approximation to G_{21}; when these terms are added to $Q_0\cos\theta$, we have the second approximation to f'_{21}, as previously[1,2] described.

Here we are concerned with (12), the partial differential equation which determines $Q_0(\kappa, r)$. The solution is

$$\begin{aligned}Q_0(\varkappa, r) = {} & -(2n^2 Xe\beta/\mu kT\,\varkappa^2 r^2)[\exp(-\varkappa r)(1 \\ & + \varkappa r) + A_0\exp(-q\varkappa r)(1 + q\varkappa r) \\ & + B_0\exp(q\varkappa r)(1 - q\varkappa r)]\end{aligned} \tag{18}$$

Since Q_0 must vanish for $r = \infty$, $B_0 = 0$. Since Q_0 is part of f'_{ji}, condition (1) requires that

$$\begin{aligned}\lim \{ & [\exp(-\varkappa r)(1 + \varkappa r) \\ & + A_0\exp(-q\varkappa r)(1 + q\varkappa r)]/\varkappa^2 r^2\} \neq \infty, \quad c \to 0\end{aligned} \tag{19}$$

Expand the exponentials in (19) and let

$$A_0 = a_0 + a_1 \varkappa R + a_2 \varkappa^2 R^2 + \cdots \quad (20)$$

The result is

$$\lim [(1 + a_0)/\varkappa^2 + a_1 R/\varkappa + (a_2 - a_0/4 - 1/2)R^2 + (a_0 q/24 + a_1/4 + a_3 + 1/6)\varkappa R^3 + \ldots] \neq \infty \quad (21)$$

To keep the quantity in brackets finite at $\kappa = 0$, a_0 must equal -1 and a_1 must be 0. However the coefficients a_2, a_3, etc. remain unknown; condition (1) shows only that

$$A_0 = -1 + a_2 \varkappa^2 + a_3 \varkappa^3 + \ldots \quad (22)$$

For the limit of zero concentration, $A_0 = -1$; this value was used in the 1975 derivation, by substitution in the right-hand side of (15). Since G_{21} leads to terms of order c and higher in $\Lambda(c)$, retention of the terms of order $\varkappa^2$ in (20) would generate terms of order c^2 and higher in $\Lambda(c)$. As corrections to corrections, this effect probably is negligible, but the presence of $a_2\varkappa^2$ in Q_0 will produce additional terms of order c in $\Lambda(c)$.

The consequences of the approximation $A_0 \approx -1$ will now be considered. It has been shown[3] that conductance data at low concentrations can be reproduced by the semi-empirical equation

$$\Lambda = \Lambda_0 - Sc^{1/2} + Ec \log c + J_1 c + J_2 c^{3/2} \quad (23)$$

where S and E are theoretically predictable coefficients which depend only on DT, η, and valence type, and J_1 and J_2 are the intercept and slope of a plot of

$$y = (\Lambda - \Lambda_0 + Sc^{1/2} - Ec \log c)/c \quad (24)$$

against $c^{1/2}$. Equation 23 is a three-parameter equation: $\Lambda = \Lambda(c; \Lambda_0, J_1, J_2)$ where J_1 and J_2 can be evaluated directly from the data. The 1975 conductance function is also a three-parameter equation: $\Lambda = \Lambda(c; \Lambda_0, K, R)$, where K is the pairing constant and R is the diameter of the Gurney cospheres surrounding unpaired ions. In principle, analyzing a set of conductance data by use of the 1975 equation is equivalent to solving the equations

$$f_1(K, R) = J_1 \qquad f_2(K, R) = J_2 \quad (25)$$

for K and R. Let K' and R' be the values obtained for a given set of data using the 1975 equation with $A_0 = -1$. Now if a new equation were derived in which the higher terms of $A(\varkappa R)$ were explicit, the coefficients in f_1 and f_2 would be changed, because terms of order $\varkappa^2$ and higher in $A(\varkappa R)$ would lead to additional terms of order c and higher in $\Lambda(c)$. Consequently the values K'' and R'' obtained using the new equation would be different from K' and R', but the limiting conductances will be the same because S and E are unchanged. Furthermore, for several sets of data (for example, a given salt in a series of mixtures of two solvents), one might expect to find the same sequence of values; i.e., if $K'_1 > K'_2 > K'_3$, etc. then $K''_1 > K''_2 > K''_3$, etc.

Finally, a new boundary condition is proposed to replace (1). The distribution function $f_{21} = n_2 n_{21}$ is proportional to the concentration of ions of species 1 at a distance r from a reference ion of species 2. By definition of the 1975 model, unpaired ions are those whose cospheres contain only the reference ion and therefore n_{21} is zero for distances $a \leq r \leq R$ from unpaired ions of species 2. In terms of f_{21}, the corresponding boundary condition is

$$f_{21}(R) = 0 \quad (26)$$

which leads to

$$Q_0(R) = 0 \quad (27)$$

as the condition which Q_0 must satisfy. Substituting $r = R$ in (18) and using (27) gives

$$A_0(t) = -\exp(-t)(1 + t)/\exp(-qt)(1 + qt) \quad (28)$$

where $t = \varkappa R$. [Note that $A_0(0) = -1$.] The corresponding term in the relaxation field is obtained by integration [ref 1, eq 2.45]; the result is

$$\Delta X_0/X = -\beta \varkappa /6(1 + q)(1 + t)(1 + qt) \quad (29)$$

where $\beta = e^2/DkT$. Work on the evaluation of the higher terms of the relaxation field and of the hydrodynamic terms in $\Lambda(c)$ using (26) as the fourth boundary condition is in progress.

References and Notes

(1) R. M. Fuoss, *J. Phys. Chem.*, **79**, 525 (1975).
(2) R. M. Fuoss, *J. Phys. Chem.*, **80**, 2091 (1976).
(3) R. M. Fuoss, *Proc. Natl. Acad. Sci. U.S.A.*, **71**, 4491 (1974).

Sterling Chemistry Laboratory
Yale University
New Haven, Connecticut 06520
Raymond M. Fuoss

Received May 9, 1977

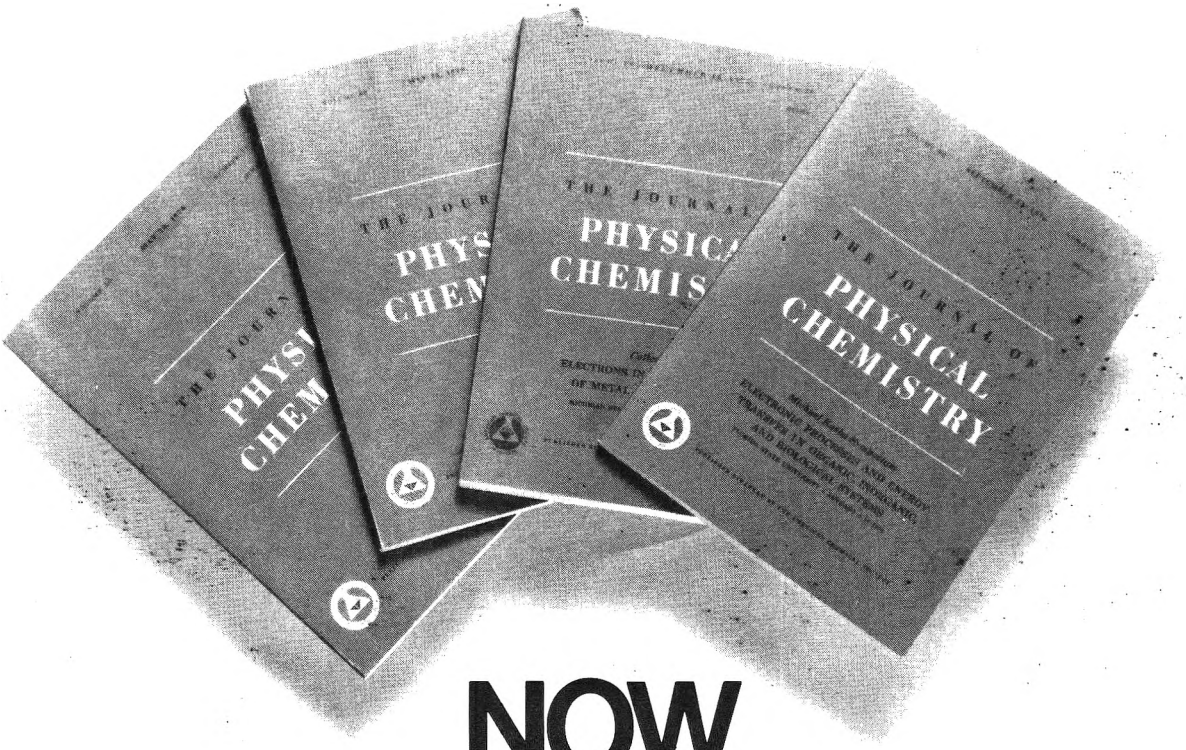

NOW you can buy all four special issues of The Journal of Physical Chemistry

and *save money on three of them.*

By buying the December 16, 1976 J. L. Franklin issue for the regular price of $4.75, you can get the **three other special issues for only $10.00!**

The Franklin issue consists of a collection of papers in theoretical and applied research, especially thermodynamics and energetics.

The other issues are:

- **Colloque Weyl IV.**
  Electrons in Fluids—The Nature of Metal-Ammonia Solutions
- **Michael Kasha**
  Symposium—Electronic Processes and Energy Transfer in Organic, Inorganic, and Biological Systems
- **Richard C. Lord**
  Issue consists of contributions from colleagues, former students, and associates of Dr. Lord. Papers are on spectroscopy and related subjects

You can order just one or two of the issues instead of all three. In that case, the price is $4.00 per issue. But please remember, it is necessary to buy the Franklin issue at the regular price before you can take advantage of the lower price.

Just fill out the form and mail it back to us today. We'll see that you receive the issue or issues of your choice just as soon as we can process your order.

MAIL WITH REMITTANCE TO:

Business Operations
American Chemical Society
1155 16th Street, N.W.
Washington, D.C. 20036

Please send me the following JOURNAL OF PHYSICAL CHEMISTRY SPECIAL ISSUES:

J. L. Franklin issue	☐ $4.75
Colloque Weyl IV. Issue	☐ $4.00*
Michael Kasha Symposium	☐ $4.00*
Richard C. Lord Issue	☐ $4.00*

*All three ☐ $10.00

I am enclosing _____.

☐ Check ☐ Money Order

Please print clearly.

NAME _____

ADDRESS _____

CITY _____

STATE/
COUNTRY _____ ZIP _____

A new concept in scientific publishing:

Journal of Chemical Research

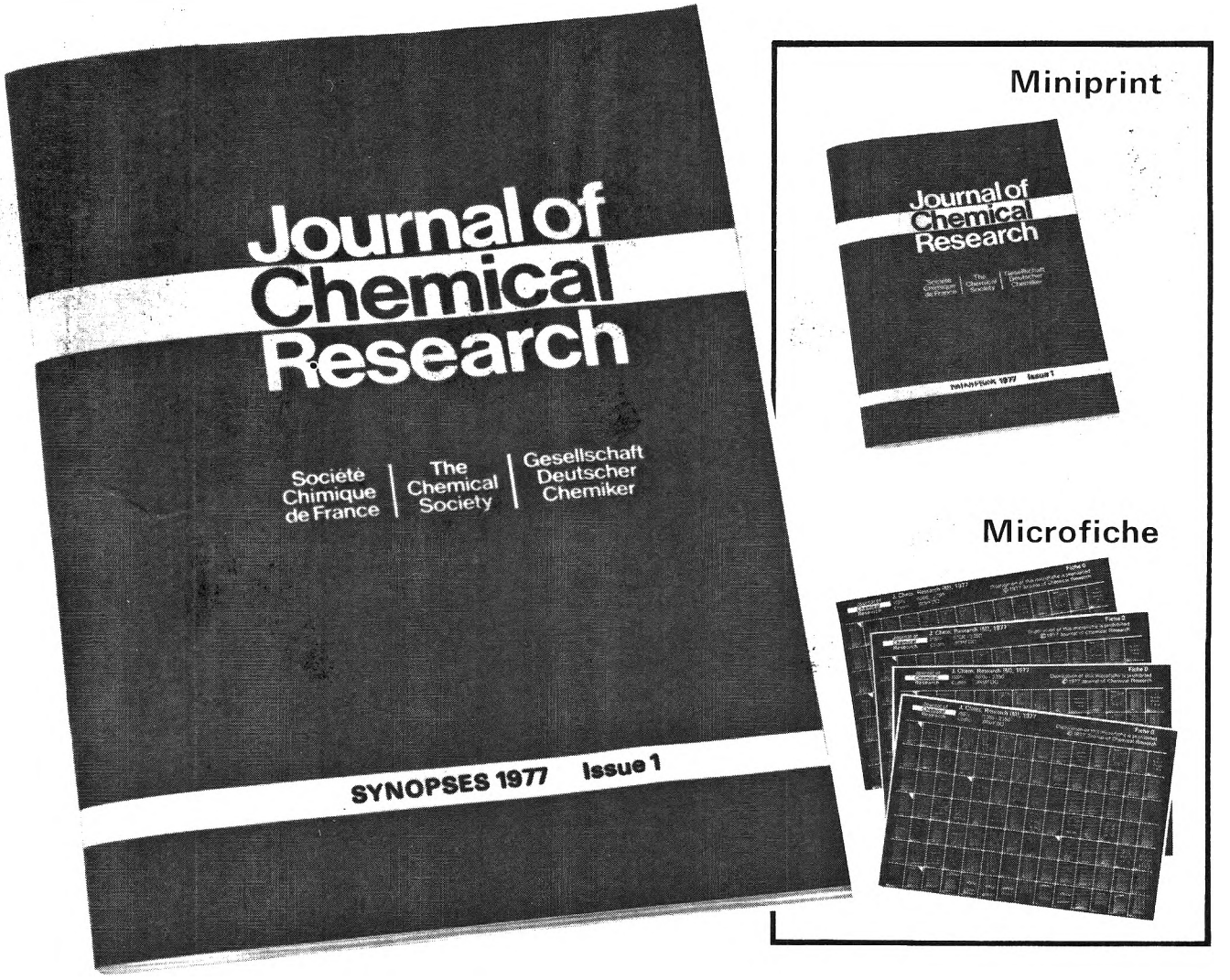

Journal of Chemical Research is a new multi-national journal which is being published in synopsis format backed up simultaneously with full texts in two forms – microfiche and miniprint. It was launched in January 1977 by The Chemical Society, Gesellschaft Deutscher Chemiker and Société Chimique de France as the first step towards the development of a more logical system of chemical primary publications.

It covers all kinds of chemistry and appears in two parts: Part S caters for current awareness needs and contains short synopses of papers in an easily browsable form; Part M fulfils the archival role of the journal and contains the full texts of the papers appearing in Part S in two alternative forms – microfiche and miniprint.

For sample copies and subscription details please complete and return the coupon:

To: The Marketing Officer, The Chemical Society, Burlington House, London W1V 0BN, England.
Please send me a sample copy and subscription details of JOURNAL OF CHEMICAL RESEARCH.

Name .....

Address .....

Founding Sponsors:

The Chemical Society
Gesellschaft Deutscher Chemiker
Société Chimique de France

Supporting Societies:

Norsk Kjemisk Selskap Société Chimique de Belgique
Verein Österreichischer Chemiker Vlaamse Chemische Vereniging
Deutsche Gesellschaft für Chemisches Apparatewesen